Crystallography Reports, Vol. 49, No. 2, 2004, pp. 149–157. Translated from Kristallografiya, Vol. 49, No. 2, 2004, pp. 199–207.

CRYSTAL CHEMISTRY

On the Mechanism of Trace-Element Uptake during the Hydrothermal Growth of Sulfide Mineral Crystals[1]

V. L. Tauson, D. N. Babkin, I. Yu. Parkhomenko, and V. I. Men'shikov

Vinogradov Institute of Geochemistry, Siberian Division, Russian Academy of Sciences, ul. Favorskogo 1a, Irkutsk, 664033 Russia

e-mail: vltauson@igc.irk.ru

Received March 3, 2003

Abstract—The stable species of cadmium and mercury are formed in iron and lead sulfides at elevated temperatures and pressures under hydrothermal conditions. Their formation proceeds through different mechanisms. The most general mechanism involves the uptake of trace elements in the form of structural species due to isomorphous exchange. The results obtained for cadmium in pyrrhotite indicate that structural defects substantially affect the incorporation of impurities into the crystal structure. It is found that trace elements are accumulated on the surface in the absence of defects and are incorporated into the crystal bulk in the form of structural impurities in the presence of defects. Moreover, at elevated temperatures and pressures, trace elements can form their own (surface nonautonomous) phases. These phases are formed not only at trace-element concentrations close to saturation (Cd in $Fe_{1.0}S$) but also under conditions far from saturation as a result of the interaction of trace elements with the oxidized surface of the mineral (the cadmium uptake by galena with the formation of either a sulfate surface phase or a sulfate–chloride surface phase). An important mechanism of trace-element uptake by sulfides during the hydrothermal growth of crystals is associated with external and internal adsorption of impurities by defects. This adsorption manifests itself both in an increase in the content of sorbed mercury in galena at a high sulfur activity due to the interaction of mercury with lead vacancies and in the formation of dislocation cadmium species, which results in an increase in the coefficient of cadmium distribution in the crystal–solution system. © *2004 MAIK "Nauka/Interperiodica".*

INTRODUCTION

At present, the mechanisms of trace-element uptake during the hydrothermal growth of sulfide crystals (the main ore-forming minerals) are poorly understood. Although data on the isomorphous uptake during growth of quartz and beryl crystals activated by different impurities are available in the literature, as has been noted recently by Widler and Seward [1], no experimental investigations into surface adsorption have been performed under hydrothermal conditions. However, knowledge of these mechanisms is particularly important both for the development of the technique of activating crystals by impurities in the course of the hydrothermal growth and for the understanding of the geochemistry of trace elements and practical use of their indicator properties. In our recent work [2], we demonstrated that the mechanism of absorption (uptake) of cadmium impurities during the hydrothermal growth of iron sulfide crystals involves the formation of strongly adsorbed species in the form of a surface compound (or complex) at relatively low impurity concentrations and the formation of the surface nonautonomous phase at impurity concentrations close to saturation of the mineral with cadmium. The nonautonomy implies that such phases cannot exist independently; i.e., they exist only in an ensemble with other (as a rule, bulk) phases of the same crystals. Strongly adsorbed species of ore elements can occur on the surface of hydrothermally synthesized minerals [3, 4]. From the aforesaid, it is clear that, to date, only the first steps have been made toward the elucidation of the mechanisms of trace-element uptake at elevated temperatures and pressures under dynamic conditions of crystal growth. In this work, we experimentally investigated the trace-element uptake by sulfide mineral phases during growth of sulfide mineral crystals under hydrothermal conditions simulating natural endogenous mineral formation.

EXPERIMENTAL

Crystals of stoichiometric pyrrhotite with cadmium impurities were prepared according to the standard procedure of thermal-gradient synthesis under hydrothermal conditions. The crystals were grown in autoclaves equipped with floating-type titanium inserts with a volume of approximately 50 cm^3 in a 10% NH_4Cl solution at a temperature of 450°C and a pressure of 1 kbar (100 MPa) [2, 5]. The initial batch had the composition Fe + S + CdS. Samples of nonstoichiometric pyrrhotite were synthesized in the Fe–S–ZnS–PbS–CdS system under the same conditions. The duration of the synthe-

[1] This work was presented at the National Conference on Crystal Growth (NCCG-2002, Moscow).

1063-7745/04/4902-0149$26.00 © 2004 MAIK "Nauka/Interperiodica"

sis was 12 days. The isothermal conditions were maintained over a period of the first three days in order to homogenize the batch and to provide close-to-equilibrium conditions in the course of subsequent recrystallization, during which the temperature difference across the outer wall of the autoclave was equal to 10 K. The experiments were finished by quenching the autoclaves in cold running water.

The galena crystals containing mercury and cadmium impurities were synthesized in sealed silica glass (optical quality) tubes in a 5% NH_4Cl solution at a temperature of 400°C and a pressure of 500 bar. The batch consisted of PbS with additives of 0.1–1.0 wt % HgS and CdS. The tubes were placed in standard stainless steel autoclaves. The temperature difference across the outer wall of the autoclave was equal to 10–15 K, and the duration of the synthesis was 8 days. In the experiments, the activities of sulfur and oxygen ions were maintained using buffer mixtures placed in gold tubes, which were closed but not welded. Samples of a high-temperature fluid (i.e., a supercritical water–salt solution from which the PbS crystals were grown) were taken with the use of silica glass samplers. In the course of the experiments, the fluid filled the entire volume of the sampler. Upon quenching, the fluid partially condensed in the form of a solution whose chemical composition was identical to that of the fluid.

The surface of the crystals grown was analyzed using X-ray photoelectron spectroscopy and Auger electron spectroscopy on a Riber LAS-3000 spectrometer (equipped with a hemispherical analyzer for electrons with a retarding potential) and an Auger electron spectrometer of the cylindrical mirror type. Atoms of the sample surface were excited by AlK_α radiation from an aluminum anode (λ = 1486.6 eV; emission current, 20 mA; tube voltage, 10 kV). The spectra were calibrated against the C 1*s* line (binding energy, 285 eV). The Auger electron spectra were recorded in the differential form $dN(E)/dE$ (primary beam energy, 2.5 keV; modulation voltage across the outer analyzer cylinder, 2.3 V). The sample surface was etched with the use of an Ar ion beam (energy, 2 keV; emission current, 20 mA) at a rate of the order of 0.1 nm/s. The residual pressure in an analytical chamber was equal to 5×10^{-10} Torr. The spectra were processed by standard methods for extracting qualitative and quantitative information on the surface composition [6, 7]. The atomic concentrations of elements were calculated from the intensities of Auger peaks and the elemental sensitivity coefficients. The errors in determining the peak position and the elemental composition of the surface were equal to ±0.1 eV and ±10%, respectively.

Additional information regarding the adsorbed species of impurity elements was obtained using the thermal atomic absorption (TAA) analysis. The TAA method is based on a combination of atomic absorption spectrometry and thermal analysis. In this case, the recording of an atomic absorption spectrum is attended by controlling (measuring) the temperature of element release. The temperature of element release for a particular species, as a rule, is preliminarily determined by calibrating, for the most part, against the synthetic minerals with known species of the studied elements. Mercury and, especially, cadmium are convenient objects of investigation with the use of thermal atomic absorption. These elements are characterized by well-resolved thermal peaks corresponding to the element release and low detection limits (1.0 and 0.1 ng, respectively) [3, 8]. The analytical setup implementing the TAA method was described in detail in our earlier work [8]. This setup consisted of a Perkin-Elmer-503 atomic absorption spectrometer equipped with a deuterium corrector for background absorption, a light source of an element to be analyzed, an HGA-72 graphite furnace (atomizer), a programmable heater, and a temperature meter involving a thermocouple and a two-coordinate potentiometer. The thermocouple signal was plotted along the *X* coordinate, and the absorption signal from the spectrometer was plotted along the *Y* coordinate. The TAA curves of element release thus obtained were written on chart paper of the potentiometer. For a quantitative analysis, the areas under the thermal peaks were determined by a digital integrator. In the course of thermal atomic absorption analysis, platinum boats served as sample containers. In order to measure the temperature parameters of the element release more precisely, the platinum boat was completed with a thermocouple mounted in a special graphite holder in the furnace. In this work, the concentrations of trace elements were relatively high and the accurate quantitative analysis was complicated by an insufficient resolution of thermal peaks and the necessity of using a powder diluent. In our experiments, the powder diluent (Al_2O_3, analytical grade) did not contain cadmium and mercury at the level of detection sensitivity of the method [3]. For these reasons, our data on the elemental composition in different species are approximate and the error in determining the content of elements is equal to ±30%.

The X-ray powder diffraction analysis of the products synthesized and the determination of the pyrrhotite composition for calculating the sulfur activity were performed on a DRON-3 diffractometer (FeK_α radiation, Mn filter) according to the standard technique [9]. After the experiments, the solutions were analyzed for cadmium by flame atomic absorption spectrometry. The mercury content in the solutions was determined using the cold vapor technique on an atomic absorption spectrometer and an atomic fluorescence spectrometer.

RESULTS AND THEIR ANALYSIS

Cadmium in pyrrhotite. Stoichiometric pyrrhotite forms small-sized (up to 1–1.5 mm) hexagonal short-prismatic and platelike crystals. In each experiment, we obtained crystals of two types, namely, crystals with brass yellow lustrous faces and crystals with dull darker faces. According to the X-ray powder diffraction data,

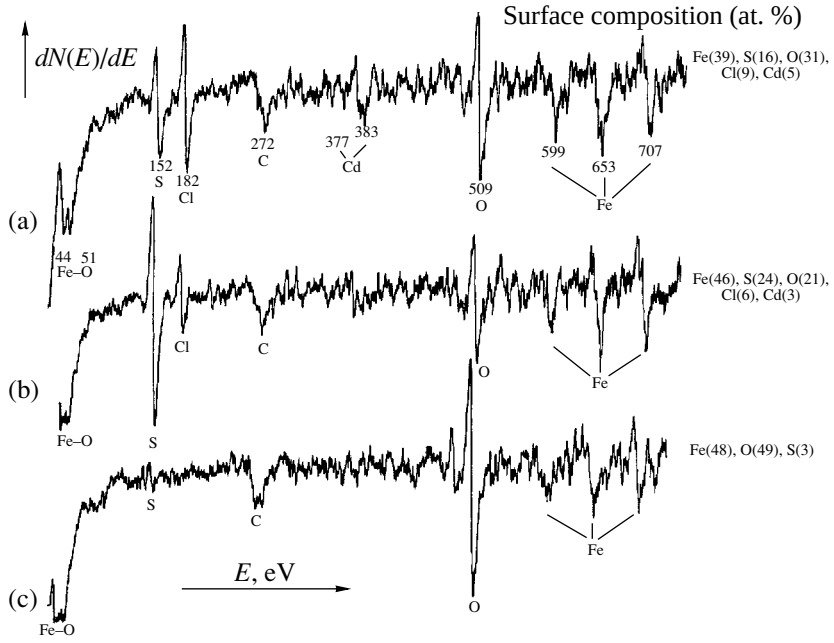

Fig. 1. Differential Auger electron spectra of the hydrothermally grown crystals of stoichiometric pyrrhotite FeS with Cd impurities (~10^{-2} wt %): (a) crystals with a lustrous surface, (b) the same crystals after ion etching for 20 min (decrease in the Cd, Cl, O contents at the surface), and (c) crystals with a dull surface (iron oxide). Conditions of hydrothermal growth: temperature, 450°C; pressure, 1 kbar; 10% NH_4Cl solution.

the α-Fe phase is retained in the batch and the products contain magnetite in the form of octahedra up to 2 mm in size. Crystals of nonstoichiometric $Fe_{0.88}S$ pyrrhotite grown in the Fe–S–ZnS–PbS–CdS system are larger in size (up to 3–4 mm) and more isometric in shape. These crystals are formed in a three-phase mixture with sphalerite and galena. It should be noted that galena and, especially, sphalerite readily absorb cadmium through the mechanism of isomorphous exchange; moreover, the incorporation of CdS into FeS is considerably facilitated in the presence of vacancies in the structure [5]. In this respect, it was of interest to investigate the behavior of cadmium in the experiment, especially when the impurity concentration is relatively high but cadmium cannot form its own phase.

Stoichiometric pyrrhotite crystals have an oxidized surface. The X-ray photoelectron spectrum of the stoichiometric pyrrhotite crystal contains the Fe $2p_{3/2}$ peak, which indicates the presence of iron in both valence states, as is the case in magnetite. Two types of crystals observed in the experiments differ in the chemical composition of their surfaces. In the case of crystals with lustrous faces, the surface is less oxidized and contains cadmium (Fig. 1a). The ion etching leads to a decrease in the cadmium, chlorine, and oxygen contents. After etching, the surface composition approaches the stoichiometric composition, i.e., (Fe + Cd) / (S + O + Cl) ≃ 1 (Fig. 1b). The crystals with dull faces are characterized by an oxidized surface free of cadmium (Fig. 1c). It is worth noting that the sorption of cadmium by magnetite Fe_3O_4 is substantially weaker than the sorption of this element by simultaneously growing stoichiometric pyrrhotite [2, 5]. Table 1 presents the experimental data for cadmium in stoichiometric pyrrhotite samples in comparison with the results obtained in this work and data available in the literature for reference (different chemical) compounds of cadmium. Since the chemical shifts are relatively small, the problem regarding the identification of particular cadmium species on the surface calls for more detailed analysis of the spectroscopic data and their comparison with the results of the TAA measurements. Figure 2 depicts the TAA curves of cadmium release from pyrrhotites of different compositions. For stoichiometric pyrrhotite, cadmium is an incompatible element: it is completely located in the surface layer and is incorporated through the sorption. Consequently, despite the low concentration (10^{-2}–10^{-4}%), cadmium is observed in the surface layer (Fig. 1a). The curves of cadmium release measured in the course of thermal atomic absorption analysis exhibit one or two peaks associated with surface cadmium species (Fig. 2). The two upper curves in Fig. 2 correspond to stoichiometric pyrrhotite with different cadmium contents (for convenience of comparison, the upper curve is drawn on an enlarged scale along the ordinate axis). It can be seen from Fig. 2 that the own mineral (sulfide) species is observed only at high cadmium concentrations close to saturation, whereas the sorbed species is predominant at low concentrations. The lower curve in Fig. 2 corresponds to the nonstoichiometric pyrrhotite formed together with galena and sphalerite upon the hydrother-

Table 1. X-ray photoelectron and Auger electron spectroscopic data for cadmium in different compounds and synthesized pyrrhotite

Sample	Binding energy of Cd $3d_{5/2}$ photoelectrons, eV		Energy of $M_4N_{45}N_{45}$ Auger transition, eV
	our data	data available in the literature	
Cd (metallic)	404.8	404.9–405.1 [6.7]	380.1–380.5 [6]
CdO	404.5	404.2 [6], 405.2 [7]	382.4 [6], 382.2 [7]
CdS	405.2	405.3 [6.7]	381.3 [6]
$CdCl_2$	406.5*	406.1 [7]	
$Cd(OH)_2$		405.1 [6]; 405.0 [7]	380.0 [6]
Po1(2×10^{-4})	404.8		not determined
Po2(3×10^{-4})	404.6		
Po3(1×10^{-2})	405.0		382–383**
Po4(7×10^{-2})	405.2		not determined

Note: Po1–Po4 are the samples of stoichiometric pyrrhotite. The total Cd contents (wt %) are given in parentheses.
* 2.5-Hydrated salt (cadmium chloride hemipentahydrate).
** Our data.

mal cocrystallization of components in the Fe–S–ZnS–PbS–CdS system. The miscibility increases by more than two orders of magnitude, and the structural species dominates significantly. Therefore, it can be concluded that, in this case, cadmium manifests itself as a compatible element. Cadmium is not observed in the surface layer by spectroscopic methods, because it is uniformly distributed throughout the bulk of the crystal. Judging from the photoelectron binding energies, the cadmium state in stoichiometric pyrrhotite at low cadmium contents is similar to the cadmium state in oxide (i.e., there exist Cd–O bonds). The presence of this surface species in the sample is responsible for the peak with a maximum at ~600°C in the TAA curve (Fig. 2). From analyzing the data presented in Table 1, it follows that the occurrence of chloride species in the sample can be excluded, even though the chlorine content in the surface layer is rather high (Fig. 1). From chemical considerations and taking into account the energy of the *MNN* Auger transition, it is unrealistic that cadmium can be sorbed in the form of a hydroxide. At the same time, it is highly improbable that cadmium in the surface layer can occur in the form of pure CdO. This is confirmed by the TAA data obtained for CdS and CdO [3, 5]. The second cadmium form with a release temperature of ~700°C (Fig. 2) is a surface sulfide species [2, 5]. It should also be kept in mind that the sulfide species is absent on the surface of a coarsely crystalline magnetite formed together with pyrrhotite. It is this oxide species of cadmium that could be expected upon sorption on magnetite. However, the content of sorbed cadmium in the case of the magnetite is substantially less (by approximately one order of magnitude) than that of the pyrrhotite. This suggests that sulfur should enter into the sorbent composition in order to provide efficient binding of cadmium. With due regard for all the results obtained, we can draw the inference that the first low-temperature cadmium species adsorbed by pyrrhotite at low cadmium contents represents a cadmium compound with oxygen and sulfur. It is less probable that this compound will contain chlorine, even though the presence of $CdCl_n^{2-n}$ species on the pyrrhotite surface

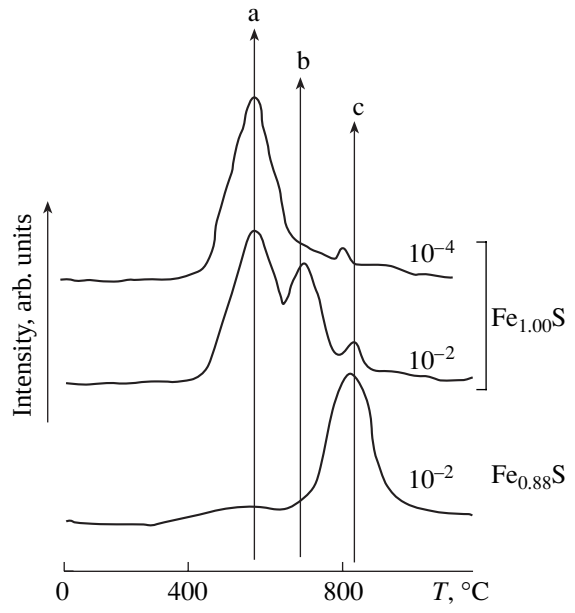

Fig. 2. TAA curves for different cadmium species in pyrrhotites synthesized under hydrothermal conditions at a temperature of 450°C and a pressure of 1 kbar in a 10% NH_4Cl solution: (a) sorbed, (b) sulfide, and (c) structural species of cadmium. Numbers near the curves indicate the Cd content (wt %) in pyrrhotites.

Table 2. Activities of volatile components, Cd contents in different species, total and true coefficients of Cd distribution between galena crystals and solutions (the true distribution coefficient characterizes only the structural species)

Experiment no.	CdS content in batch, wt %	Fugacity of gases, bar			Cd content in different species, wt % × 10^2			Cd content in solution, wt % × 10^2	K_{tot}	K_{str}
		$-\log f_{S_2}$	$-\log f^*_{SO_2}$	$-\log f^{**}_{O_2}$	mineral	sorbed	structural			
1	0.1	>7.1	not determined			0.05	0.84	(2.9)	(0.31)	(0.29)
2	0.3	7.1	2.9	23.7	0.36	0.08	0.76	(3.0)	(0.40)	(0.25)
3	0.5	7.3	3.3	23.9	0.51	0.14	0.85	(3.5)	(0.43)	(0.24)
4	0.1	7.6	3.6	24.1	0.20	0.09	0.21	14	0.04	0.02
5	0.5	7.8	3.9	24.3	0.60	0.25	0.85	27	0.06	0.03
6	0.1	7.6	3.6	24.1		0.07	0.31	17	0.02	0.02
7	0.5	7.8	3.9	24.3		0.21	1.39	37	0.04	0.04
8	0.5	7.8	3.9	24.3		0.05	0.95	46	0.02	0.02
9	0.1	2.4	not determined		0.05		0.20 0.11	0.9	0.28	0.22 0.12
10	1.0	2.4	not determined				0.30	10	0.03	0.03
11	0.1	>7.1	not determined		0.07	0.02	0.21 0.11	1.2	0.25	0.18 0.09
12	0.5	>7.1	not determined			0.04	0.54	9	0.06	0.06
13	1.0	7.3	3.3	23.9		0.07	0.67	16	0.05	0.04

Note: The data given in parentheses are obtained for quenched solutions; the other values are determined from the analysis of the solutions in samplers. In experiments 9 and 11, the TAA spectra exhibit two peaks associated with the structural species. The contents and distribution coefficients are calculated for two variants, i.e., for the total content (the first number) and high-temperature peak (the second number). In the calculations of the total (K_{tot}) and structural (K_{str}) distribution coefficients, the contents are expressed in weight percent (wt %).

* According to the reaction $Fe_3O_4 + \frac{5}{2}S_2 = \frac{3}{x}Fe_xS + 2SO_2$.

** According to the reaction $\frac{1}{2}S_2 + O = SO_2$.

cannot be ruled out [10]. The species of cadmium under consideration is unlikely to be intermediate in the course of its incorporation into the crystal structure, because cadmium is firmly fixed and can be removed only together with the surface layer due to ion etching (Fig. 1). The above interpretation is confirmed by the increase in the photoelectron binding energy with an increase in the cadmium content (Table 1). In this case, the TAA curve is characterized by the peak attributed to the sulfide species. The sulfide species is treated as a nonautonomous phase preceding the formation of the bulk phase CdS [2, 5].

Cadmium in galena. Cubic and cubooctahedral galena crystals up to 3 mm in size, as a rule, form bulky aggregates at the top of the silica glass tube. However, in the experiments with a large sulfur excess, the rate of material transfer was not very high and several tens of crystals formed at the top could hardly be sufficient for performing the analysis. Depending on the initial composition, the buffer mixtures in the course of experiments transform into magnetite–pyrite, magnetite–pyrrhotite, magnetite–pyrite–pyrrhotite, and pyrite–elemental sulfur mixtures. The fugacities of the gases were calculated according to the reactions with the participation of these phases. The calculated fugacities, the estimated cadmium contents in different species in galena, and the cadmium contents in the solutions after the experiments are listed in Table 2. The characteristic TAA curves of cadmium species are shown in Fig. 3. Of primary interest are the following three features: (i) splitting of the peak attributed to the structural species (Fig. 3; curves *1*, *2*), (ii) manifestation of the formation of the own mineral species of cadmium (Fig. 3, curves *1–4*), and (iii) the temperature shift in the peak of the structural species (Fig. 3, curve *5*). At relatively high fugacities of sulfur, the sorbed species of cadmium are virtually absent, the mineral species content is rather high, and the peak assigned to the structural species is split. At lower fugacities of sulfur ($f_{S_2} = 10^{-7.3}$ and $10^{-7.8}$ bar), the content of mineral species, as before, is relatively high and the peak attributed to the structural species is not shifted and remains nonsplit. Finally, at $f_{S_2} = 10^{-7.8}$ bar and in the presence of

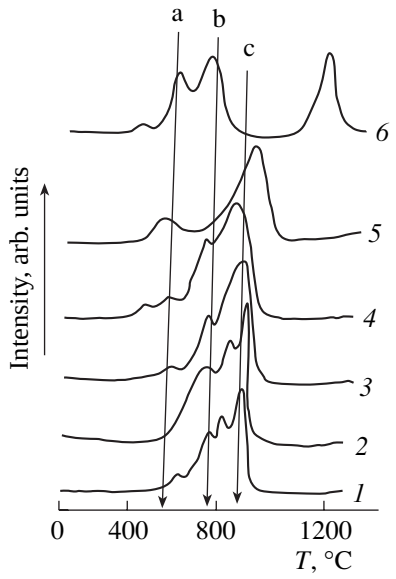

Fig. 3. TAA curves of cadmium release from (*1–5*) PbS galena and (*6*) $PbSO_4$ anglesite samples grown under hydrothermal conditions (400°C, 500 bar, 5% NH_4Cl solution) at different fugacities of volatile components *f*: (a) sorbed, (b) mineral, and (c) structural cadmium species in galena (Table 2) in (*1*) experiment 11 $f_{S_2} > 10^{-7.1}$ bar; (*2*) experiment 9, $f_{S_2} > 10^{-2.4}$ bar; (*3*) experiment 3, $f_{S_2} = 10^{-7.3}$ bar; (*4*) experiment 5, $f_{S_2} = 10^{-7.8}$ bar; (*5*) experiment 7, $f_{S_2} = 10^{-7.8}$ bar; and (*6*) experiment 7, $f_{S_2} = 10^{-7.8}$ bar.

anglesite, the peak associated with the structural species is shifted toward the high-temperature range.

The formation of mineral species of cadmium is rather unexpected, because the solubility of CdS in galena under the experimental conditions is equal to 1.5 ± 0.1 mol % or 0.7 wt % Cd [11, 12], which exceeds the highest cadmium content in the grown galenas by approximately two orders of magnitude. A comparison with the TAA curve of cadmium release from the $PbSO_4$ anglesite crystals (Fig. 3, curve *6*) formed together with galena in one of the experiments allows us to assume that the mineral form of cadmium is a sulfate species. It is interesting to note that this species is not formed on the surface of crystals in the case where the sulfate represents the bulk phase (experiment 7, curve *5*). It is reasonable that the sulfate species of cadmium is formed not in the solution region in which SO_4^{2-} ions are predominant but near the boundary of this region due to the interaction of cadmium with the oxidized surface of galena. According to Auger spectroscopy, the chlorine content is rather high in the crystals and amounts to approximately 10 at. % on the surface cleaned by ion etching (for 10 min). Therefore, the own phase of cadmium can be a double salt. Unfortunately, cadmium in the surface layer has not been revealed by electron spectroscopy and its chemical state remains unknown. This is associated with the relatively low cadmium concentration in PbS. Moreover, for the most part, cadmium is incorporated into the galena structure, in which it is uniformly distributed throughout the bulk of the crystal rather than forming an enriched surface layer, as is the case with stoichiometric pyrrhotite. The factors responsible for the shift of the TAA peak associated with the structural species of cadmium toward the high-temperature range by approximately 100 K are still unclear. We do not attribute this shift to particular cadmium species, because the coefficients of cadmium distribution between the crystal and the solution for these samples have no anomalies. A quite different situation arises with the splitting of the peak of the structural species. The splitting occurs at higher sulfur activities (and, hence, at higher relative supersaturations during the growth) and is accompanied by a drastic increase in the distribution coefficient for the solid phase (Table 2). This is a specific feature of the dislocation species, which was observed earlier for cadmium in galena [3, 13]. According to [13], the dislocation species is formed through the interaction of elastic fields of point defects (an impurity atom located at a substitutional position is a dilatation center) with nonuniform elastic fields of dislocations. As a result, cadmium is concentrated by dislocation subgrain boundaries in the galena crystals. The true coefficient of cadmium distribution between the galena crystal and the solution is equal to 0.03 ± 0.01 [Table 2; without regard for the results of experiments 9 and 11; the contents are expressed in weight percent (wt %)]. Upon the formation of dislocation species of cadmium, the distribution coefficient increases several times [13]. The sorbed species of cadmium at a content of $(1.2 \pm 0.6) \times 10^{-3}$ wt % is formed at relatively lower sulfur fugacities: $f_{S_2} = 10^{-7.1}$–$10^{-7.8}$ bar. At higher fugacities f_{S_2}, the content of this species is nearly one order of magnitude smaller: $f_{S_2} = (2 \pm 2) \times 10^{-4}$ wt %. Note also that the analysis of the quenched solutions offers overestimated coefficients of distribution, because cadmium is not retained in the solution (Table 2).

Mercury in galena. Unlike cadmium, mercury in the surface layer of the galena crystals is detected by electron spectroscopy, even though the main species of mercury is structural (Table 3), as is the case with cadmium. The approximate ratios between the sorbed and structural species of mercury were determined from the areas of the corresponding peaks in the measured TAA curves of the crystals. As can be seen from Table 3, these ratios vary over a wide range. According to Auger spectroscopy, the surface contains up to 10 at. % Hg, which suggests that the surface layer is highly enriched with mercury. The ion etching for a short time (10 min) leads to the elimination of mercury from the surface,

Table 3. Experimental results of investigations into the behavior of mercury in the PbS–(HgS,CdS)–5% NH_4Cl solution system at a temperature of 400°C and a pressure of 0.5 kbar

Experiment no. (according to Table 2)	HgS content in batch, wt %	$-\log f_{S_2}$, bar	Hg species*	Hg content in galena, wt %
4	0.1	7.6	sorbed ≪ structural	8.4×10^{-3}
5	0.5	7.8	sorbed(7), structural	1.0×10^{-1}
6	0.1	7.6	sorbed ≪ structural	5.2×10^{-3}
7	0.5	7.8	sorbed(13), structural	7.4×10^{-2}
8	0.5	7.8	sorbed(10), structural	1.1×10^{-1}
9	0.1	2.4	sorbed(25), structural	1.1×10^{-1}
10	1.0	2.4	sorbed(60), structural	6.7×10^{-1}
11	0.1	>7.1	sorbed ≪ structural	1.6×10^{-2}
12	0.5	>7.1	sorbed(1), structural	2.2×10^{-2}
13	1.0	7.3	sorbed(1), structural	4.4×10^{-2}

* The sorbed species contents estimated from the areas under the peaks are given in parentheses. In the other cases, the assessment is qualitative.

Table 4. Binding energies of Hg $4f_{7/2}$ photoelectrons (E, eV) for mercury-sorbed galena samples and reference compounds

Chemical state of mercury										
Hg on PbS		Hg (0)			Hg (I) [Hg_2^{2+}]			Hg (II)		
E, eV	reference	compound	E, eV	reference	compound	E, eV	reference	compound	E, eV	reference
100.9	[14]	Hg^0	99.2	[15]	Hg_2Cl_2	99.4	[15]	HgS	100.9	[14]
									100.8–101.0	[7]
								HgO	100.8	[7]
100.0–100.1	this work		99.8	[7]	$Hg_2(NO_3)_2$	99.8	this work	$Hg_3S_2Cl_2$	100.9	[14]
								$HgCl_2$	101.4	[7]
									100.9	[14]
									100.8	[15]

which is attended by the desorption of oxygen and, partially, chlorine. The binding energies of different mercury species are rather close to each other. This makes reliable identification of mercury species incorporated into galena difficult if not impossible. According to our data, the binding energy of Hg $4f_{7/2}$ photoelectrons for galena crystals is equal to 100.0–100.1 eV. This value is appreciably less than the binding energy of Hg $4f_{7/2}$ photoelectrons for HgS, which is identified as the mercury species sorbed from an $HgCl_2$ solution at room temperature [14], and corresponds to either the Hg(0) form or the Hg_2^{2+} cluster group (Table 4). Additional information can be obtained from the TAA curves of mercury release (Fig. 4). This curve, as a rule, contains two peaks assigned to the sorbed (250–300°C) and structural (~600°C) species. The galena crystals contain few, if any, Hg(0) species (see the first weak peak in curves *2* and *4* in Fig. 4). The behavior of mercury strongly depends on the sulfur activity. The structural species dominates at low fugacities f_{S_2}, whereas the fraction of sorbed species sharply increases at high fugacities. A comparison with the peak in the reference curve of cinnabar (Fig. 4, curve *1*) shows that the sorbed form is not a sulfide species. It is of interest that the sorbed species is formed in considerable amounts (Table 3) at a high sulfur activity (Fig. 4; curves *3*, *4*), at which the formation of sulfide species could be expected. This behavior can easily be explained in terms of the previously proposed mechanism of mercury uptake by galena upon the interaction of mercury with V_{Pb}–Pb^{4+} surface point defects of galena due to the absorption of vacancies according to the reaction V_{Pb}–$Pb^{4+} + 2Hg^0 = Pb^{2+} + Hg_2^{2+}$ (at the V_{Pb} site) [15, 16]. An

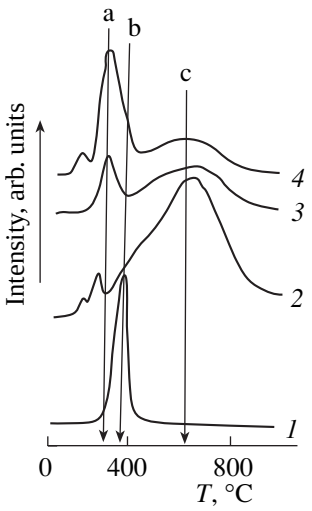

Fig. 4. TAA curves of mercury release from (*1*) the reference cinnabar sample and (*2*–*4*) galena crystals grown under different conditions: (a) sorbed, (b) sulfide, and (c) structural mercury species in (*2*) experiment 13, $f_{S_2} = 10^{-7.3}$ bar, the mercury content in galena is 0.044 wt %; (*3*) experiment 9, $f_{S_2} = 10^{-2.4}$ bar, the mercury content in galena is 0.11 wt %; and (*4*) experiment 10, $f_{S_2} = 10^{-2.4}$ bar, the mercury content in galena is 0.67 wt %.

increase in the fugacity of sulfur leads to an increase in the concentration of surface vacancies of the galena crystals, which, in turn, results in an increase in the sorption activity of galena. The analysis of the solutions from samplers demonstrated that the mercury contents in the solutions are very low (10^{-4}–10^{-5} wt %). On this basis and taking into account the data presented in Table 3, we found that the coefficients of mercury distribution between the crystal and the solution are approximately equal to 10^2–10^3; i.e., they are larger than those of cadmium by four or five orders of magnitude. According to the results obtained, galena almost completely absorbs mercury under hydrothermal conditions. However, these results call for further verification because of their poor reproducibility, which can be associated with the loss of mercury due to evaporation and adsorption during the preparation of solutions for the analysis.

DISCUSSION

Up to now, the processes of sorption of mercury, cadmium, and lead in sulfide minerals have been investigated only under normal conditions. Forssberg and Jonsson [17] assumed that mercury is adsorbed on pyrrhotite in the form a cubic sulfide, whereas lead is bound on an oxidized surface of the pyrrhotite crystal with the formation of an insoluble sulfate. More recently, Jean and Bancroft [10] proposed a simple sorption reaction in which the product represents an inner-sphere surface complex. Hydrated particles are sorbed on sulfide groups to form monolayers, which, in turn, physically sorb chloride complexes of metals. According to Hyland *et al.* [14], the sulfide form of mercury is the most strongly bound species on the galena surface, whereas the $Hg_3S_2Cl_2$ and $HgCl_x$ compounds are the most weakly bound species. However, it should be noted that the results obtained seem to be insufficiently reliable because the binding energies of different species are close to each other (Table 4). Investigations into the sorption of cadmium by pyrrhotite with the use of Raman spectroscopy, X-ray diffraction, and scanning electron microscopy have revealed a quite different situation or, more precisely, the formation of new solid phases even at low surface coverages. Upon sorption of cadmium by pyrrhotite, these solid phases are predominantly represented by elemental sulfur and CdS. Bostick *et al.* [18] assumed that the mechanism of cadmium retention is associated with the reconstruction of the pyrite surface due to the sulfur disproportionation. Thus, there exist several viewpoints regarding the mechanism of trace-element uptake by sulfides. The results obtained in the present work demonstrated that, at elevated temperatures and pressures under hydrothermal conditions, stable species of cadmium and mercury exist in iron and lead sulfides. Their formation proceeds through different mechanisms. The most general mechanism involves the uptake of trace elements in the form of structural species due to isomorphous exchange. In geochemistry, this is the standard mechanism of uptake of the so-called compatible elements. However, the data on the sorption of cadmium by pyrrhotite indicate that structural defects very strongly affect the impurity incorporation. As a consequence, the particular trace element can be either compatible or incompatible with the mineral matrix, depending on the type and concentration of structural defects. This behavior is characteristic of cadmium in nonstoichiometric and stoichiometric pyrrhotites, respectively. In addition to the structural (isomorphous) form of uptake, trace elements can form their own phase species at elevated temperatures and pressures. Following Gusarov *et al.* [19, 20], who used the Defay–Prigogine terminology, we defined these species as surface nonautonomous phases [2, 5]. These phases are formed not only at trace-element concentrations close to saturation (Cd in $Fe_{1.0}S$) but also under conditions far from saturation as a result of the interaction of trace elements with the oxidized surface of the mineral (the cadmium uptake by galena with the formation of either a sulfate surface phase or a sulfate–chloride surface phase). Furthermore, it should be emphasized that lattice defects formed as a result of variations in the physicochemical conditions play a particular role in the trace-element uptake proceeding through the mechanism of external and internal adsorption. This manifests itself both in an increase in the content of sorbed mercury (instead mercury sulfide) in galena due to the absorption of lead vacancies at a high sulfur activity

and in the formation of dislocation species of cadmium under the same conditions, which leads to a considerable increase in the coefficient of cadmium distribution in the crystal–solution system. The occurrence of this phenomenon most clearly demonstrates the difference between the processes of trace-element uptake under static normal conditions and dynamic hydrothermal conditions of crystal growth at elevated temperatures and pressures.

CONCLUSIONS

The results obtained in this work are important for the development of the technique of activating semiconductor and fluorescent crystals by impurities in the course of the hydrothermal growth. The mechanism of trace-element uptake with the participation of nonautonomous phases is of primary interest for geochemistry and mineralogy. The stability of nonautonomous phases is considerably higher than that of surface complexes. It is these phases that hold promise as an efficient tool for extracting genetic information from mineral surfaces. The occurrence of strongly sorbed heavy metal species that are stable under hydrothermal conditions at sufficiently high pressures and temperatures even for volatile elements (such as mercury) can substantially affect the applicability of the existing models of ore deposit formation. For example, the model of mercury deposit formation, according to which mercury can be completely sublimated from a sedimentary rock at moderate temperatures through the use of only volcanic heat [21], obviously needs revision. Moreover, the results obtained demonstrated for the first time that the combined use of X-ray photoelectron spectroscopy and thermal atomic absorption analysis holds much promise. A combination of these methods can be useful both in analyzing an ambiguous situation associated with small chemical shifts and in examining compatible elements, for which the isomorphous uptake dominates over the sorption uptake and the surface enrichment either is less than that for incompatible elements or is absent (cadmium in galena and nonstoichiometric pyrrhotite).

ACKNOWLEDGMENTS

We would like to thank Yu.V. Shchegol'kov for his assistance in performing the spectroscopic investigation of the surface.

This work was supported by the Russian Foundation for Basic Research, project no. 02-05-64297.

REFERENCES

1. A. M. Widler and T. M. Seward, Geochim. Cosmochim. Acta **66** (3), 383 (2002).
2. V. L. Tauson, I. Yu. Parkhomenko, V. I. Men'shikov, and K. V. Nepomnyashchikh, Geol. Geofiz. **43** (2), 182 (2002).
3. V. L. Tauson, I. Yu. Parkhomenko, and V. I. Men'shikov, Geol. Geofiz. **39** (4), 469 (1998).
4. V. L. Tauson, V. I. Men'shikov, and I. Yu. Parkhomenko, Geol. Geofiz. **41** (8), 1124 (2000).
5. V. V. Akimov, V. L. Tauson, I. Yu. Parkhomenko, *et al.*, Poverkhnost, No. 6, 31 (2002).
6. *Practical Surface Analysis by Auger and X-ray Photoelectron Spectroscopy*, Ed. by D. Briggs and M. Seah (Wiley, New York, 1983; Mir, Moscow, 1987).
7. J. F. Moulder, W. F. Stickle, P. E. Sobol, and K. D. Bomben, *Handbook of X-ray Photoelectron Spectroscopy (A Reference Book of Standard Spectra for Identification and Interpretation of XPS Data)* (Perkin-Elmer, Norwalk, CT, 1990).
8. V. L. Tauson, V. F. Gelety, and V. I. Men'shikov, *Regional and Global Mercury Cycles: Sources, Fluxes, and Mass Balances* (Kluwer, Dordrecht, 1996), p. 441.
9. P. Toulmin and P. B. Barton, Geochim. Cosmochim. Acta **28** (5), 641 (1964).
10. G. E. Jean and G. M. Bancroft, Geochim. Cosmochim. Acta **50** (7), 1455 (1986).
11. P. M. Bethke and P. B. Barton, Jr., Am. Mineral. **56** (11–12), 2034 (1971).
12. V. F. Geletiĭ, L. V. Chernyshev, and T. M. Pastushkova, Geol. Rudn. Mestorozhd. **21** (6), 66 (1979).
13. V. S. Urusov, V. L. Tauson, and V. V. Akimov, *Geochemistry of Solids* (GEOS, Moscow, 1997).
14. M. M. Hyland, G. E. Jean, and G. M. Bancroft, Geochim. Cosmochim. Acta **54** (7), 1957 (1990).
15. R. D. Seals, R. Alexander, L. T. Taylor, and J. G. Dillard, Inorg. Chem. **12**, 2485 (1973).
16. V. L. Tauson, V. I. Men'shikov, and L. D. Andrulaĭtis, Geokhimiya, No. 7, 936 (1989).
17. K. S. E. Forssberg and H. Jonsson, Scand. J. Metall. **10**, 225 (1981).
18. B. C. Bostick, S. Fendorf, and M. Fendorf, Geochim. Cosmochim. Acta **64** (2), 247 (2000).
19. V. V. Gusarov and S. A. Suvorov, Zh. Prikl. Khim. (Leningrad), No. 8, 1689 (1990).
20. V. V. Gusarov, A. A. Malkov, A. A. Malygin, and S. A. Suvorov, Neorg. Mater. **31** (3), 346 (1995).
21. A. N. Moiseyev, Econ. Geol. **66** (4), 591 (1971).

Translated by O. Borovik-Romanova

Crystallography Reports, Vol. 49, No. 2, 2004, pp. 158–168. Translated from Kristallografiya, Vol. 49, No. 2, 2004, pp. 208–218.

STRUCTURE OF ORGANIC COMPOUNDS

X-ray Mapping in Heterocyclic Design: XII. X-ray Diffraction Study of 2-Pyridones Containing Cycloalkane Fragments Annelated to the C(5)–C(6) Bond

D. V. Al'bov, O. S. Mazina, V. B. Rybakov, E. V. Babaev, V. V. Chernyshev, and L. A. Aslanov

Faculty of Chemistry, Moscow State University, Vorob'evy gory, Moscow, 119992 Russia

e-mail: albov@biocryst.phys.msu.su

Received January 23, 2003

Abstract—The structures of 4,6-dimethyl-1*H*-pyridin-2-one [a = 6.125(2) Å, b = 15.153(4) Å, and c = 14.477(4) Å, Z = 8, space group *Pbca*], the 2 : 1 : 1 complex of 4-methyl-1,5,6,7-tetrahydro-2*H*-cyclopenta[*b*]pyridin-2-one with phosphoric acid and methanol [a = 11.181(2) Å, b = 14.059(6) Å, c = 13.593(4) Å, β = 97.78(2)°, Z = 8, space group $P2_1/n$], 4-methyl-1,5,6,7,8,9-hexahydro-2*H*-cyclohepta[*b*]pyridin-2-one [a = 12.565(6) Å, b = 5.836(6) Å, c = 13.007(3) Å, β = 93.10(3)°, Z = 4, space group $P2_1/n$], and 4-methyl-5,6,7,8,9,10-hexahydrocycloocta[*b*]pyridin-2(1*H*)-one [a = 12.955(3) Å, b = 6.1595(15) Å, c = 13.038(3) Å, β = 95.50(2)°, Z = 4, space group $P2_1/n$] are determined by single-crystal X-ray diffraction. The structures are solved by direct methods and refined by the full-matrix least-squares procedure in the anisotropic approximation to R = 0.0755, 0.0644, 0.0754, and 0.0569, respectively. The structures of 4-methyl-1,5,6,7-tetrahydro-2*H*-cyclopenta[*b*]pyridin-2-one [a = 7.353(4) Å, b = 8.176(4) Å, c = 13.00(1) Å, β = 105.64(2)°, Z = 4, space group $P2_1/c$] and 2-oxo-1,2,5,6,7,8-hexahydroquinoline-3-carbonitrile [a = 5.9870(2) Å, b = 16.5280(5) Å, c = 9.6540(3) Å, β = 111.52(4)°, Z = 4, space group $P2_1/c$] are studied by the powder diffraction technique. The structures are solved using the grid search procedure and refined by the Rietveld method to R_{wp} = 0.108 and 0.058, R_{exp} = 0.032 and 0.027, R_p = 0.076 and 0.043, R_b = 0.123 and 0.077, and χ^2 = 7.9 and 3.64, respectively. In all the structures, hydrogen bonds involving the N, H, and O atoms of the pyridone fragment are formed. © *2004 MAIK "Nauka/Interperiodica".*

INTRODUCTION

This study continues our investigation into the structure of heterocyclic compounds that are able to undergo various rearrangements and, in particular, to enter into cyclization reactions [1–12]. As was done in our previous works, we perform an X-ray diffraction analysis of all the intermediates and final products of multistage cyclization reactions and rearrangements. 2-Pyridone derivatives are structural precursors in many of the systems studied earlier (scheme 1).

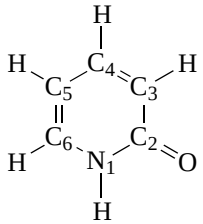

Scheme 1

In this paper, we report the structures of 4,6-dimethyl-1*H*-pyridin-2-one (**I**) and a number of its analogues that contain cycloalkane fragments annelated to the C(5)–C(6) bond, namely, 4-methyl-1,5,6,7-tetrahydro-2*H*-cyclopenta[*b*]pyridin-2-one (**IIa**), its 2 : 1 : 1 complex with phosphoric acid and methanol (**II**), 4-methyl-1,5,6,7,8,9-hexahydro-2*H*-cyclohepta[*b*]pyridin-2-one (**III**), 4-methyl-5,6,7,8,9,10-hexahydrocycloocta[*b*]pyridin-2(1*H*)-one (**IV**), and 2-oxo-1,2,5,6,7,8-hexahydroquinoline-3-carbonitrile (**V**). Data on the molecular structures of the compounds discussed in this paper are not available in the Cambridge Structural Database (version 11.02) [13].

EXPERIMENTAL

The synthesis of the compounds was performed according to the following schemes:

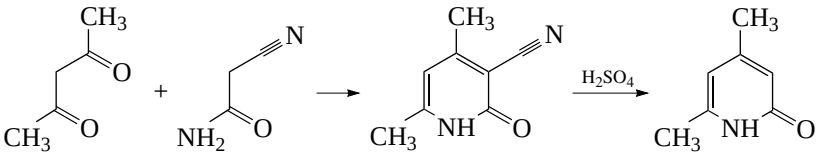

I

Scheme 2

1063-7745/04/4902-0158$26.00 © 2004 MAIK "Nauka/Interperiodica"

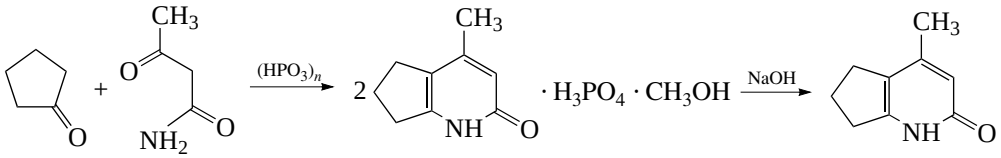

Scheme 3

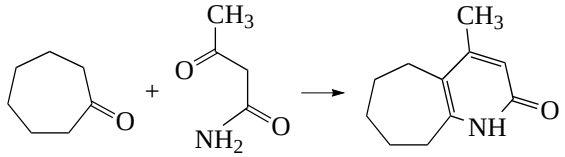

Scheme 4

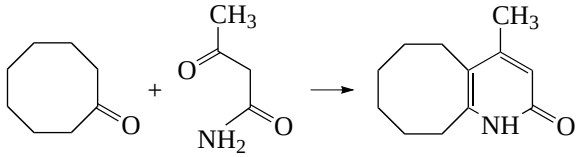

Scheme 5

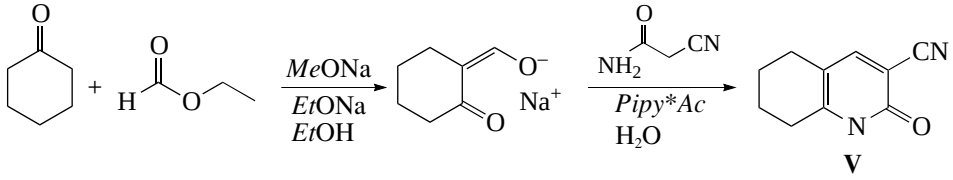

Scheme 6

Compound **I** was prepared using the procedure described in [14]. Compounds **II**, **III**, and **IV** were synthesized according to the modified procedure used in [15]: acetoacetamide (16 g), the cycloalkanone (equimolar amount), and polyphosphoric acid (80 g) were gently heated on stirring with a glass rod in a beaker. An exothermic reaction began at about 70°C, and the temperature of the mixture abruptly increased to 140°C. The reaction mixture was then stirred at 100°C to a homogeneous state (for about 5 min) and poured into hot water. A dark solution and liquid resin were formed. The resinoid residue was removed, and the

Table 1. Physicochemical parameters of the compounds synthesized

Compound	Melting temperature T_m, °C	^{1}H NMR	Reference
I	180–182	6.04 [1H, s, C(5)H]; 5.92 [1H, s, C(3)H]; 2.23 (3H, s, 6-CH_3); 2.13 (3H, s, 4-CH_3] (acetone-d_6)	[14]
IIa	245–248	5.87 [1H, s, C(3)H]; 2.72 [2H, t, C(8)H_2]; 2.61 [2H, t, C(6)H_2]; 2.06 [3H, s, C(10)H_3]; 2.04 [2H, m, C(7)H_2] (DMSO-d_6)	[15]
III	258–260	5.88 [1H, s, C(3)H]; 2.62 [2H, t, C(10)H_2]; 2.48 [2H, t, C(6)H_2]; 2.08 [3H, s, C(12)H_3]; 1.78 [2H, m, C(9)H_2]; 1.54 [4H, m, C(7)H_2, C(8)H_2] (DMSO-d_6)	[15]
IV	230–233	5.99 [1H, s, C(3)H]; 2.58 (2H, t, C(11)H_2]; 2.46 [2H, t, C(6)H_2]; 2.09 [3H, s, C(13H_3]; 1.59 [2H, m, C(10)H_2]; 1.51 [2H, m, C(7)H_2]; 1.34 [4H, m, C(8)H_2, C(9)H_2] (DMSO-d_6)	–
V	250–257	7.87 [1H, s, C(4)H]; 2.56 [2H, t, C(7)H_2]; 2.43 [2H, t, C(9)H_2]; 1.66 (4H, m, C(7)H_2, C(8)H_2] (DMSO-d_6)	[16]

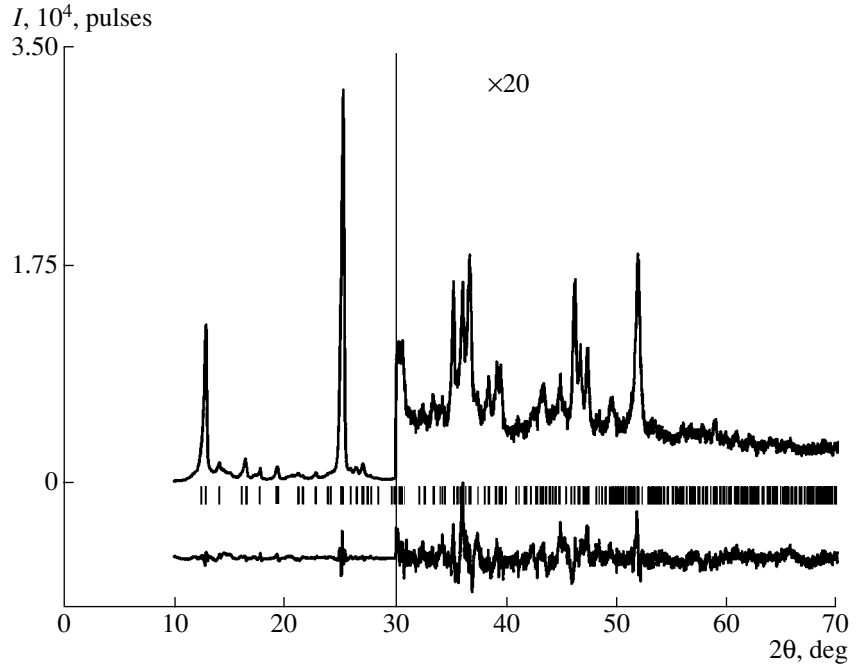

Fig. 1. Experimental and difference (Rietveld refinement) spectra for compound **IIa**.

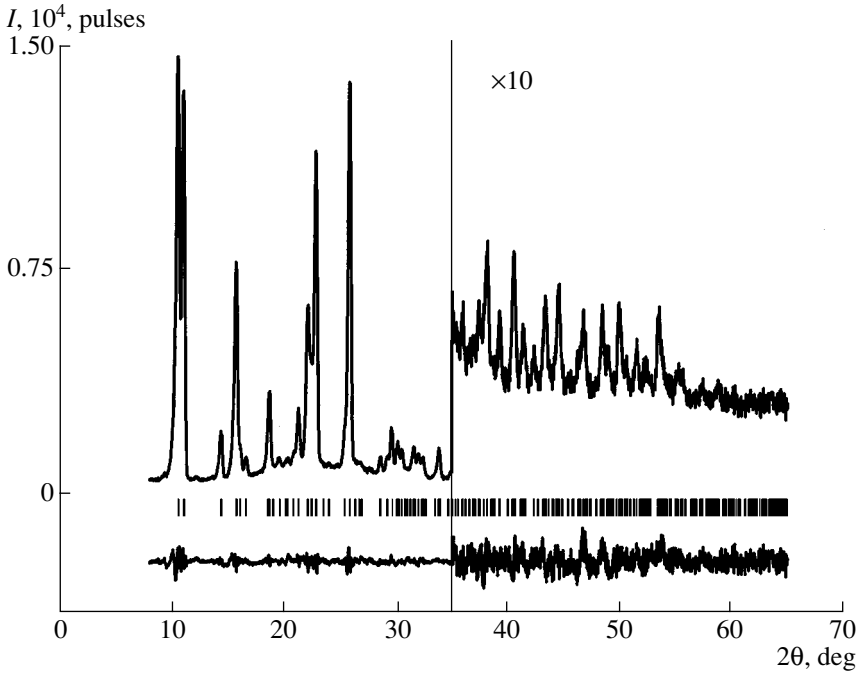

Fig. 2. Experimental and difference (Rietveld refinement) spectra for compound **V**.

solution was neutralized with solid sodium hydrogencarbonate until the formation of the precipitate was completed. The precipitate was filtered off and washed with water and acetone. In the case of cyclopentanone, the precipitate contained H_3PO_4. Recrystallization of this precipitate resulted in the formation of complex **II**, which contained methanol and phosphoric acid. Complex **II** was treated in 10% aqueous solution of NaOH with the formation of compound **IIa**. The yield of compound **IIa** was 50%, and the yields of compounds **III**

Table 2. Crystal data, data collection, and refinement parameters for the structures studied

Empirical formula	C_7H_9NO (**I**)	$C_{19}H_{29}N_2O_7P$ (**II**)	$C_9H_{11}NO$ (**IIa**)	$C_{11}H_{15}NO$ (**III**)	$C_{12}H_{17}NO$ (**IV**)	$C_{10}H_{10}N_2O$ (**V**)
Molecular weight	123.15	428.42	149.19	177.24	191.27	174.20
Crystal system	Orthorhombic	Monoclinic	Monoclinic	Monoclinic	Monoclinic	Monoclinic
Space group	*Pbca*	$P2_1/n$	$P2_1/c$	$P2_1/n$	$P2_1/n$	$P2_1/c$
a, Å	6.125(2)	11.181(2)	7.353(4)	12.565(6)	12.955(3)	5.9870(2)
b, Å	15.153(4)	14.059(6)	8.176(4)	5.836(6)	6.1595(15)	16.5280(5)
c, Å	14.477(4)	13.593(4)	13.00(1)	13.007(3)	13.038(3)	9.5640(3)
β, deg	90	97.78(2)	105.64(2)	93.10(3)	95.50(2)	111.52(4)
V, Å^3	1343.6(7)	2117.1(12)	752.6(8)	952.5(10)	1035.6(4)	888.71(5)
Z	8	4	4	4	4	4
ρ_{calcd}, g/cm^3	1.218	1.344	1.313	1.236	1.227	1.304
μ, cm^{-1}	0.82	1.73	0.86	0.79	0.78	0.70
θ range, deg	2.69 – 24.97	2.09 – 25.98	3 – 40	2.20 – 24.97	2.12 – 19.99	3 – 40
Index ranges	$0 \le h \le 7$ $0 \le k \le 18$ $0 \le l \le 17$	$-13 \le h \le 13$ $0 \le k \le 17$ $0 \le l \le 16$	$0 \le h \le 5$ $0 \le k \le 6$ $-9 \le l \le 9$	$-14 \le h \le 14$ $0 \le k \le 6$ $0 \le l \le 15$	$-12 \le h \le 12$ $0 \le k \le 5$ $0 \le l \le 12$	$-4 \le h \le 4$ $0 \le k \le 7$ $0 \le l \le 3$
Crystal size, mm	0.32 × 0.35 × 0.41	0.31 × 0.32 × 0.34		0.34 × 0.37 × 0.49	0.28 × 0.30 × 45	
Number of reflections collected	1120	4269		1576	962	
Number of unique reflections	1120	4095		1509	913	
Number of reflections in least-squares refinement/Number of parameters refined	1120/119	4095/379		1509/174	913/132	
GooF	1.105	1.023		0.926	0.941	
R_1/wR_2 for $I \ge 2\sigma(I)$	0.0755/0.1825	0.0644/0.1319		0.0754/0.1343	0.0569/0.1028	
R_1/wR_2 for all reflections	0.1523/0.2209	0.1328/0.1622		0.2563/0.2091	0.1569/0.1404	
$\Delta\rho_{max}/\Delta\rho_{min}$, e/Å^3	0.222/–0.298	0.209/–0.233		0.212/–0.209	0.201/–0.165	
Scan step			0.02			0.02
R_{wp}			0.108			0.058
R_{exp}			0.032			0.027
R_p			0.076			0.043
R_b			0.123			0.077
χ^2			7.9			3.64

Table 3. Bond lengths *d* (Å) in structure **I**

Bond	*d*	Bond	*d*
N(1)–C(6)	1.3584(8)	C(3)–C(4)	1.3526(9)
N(1)–C(2)	1.3684(8)	C(4)–C(5)	1.3951(9)
N(1)–H(1)	0.874(5)	C(4)–C(8)	1.5215(10)
O(2)–C(2)	1.2534(8)	C(5)–C(6)	1.3519(8)
C(2)–C(3)	1.4227(9)	C(6)–C(7)	1.4983(9)

Table 4. Bond angles ω (deg) in structure **I**

Angle	ω	Angle	ω
C(6)–N(1)–C(2)	124.55(5)	C(3)–C(4)–C(5)	124.55(5)
C(6)–N(1)–H(1)	119.4(3)	C(3)–C(4)–C(8)	119.4(3)
C(2)–N(1)–H(1)	116.0(3)	C(5)–C(4)–C(8)	116.0(3)
O(2)–C(2)–N(1)	119.58(5)	C(6)–C(5)–C(4)	119.58(5)
O(2)–C(2)–C(3)	125.01(6)	C(5)–C(6)–N(1)	125.01(6)
N(1)–C(2)–C(3)	115.40(5)	C(5)–C(6)–C(7)	115.40(5)
C(4)–C(3)–C(2)	121.18(6)	N(1)–C(6)–C(7)	121.18(6)

Table 5. Bond lengths *d* (Å) in structure **II**

Bond	*d*	Bond	*d*	Bond	*d*	Bond	*d*
P(1)–O(11)	1.496(2)	N(1*A*)–H(1*A*)	0.89(4)	C(8*A*)–C(9*A*)	1.481(5)	C(4*B*)–C(10*B*)	1.479(6)
P(1)–O(14)	1.512(3)	C(2*A*)–O(2*A*)	1.274(4)	N(1*B*)–C(9*B*)	1.359(5)	C(5*B*)–C(9*B*)	1.338(5)
P(1)–O(13)	1.542(3)	C(2*A*)–C(3*A*)	1.417(5)	N(1*B*)–C(2*B*)	1.367(5)	C(5*B*)–C(6*B*)	1.498(5)
P(1)–O(12)	1.544(3)	C(3*A*)–C(4*A*)	1.370(5)	N(1*B*)–H(1*B*)	0.88(4)	C(6*B*)–C(7*B*)	1.524(7)
O(12)–H(12)	0.89(7)	C(4*A*)–C(5*A*)	1.402(5)	C(2*B*)–O(2*B*)	1.271(4)	C(7*B*)–C(8*B*)	1.520(7)
O(13)–H(13)	0.94(7)	C(4*A*)–C(10*A*)	1.499(5)	C(2*B*)–C(3*B*)	1.410(5)	C(8*B*)–C(9B)	1.508(5)
O(14)–H(14)	0.86(8)	C(5*A*)–C(9*A*)	1.358(5)	C(3*B*)–C(4*B*)	1.366(5)	C(21)–O(21)	1.387(7)
N(1*A*)–C(2*A*)	1.356(5)	C(5*A*)–C(6*A*)	1.505(5)	C(4*B*)–C(5*B*)	1.424(5)	O(21)–H(21)	0.86(5)
N(1*A*)–C(9*A*)	1.359(4)	C(7*A*)–C(8*A*)	1.538(6)				

Table 6. Bond angles ω (deg) in structure **II**

Angle	ω	Angle	ω
O(11)–P(1)–O(14)	111.85(17)	C(9*A*)–C(8*A*)–C(7*A*)	102.6(3)
O(11)–P(1)–O(13)	112.07(16)	C(5*A*)–C(9*A*)–N(1*A*)	120.3(3)
O(14)–P(1)–O(13)	109.31(18)	C(5*A*)–C(9*A*)–C(8*A*)	114.6(3)
O(11)–P(1)–O(12)	111.53(16)	N(1*A*)–C(9*A*)–C(8*A*)	125.1(3)
O(14)–P(1)–O(12)	106.88(18)	C(9*B*)–N(1*B*)–C(2*B*)	121.6(3)
O(13)–P(1)–O(12)	104.83(18)	C(9*B*)–N(1*B*)–H(1*B*)	120(2)
P(1)–O(12)–H(12)	113(4)	C(2*B*)–N(1*B*)–H(1*B*)	119(2)
P(1)–O(13)–H(13)	119(4)	O(2*B*)–C(2*B*)–N(1*B*)	117.0(3)
P(1)–O(14)–H(14)	124(5)	O(2*B*)–C(2*B*)–C(3*B*)	126.6(3)
C(2*A*)–N(1*A*)–C(9*A*)	122.8(3)	N(1*B*)–C(2*B*)–C(3*B*)	116.4(3)
C(2*A*)–N(1*A*)–H(1*A*)	119(2)	C(4*B*)–C(3*B*)–C(2*B*)	123.1(4)
C(9*A*)–N(1*A*)–H(1*A*)	119(2)	C(3*B*)–C(4*B*)–C(5*B*)	117.2(4)
O(2*A*)–C(2*A*)–N(1*A*)	119.7(3)	C(3*B*)–C(4*B*)–C(10*B*)	122.6(4)
O(2*A*)–C(2*A*)–C(3*A*)	123.5(3)	C(5*B*)–C(4*B*)–C(10*B*)	120.2(4)
N(1*A*)–C(2*A*)–C(3*A*)	116.9(3)	C(9*B*)–C(5*B*)–C(4*B*)	119.5(3)
C(4*A*)–C(3*A*)–C(2*A*)	121.4(4)	C(9*B*)–C(5*B*)–C(6*B*)	111.4(4)
C(3*A*)–C(4*A*)–C(5*A*)	118.6(3)	C(4*B*)–C(5*B*)–C(6*B*)	129.1(4)
C(3*A*)–C(4*A*)–C(10*A*)	121.5(4)	C(5*B*)–C(6*B*)–C(7*B*)	103.4(4)
C(5*A*)–C(4*A*)–C(10*A*)	119.9(4)	C(8*B*)–C(7*B*)–C(6*B*)	109.4(4)
C(9*A*)–C(5*A*)–C(4*A*)	120.0(3)	C(9*B*)–C(8*B*)–C(7*B*)	102.1(4)
C(9*A*)–C(5*A*)–C(6*A*)	109.8(3)	C(5*B*)–C(9*B*)–N(1*B*)	122.2(3)
C(4*A*)–C(5*A*)–C(6*A*)	130.2(3)	C(5*B*)–C(9*B*)–C(8*B*)	113.4(3)
C(5*A*)–C(6*A*)–C(7*A*)	104.4(3)	N(1*B*)–C(9*B*)–C(8*B*)	124.4(4)
C(6*A*)–C(7*A*)–C(8*A*)	108.3(4)	C(21)–O(21)–H(21)	105(3)

Table 7. Bond lengths *d* (Å) in structure **IIa**

Bond	*d*	Bond	*d*
N(1)–C(2)	1.43(2)	C(4)–C(10)	1.51(2)
N(1)–C(9)	1.37(2)	C(5)–C(6)	1.57(3)
N(1)–H(1)	0.86(7)	C(5)–C(9)	1.34(3)
O(2)–C(2)	1.23(2)	C(6)–C(7)	1.53(2)
C(2)–C(3)	1.41(2)	C(7)–C(8)	1.57(2)
C(3)–C(4)	1.39(2)	C(8)–C(9)	1.46(2)
C(4)–C(5)	1.40(2)		

Table 8. Bond lengths *d* (Å) in structure **III**

Bond	*d*	Bond	*d*
N(1)–C(2)	1.352(3)	C(5)–C(11)	1.383(3)
N(1)–C(11)	1.358(3)	C(5)–C(6)	1.513(4)
N(1)–H(1)	0.839(19)	C(6)–C(7)	1.491(4)
C(2)–O(2)	1.264(3)	C(7)–C(8)	1.501(4)
C(2)–C(3)	1.424(3)	C(8)–C(9)	1.563(4)
C(3)–C(4)	1.382(3)	C(9)–C(10)	1.561(4)
C(4)–C(5)	1.392(3)	C(10)–C(11)	1.467(3)
C(4)–C(12)	1.507(4)		

Table 9. Bond angles ω (deg) in structure **III**

Angle	ω	Angle	ω
C(2)–N(1)–C(11)	124.8(2)	C(11)–C(5)–C(6)	117.5(2)
C(2)–N(1)–H(1)	124.6(13)	C(4)–C(5)–C(6)	124.1(2)
C(11)–N(1)–H(1)	110.6(13)	C(7)–C(6)–C(5)	117.1(2)
O(2)–C(2)–N(1)	121.1(2)	C(6)–C(7)–C(8)	114.8(2)
O(2)–C(2)–C(3)	123.0(2)	C(7)–C(8)–C(9)	116.1(2)
N(1)–C(2)–C(3)	115.9(2)	C(10)–C(9)–C(8)	113.7(2)
C(4)–C(3)–C(2)	120.6(2)	C(11)–C(10)–C(9)	115.1(2)
C(3)–C(4)–C(5)	120.6(2)	N(1)–C(11)–C(5)	119.7(2)
C(3)–C(4)–C(12)	118.2(2)	N(1)–C(11)–C(10)	115.2(2)
C(5)–C(4)–C(12)	121.2(2)	C(5)–C(11)–C(10)	125.1(2)
C(11)–C(5)–C(4)	118.4(2)		

Table 10. Bond lengths *d* (Å) in structure **IV**

Bond	*d*	Bond	*d*
N(1)–C(2)	1.361(3)	C(5)–C(12)	1.361(3)
N(1)–C(12)	1.381(3)	C(5)–C(6)	1.527(3)
N(1)–H(1)	0.82(2)	C(6)–C(7)	1.518(3)
C(2)–O(2)	1.273(3)	C(7)–C(8)	1.519(4)
C(2)–C(3)	1.394(4)	C(8)–C(9)	1.550(4)
C(3)–C(4)	1.355(4)	C(9)–C(10)	1.507(3)
C(4)–C(5)	1.425(3)	C(10)–C(11)	1.540(3)
C(4)–C(13)	1.504(4)	C(11)–C(12)	1.478(3)

Table 11. Bond angles ω (deg) in structure **IV**

Angle	ω	Angle	ω
C(2)–N(1)–C(12)	124.1(2)	C(12)–C(5)–C(6)	120.7(2)
C(2)–N(1)–H(1)	119.8(14)	C(4)–C(5)–C(6)	121.2(2)
C(12)–N(1)–H(1)	116.0(14)	C(7)–C(6)–C(5)	114.8(2)
O(2)–C(2)–N(1)	119.2(2)	C(8)–C(7)–C(6)	117.8(2)
O(2)–C(2)–C(3)	124.9(2)	C(7)–C(8)–C(9)	114.7(2)
N(1)–C(2)–C(3)	115.9(2)	C(10)–C(9)–C(8)	115.8(2)
C(4)–C(3)–C(2)	122.3(2)	C(9)–C(10)–C(11)	115.2(2)
C(3)–C(4)–C(5)	120.2(2)	C(12)–C(11)–C(10)	112.2(2)
C(3)–C(4)–C(13)	119.1(2)	C(5)–C(12)–N(1)	119.6(2)
C(5)–C(4)–C(13)	120.7(2)	C(5)–C(12)–C(11)	125.8(2)
C(12)–C(5)–C(4)	118.0(2)	N(1)–C(12)–C(11)	114.6(2)

Table 12. Bond lengths *d* (Å) in structure **V**

Bond	*d*	Bond	*d*
N(1)–C(2)	1.396(12)	C(5)–C(6)	1.485(12)
N(1)–C(9)	1.346(14)	C(5)–C(10)	1.588(15)
C(2)–O(2)	1.270(13)	C(6)–C(7)	1.452(14)
C(2)–C(3)	1.506(13)	C(7)–C(8)	1.623(18)
C(3)–C(4)	1.463(14)	C(8)–C(9)	1.512(13)
C(3)–C(11)	1.259(12)	C(9)–C(10)	1.254(14)
C(4)–C(10)	1.452(12)	C(11)–N(11)	1.207(9)

and **IV** were equal to 20%. Compound **V** was prepared according to the procedure described in [16]. Physicochemical characteristics of the compounds synthesized are listed in Table 1.

The experimental intensities for single crystals of compounds **I**–**IV** were measured on a CAD4 diffractometer [17] (λMoK_α, graphite monochromator, ω scan mode) at room temperature. The unit cell parameters

Table 13. Parameters of the interatomic contacts in the structures studied

D–H	*d*(*D*–H)	*d*(*D*···*A*)	*d*(H···*A*)	ω*DHA*	*A*	Symmetry code
			I			
N(1)–H(1)	0.874(1)	2.768(1)	1.895(5)	176.1(1)	O(2)	(–*x*; 1 – *y*; 1 – *z*)
			II			
N(1*A*)–H(1*A*)	0.89(4)	2.780(4)	1.89(4)	177(4)	O(11)	
N(1*B*)–H(1*B*)	0.88(4)	2.768(4)	1.89(4)	173(4)	O(21)	
O(12)–H(12)	0.89(7)	2.548(4)	1.68(7)	168(7)	O(2*A*)	
O(13)–H(13)	0.94(6)	2.589(4)	1.65(6)	173(6)	O(11)	(–*x*; 1 – *y*; 1 – *z*)
O(14)–H(14)	0.86(8)	2.462(4)	1.60(8)	175(8)	O(2*B*)	(–*x*; 1 – *y*; 1 – *z*)
O(21)–H(21)	0.86(5)	2.710(4)	1.86(5)	173(5)	O(2*A*)	(1 – *x*; 1 – *y*; 1 – *z*)
			IIa			
N(1)–H(1)	0.86(7)	2.81(1)	2.01(7)	156(7)	O(2)	(1 – *x*; *y* – 1/2; 1/2 – *z*)
			III			
N(1)–H(1)	0.839(19)	2.785(3)	1.96(2)	167(2)	O(2)	(–*x*; –*y*; 1 – *z*)
			IV			
N(1)–H(1)	0.82(2)	2.776(3)	1.96(2)	174(2)	O(2)	(1 – *x*; –*y*; 1 – *z*)
			V			
N(1)–H(1)	0.89(5)	2.71(1)	1.83(5)	171(6)	O(2)	(–1 – *x*; 1 – *y*; –*z*)

Note: *D* is a donor, *A* is an acceptor, and H is a hydrogen atom; the *d* distances and ω angles are given in angströms and degrees, respectively.

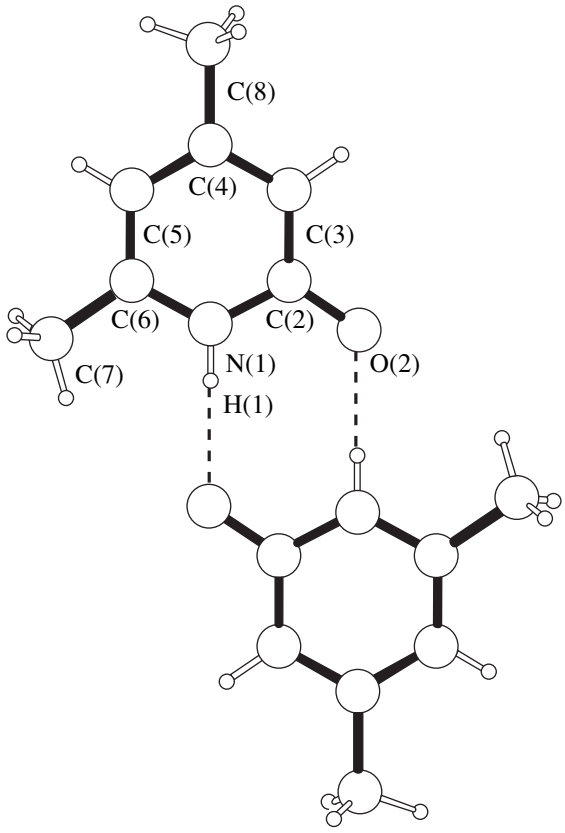

Fig. 3. Molecular structure, atomic numbering, and hydrogen bond formation for compound **I**.

were determined and refined using 25 reflections in the θ range 12°–15°. No correction for absorption was introduced because of the small linear absorption coefficients of the compounds studied and the small sizes of their crystals. The primary processing of the sets of diffraction data was performed with the WinGX98 program package [18]. All the subsequent calculations were performed with the SHELX97 program package [19]. The crystal structures were determined by direct methods. All the non-hydrogen atoms were refined in the anisotropic approximation.

The diffraction experiments for compounds **IIa** and **V** (available only in the form of powders) were performed on a DRON-3 automated powder diffractometer (NPO Burevestnik; λCuK_α; Ge monochromator; step width, 0.02° in 2θ). The unit cell parameters were determined with the ITO indexing program [20]. The space groups were determined from the systematic absences of the reflections. Preliminary data on the molecular structures of compounds **IIa** and **V** were confirmed by the ^{1}H NMR spectra. The initial geometrical models were constructed using semiempirical and empirical methods with the MOPAC 6.0 [21] and PCMODEL [22] programs. The structures were solved by the grid search procedure [23] based on the given molecular fragments. The Rietveld full-profile refinement of the structures was performed according to the MRIA program [24]. The pseudo-Voigt function was used as a profile func-

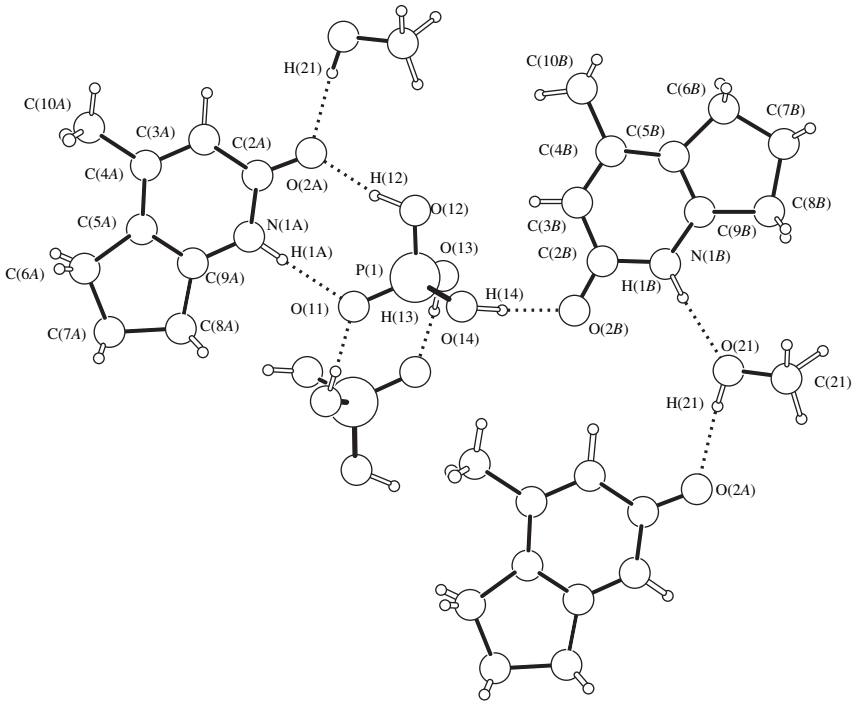

Fig. 4. Molecular structure, atomic numbering, and hydrogen bond formation for compound **II**.

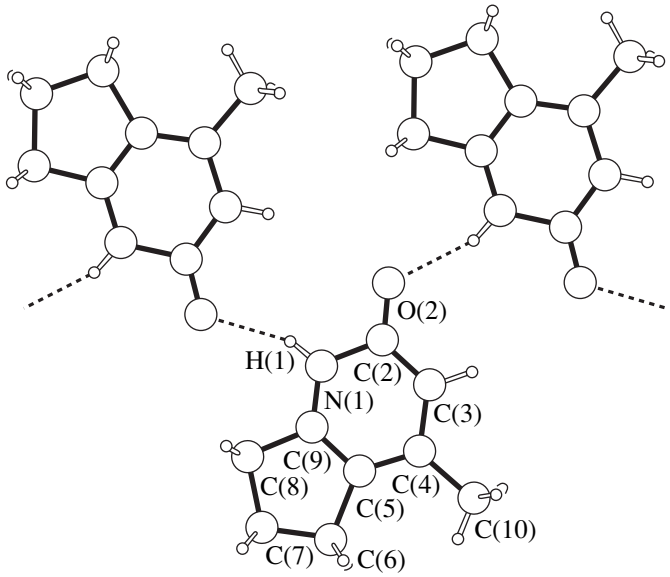

Fig. 5. Molecular structure, atomic numbering, and hydrogen bond formation for compound **IIa**.

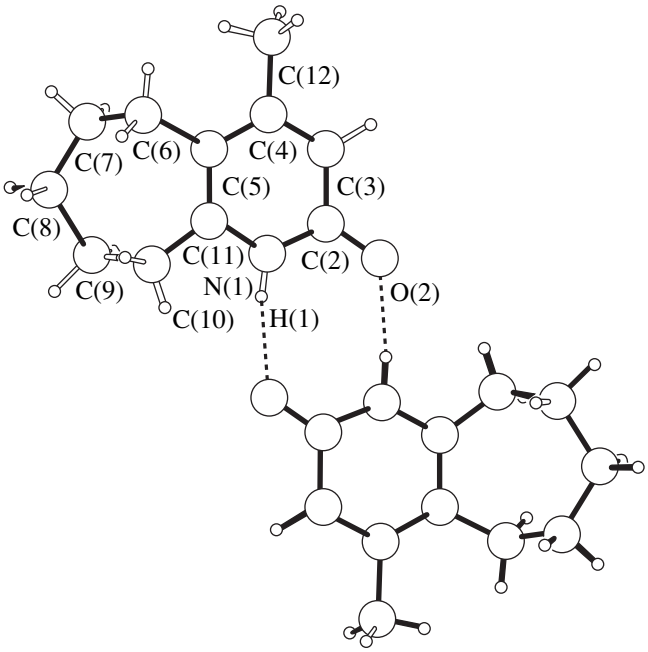

Fig. 6. Molecular structure, atomic numbering, and hydrogen bond formation for compound **III**.

tion, and the background was approximated by the Chebyshev fifth-degree polynomials. The thermal parameters of the non-hydrogen atoms of the molecular skeleton were averaged in the course of refinement.

The main experimental parameters and crystal data for the compounds studied are summarized in Table 2. The interatomic distances and bond angles are listed in Tables 3–12. The experimental and difference X-ray

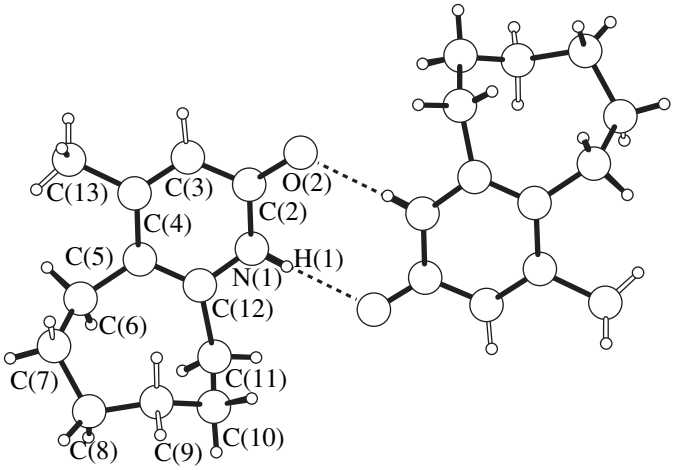

Fig. 7. Molecular structure, atomic numbering, and hydrogen bond formation for compound **IV**.

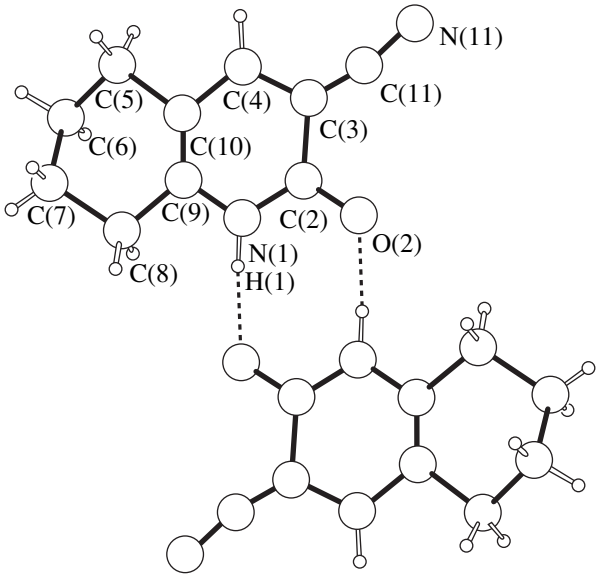

Fig. 8. Molecular structure, atomic numbering, and hydrogen bond formation for compound **V**.

spectra are shown in Figs. 1 and 2. The molecular structures with the atomic numberings are shown in Figs. 3–8. The drawings were obtained with the PLUTON96 program package [25].

Crystal data for the compounds studied are deposited in the Cambridge Structural Database (deposit nos. 213170–213175).

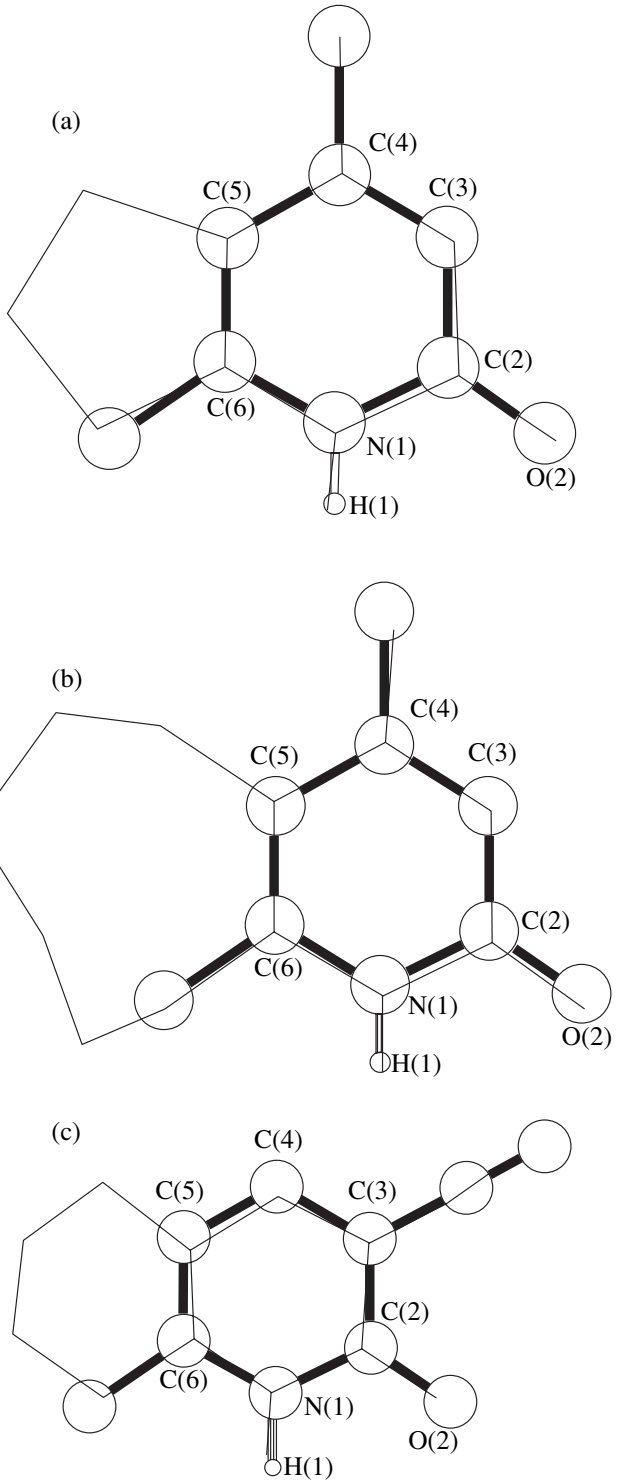

Fig. 9. Superposition of molecules: (a) **I** and **IIa**, (b) **I** and **IV**, and (c) **VII** and **V**.

RESULTS AND DISCUSSION

It is common knowledge that 2-pyridones and their salts act as ambident compounds in reactions with electrophilic agents, for example, in alkylation reactions. The methyl group or the methylene link in the 6-position of 2-pyridone substantially affects the selectivity of these reactions due to steric shielding of the nitrogen atom by the alkyl fragment. In this connection, it is of interest to determine the degree of steric shielding upon replacement of the methyl group by a cycloalkane frag-

ment that has a different size and is annelated to the C(5)–C(6) bond. The structural data for the compound with the cyclohexane fragment [2-oxo-1,2,5,6,7,8-hexahydroquinoline (**VI**)] were obtained earlier in [11]. The structure of cyanoderivative **V** was compared with that of its prototype, namely, 3-cyano-6-methylpyridin-2(1*H*)-one (**VII**), which was described in [26].

The simplest way to compare the structural transformations observed when going from the methyl group to the cycloalkane fragment in molecules **I**–**VII** is to superpose the structure of the pyridone fragment of the prototype molecule **I** and those of derivatives **II**–**V** and to compare the relative positions of the 6-CH_3 group and the methylene link in the 6-position (Fig. 9). It is clearly seen that the degree of shielding decreases only in the case of cyclopentane derivative **IIa** (the steric strain tightens the five-membered ring removing the methylene link in the 6-position from the nitrogen atom; Fig. 9a). In all other derivatives (Fig. 9b), the positions of the methylene links in the six-, seven-, and eight-membered rings almost exactly coincide with the position of the methyl group in the parent molecule **I**. A similar situation is observed when going from the methyl to cyclohexane derivative in 3-cyanopyridones **V** and **VII** (Fig. 9c).

Compounds **I**–**V** form hydrogen-bond systems, which are inherent attributes of crystal structures in this class of compounds. In compounds **I** and **III**–**V**, centrosymmetric eight-membered dimers involving the H(1)N(1)C(2)O(2) atoms of the pyridone ring are formed (Table 13, Figs. 3, 6–8).

Molecule **IIa** provides an exception to the rule of the formation of eight-membered cyclic dimers. In this compound, the pyridone atoms H(1), N(1), and O(2) are also involved in hydrogen bonding but the type of binding is different: in the crystal structure, infinite chains are formed instead of dimeric fragments (Fig. 5). Compound **II** is characterized by a more extended hydrogen-bond system, which includes not only heterocyclic molecules but also molecules of orthophosphoric acid and solvate methanol. Figure 4 shows that, in the crystal structure, dimeric fragments are formed only via the hydrogen bonds of H_3PO_4 molecules. The hydrogen bonds formed by two crystallographically independent pyridone molecules (*A* and *B*) are different in type. Molecule *A* forms three hydrogen bonds, namely, two bonds with H_3PO_4 and one bond with the methanol molecule. Molecule *B* forms only two hydrogen bonds, namely, one bond with H_3PO_4 and one bond with the methanol molecule. Note that the solvate molecule acts as both a donor and an acceptor (Table 13). The parameters of the hydrogen bonds were calculated using the PARST95 program [27].

ACKNOWLEDGMENTS

This work was supported by the International Association of assistance for the promotion of cooperation with scientists from the New Independent States of the former Soviet Union (project INTAS no. 00-0711). We also acknowledge the support of the Russian Foundation for Basic Research in the payment of the license for using the Cambridge Structural Database, project no. 02-07-90322.

REFERENCES

1. V. B. Rybakov, S. G. Zhukov, E. V. Babaev, *et al.*, Kristallografiya **44** (6), 1067 (1999) [Crystallogr. Rep. **44**, 997 (1999)].
2. V. B. Rybakov, S. G. Zhukov, E. V. Babaev, *et al.*, Kristallografiya **45** (1), 108 (2000) [Crystallogr. Rep. **45**, 103 (2000)].
3. V. B. Rybakov, S. G. Zhukov, E. V. Babaev, *et al.*, Kristallografiya **45** (2), 292 (2000) [Crystallogr. Rep. **45**, 261 (2000)].
4. V. B. Rybakov, S. G. Zhukov, K. Yu. Pasichnichenko, and E. V. Babaev, Koord. Khim. **26** (9), 714 (2000).
5. V. B. Rybakov, S. G. Zhukov, E. V. Babaev, and E. J. Sonneveld, Kristallografiya **46** (3), 435 (2001) [Crystallogr. Rep. **46**, 385 (2001)].
6. V. B. Rybakov, S. I. Troyanov, E. V. Babaev, *et al.*, Kristallografiya **46** (6), 1069 (2001) [Crystallogr. Rep. **46**, 986 (2001)].
7. V. B. Rybakov, E. V. Babaev, K. Yu. Pasichnichenko, and E. J. Sonneveld, Kristallografiya **47** (1), 76 (2002) [Crystallogr. Rep. **47**, 69 (2002)].
8. V. B. Rybakov, E. V. Babaev, and V. V. Chernyshev, Kristallografiya **47** (3), 473 (2002) [Crystallogr. Rep. **47**, 428 (2002)].
9. V. B. Rybakov, E. V. Babaev, and K. Yu. Pasichnichenko, Kristallografiya **47** (4), 678 (2002) [Crystallogr. Rep. **47**, 622 (2002)].
10. V. B. Rybakov, E. V. Babaev, A. A. Tsisevich, *et al.*, Kristallografiya **47** (6), 1042 (2002) [Crystallogr. Rep. **47**, 973 (2002)].
11. D. V. Al'bov, V. B. Rybakov, E. V. Babaev, and L. A. Aslanov, Kristallografiya **48** (2), 277 (2003) [Crystallogr. Rep. **48**, 280 (2003)].
12. V. B. Rybakov, L. G. Boboshko, N. I. Burakov, *et al.*, Kristallografiya **48** (4), 627 (2003) [Crystallogr. Rep. **48**, 576 (2003)].
13. F. H. Allen and O. Kennard, Chem. Design Autom. News **8** (1), 31 (1993).
14. G. Bardhan, J. Chem. Soc., 2231 (1929).
15. T. Kato, M. Sato, M. Noda, and T. Itoh, Chem. Pharm. Bull. (Tokyo) **28**, 2244 (1980).
16. J. B. Paine, J. Heterocycl. Chem. **24**, 351 (1987).
17. *Enraf–Nonius CAD4 Software: Version 5.0* (Enraf–Nonius, Delft, Netherlands, 1989).
18. L. J. Farrugia, *WinGX98: X-ray Crystallographic Programs for Windows* (Univ. of Glasgow, UK, 1998).

19. G. M. Sheldrick, *SHELX97: Program for the Solution and Refinement of Crystal Structures* (Univ. of Göttingen, Germany, 1997).

20. J. W. Visser, J. Appl. Crystallogr. **2**, 89 (1969).

21. J. J. P. Stewart, *MOPAC 6.0: QCPE Program No. 455* (Department of Chemistry, Indiana Univ., Bloomington, USA, 1990).

22. *PCMODEL 7.0: Molecular Modelling Software for the Windows 95/NT. Sarena Software* (Bloomington, USA, 1999).

23. V. V. Chernyshev and H. Schenk, Z. Kristallogr. **213**, 1 (1998).

24. V. B. Zlokazov and V. V. Chernyshev, J. Appl. Crystallogr. **25**, 447 (1992).

25. A. L. Spek, *PLUTON96: Molecular Graphics Program* (Univ. of Utrecht, Netherlands, 1996).

26. M. Munakata, Wu Liang Ping, M. Yamamoto, *et al.*, J. Am. Chem. Soc. **118**, 3117 (1996).

27. M. Nardelli, J. Appl. Crystallogr. **28**, 259 (1995).

Translated by I. Polyakova

Crystallography Reports, Vol. 49, No. 2, 2004, pp. 169–174. Translated from Kristallografiya, Vol. 49, No. 2, 2004, pp. 219–223.

REAL STRUCTURE OF CRYSTALS

Redistribution of Thermoelastic Stresses in Shaped Crystals: Numerical Simulation[1]

L. L. Kuandykov and S. I. Bakholdin

Ioffe Physicotechnical Institute, Russian Academy of Sciences, Politekhnicheskaya ul. 26, St. Petersburg, 194021 Russia

e-mail: Lev@mail.ioffe.ru

Received February 26, 2003

Abstract—The shape of crystals was considered for the first time as an important factor controlling thermoelastic stresses during crystal growth. It was found on the basis of numerical simulation that thermoelastic stresses can be redistributed by varying the shape of a crystal during growth. In this way, large weakly stressed regions can be obtained in the crystal owing to the formation of locally stressed regions. As an example, a model of a sapphire ribbon (50×175 mm^2) divided by waists into three plates (50×50 mm^2) is discussed. Different crystallographic orientations and slip systems are considered. © *2004 MAIK "Nauka/Interperiodica".*

INTRODUCTION

It is well known that thermoelastic stresses in single crystals are determined by three main factors, namely, the curvature of the thermal field in a crystal [1, 2], the crystallographic orientation [3, 4], and the crystal shape [5–8]. Conventional methods for reducing thermoelastic stresses are concerned with smoothing (linearization) of the thermal field [9–11] and choosing an appropriate crystallographic orientation [4]. In any case, the crystal shape remains invariable. Now, the question is what to do if it is necessary to reduce thermoelastic stresses further, but it is impossible to improve the thermal field, and the crystallographic orientation is strictly specified. The aim of this study is to demonstrate that the shape of a crystal can be an important parameter controlling thermoelastic stresses that is no less important than the other two.

A Criterion for Evaluation of Thermoelastic Stresses

The Schmidt law is commonly used when it is necessary to find out whether stresses are critical or not. According to this law, shear stresses in a given slip system can cause plastic strains and, hence, the multiplication of dislocations, beginning from some critical value τ^* (for sapphire single crystals, τ^* at 1800°C is 1 and 10 MPa for the basal and prismatic slip systems, respectively [12]).

The stresses averaged according to the von Mises scheme provide the most typical estimate for the level of thermoelastic stresses:

$$\sigma_{VM} = \sqrt{(\sigma_x - \sigma_y)^2 + (\sigma_y - \sigma_z)^2 + (\sigma_z - \sigma_x)^2 + 6(\tau_{xy}^2 + \tau_{yz}^2 + \tau_{zx}^2)}/\sqrt{2},$$

where σ_x, σ_y, σ_z, τ_{xy}, τ_{yz}, and τ_{zx} are the components of the stress tensor $\boldsymbol{\sigma}$.

However, in practice, it is not correct to compare τ^* with σ_{VM} owing to the crystal anisotropy. It is more appropriate to compare τ^* with the root-mean-square value of the shear stress calculated for a specific slip system at a given crystallographic orientation: $\tau_{ms} = \sqrt{(\tau_1^2 + \tau_2^2 + \ldots + \tau_n^2)/n}$, where τ_i is the shear stress in the direction i for the specific slip system.

Calculation of Thermoelastic Stresses

It is possible to analytically calculate the components of the tensor $\boldsymbol{\sigma}$ only for crystals of relatively simple shapes, such as ribbon or infinite rods. The analytical calculation is usually performed using an approximation implying the isotropy of elasticity. The formulas for maximum thermoelastic stresses in a rod ($\tau^* \sim R^2T''$) and ribbon ($\tau^* \sim b^2T''$) were obtained in [13] by integrating the equations of the elasticity theory. Here, R is the rod radius, b is the ribbon width, and T'' is the second derivative of temperature along the pulling direction in the crystal.

The finite-element method is most commonly used in numerical calculations of thermoelastic stresses. This method has been successfully used in calculations of thermoelastic stresses in GaAs crystals grown by the vapor-pressure-controlled Czochralski technique [14], Gd_2SiO_5 (GSO) crystals grown by the conventional Czochralski technique [4], and in the following crystals subjected to annealing: GaAs [15], GaSb (Czochralski

[1] This work was presented at the National Conference on Crystal Growth (NCCG-2002, Moscow).

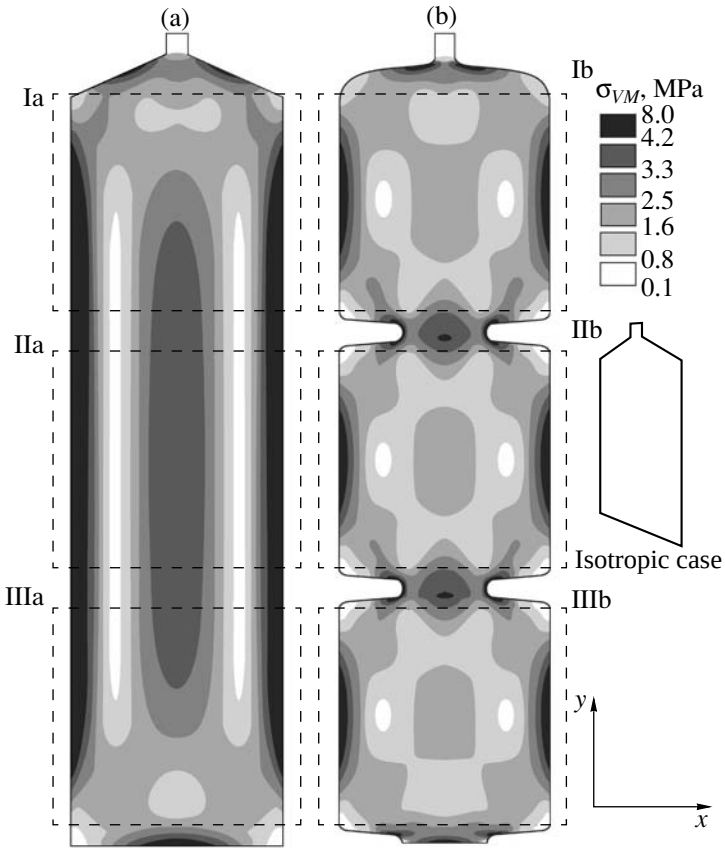

Fig. 1. Two-dimensional model for the distribution of thermoelastic stresses averaged according to the von Mises scheme (σ_{VM}) in sapphire ribbons (the isotropic case): (a) ribbon *A*, conventional profile, 50×175 mm^2; (b) variable profile with waists (the height and width of a waist being 10 and 20 mm, respectively). Dashed lines indicate the sectors 50×50 mm^2 in size. The maximum values of σ_{VM} are 8.0 and 7.0 MPa for ribbons *A* and *B* (in the waist), respectively.

grown) [16], Al_2O_3 hemispheres (the Stepanov technique, growth from an element of shape (GES)) [17], and Al_2O_3 [18] and Si [19] ribbons (the Stepanov technique, edge-defined film-fed growth (EFG)). The calculations are performed using both multipurpose software packages (FIDAP [20], MARC [21, 22], CFD-ACE+ [23], Cosmos/M [24], etc.) and programs specially developed for the simulation of the crystal growth (CrysVUN++ [25] and STHAMAS [26]).

Single-Crystal Sapphire Plates

Single-crystal sapphire plates of different sizes (from 10×10 to 50×50 mm^2) are used in microelectronics, ophthalmology, the watch-making industry, and other fields of science and technology, where sapphire is indispensable due to its unique characteristics. The most efficient way to produce square sapphire plates is the cutting of single-crystal ribbons grown by the Stepanov technique (EFG). It is clear that stress on such ribbons should be kept as low as possible if we want to preserve the mechanical characteristics of sapphire. To reduce residual stresses in a ribbon, we must, first of all, reduce the thermoelastic stresses arising during crystal growth.

SIMULATION OF THERMOELASTIC STRESSES

To reveal the effect of changes in the shape of a crystal on the distribution of thermoelastic stresses in the crystal, we developed two two-dimensional models of ribbons of conventional (Fig. 1a) and variable (Fig. 1b) shapes. The calculation of thermoelastic stresses was performed in an isotropic approximation using the Cosmos/M software package (version 2.6). For both ribbons, the model temperature field had the form $T(y) = 8.7y + 0.005y^2 + 2050$ (Fig. 2). Such a field was chosen for the following reasons: First, the field shows almost ideal linearity; therefore, it is impossible to reduce thermoelastic stresses by further smoothing the thermal field. Second, the field is characterized by the constant curvature $T_y'' = 0.01$, which does not affect the distribution of thermoelastic stresses but only their absolute values.

The length of both ribbons was 175 mm (plus 10 mm allocated for the growing portion); their width was 50 mm; the width of a seed was 10 mm; and the height and the width of the waist were 10 and 20 mm, respectively. In our calculations, we used the following values for the sapphire characteristics: the Young modulus $E = 0.435 \times 10^{12}$ Pa, Poisson's ratio $N_{xy} = 0.27$, and thermal expansion coefficient $\alpha = 0.88 \times 10^{-5}$ K^{-1} [27]. The boundary conditions were as follows: the rigidly fixed seed and the absence of external forces along the rest of the crystal perimeter (the free surface).

A Cosmos/M software package was used to compute the components of the tensor $\boldsymbol{\sigma}$ in the isotropic approximation. In the next stage, the components of $\boldsymbol{\sigma}$ were converted to components of the shear-stress tensor $\boldsymbol{\tau}$ for different crystallographic orientations of the ribbon in the basal and prismatic slip systems. The algorithm for the conversion of $\boldsymbol{\sigma}$ to $\boldsymbol{\tau}$ has been described in [28].

In some cases, the isotropic approximation is not so bad, for example, for crystals with cubic symmetry and even for sapphire crystals. For the latter, however, the error is no less than 30% [29]. Therefore, we present the results of both calculations (for isotropic and anisotropic cases).

Isotropic Case (von Mises Stresses σ_{VM})

The distribution of thermoelastic stresses is shown in Figs. 1a and 1b for ribbons with the conventional (ribbon *A*) and variable (ribbon *B*) profiles. The dashed lines mark similar sectors 50×50 mm^2 in size. The maximum and average values of σ_{VM} for each sector are listed in the table. The maximum value of σ_{VM} for the waists is 7.0 MPa; i.e., it does not exceed the maximum value of σ_{VM} for ribbon *A*. Note that the differences in the stress values for ribbons *A* and *B* should depend on the ribbon width and the waist size; in the example under discussion, they may exceed 20–30%.

Anisotropic Case (Root-Mean-Square Shear Stresses τ_{ms})

Here, we deal with the anisotropy of the possible plastic strain. The thermoelastic-stress tensor $\boldsymbol{\sigma}$ was taken from the previous calculations. The root-mean-square shear stresses τ_{ms} were determined by conversion from the components of $\boldsymbol{\sigma}$ for seven crystallographic orientations of a single-crystal sapphire ribbon in the basal and prismatic slip systems.

We use the notation "PS*kl*" and "BS*kl*" for prismatic (PS) and basal (BS) slip systems in a ribbon with a *k*-oriented surface and a pulling direction along *l*. The *k*, *l* pair completely determines the crystallographic orientation of the ribbon. The following seven orientations were studied: *ca* = $(0001)\langle\bar{1}2\bar{1}0\rangle$, *cm* = $(0001)\langle10\bar{1}0\rangle$, *ac* = $\{\bar{1}2\bar{1}0\}(0001)$, *am* = $\{\bar{1}2\bar{1}0\}\langle10\bar{1}0\rangle$, *aR* = $\{10\bar{1}2\}\langle\bar{1}2\bar{1}0\rangle$, *mc* = $\{10\bar{1}0\}(0001)$, and *Ra* = $\{10\bar{1}2\}\langle\bar{1}2\bar{1}0\rangle$.

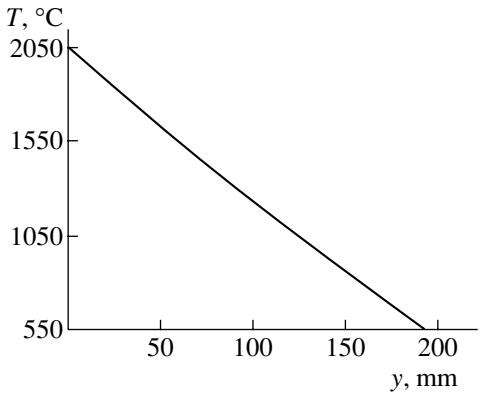

Fig. 2. Model thermal field for all the ribbons: $T(y) = -8.7y + 0.005y^2 + 2050$ (°C).

In spite of the large difference between the distributions of thermoelastic stresses for $7 \times 2 = 14$ cases, we decided not to present all the results here in order to avoid redundancy of information and parallelism in some figures. In this paper, we present the most interesting distributions of τ_{ms} (both for ribbons *A* and *B*): PS*am* + BS*am* (Fig. 3) and PS*aR* + BS*aR* (Fig. 4). To use the figures in the most efficient way, let us note that the distribution pattern for τ_{ms} in PS*ca*, PS*cm*, and PS*Ra* is similar to the distribution of σ_{VM} shown in Fig. 1.

The components τ_{ms} in BS*ca* and BS*cm* vanish due to the absence of the basal slip in the two-dimensional simulation for the ribbons with orientations *ca* and *cm*. However, even in the three-dimensional model for relatively thin ribbons with orientations *ca* and *cm*, the value of τ_{ms} is much smaller for the basal than for the prismatic slip.

In contrast to Fig. 1, the sectors 50×50 mm^2 are not marked in Figs. 3 and 4. Nevertheless, all the calculated data were analyzed to find out the effect of waists on the magnitude of thermoelastic stresses in these sectors for each of seven orientations under consideration. It was found that sectors I, II, and III of ribbon *B*, in comparison with the corresponding sectors of ribbon *A*, are:

Comparison of maximum and average values of σ_{VM} in sectors I, II, and III of sapphire ribbons **A** and **B** (see Fig. 1) for the isotropic case

Sector no.	σ_{av}, MPa	σ_{max}, MPa	Sector no.	σ_{av}, MPa	σ_{max}, MPa
Ia	2.5	7.5	Ib	2.0	6.3
IIa	2.9	8.0	IIb	1.9	6.0
IIIa	2.5	7.5	IIIb	1.9	6.0

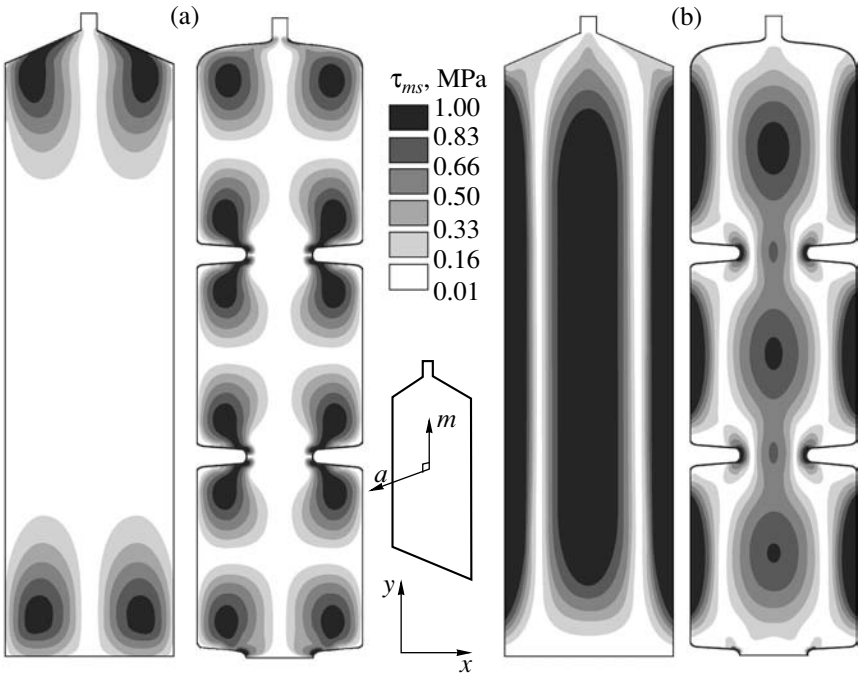

Fig. 3. Two-dimensional model for the distribution of thermoelastic stresses (the root-mean-square shear stress τ_{ms}) in a sapphire ribbon (the anisotropic case) with the surface orientation $\{\bar{1}2\bar{1}0\}$ and the pulling direction $\langle 10\bar{1}0\rangle$ (*am*): (a) basal slip (BS*am*) and (b) prismatic slip (PS*am*).

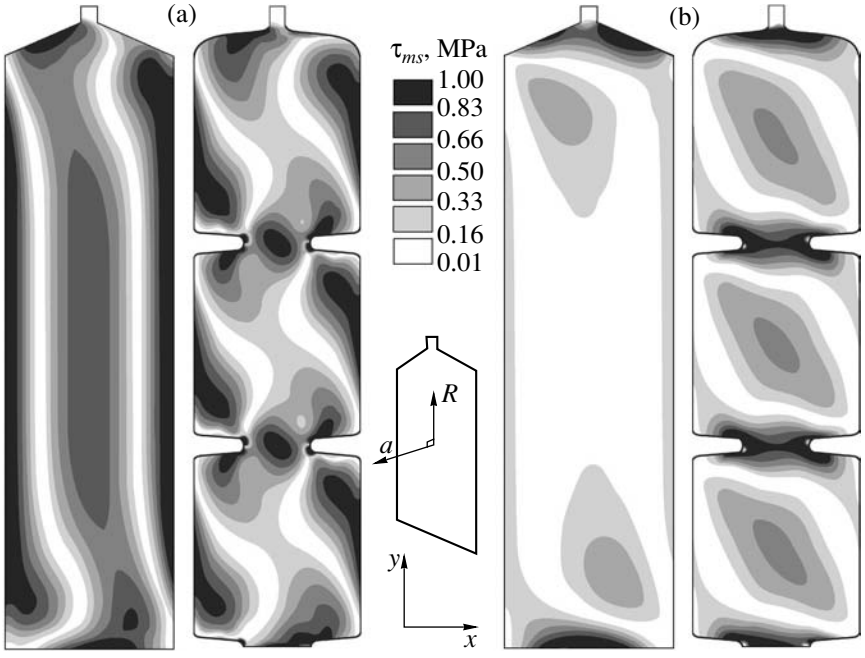

Fig. 4. Two-dimensional model for the distribution of thermoelastic stresses (the root-mean-square shear stress τ_{ms}) in a sapphire ribbon (the anisotropic case) with the surface orientation $\{\bar{1}2\bar{1}0\}$ and the pulling direction $\langle 10\bar{1}2\rangle$ (*aR*): (a) basal slip (BS*aR*) and (b) prismatic slip (PS*aR*).

(i) superior with respect to the average and maximum values of τ_{ms} for the orientations *ca* and *cm* (in the two-dimensional model);

(ii) superior with respect to the maximum values of τ_{ms} for the orientations *Ra* and *am* (see Fig. 3 for *am*); and

(iii) at a disadvantage with respect to the average and maximum values of τ_{ms} for the orientations *ac* and *mc*.

A significant redistribution of thermoelastic stresses is observed for the orientation *aR* (Fig. 4).

DISCUSSION

Our studies of the distribution of thermoelastic stresses in a ribbon with a wavy profile showed that the maximum thermoelastic stresses (σ_{VM}) at convex parts of the ribbon were lower than at concave parts. In addition, the concavity favored the localization of thermoelastic stresses, whereas the convexity led to their spreading. In the model under consideration, the effect of convexity and concavity can be seen at the waist edges. Thus, we decided to check by numerical simulation whether it is possible to obtain several plates with low stresses using one ribbon with locally stressed waists.

The simulation for the isotropic case demonstrated that the average and maximum values of thermoelastic stresses in sectors 50×50 mm^2 in size (indicated by the dashed lines in Fig. 1) are lower in the ribbon with waists. It is clear that such a redistribution of thermoelastic stresses is caused only by the shape variation. It should be noted that actual waists should also lead to distortions of the thermal field in the crystal. However, to demonstrate clearly the effect of shape variation on the distribution of thermoelastic stresses, we need to apply the same thermal field to both ribbons.

In the anisotropic case, the situation is more complicated due to the existence of different slip systems, along with some crystallographic features. In our section dealing with the numerical simulation, we tried to classify the effects of waists on the distribution of thermoelastic stresses. However, for further analysis, it is necessary to take into account that the onset of plastic deformation in the basal plane corresponds to lower stresses as compared to the prismatic plane (at $t >$ 1000°C [30]).

It is convenient to explain the mechanism underlying the redistribution of thermoelastic stresses by looking to sectors IIa and IIb in Fig. 1. The component σ_x is nearly the same for sectors IIa and IIb, but σ_y in IIb is smaller because this sector is bounded from above and below by the free surface (everywhere except at the waists). Therefore, in the isotropic case, the average value of the thermoelastic stresses σ_{VM} is lower in sector IIb. In the anisotropic crystal, the situation is not so straightforward. The thermoelastic stresses (τ_{ms}) in the sectors between waists will be lower than those in the similar sectors in the conventional ribbon only when the projection of σ_y onto the corresponding slip plane for the specific crystallographic orientation is dominant over the projections of other components. The waists under consideration may suggest an erroneous analogy with the so-called Dash necking [31, 32]. However, the well-known and remarkable idea of Dash of reducing the dislocation density in the stage of continuous growth by making a small waist at the seed has nothing in common with macroscopic control over the thermoelastic stresses.

CONCLUSIONS

It was demonstrated that the shape of a crystal can be an actual parameter controlling the magnitude and distribution of thermoelastic stresses directly during crystal growth that is no less important than the curvature of the thermal field in the crystal and the crystallographic orientation. The numerical simulation of thermoelastic stresses was performed for a single-crystal sapphire ribbon with waists. The redistribution of thermoelastic stresses in the crystal when its shape was varied was found. Different crystallographic orientations and slip systems were considered. The redistribution of thermoelastic stresses in the crystal with the varied shape makes it possible to obtain large weakly stressed regions in the crystal owing to the formation of localized regions with higher stresses.

ACKNOWLEDGMENTS

We are deeply grateful to P.I. Antonov and E.V. Galaktionov for their help.

REFERENCES

1. B. A. Boley and J. H. Weiner, *Theory of Thermal Stresses* (Wiley, New York, 1960; Mir, Moscow, 1964).
2. R. W. Gurtler, J. Cryst. Growth **50**, 69 (1980).
3. M. I. Musatov, G. V. Anan'eva, and I. V. Morova, Opt. Mekh. Prom., No. 7, 39 (1978).
4. N. Miyazaki, T. Tamura, K. Kubashige, *et al.*, J. Cryst. Growth **182**, 73 (1997).
5. M. G. Mil'vidskiĭ and V. B. Osvenskiĭ, in *Proceedings of IV All-Union Meeting on Crystal Growth* (Erevan, 1972), p. 50.
6. S. S. Vakhrameev, M. G. Mil'vidskiĭ, V. B. Osvenskiĭ, *et al.*, in *Crystal Growth* (Nauka, Moscow, 1977), Vol. 12, p. 287.
7. P. I. Antonov, E. V. Galaktionov, V. M. Krymov, *et al.*, Izv. Akad. Nauk SSSR, Ser. Fiz. **40** (7), 1414 (1976).
8. P. I. Antonov, E. V. Galaktionov, V. M. Krymov, *et al.*, Izv. Akad. Nauk SSSR, Ser. Fiz. **40** (7), 1419 (1976).
9. P. I. Antonov, E. V. Galaktionov, V. M. Krymov, *et al.*, J. Cryst. Growth **50**, 325 (1980).
10. K. W. Kelly, K. Koai, and S. Motakef, J. Cryst. Growth **113**, 254 (1991).

11. D. E. Bornside, T. A. Kinney, and R. A. Brown, J. Cryst. Growth **108**, 779 (1991).
12. S. I. Bakholdin, E. V. Galaktionov, and V. M. Krymov, Izv. Ross. Akad. Nauk, Ser. Fiz. **63** (9), 1816 (1999).
13. P. I. Antonov and V. M. Krymov, Izv. Akad. Nauk SSSR, Ser. Fiz. **44** (2), 244 (1980).
14. Ch. Frank, K. Jacob, M. Neubert, and P. Rudolph, J. Cryst. Growth **213**, 10 (2000).
15. M. Metzger, J. Cryst. Growth **230**, 210 (2001).
16. P. Boiton, N. Giacometti, T. Duffar, *et al.*, J. Cryst. Growth **206**, 159 (1999).
17. F. Theodore, T. Duffar, J. L. Santailler, *et al.*, J. Cryst. Growth **204**, 317 (1999).
18. F. Theodore, T. Duffar, and F. Louchet, J. Cryst. Growth **198–199**, 232 (1999).
19. H. M. Ettouney and J. P. Kalejs, J. Cryst. Growth **82**, 17 (1987).
20. *FDI 7.52 Documentation* (Fluid Dynamics Int., 1993).
21. *MARC K 6.2 Documentation* (Marc Analysis Res. Corp., 1995); www.marc.com.
22. J. L. Santailler, T. Duffar, F. Theodore, *et al.*, J. Cryst. Growth **180**, 698 (1997).
23. *User's Manual of CFD-ACE V.5* (CFD Res. Corp., 1998); www.cfdrc.com.
24. *Cosmos/M Documentation v.2.6* (Structural Research and Analysis Corp., 2002); www.cosmosm.com.
25. M. Kurz, A. Pustai, and G. Müller, J. Cryst. Growth **198–199**, 101 (1999).
26. J. Fainberg, H.-J. Leister, and G. Müller, J. Cryst. Growth **180**, 517 (1997).
27. *Ruby and Sapphire*, Ed. by M. V. Klassen-Neklyudova and Kh. S. Bagdasarov (Nauka, Moscow, 1974).
28. S. I. Bakholdin, E. V. Galaktionov, V. M. Krymov, and V. D. Slobodinskiĭ, Izv. Ross. Akad. Nauk, Ser. Fiz. **58** (9), 32 (1994).
29. P. I. Antonov, S. I. Bakholdin, E. V. Galaktionov, *et al.*, J. Cryst. Growth **52**, 404 (1981).
30. K. P. D. Lagerluf, A. H. Heuer, J. Castaing, and J. P. Riviere, J. Am. Ceram. Soc. **77** (2), 385 (1994).
31. W. C. Dash, J. Appl. Phys. **30**, 459 (1959).
32. W. C. Dash, J. Appl. Phys. **31**, 736 (1960).

Translated by K. Kugel

Crystallography Reports, Vol. 49, No. 2, 2004, pp. 175–179. Translated from Kristallografiya, Vol. 49, No. 2, 2004, pp. 224–228.

REAL STRUCTURE OF CRYSTALS

Correlation of the Structural Imperfection and Morphology of $Bi_4Ge_3O_{12}$ Crystals Grown by the Low-Gradient Czochralski Method[1]

V. N. Shlegel', Yu. V. Shubin, and N. V. Ivannikova

Institute of Inorganic Chemistry, Siberian Division, Russian Academy of Sciences, pr. Akademika Lavrent'eva 3, Novosibirsk, 630090 Russia

e-mail: shlegel@che.nsk.su

Received February 26, 2003

Abstract—This paper reports on the results of investigations into the morphological structure of the facets of $Bi_4Ge_3O_{12}$ crystals grown by the Czochralski method under the conditions of low temperature gradient (0.1–1 K/cm). A correlation between the morphological features of the facets at the crystallization front and the formation of defects in the bulk of the crystal is revealed. It is demonstrated that the {112} facets remain regular while the growing surface deviates from the (112) crystallographic plane by an angle of up to 1°. At larger deviations, there occurs a crossover from the stable facet growth to the growth of macrosteps or normal growth depending on the growth conditions. © *2004 MAIK "Nauka/Interperiodica".*

INTRODUCTION

Bismuth orthogermanate $Bi_4Ge_3O_{12}$ is a well-known scintillation crystal, which is widely used in high-energy physics, medical engineering, and other fields. Bismuth orthogermanate has a strong tendency to faceting due to the large entropy of crystallization (according to the Jackson criterion, the larger the entropy of crystallization, the greater the tendency toward layer growth). The facet effect is observed during the growth of $Bi_4Ge_3O_{12}$ crystals by the traditional Czochralski method at high temperature gradients (50–200 K/cm). This effect is characteristic of many crystals and brings about the formation of rodlike irregularities in the crystal bulk. As a rule, the facet formation at the crystallization front is treated as a result of the deviation from optimum growth conditions. In order to prevent the facet formation, it is common practice to increase the temperature gradient, which, however, leads to an enhancement of thermal stresses in the growing crystal.

Takano *et al.* [1] and Migarlovskaya *et al.* [2] noted that the homogeneity of a material is improved and the dislocation density decreases in regions corresponding to layer (facet) growth. Consequently, the inhomogeneity of the crystal properties is caused not by the facet growth but by the coexistence of the normal and facet growth mechanisms. The crystal regions growing through these mechanisms are characterized by a difference in dislocation densities and impurity concentrations, which results in the formation of a complex surface relief and inclusions at the boundaries of these regions.

The low-gradient Czochralski method, as applied to the growth of $Bi_4Ge_3O_{12}$ crystals, makes it possible to perform crystallization through the facet growth mechanism over the entire front of crystallization. A decrease in the temperature gradient, an increase in the pulling rate, and a variation in the temperature profile allow one to avoid the simultaneous formation of faceted and rounded regions. The stabilization of the facet growth of $Bi_4Ge_3O_{12}$ crystals is favored by the fact that molten bismuth orthogermanate is almost completely nontransparent to thermal radiation (the absorption coefficient is greater than 10^4 m^{-1}), whereas crystalline bismuth orthogermanate is a highly transparent material (the absorption coefficient is less than 3 m^{-1}) [3]. As a consequence, the unstable growth with the formation of inclusions predominantly occurs at the stage of forming facets in the course of crystal growth from a seed to a complete cross section. Once the faceted crystallization front has been completely formed, it is retained for almost as long as the growth proceeds. Imperfections of the faceted surface of the crystal with the formation of macrosteps in peripheral regions of the facets and inclusions in the crystal bulk can arise only at the final stage of the growth.

Large-sized $Bi_4Ge_3O_{12}$ crystals with a fully faceted crystallization front up to 450 mm long and 130 mm in transverse size were grown at low gradients in [4]. The size of facets at the crystallization front in these crystals is as large as 100 cm^2. The morphology of such large facets formed in the course of growth from a melt is still poorly understood.

[1] This work was presented at the National Conference on Crystal Growth (NCCG-2002, Moscow).

1063-7745/04/4902-0175$26.00 © 2004 MAIK "Nauka/Interperiodica"

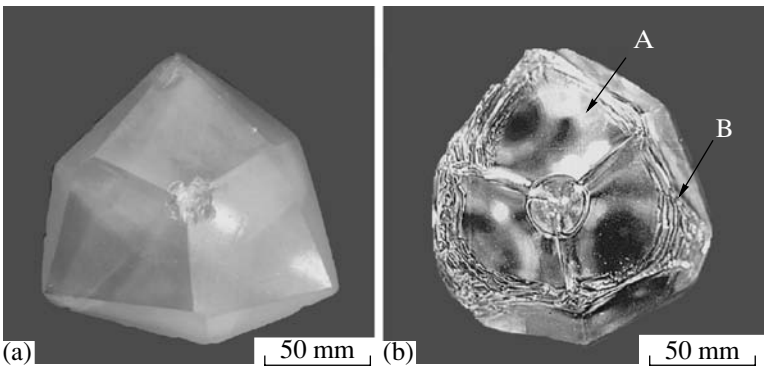

Fig. 1. Types of crystallization fronts formed upon growth of $Bi_4Ge_3O_{12}$ crystals along the [111] direction. (a) The crystallization front formed by the (112) facets and (b) the crystallization front with imperfections: (A) a flat region and (B) macrosteps.

Investigation into the real structure of crystals grown under these conditions revealed a very high degree of crystal perfection in the crystal bulk. The half-width of the diffraction curves recorded on a quadruple-crystal X-ray spectrometer does not exceed 10″ [5, 6].

The crystals exhibits a unique optical homogeneity (an absorption length of up to 30 m at $\lambda = 480$ nm) and possesses high resistance to gamma radiation.

In this work, we analyzed a correlation of the type and distribution of structural defects in crystals with the shape and structure of facets at the crystallization front.

EXPERIMENTAL

The facet surfaces were investigated with the use of samples of polyhedral crystallization fronts with visually flat facets and facets characterized by different degrees of surface imperfection. These samples were prepared by terminating the growth at different stages of the process through a rapid removal of the crystal from the melt (~100 mm/min). In the case when the crystal was rapidly lifted, a drop formed upon detachment on the lower part of the polyhedral front either was very small or was not observed at all.

The relief of the natural growth surfaces was examined in front fragments cut out parallel to the {112} crystallographic planes. The measurements were performed on an *x*–*y* coordinate table. The thickness of the plate was measured by a micrometer (scale division, 1 μm; radius of probe curvature, 0.25 mm).

The real structure of the samples was studied by X-ray topography and high-resolution X-ray diffractometry. The topograms were recorded on a double-crystal X-ray spectrometer [Cu$K_{\alpha 1}$ radiation; Si(004) monochromator; (035) surface; asymmetrical reflection; glancing angle, ~3.5°]. Prior to recording, the surfaces of natural growth facets were ground with the aim of eliminating irregularities and deviations from the (112) crystallographic plane. The grinding was carried out with SiC powders (40, 20, 8 μm). In order to relieve stresses caused by the grinding, the samples were etched in a 3 M HCl solution for 5 min.

The diffraction curves were measured on a double-crystal X-ray diffractometer [Ni$K_{\alpha 1}$ radiation, Ge(004)

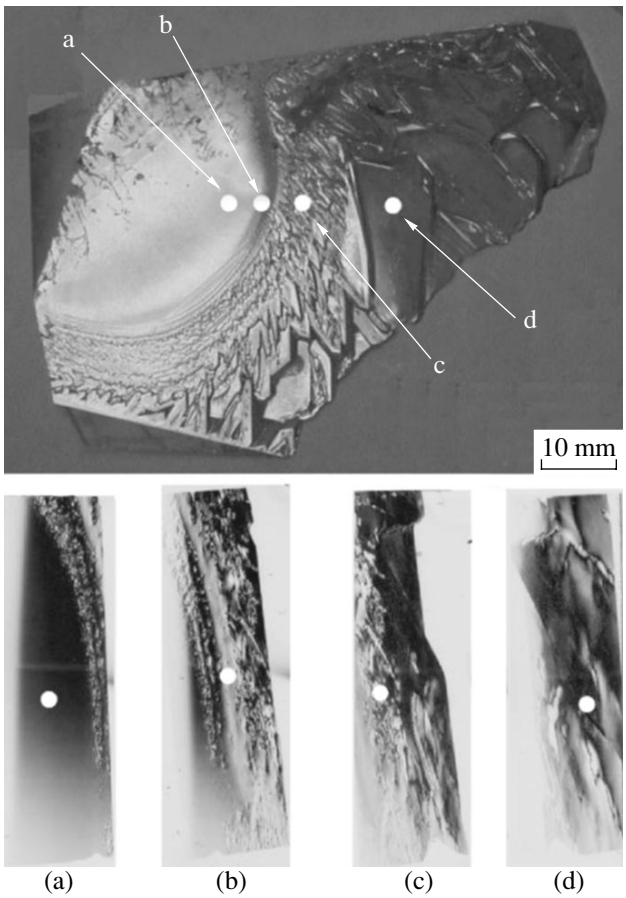

Fig. 2. Fragment of the (112) facet with (a) flat region, (b) transition region, and (c) small-sized and (d) large-sized macrosteps. X-ray topograms of the corresponding regions are shown at the bottom.

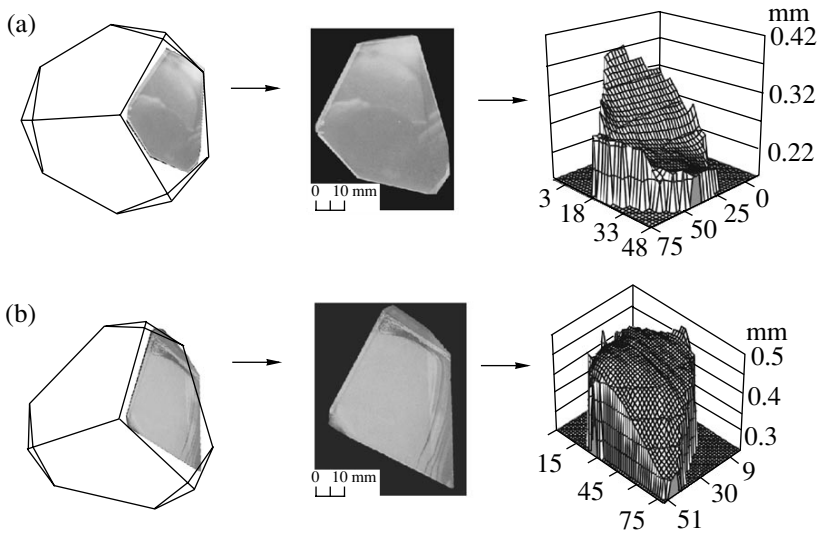

Fig. 3. (a) Concave and (b) convex relief of visually flat facets.

monochromator, (001) surface, symmetrical reflection]. The samples were set in a symmetric Bragg geometry and the (+, –) nondispersive configuration.

RESULTS AND DISCUSSION

Figure 1 illustrates the types of crystallization front formed during growth of the $Bi_4Ge_3O_{12}$ crystals along the ⟨111⟩ direction. The shape of the crystallization front surface can change with variations in the growth conditions, growth stage, etc. The facets studied are rather large in size (50–80 cm^2), and different surface regions can differ in morphological structure. The types of surface regions can be conventionally divided into four groups: flat regions, small-sized macrosteps, large-sized macrosteps (with a length of up to 1 cm), and rounded regions. A fragment of the imperfect facet containing regions with different morphologies is shown in Fig. 2.

As was noted above, the disturbance of the facet regularity, the growth of macrosteps, and the coexistence of different growth mechanisms at the crystallization front lead to the formation of different-type inclusions in the crystal bulk. When examining the crystals in a laser beam or an intense narrow beam of visible light, it is possible to distinguish at least four types of inclusions: large-sized inclusions a few millimeters in size, small-sized uniformly distributed light-scattering centers (fog), a structured fog, and gas bubbles up to 1 mm in size.

The analysis of the arrangement of the above inclusions in the crystal regions adjacent to the crystallization front demonstrates that there is a correlation between the inclusion distribution and the surface relief. The high-quality material (without inclusions) is predominantly observed in regions formed by visually flat parts of the facets whose deviation from the (112) plane does not exceed 1°. The topogram of one of these regions (Fig. 2a) indicates a high degree of crystal perfection. This is also confirmed by the measured half-width of the diffraction curve (23″).

Figure 3 presents the results of measuring the surface relief of visually flat facets. The plates parallel to

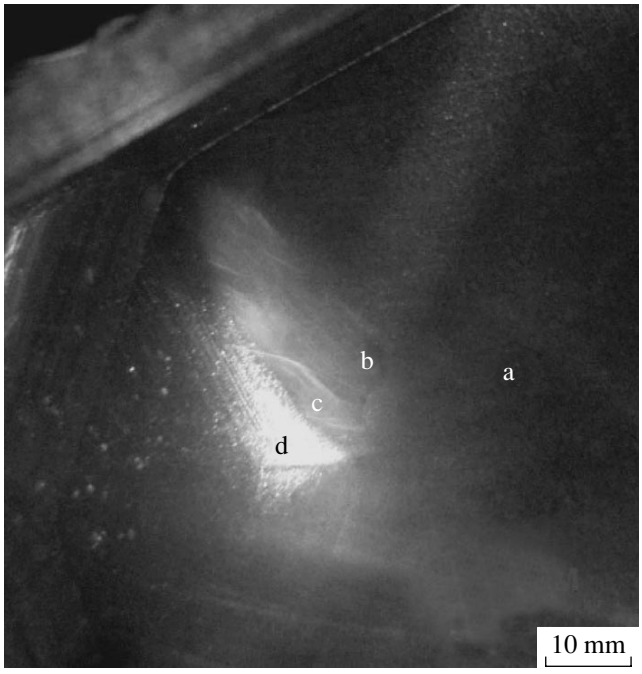

Fig. 4. Illustration of scattering of the directed light beam in the region with large-sized inclusions (the section is perpendicular to the growth direction): (a) the region without inclusions, (b) fog, (c) structured fog, and (d) large-sized inclusions.

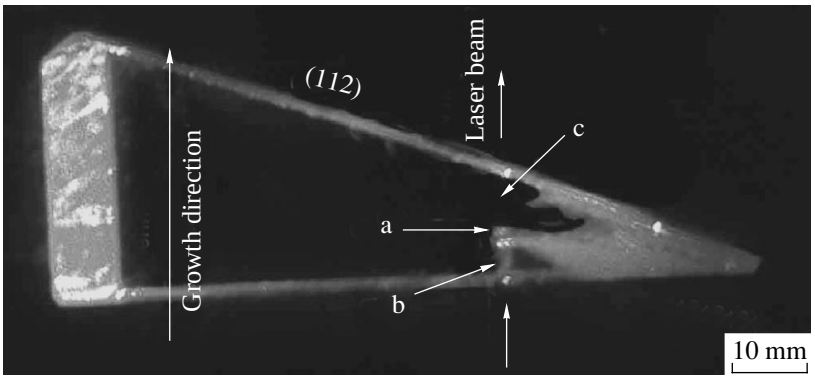

Fig. 5. Illustration of scattering of the laser beam in the region with large-sized inclusions (the section is parallel to the growth direction): (a) a large-sized inclusion in the laser beam, (b) scattering centers (fog) ahead of the large-sized inclusion, and (c) the transparent region to the back of the inclusion.

one of the facets were cut out from the faceted front of the crystal. The surface of the cut was oriented accurate to within ±0.1° along the (112) plane. The micrographs of the plates and their schematic arrangement at the crystallization front are shown at the left of Fig. 3. The results of micrometric measurements are presented at the right of this figure. Owing to an enlarged scale along the *Z* axis, it is possible to observe the concavity (Fig. 3a) and convexity (Fig. 3b) of the visually flat regions, which gradually transform into rounded macrosteps at the periphery of the facets. According to the X-ray diffraction data, the flat regions of the facets deviate from the (112) singular plane by up to 1°.

The small-sized transition regions between the regular facets and macrosteps remain smooth and can deviate from the singular direction by 1°–3°. Small-sized scattering centers (fog) appear in the bulk adjacent to the crystal (Fig. 4, region b). The width of this transition region, as a rule, does not exceed 2–3 mm (Fig. 2b) but, sometimes, can be as large as 10–15 mm. In the case of a sufficiently wide transition region, it is possible to observe a nonuniform distribution of scattering centers, namely, a structured fog (Fig. 4, region c). This region is characterized by the formation of dislocations whose density can be as high as 100 cm^{-2} or more. Then, there arises a disordered granular structure with grain sizes of approximately 0.1–0.3 mm.

After the transition region, we observe a region of small-sized macrosteps, which can develop and increase in size (Fig. 2). An analysis of the experimental data on the surface relief of flat regions in the region of macrosteps demonstrates that, within the limits of experimental error, these flat regions coincide with the (112) crystallographic planes, whereas the mean planes of macrosteps can deviate from the (112) plane by 3°–7°. The area and height of the macrosteps observed at the crystallization front increase away from the transition region. The macrosteps in the topogram manifest themselves as large-sized grains with a distorted crystal lattice (Fig. 2d). The size of grains increases and their mutual misorientation decreases with an increase in the distance from the transition region. Large-sized flat regions in the region of macrosteps consist of large-sized grains with a distorted crystal lattice and a small number of low-angle boundaries. The misorientation angle between the grains is equal to 10″–20″. The half-width of the diffraction curve recorded for the largest flat region in the macrostep region is equal to 32″. This implies that the subgrains are characterized by a rather high degree of crystal perfection. Large-sized inclusions that are irregular in shape are formed in the region of macrosteps. Note that the region with small-sized scattering centers (fog) is always observed before the appearance of large-sized inclusions. The micrographs of laser beam scattering in the sample with large-sized inclusions are displayed in Fig. 5. The laser beam passes along the growth direction. It can be seen from Fig. 5 that, first, small-sized scattering centers are formed in the crystal bulk (Fig. 5, region b). Then, a large-sized inclusion (Fig. 5, region a) appears in the crystal. However, thereafter, the perfect (homogeneous) crystal continues to grow.

Under certain growth conditions, the angle between the growth surface and the (112) plane becomes larger than 10°. In this case, the crossover to the normal growth occurs gradually and the front surface becomes rounded in shape.

CONCLUSIONS

Thus, in this work, we thoroughly investigated the specific features of the morphology of the $Bi_4Ge_3O_{12}$ crystals grown by the low-gradient Czochralski method. It was demonstrated that, depending on the growth conditions, visually flat facets can deviate from the (112) crystallographic planes in different directions. The defect formation in the crystal is associated with the shape and structure of facets at the crystallization front. In the case where the facets deviate from the (112) crystallographic planes by no more than 1°, the growth of a perfect crystal occurs in the system. The

deviation of the (112) facets from their nominal position by 2°–7° is responsible for the formation of inclusions with different sizes [from small-sized scattering centers (fog) to 3–5-mm inclusions] and a granular structure. The results obtained are essential to the understanding of the growth mechanism of $Bi_4Ge_3O_{12}$ crystals and can be used to optimize the growth processes.

REFERENCES

1. S. Takano, S. Esashi, K. Mori, and T. Namikata, J. Cryst. Growth **24–25**, 437 (1974).
2. M. S. Migarlovskaya, M. R. Raukhman, and I. A. Strel'nikova, in *Crystal Growth* (Nauka, Moscow, 1972), Vol. 9, p. 142.
3. I. Yu. Evstratov, S. Rukolaine, V. S. Yuferev, *et al.*, J. Cryst. Growth **235**, 371 (2002).
4. Yu. A. Borovlev, N. V. Ivannikova, V. N. Shlegel, *et al.*, J. Cryst. Growth **229**, 305 (2001).
5. A. Murthy, M. Ravikumar, A. Choubey, *et al.*, J. Cryst. Growth **197**, 865 (1999).
6. A. Choubey, G. Bhagvannarayana, Yu. V. Shubin, *et al.*, Z. Kristallogr. **217**, 515 (2002).

Translated by O. Borovik-Romanova

Crystallography Reports, Vol. 49, No. 2, 2004, pp. 180–183. Translated from Kristallografiya, Vol. 49, No. 2, 2004, pp. 229–233.

REAL STRUCTURE OF CRYSTALS

Defects of Different Sizes in Large Paratellurite Single Crystals[1]

A. I. Kolesnikov, I. A. Kaplunov, and I. A. Terent'ev

Tver State University, Sadovyĭ per. 35, Tver, 170002 Russia

e-mail: ivan.kaplunov@tversu.ru

Received March 3, 2003

Abstract—Paratellurite single crystals have good acoustooptical properties that are important for various devices, such as deflectors, modulators, and tunable noncollinear filters. Paratellurite single crystals of up to 80 mm in diameter and 100 mm in height were grown using the Czochralski method from ultrapure melts. Optical anomalies in the grown crystals—gas bubbles, striations, impurity inclusions with nearby stresses, and regions with high dislocation densities—were studied with chemical, X-ray, and optical methods. © *2004 MAIK "Nauka/Interperiodica"*.

INTRODUCTION

Paratellurite single crystals, belonging to the noncentrosymmetric point symmetry group 422, exhibit piezoelectric properties. Their main piezoelectric parameters are as follows: piezoelectric modulus $d_{14} = 2.44 \times 10^{-7}$ C/d, piezoelectric constant $e_{14} = 0.648 \times 10^{-5}$ C/cm^2, and electromechanical coupling coefficient $k_{[001]} \sim 10\%$ [1]. However, the most important field of application of paratellurite is acoustooptics, because this material has the unprecedentedly large acoustooptical quality factor $M_2 = 510$ (with respect to fused quartz) in the spectral range 0.35–5 μm. This makes it possible to obtain a high acoustooptic diffraction efficiency (up to 80%) at extremely low control power (0.5 W and lower) [2]. In principle, acoustooptical devices can be designed in which paratellurite crystals serve simultaneously as both piezoelectric transducers and acoustooptical guides. In this case, relatively complex processes for fabricating piezoelectric transducers on the basis of lithium niobate crystals and their attachment to paratellurite crystals would be excluded. Due to the large difference in the refractive indices for ordinary and extraordinary waves, $N_o - N_e$, paratellurite crystals can also be used for manufacturing polarization prisms. Fairly large (up to $60 \times 40 \times 40$ mm^3) elements made of paratellurite single crystals of extremely high optical quality should be used in the aforementioned devices. However, the problem of stable growth of such crystals has not been completely solved [3]. Paratellurite single crystals of appropriate size and acceptable quality are grown only by the Czochralski method from dioxide tellurium melt containing no less than 99.995% of the main substance in platinum crucibles. The growth takes place in resistance furnaces in air at normal pressure. The [110] direction, which is perpendicular to the most developed singular face, is generally used for pulling.

Depending on the growth conditions, the crystals described here contained, to one extent or another, structural defects and related optical anomalies characteristic of paratellurite that are well-known from numerous publications [3–6]. Among these were gas bubbles and their associates, regions with high dislocation densities, small-angle boundaries, impurity inclusions, and regions with significant anomalous biaxiality. Striations were studied in detail for the first time.

EXPERIMENTAL RESULTS

Polarization optical systems, as well as different schemes based on the interference of polarized rays, were used to investigate the crystals by optical methods. Selective chemical etching in Na_2CO_3 solution was

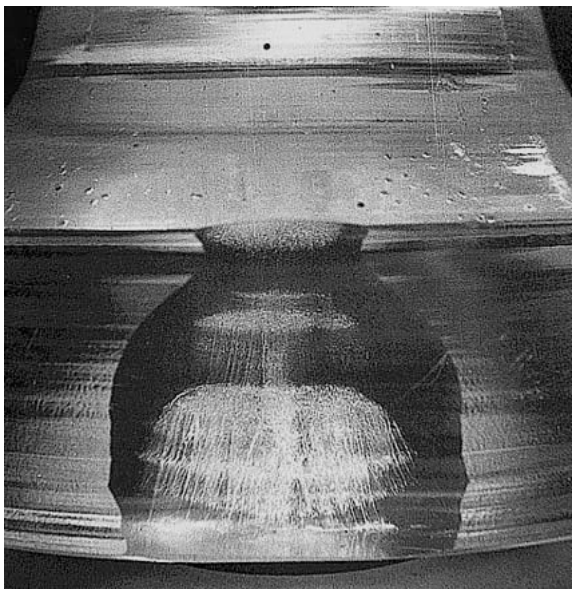

Fig. 1. Cut of a paratellurite single crystal with periodic inclusions of bubbles in the form of string-like associates.

[1] This work was presented at the National Conference on Crystal Growth (NCCG-2002, Moscow).

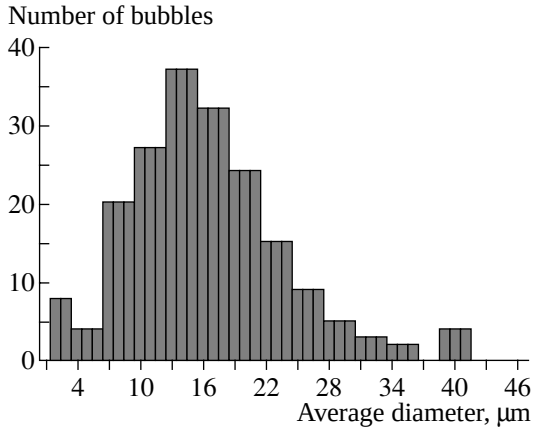

Fig. 2. Histogram of bubble-size distribution.

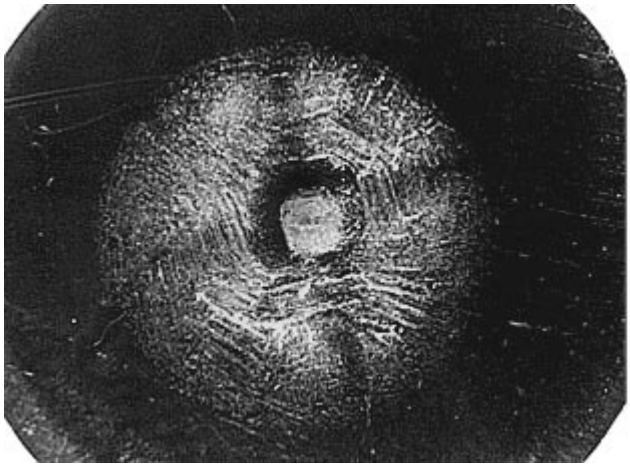

Fig. 3. Sectoriality in the distribution of bubbles. Dark areas correspond to the regions of the growth of the {110} faces of pyramids. The cut is perpendicular to the growth axis [110].

used to reveal dislocations. X-ray analysis included the measurement of the unit-cell parameters in the vicinity of defects and determination of deviations of interplane distances $\Delta d/d$, which were used to calculate stresses.

A classification system that has been accepted in a number of studies [7] distinguishes three levels of optical anomalies on the scale l of crystal inhomogeneity: the macroscopic level ($l > 1$ μm), mesoscopic level (100 Å $< l <$ 1 μm), and microscopic level ($l <$ 100 Å). According to this classification system, bubbles and striations are connected to macroscopic optical anomalies. Defects responsible for meso- and microscopic anomalies are associated with macroscopic anomalies. For example, dislocations and impurities are directly responsible for the appearance of anomalous biaxiality and striations. However, in the practical evaluation of the quality of paratellurite crystals, macroscopic optical anomalies are fixed: bubbles, striations, and subfilamentary scattering inclusions.

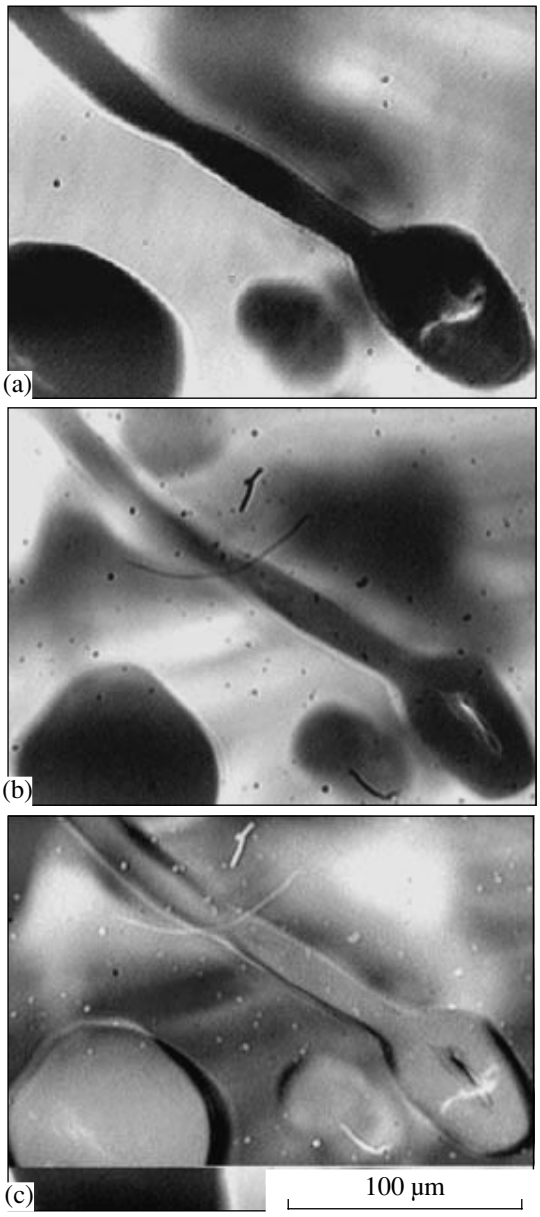

Fig. 4. Gas inclusions in the same region of a paratellurite crystal (a) before and (b) after two-stage annealing at 680 and 700°C (for 48 h in each stage); (c) computer subtraction of images (a) and (b).

Gas bubbles and strain-like associates of bubbles are shown in Fig. 1. Figure 2 shows a typical histogram of the size distribution of gas bubbles. Sectoriality is observed in the spatial distribution of bubbles, which is related to the morphological features of the crystallization front (Fig. 3). The concentration of bubbles is lowest in the growth pyramids of the {110} faces.

High-temperature postgrowth annealing of samples with bubbles leads to slow facing of the bubble walls in the {110} and {101} planes. The motion of bubbles along the direction opposite the temperature gradient direction was observed. The velocity of the motion was

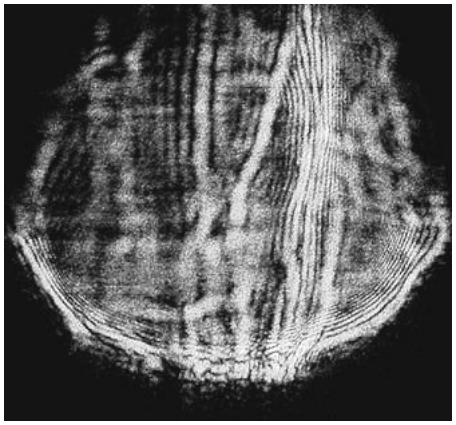

Fig. 5. Striations extended along the [001] direction in a sample cut perpendicular to the growth axis.

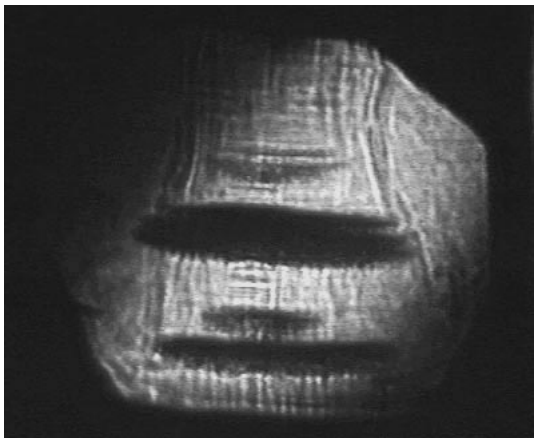

Fig. 6. Optical inhomogeneities—striations and bubble associates—in a paratellurite crystal. The crystal was imaged perpendicular to the [110] growth axis along the $[\bar{1}10]$ direction.

in the range 10–30 Å/s. Figure 4 shows the images of a region with bubbles before and after annealing and the results of computer-image subtraction.

Striations are regions of local compressions and stretches in crystals. They manifest themselves due to the photoelastic effect in the form of dark bands under illumination of crystal samples using wide laser beams. To obtain images, we used a He–Ne laser (λ = 0.673 μm) and an YAG laser with frequency doubling (λ = 0.53 μm). Figure 5 shows the image with striations extended predominately along the [001] direction. The imaging was performed along the [110] direction (the growth axis). Figure 6 shows the same crystal imaged perpendicular to the lateral surface (along the $[1\bar{1}0]$ direction). Along with striations, dark regions with inclusions of bubbles can be seen. Striations, located approximately along the growth axis, separate the regions corresponding to the growth of the front face from the regions corresponding to rounded portions of the crystallization front in the material volume. Indeed, calculations based on the known values of the elastic constants c_{ik} and the form of the elastic-rigidity tensor for the point symmetry group (422) [1], show that the compressive or tensile stresses along the direction perpendicular to the [001] axis are due to the shear strains ε_{12} and ε_{21} due to the interface curvature.

According to the data from X-ray diffraction analysis, the maximum distortions of the interplane distances $\Delta d/d$ and the corresponding maximum stresses (10–100 N mm^{-2}) are observed in the regions of striations. Maximum dislocation-density values (which significantly exceeded the value averaged over samples) were revealed in the same regions (Fig. 7).

The interrelation of the growth conditions with defects in paratellurite crystals has been considered earlier [3]. In this study, some of the process parameters (pulling rate, rotation rate, heating-unit design) were deliberately changed. We took into account the consid-

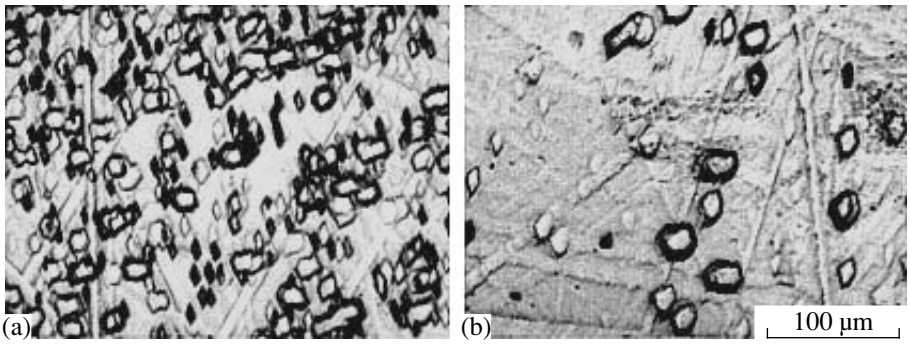

Fig. 7. Etch pits in the (110) plane of a paratellurite crystal 75 mm in diameter. (a) A region with the high dislocation density (N_d = 2.7×10^5 cm^{-2}) at the location of an optical inhomogeneity (striation); (b) a region with a dislocation density corresponding to the sample-averaged value ($N_d = 2.4 \times 10^4$ cm^{-2}).

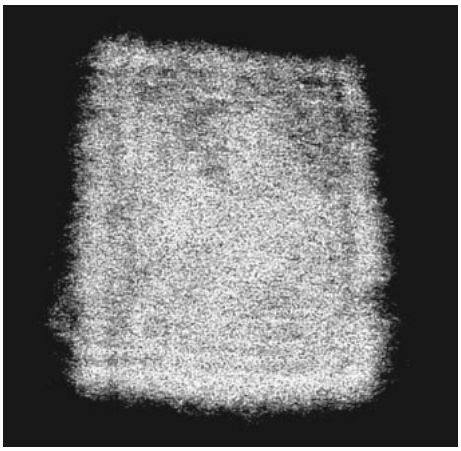

Fig. 8. Image in laser light of an acoustooptical guide made of α-TeO_2 containing no striations or other optical inhomogeneities. This acoustooptical guide was tested in a spectrophotometer for astrophysical observations.

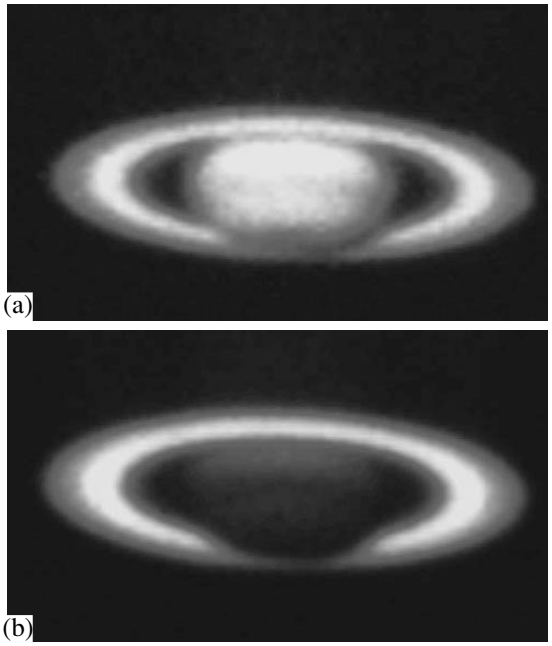

Fig. 9. Images of Saturn obtained at λ = (a) 8500 and (b) 8870 Å using an acoustooptic spectrophotometer based on a paratellurite crystal.

erations on inhomogeneities in alexandrite ($BeAl_2O_4 : Cr^{3+}$) and gadolinium–scandium–gallium garnet ($Cd_3Se_xGa_{5-x}O_{12} : Nd^{3+}$) crystals presented in [8], where the concept of the fundamental impossibility (and lack of necessity) of simultaneous elimination of defects of different types in oxide crystals grown from melts was justified.

CONCLUSIONS

Thus, abandoning the goals of completely eliminating of bubbles and maximizing development of the (110) face at the crystallization front, we managed to realize a stable formation of crystals without striations. However, narrow regions containing bubbles are almost always present at the center of such crystals. An acoustooptical guide made of α-TeO_2 with dimensions $35 \times 35 \times 60$ mm^3 along the [110], [$\bar{1}$10], and [001] axes, respectively, is shown in Fig. 8 in transmitted laser light. This sample contains no bubbles, and no striations or anomalous biaxiality are observed. In August 2001, an acoustooptic spectrophotometer for making astronomical observations was fabricated on the basis of this crystal and successfully tested in the Crimean Laboratory of the Sternberg State Astronomical Institute. Unique spectral images without optical distortions of the planetary nebula NGC 7027, the planet Saturn, and the turbulent disk of the star γ-Cyg were obtained using this spectrophotometer. Figure 9 shows the images of Saturn that were obtained using an acoustooptic filter with λ = 8500 Å and in the absorption band of methane with λ = 8870 Å (recorded by V.M. Lyutyĭ and V.Ya. Molchanov). The high image quality is evidenced by the fact that the Cassini division—the gap between the rings near the outer disk edge—is distinctly seen. The atmosphere of the giant planet consists mainly of methane, in the absorption band of which the brightness of Saturn falls by almost an order of magnitude.

The dimensions and optical homogeneity of paratellurite crystals obtained by date are not problematic. In the near future, technology for growing crystals 100–120 mm in diameter and more than 100 mm in height should be mastered in view of new promising applications of such crystals in acoustooptics and optics.

REFERENCES

1. A. A. Blistanov, V. S. Bondarenko, N. V. Perelomova, *et al*., *Acoustic Crystals* (Nauka, Moscow, 1982).
2. L. N. Magdich and V. Ya. Molchanov, *Acoustooptic Devices and Their Applications* (Gordon and Breach, New York, 1989).
3. A. I. Kolesnikov, R. M. Grechishkin, and I. A. Terent'ev, *Physics of Crystallization* (Tver. Gos. Univ., Tver, 2002), p. 18.
4. J. G. Grabmaier, J. Cryst. Growth **20**, 82 (1979).
5. I. Foldvari, R. Voszka, and A. Peter, J. Cryst. Growth **59**, 651 (1982).
6. A. P. Kalashnikov, Dokl. Akad. Nauk SSSR **263**, 1132 (1982) [Sov. Phys. Dokl. **27**, 279 (1982)].
7. A. G. Shtukenberg and Yu. O. Punin, *Regularities of Evolution of the Earth's Crust* (S.-Peterb. Gos. Univ., St. Petersburg, 1996), Vol. 2, p. 318.
8. E. G. Tsvetkov, G. M. Rylov, and A. M. Yurkin, Kristallografiya **44** (2), 308 (1999) [Crystallogr. Rep. **44**, 273 (1999)].

Translated by Yu. Sin'kov

Crystallography Reports, Vol. 49, No. 2, 2004, pp. 184–187. Translated from Kristallografiya, Vol. 49, No. 2, 2004, pp. 234–238.

REAL STRUCTURE OF CRYSTALS

Low-Angle Boundaries in Germanium[1]

I. A. Kaplunov and A. I. Kolesnikov

Tver State University, Tver, Russia

e-mail: ivan.kaplunov@tversu.ru

Received February 26, 2003

Abstract—Possible mechanisms of formation of dislocation defects—low-angle boundaries—in germanium single crystals used in optics are considered. © *2004 MAIK "Nauka/Interperiodica".*

INTRODUCTION

To a large degree, the distribution of dislocations in the bulk of single crystals is determined by dislocation motion and interaction in stress fields. Under conditions of limited paths, the microredistribution of dislocations in the local regions of a crystal may take place and give rise to the formation of characteristic defect arrangements such as glide bands, low-angle boundaries, etc. [1–5]. Low-angle boundaries considerably deteriorate the structural perfection of a single crystal, thus preventing the use of this crystal for preparing substrates of radiation-resistant photoelectric transducers, whose production requires the use of germanium single crystals with low dislocation densities having no two-dimensional linear structural defects. Low-angle boundaries deteriorate the optical properties of single crystals—presumably, they give rise to scattering of infrared radiation in germanium single crystals [6]. Also, low-angle boundaries can give rise to direct polycrystallization during growth of ingots.

OBJECTS OF STUDY. RESULTS

We studied low-angle boundaries in germanium single crystals grown along various crystallographic directions by various methods and with different ingot and crystallization-front geometries.

Figure 1 shows the length of low-angle boundaries, L, in the section normal to the growth direction of Stepanov- and Czochralski-grown germanium single crystals as a function of the crystal height, h. One can clearly see the tendency to increase in the total length of low-angle boundaries with an increase in the linear dimensions of crystals grown with a concave (into the crystal) crystallization front (curves *1* and *2*). For single crystals with a convex crystallization front with respect to the melt (curve *3*), the total length of the low-angle boundaries remains practically unchanged. Since the single crystals studied had different diameters, a more detailed characterization requires the construction of the dependence of the density of the low-angle boundaries in the cross section (of the area S) as a function of the crystal height (Fig. 2). The minimum constant density of the low-angle boundaries is characteristic of the Czochralski-grown crystals with a convex crystallization front with respect to the melt. The crystals grown by the Stepanov method have a considerably higher low-angle boundary density; an increase in this density is observed at the initial (relative to the crystal height) part of the ingot. The distribution of the low-angle boundaries was also analyzed on large disk-like germanium single crystals grown by the method of directional crystallization. Figure 3 shows the typical dependence of the density of the low-angle boundaries averaged over the cross section for germanium crystals 200 mm in diameter; it is seen that the density considerably increases along the crystal height. In this case, the density of low-angle boundaries is lower by an order of magnitude that the density for single crystals grown by pulling from the melt by the Stepanov method.

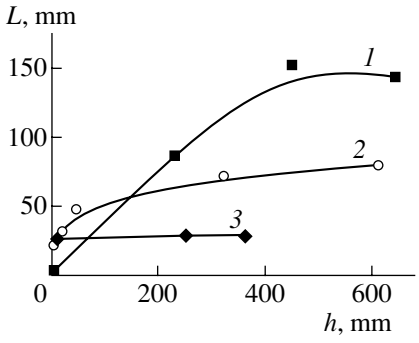

Fig. 1. Total length L of small-angle boundaries in the crystal section as a function of the height h of a crystal with a crystallization front concave with respect to the crystal and (*1*) grown by the Stepanov method, the crystallization front concave with respect to the crystal, (*2*) grown by Czochralski method, diameter 43 mm, crystallization front concave with respect to the crystal, and (*3*) grown by the Czochralski method, diameter 48 mm, crystallization front convex with respect to the melt [9].

[1] This work was presented at the National Conference on Crystal Growth (NCCG-2002, Moscow).

1063-7745/04/4902-0184$26.00 © 2004 MAIK "Nauka/Interperiodica"

In all the crystals where we studied the distribution of the low-angle boundaries over the cross section, the low-angle boundaries had different lengths, which could be explained by the mechanisms of their formation during growth of germanium single crystals from melts.

DISCUSSION

Several mechanisms of low-angle boundary formation are known. Some researchers explain their formation during growth of germanium single crystals with polygonization processes—restructuring of dislocations (forming glide bands or glide lines) into walls (low-angle boundaries) [1–5].

One point of view has it that formation of low-angle boundaries is caused by the field of thermal stresses in a growing single crystal. The formation of low-angle boundaries in this case is caused by migration of mobile dislocations under the action of thermal stresses in single-crystal regions where their level is close to zero [4, 5, 7].

Formation of low-angle boundaries is also associated with the growth mechanism (nucleation) [2, 8]. In this case, one considers the interface (crystallization front) at which several two-dimensional nuclei are formed at different sites. If the layers growing from various nuclei arrive at the site of their junction somewhat misoriented, then dislocations are formed and give rise to the formation of low-angle boundaries located in the planes parallel to the growth direction. If the single-crystal regions growing from various nuclei arrive at the site of their junction with the same orientations, no dislocations are formed. The orientations of the regions growing from various nuclei depend on the surface perfection—the existence of dislocations and their number.

The study of the character of the low-angle boundary distribution in the crystals showed that the mechanisms of their formation can differ and depend on the temperature conditions and the growth method.

Stepanov method. Single crystals grown by the Stepanov method along the ⟨111⟩ direction are characterized by a high density of low-angle boundaries determined by the *L*/*S* ratio. These low-angle boundaries are located mainly in the cross-section regions formed by "implicit" faces. Low-angle boundaries directed from the implicit faces along the ⟨112⟩ direction are predetermined by the crystallization front concave with respect to the crystal. Low-angle boundaries are diffuse straight lines consisting of several parallel closely located rows of dislocation. Single crystals thus grown have a crystallization front concave into the crystal and, therefore, one can assume that the nuclei at the crystallization front nuclei can be formed not only at the side surface around the explicit faces but also at certain distances from the side surface—on the steps of the {111} planes formed at a pronounced curvature of the crystallization front. Such an arrangement of two-dimensional nuclei can give rise to the formation of additional rather short low-angle boundaries of various orientations. In this case, the total number of low-angle boundaries is rather

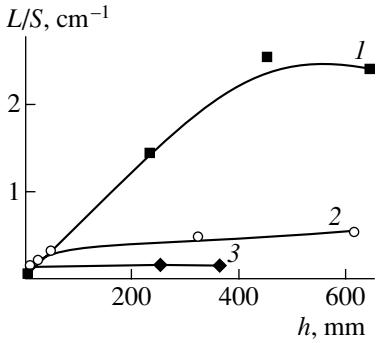

Fig. 2. Density of low-angle boundaries averaged over the section *L*/*S* as a function of height *h* in (*1*) crystals grown by the Stepanov method, the crystallization front concave with respect to the crystal; (*2*) crystals grown by the Czochralski method, the crystallization front concave with respect to the crystal; and (*3*) crystals grown by the Czochralski method, the crystallization front convex with respect to the melt.

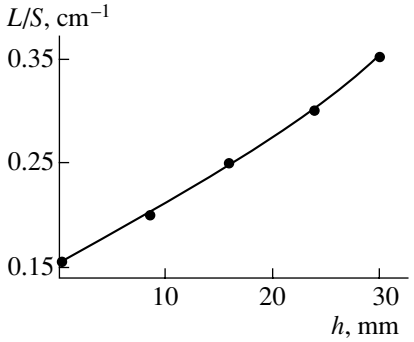

Fig. 3. Density of low-angle boundaries averaged over the section *L*/*S* as a function of height *h* for a germanium crystal with a diameter of 200 mm.

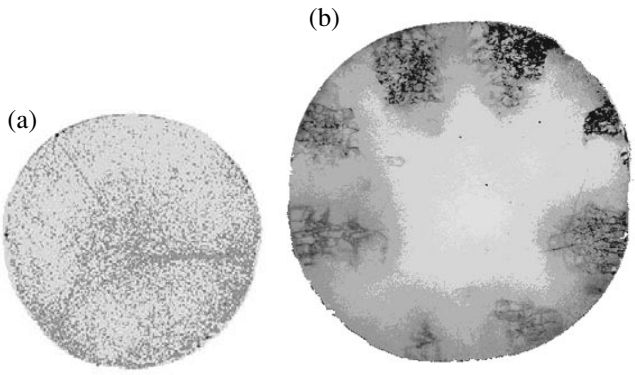

Fig. 4. Arrangement of low-angle boundaries over the section of crystals grown along the (a) ⟨111⟩ and (b) ⟨100⟩ directions.

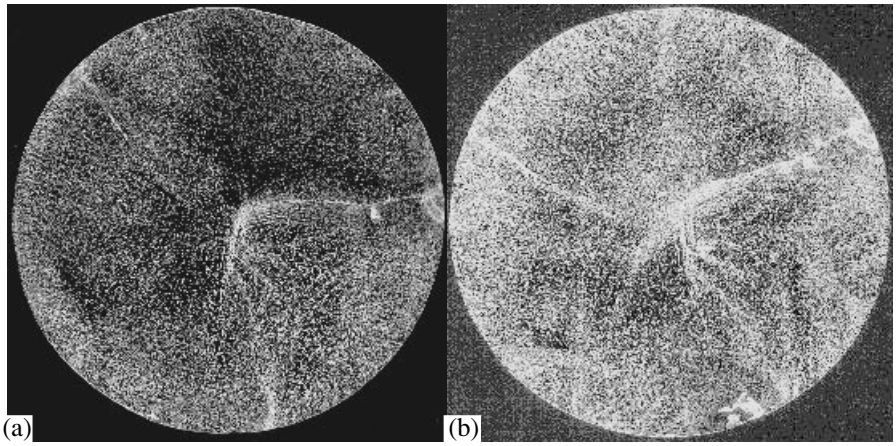

Fig. 5. Macrodistribution of dislocations in a section of a germanium ingot with a diameter of 65 mm (a) before annealing and (b) after 24-h-annealing at 880°C.

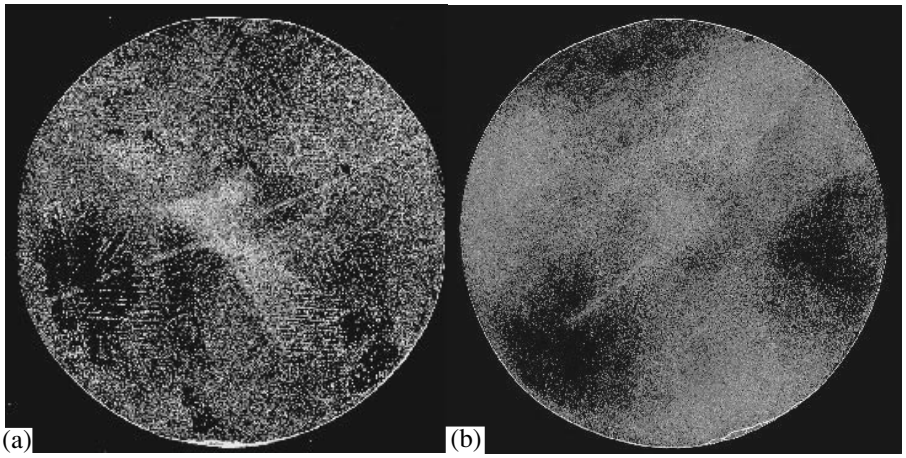

Fig. 6. Macrodistribution of dislocations in a section of a germanium ingot with a diameter of 60 mm: (a) before annealing and (b) after 24-h-annealing at 920°C.

large, which is confirmed by the experiments. On the whole, one can draw the conclusion that the main mechanism of low-angle boundary formation in Stepanov-grown single crystals is that related to nucleation.

It can also be noted that the mechanism of low-angle boundary formation by polygonization can take place only in some crystals, because the single crystals grown showed no obvious glide bands.

Czochralski method. Czochralski-grown single crystals had close geometric dimensions and were grown under close temperature conditions. However, their geometries were different—they had different curvature radii along the ⟨111⟩ and ⟨100⟩ growth directions. The distribution of the low-angle boundaries over crystal cross sections and their densities indicate that their formation is associated with the growth mechanism (nucleation) and the field of thermal stresses in crystals. Single crystals with a crystallization front concave with respect to the crystals have the same character of the arrangement of the low-angle boundaries as in the Stepanov-grown crystals, which is explained by the mechanism of low-angle boundary formation. The main pattern of the low-angle boundary arrangement in the crystal section is straight lines located in three {110} planes parallel to the growth axis of the single crystal and forming an angle of 19°28′. Low-angle boundaries of this type are shown in Fig. 4a. With an increase of the ingot length, low-angle boundaries also grow—the number of their side branches increases, so that, finally, they occupy practically the whole cross section of the crystal.

The arrangement of low-angle boundaries in the single crystal grown along the ⟨100⟩ direction is shown in Fig. 4b (transverse cross section of the single crystal normal to the growth axis with the well-developed low-angle boundary structure. The maximum boundary concentration at the given crystallographic orientation

is clearly seen in eight regions at the ingot periphery. This low-angle boundary arrangement can be associated with the presence of the initial crystallization centers and growth of individual layers at the crystallization front proceeding from these centers. On the whole, the analysis of the crystal structure of crystals grown along the ⟨100⟩ direction shows that the presence and further development of low-angle boundaries in some regions results in considerable misorientation of these regions, and, then, in fast polycrystallization. On the contrary, the investigations show that in crystals grown along the ⟨111⟩ direction, one observes a very high density of low-angle boundaries without obvious transition to polygonization.

In single crystals with a crystallization front convex with respect to the melt, which were grown along the ⟨111⟩ direction, the formation and further development of low-angle boundaries in the regions of implicit faces is not observed at all. In this case, the arrangement of the low-angle boundaries over the section shows no specific crystallographic features.

The density (length) of low-angle boundaries is minimal and remains almost constant. If one takes into account that, in this case, the growth mechanism of grain-boundary formation does not work despite the fact that the crystal has low-angle boundaries, then the most probable explanation of this phenomenon is the existence of a field of thermal stresses, whose action results in the accumulation of mobile dislocations in the vicinity of the crystallization front and their motion in the single-crystal region with the minimum level of thermal stresses.

Effect of annealing on low-angle boundaries. To evaluate the effect of high-temperature annealing on the arrangement and number of low-angle boundaries, the samples cut out from the single crystals grown were annealed at 800–920°C. At these temperatures (exceeding the plasticity point at about 600°C), dislocations move intensely, are redistributed over the volume, and emerge to the free surface of the crystal. Dislocation motion is caused by the forces of internal stresses caused by the existence of dislocations. The processes of dislocation motion decrease and level the stresses in the ingots and also reduce the dislocation density. Low-angle boundaries play the role of obstacles on the path of moving dislocations and concentrate these dislocations. This process is well illustrated by the comparison of the macrostructure of the individual sections of single-crystal specimens before and after their high-temperature annealing (Fig. 5). In the sections, low-angle boundaries become broader and their lengths increase. Annealing the crystals with high dislocation density (above $(5–8) \times 10^4$ cm^{-2}), one may observe another effect—glide bands forming a six-ray star (Fig. 6).

CONCLUSIONS

Considering the formation of low-angle boundaries in a single-crystal germanium, one can draw the conclusion that the main mechanisms of their manifestation are the action of the field of thermal stresses and the growth (nucleation) mechanism. Low-angle boundaries are important structural defects in single-crystal germanium and limit its use in a number of practical applications. Single crystals free of low-angle boundaries with a low dislocation density $(3–5) \times 10^3$ cm^{-2} can be grown only in the presence of a low-gradient temperature field.

REFERENCES

1. R. G. Rhodes, *Imperfections and Active Centres in Semiconductors* (Pergamon, Oxford, 1964; Metallurgiya, Moscow, 1968).
2. *Imperfections in Semiconductor Crystals*, Ed. by D. A. Petrov (Metallurgiya, Moscow, 1964).
3. M. G. Mil'vidsky and V. B. Osvenskiĭ, *Structural Defects in Semiconductor Single Crystals* (Metallurgiya, Moscow, 1984).
4. *Growth of Single Crystals*, Ed. by N. N. Sheftal' (Inostrannaya Literatura, Moscow, 1963), p. 301.
5. M. G. Mil'vidsky, *Semiconductor Materials in Modern Electronics* (Nauka, Moscow, 1986).
6. I. A. Kaplunov and A. I. Kolesnikov, Poverkhnost, No. 2, 14 (2002).
7. A. Ya. Nashel'skiĭ, *Technology of Production of Special Materials for Electronics* (Metallurgiya, Moscow, 1993).
8. I. V. Salli and É. S. Fal'kevich, *Shape Control in Crystal Growth* (Naukova Dumka, Kiev, 1989).
9. I. A. Kaplunov, *Physics of Crystallization* (Tver. Gos. Univ., Tver, 1999), p. 36.

Translated by L. Man

Crystallography Reports, Vol. 49, No. 2, 2004, pp. 188–192. Translated from Kristallografiya, Vol. 49, No. 2, 2004, pp. 239–243.

REAL STRUCTURE OF CRYSTALS

Formation of Microdefects in Semiconductor Silicon[1]

V. I. Talanin*, I. E. Talanin*, and D. I. Levinzon**

** Zaporozh'e State Engineering Academy, Zaporozh'e, Ukraine*

e-mail: V.I.Talanin@mail.ru

*** Zaporozh'e Institute of State and Municipal Government, Zaporozh'e, Ukraine*

Received March 3, 2003

Abstract—The distribution patterns and physical nature (the sign of the lattice strain) of growth microdefects in dislocation-free Si single crystals grown by the floating-zone and Czochralski methods were studied by selective etching and transmission electron microscopy. Mechanisms of formation and transformation of growth microdefects, depending on the crystal growth rate, are proposed. A heterogeneous mechanism of formation of microdefects is considered. © *2004 MAIK "Nauka/Interperiodica".*

INTRODUCTION

Several theoretical models have been proposed to reveal the nature of microdefects and the regularities of their formation. These models are based on different hypotheses and experimental data. The starting point in constructing each model is ascertaining the type and nature of the intrinsic point defects dominant in temperature ranges close to the melting point. Presently, the Voronkov recombination diffusion model [1] is generally accepted. This model suggests that the type of dominant defects is determined by the recombination between intrinsic Si interstitials and vacancies immediately after a crystal has been cooled and depends on the ratio between the growth rate v and the axial temperature gradient G [1]. According to this model, a crystal can only be grown either in the interstitial regime (at small growth rates) or in the vacancy regime (at high growth rates). Theoretically, at some value of the ratio $v/G = C_{crit}$, almost complete mutual annihilation of intrinsic point defects should occur, which corresponds to the conditions of defect-free crystal growth or to a defect-free region in a crystal. Although the Voronkov model (developed initially for Czochralski-grown (CZ) Si crystals) was recently proposed for Si crystals grown by the floating-zone (FZ) method [2], it, as well as other models (equilibrium and nonequilibrium interstitial, drop, vacancy, vacancy–interstitial), cannot adequately describe the crystal growth created by the above methods and, in some cases, contradicts the known experimental data. Hence, new experiments and a deeper insight into the physical nature of microdefects in FZ-Si and CZ-Si are required to reveal the general mechanism of formation, growth, and transformation of microdefects. With this purpose in mind, we performed a complex experimental investigation of both types of crystals along the following lines:

(i) study and ascertainment of the physical nature (the sign of the lattice strain) of different types of microdefects;

(ii) study of the effect of thermal growth conditions on the distribution and type of microdefects;

(iii) investigation of the transformation of growth microdefects during different thermal treatments and technological processes.

RESULTS AND DISCUSSION

The investigations were performed using optical and transmission electron microscopy (TEM). Undoped FZ-Si single crystals 30 mm in diameter with $\rho = (2–4) \times 10^3$ Ω cm and *n*-type CZ-Si single crystals 50 mm in diameter with $\rho = 10–50$ Ω cm were used. As practice shows, microdefects of all known types are formed in crystals in this range of diameters, whereas, in large-diameter crystals, only a limited number of microdefect types manifest themselves due to different thermal growth conditions. This complex approach allowed us not only to confirm the results obtained previously, but also to obtain new experimental data that, in our opinion, make it possible to ascertain a generalized (unified) mechanism of formation, growth, and transformation of microdefects in Si, independent of the growth method.

The following facts were ascertained experimentally for FZ-Si [3–5].

(i) *A* microdefects are interstitial dislocation loops 1–50 μm in size with the Burgers' vector $b = 1/2$ [110]. These lops lie in the {111} and {110} planes.

(ii) *B* microdefects are clusters of interstitial point defects 20–50 nm in size lying in the {100} and {111} planes.

(iii) *D* microdefects are clusters of interstitial point defects 4–10 nm in size.

[1] This work was presented at the National Conference on Crystal Growth (NCCG-2002, Moscow).

1063-7745/04/4902-0188$26.00 © 2004 MAIK "Nauka/Interperiodica"

(iv) *C* microdefects are identical to *D* microdefects with respect to the contrast of electron-microscopy images, the sign of the lattice strain, and the size. Therefore, there is no point in distinguishing *C* microdefects as an individual type.

(v) At high growth rates (more than 6 mm/min), along with interstitial microdefects, vacancy microdefects arise. They are located in the same regions of a crystal.

It has been ascertained experimentally that *D* microdefects in FZ-Si crystals grown at high rates are formed before *B* microdefects, which, in turn, arise at lower growth rates. *A* microdefects are observed at growth rates below those at which *B* microdefects are visualized. Quenching of FZ-Si crystals grown at v = 6 mm/min leads to the formation of a region with a low concentration of defects (low-defect region) between the crystallization front and the region containing *D* microdefects. Electron-microscopy measurements showed that the low-defect region contained both interstitial and vacancy defects 4–7 nm in size with a concentration of $\sim 4.5 \times 10^{13}$ cm^{-3}. The crystals grown at v = 9 mm/min, with subsequent quenching, contained both interstitial and vacancy microdefects in comparable concentrations [6].

Additional information on the nature and properties of microdefects in FZ-Si was obtained by studying crystals grown with a gradual change in the growth rate: v = 5.0, 6.0, 7.0, and 7.5 mm/min. In the regions grown at v = 5–6 mm/min, *D* microdefects are distributed in the form of a "channel" at the center. In the regions grown at v = 7.0 and 7.5 mm/min, the channel transforms into a ring due to the appearance of a low-defect region at the center. When the growth rate becomes as high as 8–9 mm/min, the ring vanishes. Electron-microscopy measurements showed the presence of interstitial microdefects 5–8 nm in size with a concentration of $\sim 10^{13}$ cm^{-3} in the channel. Similar results were obtained in studies of the defects inside the ring. It was ascertained that both interstitial and vacancy microdefects are present simultaneously in the low-defect inner region of the ring [7].

Studying of CZ-Si crystals revealed that the distribution of microdefects changes from predominantly band-like at v = 0.5–2 mm/min to predominantly uniform at v > 2 mm/min (for a diameter of 50 mm). As the growth rate of a crystal with a diameter of 50 mm increases, a ring of uniformly distributed microdefects arises around the low-defect region. The electron-microscopy studies revealed defects 4–12 nm in size with a concentration of $\sim 10^{13}$–10^{14} cm^{-3} in both the ring region and the low-defect inner region. Only interstitial defects were found in the ring region, and both vacancy and interstitial defects were present in the low-defect region [8, 9]. As the crystal growth rate increased to 3 mm/min, the ring vanished.

Summarizing the experimental results, we can say that the most important and interesting data were obtained by studying FZ-Si and CZ-Si crystals grown with a variable rate. These experiments allowed us to ascertain the identity of the processes of defect formation in both types of crystals, which consists in the following.

(i) The transformation of microdefects occurs in several successive stages: from vacancy and interstitial microdefects to large defects with a strong strain contrast. In the course of this transformation, the defects increase in size and their concentration decreases.

(ii) Under certain thermal-growth conditions, a ring of uniformly distributed interstitial microdefects is formed. The ring region contains both interstitial and vacancy microdefects.

(iii) With an increase in the growth rate, the inner ring diameter increases until the ring disappears (for a constant crystal diameter).

Thus, it has been ascertained that interstitial and vacancy microdefects (the latter being transformed into interstitial ones) are formed both in FZ-Si and CZ-Si dislocation-free crystals cooled from the crystallization temperature. Further transformation of interstitial microdefects occurs as follows: $D \longrightarrow B \longrightarrow A$. During the decomposition of a supersaturated solid solution of intrinsic point defects, background oxygen and carbon impurities are formation centers for microdefects [7]. Figure 1 shows the schematic diagram of formation and transformation of microdefects for crystals grown by both methods. The dependence of the concentration and type of microdefects in FZ-Si on the growth rate is shown in Fig. 2.

On the basis of the experimental results that were obtained, a heterogeneous impurity–vacancy–interstitial model of formation and transformation of growth microdefects in Si crystals of high structural quality was proposed in [6, 7]. This model is based on the following assumptions: (i) the concentrations of intrinsic point defects near the crystallization front at the melting temperature are approximately equal; (ii) the recombination of intrinsic point defects at high temperatures is hindered; (iii) background oxygen and carbon impurities serve as formation centers in the processes of further growth and transformation of microdefects; and (iv) the supersaturated solid solution of intrinsic point defects in Si decomposes upon cooling via two independent mechanisms—vacancy and interstitial.

The model proposed corresponds to the equations

$$n\mathrm{O}_i + V_{\mathrm{Si}} \longrightarrow n(V\mathrm{O}_2)$$

$$\longrightarrow \text{vacancy microdefects},$$

$$n(V\mathrm{O}_2) + \mathrm{O}_i + \ldots + n\mathrm{O}_i \longrightarrow n[(V_n\mathrm{O}_n) + I_{\mathrm{Si}}]$$

$$\longrightarrow D \text{ microdefects}$$

for the vacancy mechanism and

$$C_s + I_{\mathrm{Si}} \longrightarrow (C_sI_{\mathrm{Si}}) \longrightarrow D \text{ microdefects},$$

$$(C_sI_{\mathrm{Si}}) + \mathrm{O}_i \longrightarrow n[(C_sI_{\mathrm{Si}}) + \mathrm{O}_i] \longrightarrow B \text{ microdefects},$$

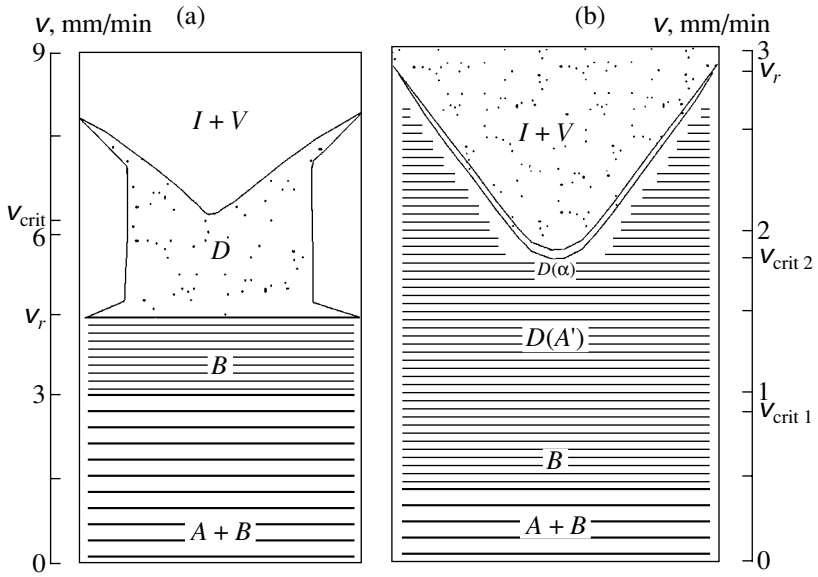

Fig. 1. Schematic diagram of the formation and transformation of microdefects in (a) FZ-Si single crystals 30 mm in diameter and (b) CZ-Si single crystals 50 mm in diameter. v_{crit} and $v_{crit\ 2}$ are the experimentally determined growth rates at which vacancy microdefects arise and disappear, respectively; v_r is the growth rate at which remelting is suppressed; and $v_{crit\ 1}$ is the theoretically calculated growth rate at which vacancy microdefects arise and interstitial microdefects disappear (according to the Voronkov model).

$$B \text{ microdefects} + I_{Si} \longrightarrow A \text{ microdefects}$$

for the interstitial mechanism. When the vacancy mechanism is realized, both the vacancy–impurity aggregation and the formation of vacancy clusters (so-called microvoids) may occur [10]. The vacancy–impurity aggregation leads to the formation of oxygen microprecipitates, which, in turn, gives rise to an excessive matrix volume. As a result, one vacancy is absorbed per two oxygen atoms. The aggregation is accompanied by the emission of intrinsic interstitials. The absorption of vacancies and impurities by growing microdefects leads to the decrease in the concentration of vacancies in comparison with the concentration of oxygen. As a result, precipitates additionally absorb oxygen without the participation of vacancies, their size increases, and the strain of the vacancy type around them transforms into the strain of the interstitial type. The parameter $C_{crit} = V/G$ determines the conditions of the disappearance or appearance of vacancy microdefects.

A vacancy aggregation may occur when large crystals are grown. For example, in TEM studies of LST defects [11, 12], it was suggested that these defects have a vacancy type and, thus, are microvoids. This idea was based on the fact that the oxygen concentration at the center of a defect is lower than at its periphery. At the same time, these results indicate that the formation of vacancy microdefects is heterogeneous.

In the case of the interstitial mechanism, carbon atoms serve as catalysts, this leading to agglomeration of intrinsic (Si) interstitials and C atoms. The growth of interstitial microdefects decreases the concentration of intrinsic interstitials, which provides conditions for the impurity precipitation. The formation of impurity-phase particles is accompanied by the emission of intrinsic interstitials.

Thus, both mechanisms (vacancy and interstitial) lead to the formation of two types of interstitial *D* microdefects: interstitial agglomerates (sinks for Si interstitials) and impurity precipitates (sources of these atoms). Initially, these microdefects are uniformly distributed small *B* microdefects; then, they are transformed into *A* microdefects.

Analysis of the data in Fig. 1 shows that, at a gradual increase in the growth rate of FZ-Si crystals, microdefects of one type gradually transform into microdefects of another type. Large swirls of *A* microdefects are replaced with smaller swirls of *B* microdefects. When the growth rate attains the value v_r at which the effect of remelting is suppressed, *B* microdefects transform into uniformly distributed *D* microdefects. We refined the value of v_r for FZ-Si and determined it to be ~4.5 mm/min. Our experiments show that, when the growth rate exceeds some critical value v_{crit}, vacancy microdefects manifest themselves in the crystals grown, while, at growth rates below v_{crit}, only interstitial microdefects are observed. At $v > v_r$, interstitial *D* microdefects generally form a channel, which then (at $v \geq v_{crit}$) begins to diverge to the crystal periphery, forming a ring. With a further increase in the growth rate, the ring formed by interstitial microdefects decreases in size. At $v \sim$ 8–9 mm/min, this ring vanishes, and vacancy and interstitial microdefects with

approximately equal concentrations coexist in the total volume of the crystal.

Thus, with an increase in the growth rate, continual transformation of interstitial microdefects occurs: at $v > v_{crit} = 6–6.5$ mm/min, vacancy microdefects arise, the concentration of which increases with increasing v up to the value of about 9 mm/min, at which the concentrations of microdefects of both types are approximately equal.

For CZ-Si crystals 50 mm in diameter, the aforementioned transformation of defects occurs at lower growth rates. Microdefects become uniformly distributed in the range $1.5 < v < 2$ mm/min. However, swirls formed by interstitial *A* and *B* microdefects should be present only at $v < v_{crit\,1}$, where $v_{crit\,1}$ is defined as the growth rate corresponding to the appearance of vacancy microdefects and disappearance of interstitial microdefects [1, 2]. According to our estimates, this rate should be in the range 0.8–1.2 mm/min for crystals that are 50 mm in diameter.

The experimental results reported here indicate that the defects observed in the vacancy mode (at $v > v_{crit\,1}$) in the ring region are of the interstitial type. Subsequent thermal treatments transform these defects into extrinsic stacking faults [13]. In addition, it was ascertained recently that the defects outside the ring are interstitial dislocation loops [14]. Only in the inner region of the ring, where interstitial and vacancy defects coexist, is the condition for the vacancy growth satisfied. This inconsistency between experiment and theory can be explained in two ways. First, we may suggest that the concentrations of oxygen and carbon impurities in CZ-Si crystals are one to two orders of magnitude higher than in FZ-Si crystals. Therefore, vacancy microdefects may grow, and their strain signs may become off the interstitial type, even in the vacancy mode. For this reason, the region with the band-like distribution of *D* (*A*') microdefects should also contain only interstitial defects. Second, we should bear in mind that the value of v_{crit} is determined only by the real thermal conditions of the crystal growth; i.e., by analogy with FZ-Si, $v_{crit} = v_{crit\,2}$ for CZ-Si.

It has been previously [15] that, at $v > v_{crit\,1}$, the distribution of microdefects may be either band-like (*A* microdefects) or uniform (α microdefects). Defects of both types correlate with *D* microdefects. However, we consider the microdefects in the ring region to be similar to *D* microdefects in FZ-Si crystals. Due to the specific growth conditions, these microdefects have a uniform ring distribution similar to the that of interstitial *D* microdefects in FZ-Si single crystals. Such a ring of uniformly distributed *D* (α) microdefects separates the region of interstitial *D* (*A*') microdefects in the band-like distribution and the region of coexistence of vacancy and interstitial microdefects similarly to the situation observed in FZ-Si crystals. According to the proposed mechanism, the thermal conditions for the growth of large Si single crystals probably correspond to the conditions under which a ring of defects will appear in the crystal cross section. An increase in the crystal diameter should lead to a decrease in the inner ring diameter [16].

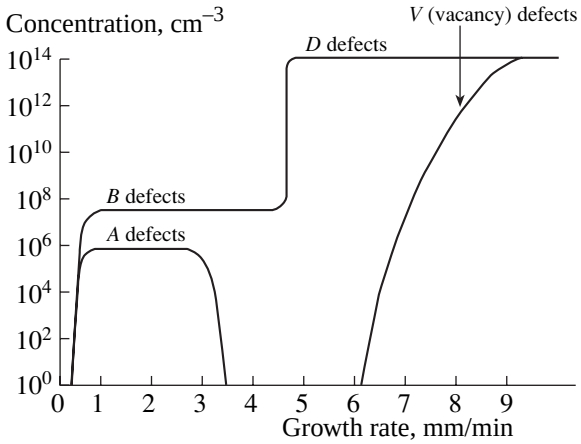

Fig. 2. Dependences of the concentration and type of microdefects in FZ-Si crystals (30 mm in diameter) on the growth rate.

CONCLUSIONS

The proposed mechanism of formation, development, and transformation of growth microdefects makes it possible to explain the experimental results obtained for semiconductor Si and reveal a relationship between the atomic-level processes and the real thermal growth conditions. Since the formation of different types of microdefects is caused by the presence of residual carbon and oxygen impurities as well as changes in the crystal growth conditions, defect formation can be controlled by (i) choosing optimal growth conditions and improving the quality of the initial blend and (ii) introducing special dopants and additional treatments.

REFERENCES

1. V. V. Voronkov, J. Cryst. Growth **59** (3), 625 (1982).
2. V. V. Voronkov and R. Falster, J. Cryst. Growth **194** (1), 76 (1998).
3. A. A. Sitnikova, L. M. Sorokin, I. E. Talanin, *et al.*, Fiz. Tverd. Tela (Leningrad) **28** (5), 1856 (1986) [Sov. Phys. Solid State **28**, 1032 (1986)].
4. I. E. Talanin, D. I. Levinzon, and V. I. Talanin, Izv. Vyssh. Uchebn. Zaved., Mater. Élektron. Tekh., No. 4, 21 (2000).
5. I. E. Talanin, V. I. Talanin, and D. I. Levinzon, Poverkhnost, No. 3, 72 (2002).
6. V. I. Talanin, I. E. Talanin, and D. I. Levinson, Semicond. Sci. Technol. **17** (2), 104 (2002).

7. V. I. Talanin, I. E. Talanin, and D. I. Levinson, Cryst. Res. Technol. **37** (9), 983 (2002).
8. V. I. Talanin, I. E. Talanin, and D. I. Levinzon, *High-Purity Metal and Semiconductor Materials* (NNTs KhFTI, Kharkov, 2002), p. 74.
9. V. I. Talanin and I. E. Talanin, Phys. Status Solidi A **200** (2), 297 (2003).
10. V. V. Voronkov, in *Crystal Growth* (Nauka, Moscow, 1990), Vol. 18, p. 183.
11. M. Kato, T. Yoshida, Y. Ikeda, and Y. Kitagawara, Jpn. J. Appl. Phys. **35** (11), 5597 (1996).
12. M. Nishimura, S. Yoshino, H. Motoura, *et al.*, J. Electrochem. Soc. **143** (10), L243 (1996).
13. K. Nakai, M. Hasebe, K. Ohta, and W. Ohashi, J. Cryst. Growth **210** (1), 20 (2000).
14. J. Furukawa, H. Tanaka, Y. Nakada, *et al.*, J. Cryst. Growth **210** (1), 26 (2000).
15. N. I. Puzanov and A. M. Éĭdenzon, Tsvetn. Met., No. 4, 69 (1988).
16. W. Von Ammon, E. Dornberger, and P. O. Hansson, J. Cryst. Growth **198** (1), 390 (1999).

Translated by Yu. Sin'kov

Crystallography Reports, Vol. 49, No. 2, 2004, pp. 193–196. Translated from Kristallografiya, Vol. 49, No. 2, 2004, pp. 244–247.

REAL STRUCTURE OF CRYSTALS

Phase Equilibria of A^3B^5 Quinary Systems with an Elastically Strained Solid Phase[1]

V. V. Kuznetsov*, É. R. Rubtsov*, V. I. Ratushnyĭ, and E. A. Kognovitskaya*****

** St. Petersburg State Electrotechnical University, ul. Professora Popova 5, St. Petersburg, 197376 Russia*
e-mail: vvkuznetsov@mail.eltech.ru
*** South Russian State Technical University (Volgodonsk Branch), pr. Lenina 75, Volgodonsk, 347340 Russia*
**** Ioffe Physicotechnical Institute, Russian Academy of Sciences,*
Politekhnicheskaya ul. 26, St. Petersburg, 194021 Russia

Received March 3, 2003

Abstract—The contribution of the elastic component of the excess energy of mixing is determined for A^3B^5 quinary solid solutions. A relationship is derived for the activities of the components in an elastically strained solid phase of the quinary solid solutions. The correctness of the possible assumptions used in the calculation of the activity coefficients of the solid phase of a quinary solution is analyzed. The contact supercooling in the vicinity of the binary substrate isoperiods is calculated for a number of A^3B^5 quinary systems. It is shown that the negative contact supercoolings correspond to the thermodynamic instability boundaries of the quinary solid solutions. © *2004 MAIK "Nauka/Interperiodica".*

Quinary semiconductor systems offer the advantage that they make it possible to control three parameters independently, which is of considerable importance in choosing materials used for the design of ideal heterojunctions [1]. However, practical use of the quinary semiconductor systems is limited by the technological problems associated with both the multiparametricity of the epitaxial process and the absence of adequate thermodynamic description of these systems.

Earlier [1–3], we proposed a technique for predicting the fundamental properties of heterostructures and derived phase equilibrium equations for A^3B^5 quinary systems. However, the consistent analysis of the role played by elastic strains arising from the lattice mismatch in the heterostructure has been performed only for ternary and quaternary systems based on A^3B^5 compounds [4, 5]. For these systems, equations of the coherent phase diagram have also been derived and approved [5, 6]. In this study, we extended the above notions to quinary systems.

It is known that the lattice mismatch of an epitaxial layer and the substrate leads to coherent, semicoherent, or incoherent solid-phase coalescence [5].

Since the contribution of the strain energy to the excess energy of mixing is positive, an elastically strained solid solution can be at equilibrium only with a supersaturated liquid phase. Supersaturation can be achieved either by an additional dissolving of the solid phase in contact with the liquid phase or as a result of supercooling of the whole system prior to contact by the so-called value of contact supercooling ΔT_C.

Elastic strains affect the free energy of the solid solution, thus changing the solubility limits of the solid solution components and the boundaries of the region of existence of the solid solution itself. For an elastically strained epitaxial layer of the solid solution, the mixing energy can be represented by the sum

$$G^m = G^{em} + G^{el}, \quad (1)$$

where G^{em} is the mixing energy of the unstrained solid phase and G^{el} is the elastic energy of the strained solid phase.

The properties of real solutions are characterized by the excess functions of mixing: $\Delta G^{ex} = \Delta G^{em} - \Delta G^{id}$, that is, $\Delta G^{em} = \Delta G^{ex} + \Delta G^{id}$, where G^{ex} and G^{id} are the excess energies of mixing of the unstrained real solid solution and the ideal solid solution, respectively.

Within the model of a regular solution, we have $\Delta H^{ex} = \Delta H^{\text{mix}} \neq 0$, $\Delta S^{ex} = 0$, $\Delta S^{\text{mix}} = \Delta S^{id}$, and $\Delta G^{ex} = \Delta H^{ex} = \Delta H^{\text{mix}}$, where ΔH^{mix} and ΔS^{mix} are the enthalpy of mixing and the entropy of mixing, respectively, and ΔS^{ex} and ΔH^{ex} are the excess enthalpy of mixing and the excess entropy of mixing, respectively.

According to the inferences made in [7], the mixing energy of the unstrained solid phase can be expressed in

[1] This work was presented at the National Conference on Crystal Growth (NCCG-2002, Moscow).

the form

$$G^{em} = RT\sum_{i=1}^{5} n_i \ln\left(\frac{n_i}{n}\right) + \sum_{p=1,\,p<k}^{5} \alpha_{pk}^{s}\frac{n_p n_k}{n} - \sum_{i=1}^{2}\sum_{j=3}^{5} \alpha_{ij}^{s} n_{ij} = G^{id} + G^{ex}. \quad (2)$$

Here, α_{ij}^{s} and α_{pk}^{s} are the parameters of interatomic interaction in the solid phase [3]; n_i, n_p, and n_k are the numbers of moles of the ith, pth, and kth components, respectively; n_{ij} is the number of moles of the ijth binary component ($n_1 + n_2 = n_3 + n_4 + n_5 = n = n_{13} + n_{14} + n_{15} + n_{23} + n_{24} + n_{25}$ is the number of moles of the solid solution); and G^{ex} is the excess energy of mixing of the unstrained solid phase.

The elastic energy per mole of the solid solution with a sphalerite structure can be written as

$$G^{el} = \lambda_{ikl}\frac{V_m}{a_s^2}(a - a_s)^2 = \sigma(a - a_s)^2, \quad (3)$$

where a is the lattice constant of the epitaxial layer; a_s is the lattice constant of the substrate; $V_m = N_0 a^3/4$ is the mole volume (N_0 is the Avogadro number); and λ_{ikl} is the reduced modulus of elasticity, which is determined from the interpolation expression

$$\begin{aligned}\lambda_{ikl}(x, y, z) &= \lambda_{ikl,\,BE} + (\lambda_{ikl,\,BC} - \lambda_{ikl,\,BE})y \\ &+ (\lambda_{ikl,\,BD} - \lambda_{ikl,\,BE})z + (\lambda_{ikl,\,AE} - \lambda_{ikl,\,BE})x \\ &+ (\lambda_{ikl,\,AC} - \lambda_{ikl,\,BC} - \lambda_{ikl,\,AE} + \lambda_{ikl,\,BE})xy \\ &+ (\lambda_{ikl,\,AD} - \lambda_{ikl,\,BD} - \lambda_{ikl,\,AE} + \lambda_{ikl,\,BE})xz.\end{aligned} \quad (4)$$

The reduced moduli of elasticity of binary compounds (components of the system) are calculated with due regard for the crystallographic orientation of the substrate and, hence, the epitaxial layer. If the layer is aligned parallel to the (100) plane, it is easy to obtain the following expression for the reduced modulus of elasticity:

$$\lambda_{100} = C_{11} + C_{12} - 2C_{12}^2/C_{11}. \quad (5)$$

For a layer parallel to the (111) plane, the above expression takes the form

$$\lambda_{111} = \frac{6C_{44}(C_{11} + 2C_{12})}{C_{11} + 2C_{12} + 4C_{14}}. \quad (6)$$

The numerical values of the moduli of elasticity C_{44}, C_{11}, and C_{12} and reduced moduli of elasticity λ_{100} and λ_{111} of the A^3B^5 binary compounds are given in [5].

The strain of the epitaxial layer in the substrate plane can be calculated from the equation

$$\varepsilon_s = -\frac{a - a_s}{a} = -\frac{1}{a}\left[\frac{\partial a}{\partial x}(x - x_s) + \frac{\partial a}{\partial y}(y - y_s) + \frac{\partial a}{\partial z}(z - z_s)\right], \quad (7)$$

where x_S, y_S, z_S and x, y, z are the concentrations determining the compositions of the substrate and the epitaxial layer, respectively, and a is the lattice constant of the solid solution in the free (unstrained) state.

The elastic strain affects the activities of the components only in the solid phase, whereas the functions of the liquid state remain unchanged.

For an elastically strained medium, the activity coefficients of binary components γ_{ij} are related to the partial excess free energy by the equation

$$RT\ln\gamma_{ij}^{S} = \frac{\partial}{\partial n_{ij}}(G^{ex}n + G^{el}n). \quad (8)$$

For simplicity, in the subsequent equations, we introduce the designation

$$RT\ln\gamma_{ij}^{S,\,el} = \frac{\partial(G^{el}n)}{\partial n_{ij}}. \quad (9)$$

As a result, we have

$$RT\ln\gamma_{ij}^{S} = RT\ln\gamma_{ij}^{S,\,ex} + RT\ln\gamma_{ij}^{S,\,el}, \quad (10)$$

where $\gamma_{ij}^{S,\,ex}$ is defined by expressions (11) given in [1].

Representing the elastic energy in the form of expression (3) and taking into account that $x_{ij} = n_{ij}/n$, we obtain

$$RT\ln\gamma_{ij}^{S,\,el} = \frac{\partial[\sigma(a - a_s)^2 n]}{\partial n_{ij}} = \sigma(a - a_s)^2 + 2n\sigma(a - a_s)\frac{\partial a}{\partial n_{ij}}. \quad (11)$$

This equation is based on the assumption that the elastic constants included in the factor σ are virtually independent of the composition of the solid solution.

Differentiation of the interpolation expression for the lattice constant of the quinary solid solution [1] gives

$$\begin{aligned}n\partial a/\partial n_{13} &= a_{13} - a + (1 - x)[-a_{1235}(1 - y) + a_{1245}z], \\ n\partial a/\partial n_{14} &= a_{14} - a + (1 - x)[a_{1235}y - a_{1245}(1 - z)], \\ n\partial a/\partial n_{15} &= a_{15} - a + (1 - x)[a_{1235}y + a_{1245}z], \\ n\partial a/\partial n_{23} &= a_{23} - a + x[a_{1235}(1 - y) - a_{1245}z], \\ n\partial a/\partial n_{24} &= a_{24} - a + x[-a_{1235}y + a_{1245}(1 - z)],\end{aligned} \quad (12)$$

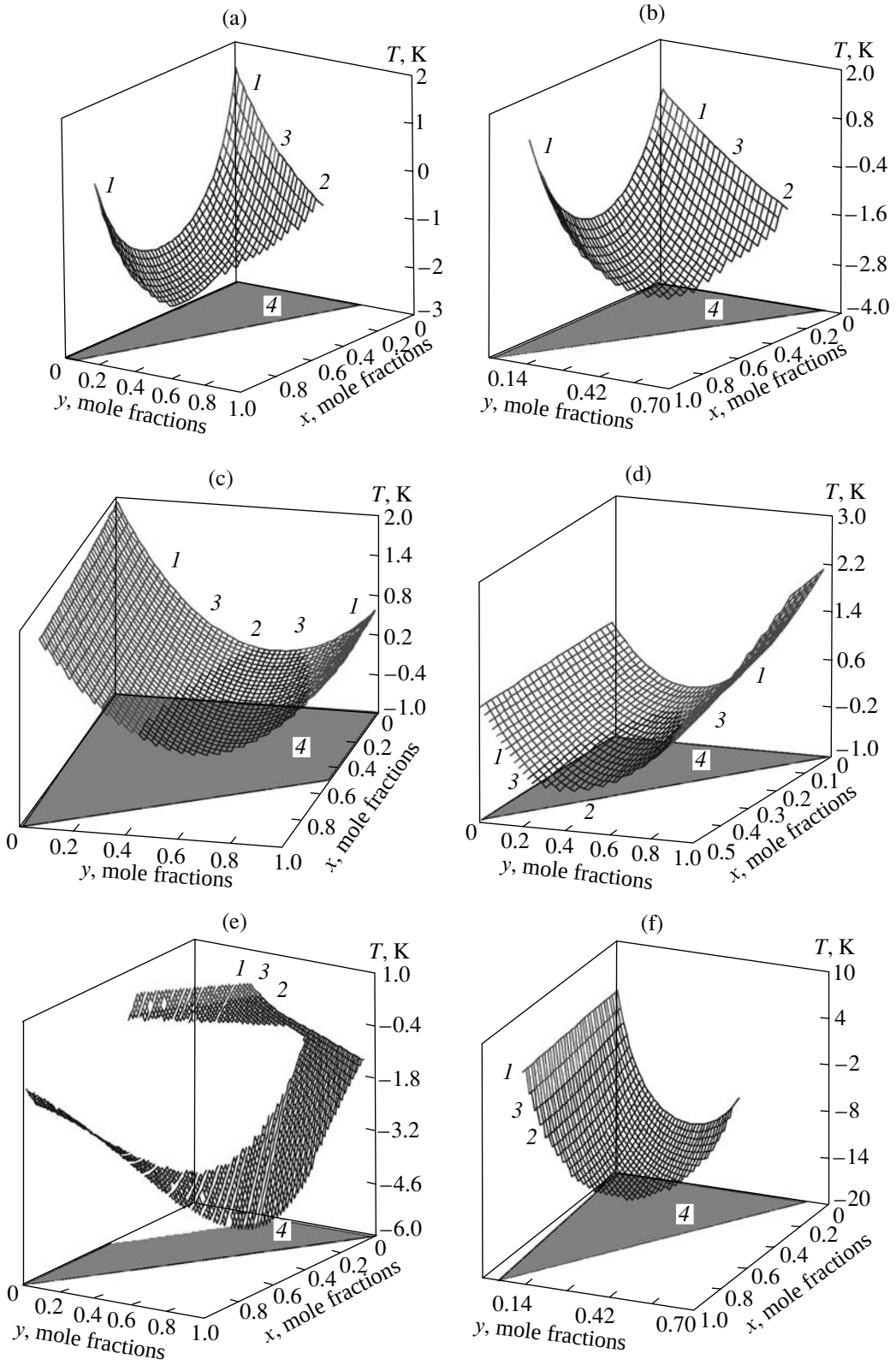

Fig. 1. Contact supercooling in A^3B^5 quinary systems: (a) $Ga_xIn_{1-x}P_yAs_zSb_{1-y-z}$/InAs at T = 773 K, f = –1%, ⟨111⟩; (b) $Ga_xIn_{1-x}P_yAs_zSb_{1-y-z}$/GaSb at T = 773 K, f = –1%, ⟨100⟩; (c) $Al_xGa_yIn_{1-x-y}P_zAs_{1-z}$/GaAs at T = 1073 K, f = –1%, ⟨100⟩; (d) $Al_xGa_yIn_{1-x-y}P_zAs_{1-z}$/InP at T = 1073 K, f = 1%, ⟨100⟩; (e) $Al_xGa_yIn_{1-x-y}As_zSb_{1-z}$/InP at T = 773 K, f = –1%, ⟨100⟩; and (f) $Al_xGa_yIn_{1-x-y}P_zSb_{1-z}$/GaSb at T = 773 K, f = –2%, ⟨100⟩. Designations: (*1*) positive values, (*2*) negative values, (*3*) range of circumzero values, and (*4*) projection of the isoperiod section.

$$n\partial a/\partial n_{25} = a_{25} - a + x[-a_{1235}y - a_{1245}z],$$

where $a_{1235} = a_{13} + a_{25} - a_{15} - a_{23}$, $a_{1245} = a_{14} + a_{25} - a_{15} - a_{24}$.

After substituting the partial derivatives (12) into relationship (11), we obtain the following expressions for the activity coefficients of the elastically strained quinary solid phase:

$$\begin{aligned}
RT\ln\gamma_{13}^{S,el} &= \sigma(a-a_s)(2a_{13}-a-a_s \\
&+ 2(1-x)[-a_{1235}(1-y)+a_{1245}z]), \\
RT\ln\gamma_{14}^{S,el} &= \sigma(a-a_s)(2a_{14}-a-a_s \\
&+ 2(1-x)[a_{1235}y-a_{1245}(1-z)]), \\
RT\ln\gamma_{15}^{S,el} &= \sigma(a-a_s)(2a_{15}-a-a_s \\
&+ 2(1-x)[a_{1235}y+a_{1245}z]), \\
RT\ln\gamma_{23}^{S,el} &= \sigma(a-a_s)(2a_{23}-a-a_s \\
&+ 2x[a_{1235}(1-y)-a_{1245}z]), \\
RT\ln\gamma_{24}^{S,el} &= \sigma(a-a_s)(2a_{24}-a-a_s \\
&+ 2x[-a_{1235}y+a_{1245}(1-z)]), \\
RT\ln\gamma_{25}^{S,el} &= \sigma(a-a_s)(2a_{25}-a-a_s \\
&+ 2x[-a_{1235}y-a_{1245}z]).
\end{aligned} \tag{13}$$

By ignoring the terms of the form $(a_{13} + a_{25} - a_{15} - a_{23})(1-x)(1-y)$, we derive the expression

$$RT\ln\gamma_{ij}^{S,el} = \sigma(a-a_s)(2a_{ij}-a-a_s), \tag{14}$$

which is often used for both quaternary [5] and quinary [3] systems. However, this simplification is not necessarily correct and can result in large errors, especially in the vicinity of the isoperiod. Taking into account that $a_{ij}^s = x_i^S x_j^S \gamma_{ij}^S$, we should add one more term (13) to each expression (11) derived in [3] for the activities of the binary components in the solid phase.

Finally, the equations of the coherent phase diagram of quinary systems can be represented in the generalized form

$$\begin{aligned}
&\Delta S_{ij}^{\text{melt}}(T_{ij}^{\text{melt}} - T) + RT\ln\frac{4x_i^l x_j^l \gamma_i^l \gamma_j^l}{\gamma_i^{sl}\gamma_j^{sl}} \\
&= RT\ln x_i^s x_j^s + RT\ln\gamma_{ij}^{s,ex} + RT\ln\gamma_{ij}^{s,el}.
\end{aligned} \tag{15}$$

It is expedient to calculate the coherent phase diagram in the composition region of solid solutions that corresponds to the condition of isoperiod substitution. It is evident that, for the isoperiod surface, the contribution of elastic strains to the excess energy of mixing of the epitaxial layer is equal to zero and the coherent phase diagram is identical to the equilibrium phase diagram. In practice, the composition of the epitaxial layer can differ from the composition corresponding to isoperiod substitution. This leads to a lattice mismatch of the substrate and the epitaxial layer. It is convenient to simulate and analyze the coherent phase diagram by specifying the mismatch f with respect to the chosen substrate.

The nonequilibrium contribution due to the elastic strains was evaluated from the calculated contact supercoolings ΔT_C by analogy with the calculations performed in [6] for quaternary systems. In our calculations, we used the interaction parameters taken from [1]. Some examples of calculated contact supercoolings are given in the Fig. 1. It is seen from the plots that the contact supercooling has negative values over wide ranges of the phase space. Note that the ranges of negative contact supercoolings coincide with the ranges of thermodynamic instability of quinary solid solutions. This is explained by the changes in the curvature of the dependence of the free energy on the composition of the solid solution in these ranges.

REFERENCES

1. É. R. Rubtsov, V. S. Sorokin, and V. V. Kuznetsov, Zh. Fiz. Khim. **71** (3), 415 (1997).
2. V. V. Kuznetsov, E. R. Rubtsov, V. I. Ratushny, and L. S. Lunin, Inst. Phys. Conf. Ser., No. 155, 335 (1997).
3. É. R. Rubtsov, V. V. Kuznetsov, and O. A. Lebedev, Neorg. Mater. **34** (5), 525 (1998).
4. V. V. Kuznetsov and É. R. Rubtsov, Izv. Vyssh. Uchebn. Zaved., Mater. Élektron. Tekh., No. 2, 48 (1998).
5. V. V. Kuznetsov, P. P. Moskvin, and V. S. Sorokin, *Nonequilibrium Phenomena in the Course of Liquid Heteroepitaxy of Semiconductor Solid Solutions* (Metallurgiya, Moscow, 1991).
6. V. V. Kuznetsov, P. P. Moskvin, and V. S. Sorokin, J. Cryst. Growth **88**, 241 (1988).
7. A. A. Selin and V. A. Khanin, Zh. Fiz. Khim. **53** (11), 2734 (1979).

Translated by I. Polyakova

Crystallography Reports, Vol. 49, No. 2, 2004, pp. 197–201. Translated from Kristallografiya, Vol. 49, No. 2, 2004, pp. 248–252.

REAL STRUCTURE OF CRYSTALS

Internal Deformations in Substitutional Quaternary Solid Solution A^3B^5 [1]

I. I. Parfenova

St. Petersburg State Electrotechnical University, St. Petersburg, Russia

e-mail: SiC.Me@eltech.ru; iparf@hotbox.ru

Received February 26, 2003

Abstract—A model that describes the bond-length distributions in quaternary A^3B^5 solid solutions and allows one to consider large clusters using a minimum of computational resources is suggested. The analytical expression for the radial-distribution function is obtained. The results of the modeling describe the known experimental data well. For a number of solid solutions, the deformation energy is evaluated in the approximation of the valent force field. It is shown that the main contribution to the energy comes from the bond-length dispersion.

INTRODUCTION

Along with a chemical disorder, solid solutions are also characterized by a structural disorder. The deformation energy of ternary semiconductor solid solutions semiconductors has been considered in numerous works, whereas the analogous problems for quaternary solid solutions have never received sufficient attention. Below, we suggest a simple quasi-continuum model of structural disorder in quaternary semiconductor solid solutions that requires a minimum of computational and time resources.

We studied the region of a quaternary solid solution surrounded by an infinite volume of a binary AC compound. We considered solutions with both substitutions in only one $AC_{1-x-y}B_xD_y$ sublattice and solutions with substitutions in two $A_{1-x}B_xC_{1-y}D_y$ sublattices. The displacement field from one substituted site was considered to be spherically symmetric and, at a sufficient distance, could be described by the continuum approximation [1]. In the direct vicinity of the substituted site, this approximation becomes invalid, and the displacements of the atoms closest to the substituted one are larger by a factor of 1.9 than in the continuum limit [1]. The displacements that arise due to substitution of individual sites were taken to be independent and linearly interacting. The resulting displacement $\Delta\mathbf{R}$ was determined by averaging over a large number of configurations of the substituted sites. If an atom C at the site $\mathbf{r}_n$ in the $AC_{1-x-y}B_xD_y$ solid solution is substituted by an atom B with the probability x and by an atom D with the probability y, the partial distribution function of interatomic distances has the form

$$g_{\mathbf{r}_n}(\Delta\mathbf{R}) = (1-x-y)\delta(\Delta\mathbf{R}) + x\delta[\Delta\mathbf{R}-\Delta\mathbf{d}_1(\mathbf{r}_n)] + y\delta[\Delta\mathbf{R}-\Delta\mathbf{d}_2(\mathbf{r}_n)], \quad (1)$$

where $\Delta\mathbf{d}_1$ and $\Delta\mathbf{d}_2$ are the displacements due to different species of substitutional atoms. The Fourier transform of this quantity is

$$g_{\mathbf{r}_n}(\mathbf{q}) = F\{g_{\mathbf{r}_n}(\Delta\mathbf{R}), \mathbf{q}\} = \int g_{\mathbf{r}_n}(\Delta\mathbf{R})\exp(2\pi i\mathbf{q}\Delta\mathbf{R})d(\Delta\mathbf{R}) \quad (2)$$
$$= 1-x-y+x\exp(2\pi i\mathbf{q}\Delta\mathbf{d}_1)+y\exp(2\pi i\mathbf{q}\Delta\mathbf{d}_2).$$

The total distribution function can be represented as a convolution of partial distributions. The Fourier transform of this function can be written as a product of the Fourier transforms of the constituents. In the R space, the total function is obtained by using the inverse Fourier transformation. For the case $A_{1-x}B_xC_{1-y}D_y$, the partial distribution function is

$$g_{\mathbf{r}_n}(\Delta\mathbf{R}) = \begin{cases} (1-x)\delta(\Delta\mathbf{R}) + x\delta[\Delta\mathbf{R}-\Delta\mathbf{d}_1(\mathbf{r}_n)], & (A, B) \\ (1-y)\delta(\Delta\mathbf{R}) + y\delta[\Delta\mathbf{R}-\Delta\mathbf{d}_2(\mathbf{r}_n)], & (C, D), \end{cases} \quad (3)$$

and the total distribution function has the form

$$G(\mathbf{q}) = \prod_{\mathbf{r}_n \ni A, B}(1-x+x\exp(2\pi i\mathbf{q}\Delta\mathbf{d}_1)) \times \prod_{\mathbf{r}_n \ni C, D}(1-y+y\exp(2\pi i\mathbf{q}\Delta\mathbf{d}_2)). \quad (4)$$

The results of modeling for the $A_{1-x}B_xC_{1-y}D_y$ solutions show the existence of four types of bonds, each of

[1] This work was presented at the National Conference on Crystal Growth (NCCG-2002, Moscow).

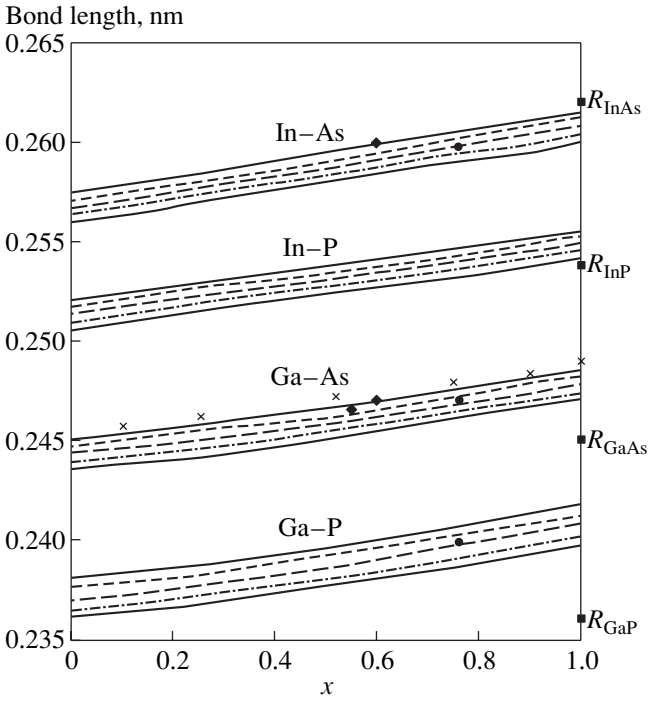

Fig. 1. Interatomic distances in $Ga_{1-x}In_xP_{1-y}As_y$. The calculated curves: solid ones $y = 0.1$ (lower one) and $y = 0.9$ (upper line). A dash-and-dot line $y = 0.25$, broken line $y = 0.5$, dotted line $y = 0.75$. The experimental data: ■ for binary compounds, ● at $y = 0.5$ [2], ◆ at $y = 0.9$ [2], and × at $y = 1$ [3].

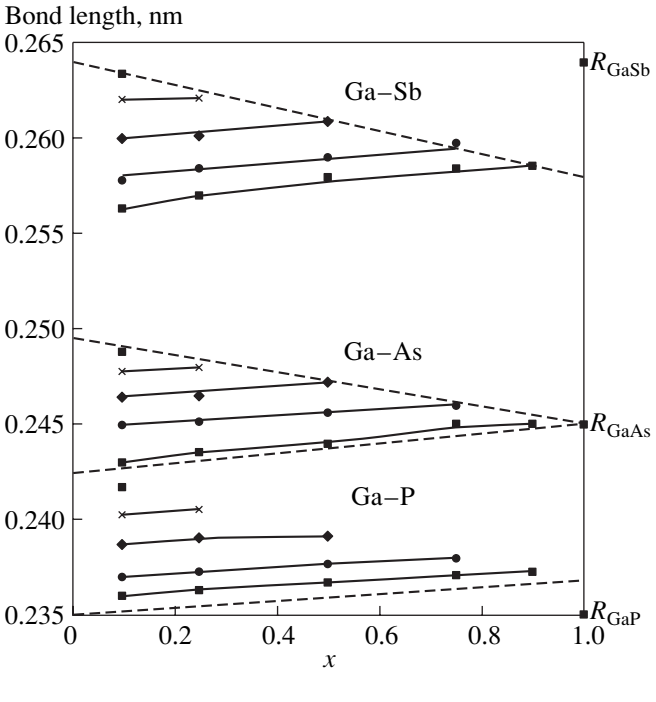

Fig. 2. Interatomic distances in the $GaP_{1-x-y}As_xSb_y$ solid solution. The compositions are indicated by ■ (lower) at $y = 0.1$, ● at $y = 0.25$, ◆ at $y = 0.5$, and × at $y = 0.75$, ■ (upper) at $y = 0.9$. The broken line are the limiting lines corresponding to the maximum and minimum possible values. The distances in the binary compounds are indicated on the right.

which slightly differs from the bond in the corresponding binary compound (Fig. 4). The variations in the bond lengths with the composition are well described by the relationships

$$\begin{aligned}
\Delta b_{AC} &= h(x + D_1 y),\\
\Delta b_{AD} &= h[x\,\mathrm{sgn}(a_{BD} - a_{AD})\\
&\quad + D_1(1-y)\,\mathrm{sgn}(a_{AC} - a_{AD})],\\
\Delta b_{BC} &= h[(1-x)\,\mathrm{sgn}(a_{AC} - a_{BC})\\
&\quad + D_1 y\,\mathrm{sgn}(a_{BD} - a_{BC})],\\
\Delta b_{BD} &= h[(1-x)\,\mathrm{sgn}(a_{AD} - a_{BD})\\
&\quad + D_1(1-y)\,\mathrm{sgn}(a_{BC} - a_{BD})];
\end{aligned} \tag{5}$$

$$h = 0.51\Delta b, \quad D_1 = \frac{a_{AD} - a_{AC}}{a_{BC} - a_{AC}}. \tag{6}$$

The dispersion in bond lengths is practically the same irrespective of the bond type and can be approximated by the expression

$$\sigma^2 = 0.62\sigma_{01}^2 \Delta b^2, \tag{7}$$

$$\begin{aligned}
\sigma_{01}^2 &= x(1-x)[D_3^2 y + (1-y)]\\
&\quad + y(1-y)[D_2^2 x + D_1^2(1-x)],
\end{aligned} \tag{8}$$

$$D_2 = \frac{a_{BD} - a_{BC}}{a_{BC} - a_{AC}}, \quad D_3 = \frac{a_{BD} - a_{AD}}{a_{BC} - a_{AC}}. \tag{9}$$

In an $AC_{1-x-y}B_xD_y$-type solid solution, the bond lengths of the initial binary compounds are also preserved. As an example, Fig. 2 shows the interatomic distances as functions of composition for the $GaP_{1-x-y}As_xSb_y$ solid solution. In this case, the dependences of the bond lengths on the composition and their dispersions are well described by the expressions

$$\begin{aligned}
\Delta b_{AC} &= h(x + D_4 y),\\
\Delta b_{AB} &= h[(1-x-y)\,\mathrm{sgn}(a_{AC} - a_{AB})\\
&\quad + yD_4\,\mathrm{sgn}(a_{AD} - a_{AB})],\\
\Delta b_{AD} &= h[(1-x-y)\,\mathrm{sgn}(a_{AC} - a_{AD})\\
&\quad + (1-y)D_4\,\mathrm{sgn}(a_{AB} - a_{AD})];
\end{aligned} \tag{10}$$

$$\begin{aligned}
\sigma^2 &= 0.62\sigma_{02}^2 \Delta b^2,\\
\sigma_{02}^2 &= x(1-x-y) + D_4^2 y(1-x-y) + D_5^2 xy;
\end{aligned} \tag{11}$$

$$D_4 = \frac{a_{AD} - a_{AC}}{a_{AB} - a_{AC}}, \quad D_5 = \frac{a_{AD} - a_{AB}}{a_{AB} - a_{AC}}. \tag{12}$$

The change in the bond angles between the bonds obtained in modeling is $\Delta\theta = \pm 1°$ with a dispersion of 3°.

Therefore, in what follows, the contribution from the change in valence angles is ignored.

DEFORMATION ENERGY

Bond deformation due to substitution of atoms results in an increase in the crystal-lattice energy. The change in the energy was determined according to the theory of the valent force field. Averaging over the configurations was performed under the assumption that the probability of a substitutional-atom appearance is proportional to the corresponding composition and that all the bonds around an atom are equivalent. Thus, we have

$$\begin{aligned}\langle U_{\text{def}}\rangle &= \sum_k\sum_i \frac{3}{2b_{ki}^{0^2}}\lambda_k\lambda_i\alpha_{ki}\\ &\times\int G[\Delta(\mathbf{b}_{ki}\mathbf{b}_{ki})][\Delta(\mathbf{b}_{ki}\mathbf{b}_{ki})]^2 d[\Delta(\mathbf{b}_{ki}\mathbf{b}_{ki})]\\ &+\sum_k\sum_i\sum_{j>i}\frac{9}{4b_{ki}^0 b_{kj}^0}\lambda_k\lambda_i\lambda_j\beta_{i,j}^k\\ &\times\int G[\Delta(\mathbf{b}_{ki}^k\mathbf{b}_{kj}^k)][\Delta(\mathbf{b}_{ki}^k\mathbf{b}_{kj}^k)]^2 d[\Delta(\mathbf{b}_{ki}^k\mathbf{b}_{kj}^k)],\end{aligned} \tag{13}$$

where G is the corresponding distribution function, the k and i atoms belong to different sublattices, λ_k is the molar fraction of the k species, and α_{ki} and $\beta_{i,j}^k$ are the force constants of extension and bending of the bonds between the k, i, and j atoms. It should be noted that for $AC_{1-x-y}B_xD_y$, $\lambda_k = 1$ and the summation over k in (13) is not necessary. The integrals in Eq. (13) can be expressed via the average and dispersion of the quantities under the integral sign. Now, ignoring the quantities of the second-order smallness and using the results of modeling, we arrive at

$$\sigma^2[\Delta(\mathbf{b}_i\mathbf{b}_i)] = 1.84\sigma_{01}^2,\quad \sigma^2[\Delta(\mathbf{b}_i\mathbf{b}_j)] = 3.45\sigma_{01}^2 \tag{14}$$

for the $A_{1-x}B_xC_{1-y}D_y$ solid solutions and

$$\sigma^2[\Delta(\mathbf{b}_i\mathbf{b}_i)] = 1.84\sigma_{02}^2,\quad \sigma_1^2[\Delta(\mathbf{b}_i\mathbf{b}_j)] = 3.45\sigma_{02}^2, \tag{15}$$

$$\sigma_2^2[\Delta(\mathbf{b}_i\mathbf{b}_j)] = 1.39\sigma_{02}^2 \tag{16}$$

for the $AB_{1-x-y}C_xD_y$ solid solutions. In the last case, we have two dispersions, σ_1 and σ_2, which are associated with two possible substitutions of atoms in the valent angle: Eq. (16) corresponds to the substitution of end atoms and Eq. (15) to the substitution of the central atom. For substitutional solutions with substitution in both sublattices, we have

$$\begin{aligned}U_1 &= 6\{[(1-x)(1-y)\Delta b_{AC}^2\alpha_{AC}\\ &+(1-x)y\Delta b_{AD}^2\alpha_{AD}+x(1-y)\Delta b_{BC}^2\alpha_{BC}\\ &+xy\Delta b_{BD}^2\alpha_{BD}]+1.88\sigma_{01}^2[(1-x)(1-y)\alpha_{AC}\\ &+(1-x)y\alpha_{AD}+x(1-y)\alpha_{BC}+xy\alpha_{BD}]\},\end{aligned} \tag{17}$$

$$\begin{aligned}U_2 &= (1-x)(1-y)(2-x-y)\Delta b_{AC}^2\beta_{AC}\\ &+(1-x)y(1-x+y)\Delta b_{AD}^2\beta_{AD}\\ &+x(1-y)(1-y+x)\Delta b_{BC}^2\beta_{BC}+xy(x+y)\Delta b_{BD}^2\beta_{BD}\\ &+x(1-x)(1-y)\frac{(\Delta b_{AC}+\Delta b_{BC})^2}{2}\beta_{A,B}^C\\ &+y(1-x)(1-y)\frac{(\Delta b_{AC}+\Delta b_{AD})^2}{2}\beta_{C,D}^A\\ &+xy(1-x)\frac{(\Delta b_{AD}+\Delta b_{BD})^2}{2}\beta_{A,B}^D\\ &+xy(1-y)\frac{(\Delta b_{BC}+\Delta b_{BD})^2}{2}\beta_{C,D}^B\\ &+3.45\sigma_{01}^2[(1-x)(1-y)(2-x-y)\beta_{AC}\\ &+y(1-x)(1-x+y)\beta_{AD}+x(1-y)(1-y+x)\beta_{BC}\\ &+xy(x+y)\beta_{BD}+2x(1-x)(1-y)\beta_{A,B}^C\\ &+2y(1-x)(1-y)\beta_{C,D}^A+2xy(1-x)\beta_{A,B}^D\\ &+2xy(1-y)\beta_{C,D}^B].\end{aligned} \tag{18}$$

For the $AC_{1-x-y}B_xD_y$ solid solutions, the corresponding equations have the form

$$\begin{aligned}U_1 &= 6\{[(1-x-y)\alpha_{AC}\Delta b_{AC}^2\\ &+x\alpha_{AB}\Delta b_{AB}^2+y\alpha_{AD}\Delta b_{AD}^2]\\ &+1.88\sigma_{02}^2[(1-x-y)\alpha_{AC}+x\alpha_{AB}+y\alpha_{AD}]\},\end{aligned} \tag{19}$$

$$\begin{aligned}U_2 &= [(1-x-y)^2+(1-x-y)]\Delta b_{AC}^2\beta_{AC}\\ &+(x^2+x)\Delta b_{AB}^2\beta_{AB}+(y^2+y)\Delta b_{AD}^2\beta_{AD}\\ &+(1-x-y)x\frac{(\Delta b_{AB}+\Delta b_{AC})^2}{2}\beta_{B,C}^A\\ &+y(1-x-y)\frac{(\Delta b_{AC}+\Delta b_{AD})^2}{2}\beta_{C,D}^A\\ &+xy\frac{(\Delta b_{AB}+\Delta b_{AD})^2}{2}\beta_{B,D}^A\end{aligned} \tag{20}$$

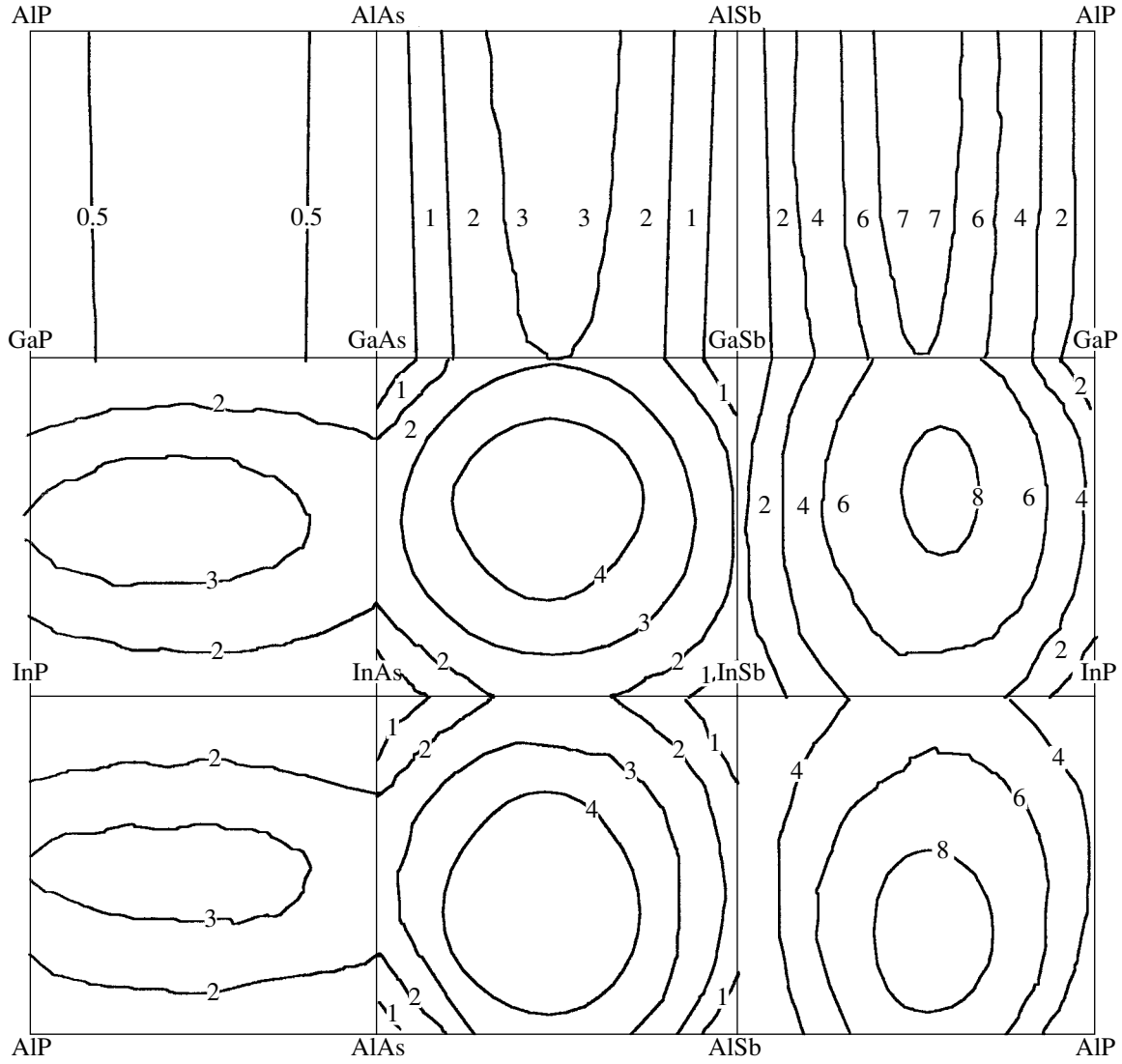

Fig. 3. Isoenergetic deformation-energy curves (kJ/mol) in the solid solutions with substitution in both $A_{1-x}B_xC_{1-y}D_y$ sublattices.

$$+ 3.45\frac{\sigma_{02}^2}{2}[(1-x-y)\beta_{AC} + x\beta_{AB} + y\beta_{AD}]$$

$$+ 1.39\sigma_{02}^2[(1-x-y)x\beta_{B,C}^A + (1-x-y)y\beta_{C,D}^A$$

$$+ xy\beta_{B,D}^A].$$

The energy of internal stresses was calculated for nine $A_{1-x}B_xC_{1-y}D_y$-type solid solutions (Fig. 3). The lowest deformation energies (0.81 kJ/mol) were observed in the $Ga_{1-x}Al_xP_{1-y}As_y$ system. It should be noted that the isoenergetic curves are asymmetric with respect to the point $x = y = 0.5$ with the high-energy range being displaced toward the components with a lower value of the lattice constant. The calculations for six $Al_{1-x}In_xP_{1-y}Sb_y$-type solid solutions are illustrated by Fig. 4. The minimum stress energies were observed in the $Ga_{1-x-y}Al_xIn_ySb$ system (the maximum value 1.46 kJ/mole) and the maximum stress values, in the $AlP_{1-x-y}As_xSb_y$ system (the maximum value 6.85 kJ/mol). The isoenergetic lines are adjacent to the side of the triangle corresponding to the maximum difference between the lattice constants of the binary components.

The contribution to the elastic deformation energy from the second term in Eq. (14) associated with bending of the valence bonds is smaller by a factor of 1.7 than the contribution from the change in the bond lengths to the closest neighboring atoms (the first terms in Eq. (14)). The scatter in the bond lengths and bond angles makes the contribution approximately 2.5 times higher than the change in the average values. Thus, the main contribution to the deformation energy in substitutional solid solutions comes from the dispersion in the interatomic bond lengths.

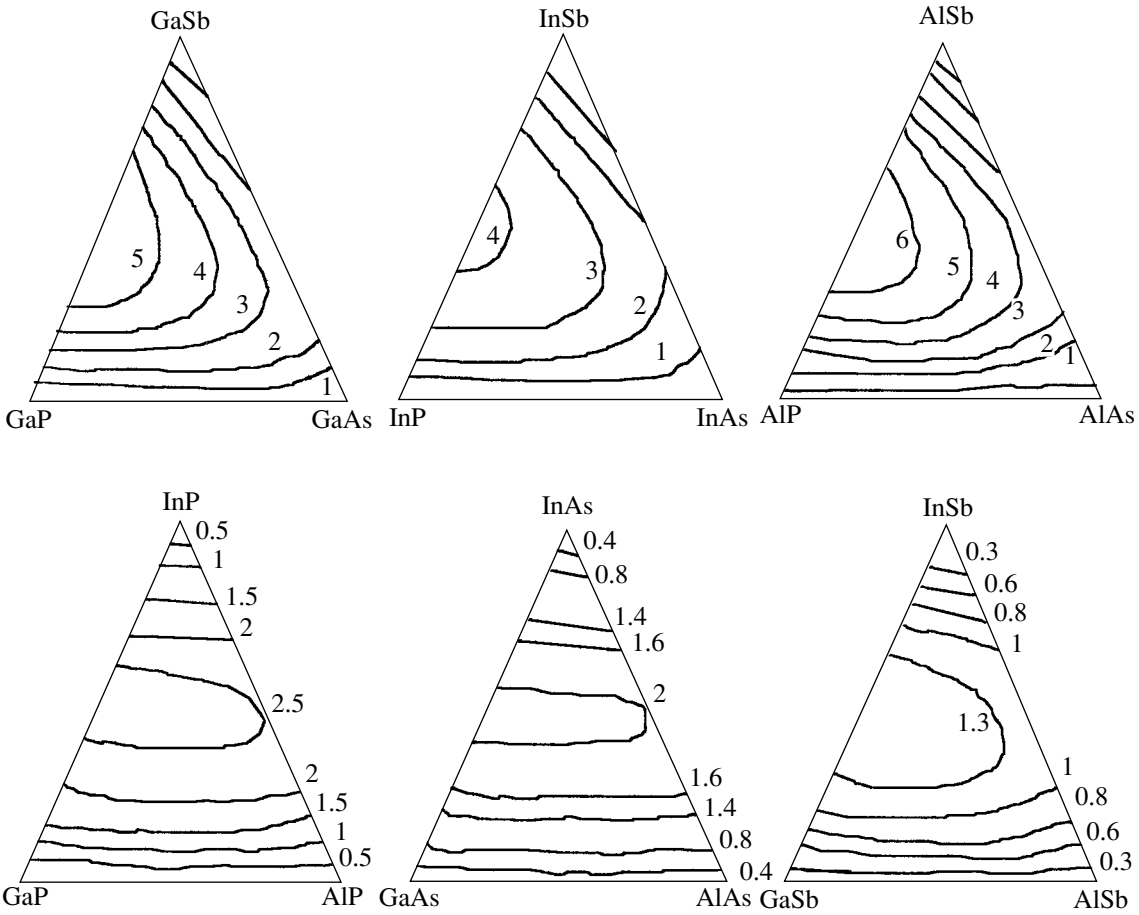

Fig. 4. Isoenergetic curves of deformation energy (kJ/mol) in solid solutions with substitutions in one $AC_{1-x-y}B_xD_y$ sublattice.

On average, the $A_{1-x}B_xC_{1-y}D_y$ solid solutions have a higher internal-deformation energy than the $AC_{1-x-y}B_xD_y$ solutions. This is associated with the dispersion in the $\Delta(\mathbf{b}_i^k\mathbf{b}_j^k)$ values related to the influence of the substitutional atoms onto their second nearest neighbors. In the $AC_{1-x-y}B_xD_y$-type solid solutions, the substitution of the end atoms of the angle, the forces acting on the second nearest neighbors, are normal to the plane of the neighboring valence angle; in the case of the substitution of the central atoms of the angle, they lie in this plane. Therefore, Eq. (15) yields a value about 2.5 times higher than the value given by Eq. (16). In the $A_{1-x}B_xC_{1-y}D_y$-type solid solutions, the substitution of exclusively end atoms is observed only on very rare occasions.

REFERENCES

1. A. A. Kopylov and I. I. Parfenova, Fiz. Tverd. Tela (Leningrad) **30** (2), 441 (1988) [Sov. Phys. Solid State **30**, 250 (1988)].
2. H. Oyanagi, Y. Takeda, T. Matsushita, *et al.*, Solid State Commun. **67** (5), 453 (1988).
3. J. C. Mikkelsen and J. B. Boyce, Phys. Rev. Lett. **49**, 1412 (1982).
4. P. N. Keating, Phys. Rev. **145** (2), 637 (1966).

Translated by L. Man

Crystallography Reports, Vol. 49, No. 2, 2004, pp. 202–205. Translated from Kristallografiya, Vol. 49, No. 2, 2004, pp. 253–256.

PHYSICAL PROPERTIES OF CRYSTALS

A Study of the Morphology and Magnetic Properties of Silicon Whiskers[1]

I. P. Ostrovskiĭ*, Ya. S. Gij*, V. M. Tsmots', and Yu. P. Pavlovskiĭ****

** Lviv Polytechnical University, Lviv, Ukraine*

e-mail: iostrov@polynet.lviv.ua

*** Pedagogical State University, Drogobych, Ukraine*

Received March 3, 2003

Abstract—Methods of growing Si whiskers are considered and the results of studying their magnetic susceptibility χ are reported. Silicon whiskers are grown using the method of chemical transport reactions in a closed bromide system. The crystals studied were divided into four groups: (i) crystals 0.1–0.9 μm in diameter, (ii) twinned crystals 1–2 μm in diameter, (iii) needle-like crystals from 5 to 1500 μm in diameter, and (iv) isometric crystals (the latter were not measured). With an increase in diameter, the whiskers of the first group changed their state from paramagnetic to diamagnetic, while the crystals of the third group showed a transition from a diamagnetic to a paramagnetic state. All these crystals show a nonlinear dependence of χ on the strength of an external magnetic field H; the nonlinearity increases with increasing the sample paramagnetism. The susceptibility of twinned samples is diamagnetic and close to the value of χ for bulk silicon, and the nonlinearity of the dependence $\chi(H)$ is insignificant. The measured values of χ of Si whiskers are explained by features of their crystal structure and chemical composition. © *2004 MAIK "Nauka/Interperiodica".*

INTRODUCTION

An important problem in modern microelectronics is the preparation of new materials. One of these is whiskers, with their high structural perfection, chemical stability, and high strength—which reaches the theoretical limit for crystals with a small cross section [1]. Development of compositional materials with specific properties on the basis of whiskers is currently in progress [2]. High-sensitivity strain gauges have been made on the basis of semiconductor whiskers [3]. Low-dimensional effects have also been established in Si whiskers: a decrease in the crystal-lattice parameter [4] and a shift of the optical-absorption edge to higher energies in submicron whiskers when their diameter is decreased [5].

There is no unified approach to the interpretation of the low-dimensional effects revealed in Si whiskers, as the distribution of impurities in crystals of different diameters is not yet known. In our opinion, study of the magnetic susceptibility χ may clarify this problem. We should note that there are no available data on the magnetic susceptibilities of Si, Ge, and Si–Ge whiskers.

In this paper, we report the results of studying the magnetic susceptibility χ of Si whiskers grown using the method of chemical transport reactions in a closed bromide system using Pt, B, and Au dopants.

[1] This work was presented at the National Conference on Crystal Growth (NCCG-2002, Moscow).

GROWTH OF SILICON WHISKERS

Silicon whiskers were grown using the method of chemical transport reactions in a closed bromide system [6]. A growth tube was loaded with silicon (growing material), gold and platinum (growth initiators), boron (dopant), and bromine (transporting agent). These components were used in the following proportions: 0.1 mg Au, 0.35 mg Pt, 0.4 mg B, and approximately 50–100 mg Br per 1 g Si. The tube was evacuated to a pressure of 10^{-5} Torr and placed into a temperature-gradient furnace. The temperature of the source region was 1200°C, and the temperature of the crystallization region was 800–1000°C. The schematic representation of the Si crystal growth is shown in Fig. 1.

It can be seen from Fig. 1 that, in the temperature range 800–850°C, the formation of whiskers with submicron diameters dominates; at 850–870°C, twins are formed; at 870–950°C, hexahedral needle-like whiskers dominate; and isometric crystals grow at 950–1000°C. *Submicron whiskers* are characterized by a quasi-cylindrical cross-section. Their growth corresponds to the initial stages of the whisker formation.

Twinned whiskers are characterized by a certain structural ordering. The base of such a twin (the so-called cocoon) (Fig. 1b) is a long whisker (l = 2–3 cm) ~2 μm in diameter, from which daughter whiskers of shorter lengths and smaller diameters branch off. All daughter crystals form the same angle of ~54° with the main crystal, which is characteristic of twinned whiskers with a ⟨110⟩ crystallographic orientation. The branches of such a specific "sprout" are, in turn, cov-

1063-7745/04/4902-0202$26.00 © 2004 MAIK "Nauka/Interperiodica"

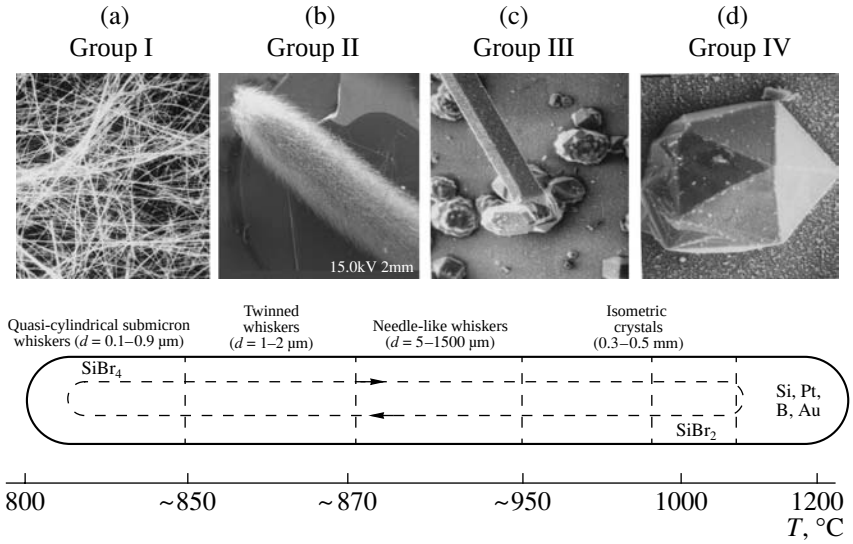

Fig. 1. Formation of different morphological types of silicon crystals, depending on the crystallization temperature: (a) quasi-cylindrical submicron whiskers (0.1–0.9 μm in diameter); (b) twinned whiskers (1–2 μm in diameter); (c) hexahedral needle-like whiskers (5–1500 μm in diameter); and (d) isometric crystals (0.1–0.5 mm).

ered by secondary daughter crystals. As a result, a cocoon located parallel to the growth-tube walls and directed towards the source region is formed in the tube. The regular cocoon structure indicates that the growth occurs under equilibrium conditions.

Needle-like crystals are hexahedra elongated in the ⟨111⟩ direction. Their diameter increases along with increasing growth temperature. *Isometric crystals* are penetration twins; in this case, spinel-law twinning occurs.

MAGNETIC SUSCEPTIBILITY OF Si WHISKERS

The magnetic susceptibility χ of silicon whiskers was studied according to the above classification. The value of χ was measured by the Faraday method [7] in magnetic fields of 0.3–4.0 kOe at 300 K. The maximum measurement error did not exceed 1%. Before measuring, samples were prepared from the grown whiskers. Submicron and twinned whiskers were packed into cylindrical glass tubes 3 mm in diameter, slightly tamped by a glass rod and filled with a low-concentration alcohol solution of BF-2 glue. Needle-like whiskers were stacked into little "sheafs" and glued with the alcohol solution of BF-2. The results of the susceptibility measurements are shown in Figs. 2 and 3, respectively.

It can be seen from Fig. 2 that, due to the increase in the diameter of the submicron crystals, their state changes from paramagnetic to diamagnetic. The diamagnetic susceptibility of silicon whiskers that are 0.7 μm in diameter exceeds the diamagnetic value of χ of bulk Si crystals, which is $\chi_{Si} = -11.6 \times 10^{-8}$ cm^3 g^{-1}. Moreover, submicron crystals show a nonlinear dependence of χ on the strength of the external magnetic field H, which decreases with an increase in the diamagnetic contribution. For submicron crystals ~0.7–0.9 μm in diameter, as well as for twinning whiskers, the nonlinearity is insignificant.

It can be seen from Fig. 3 that the paramagnetic susceptibility of needle-like whiskers increases with an increasing crystal diameter. All the crystals demonstrate nonlinearity in the dependence $\chi(H)$, which decreases with decreasing the paramagnetic contribution to the whisker susceptibility.

RESULTS AND DISCUSSION

In the analysis of the results obtained, an experimental curve $\chi(H)$ should be considered as a sum of two components. The first component, which is parallel to the abscissa axis in the case of strong fields, is independent of the magnetic-field strength. We will denote this component with χ^{ind}. In turn, this independent component consists of the lattice susceptibility χ_L and the susceptibility of paramagnetic centers χ^{par}:

$$\chi^{ind} = \chi_L + \chi^{par}. \quad (1)$$

The second component, which clearly manifests itself in weak fields, accounts for the dependence of χ on the magnetic-field strength. It can be attributed to the stress state of the whisker core or, by analogy to the susceptibility of plastically deformed crystals [8], to the ferromagnetically ordered spin groups at the dislocation structures. Therefore, it is reasonable to denote this component with χ^{fm}.

If necessary (i.e., if the nonlinearity of the dependence $\chi(H)$ was also observed in the field 4 kOe), χ^{ind} was separated from $\chi(H)$ by extrapolation of the depen-

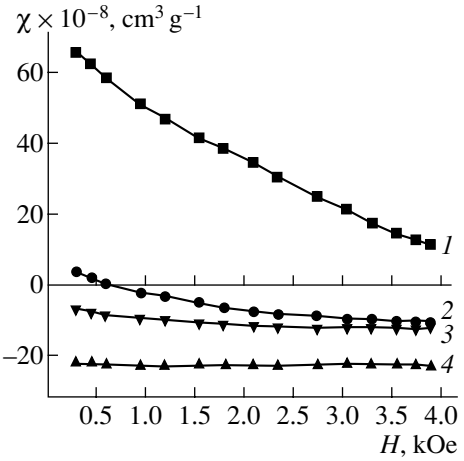

Fig. 2. Dependences of the magnetic susceptibility of submicron ((*1*) 0.1–0.2, (*2*) 0.3–0.6, and (*4*) 0.7–0.9 μm)) and (*3*) twinned Si whiskers on the magnetic-field strength.

dence $\chi(H)$ to the region of high magnetic fields (6 kOe). Hence, we will hereafter use the notation $\chi(6.0)$ interchangeably with χ^{ind}. Thus, the experimental dependence $\chi(H)$ can be represented as the sum

$$\chi(H) = \chi^{ind} + \chi^{fm} = \chi(6.0) + \chi^{fm}. \quad (2)$$

To interpret the results obtained from measuring the dependence $\chi(H)$, the dependence of $\chi(6.0)$ on the whisker diameter is shown in Fig. 4. It can be seen that crystals of the first group change their state from paramagnetic to diamagnetic when the diameter is increased, while the state of crystals of the third group changes from diamagnetic to paramagnetic. Both groups exhibit nonlinearity in the dependence $\chi(H)$, which increases along with an increasing paramagnetic contribution.

Although twins contain a significant number of dislocations, their susceptibility is diamagnetic and close to the susceptibility of bulk Si crystals in both the value and character of the dependence $\chi(H)$ ($\chi^{dia}(Si) = -11.6 \times 10^{-8}$ cm^3 g^{-1}). This can be explained as follows: dislocations in twins are growth ones; therefore, they are filled with Cottrell clouds, which means that there are no free dangling bonds in these twins and, hence, no nonlinearity in the dependence $\chi(H)$.

The paramagnetism of needle-like Si crystals can be explained by the presence of Pt atoms, which have a significant paramagnetic moment (platinum is a paramagnet with $\chi^{par}(Pt) = +110 \times 10^{-8}$ cm^3 g^{-1}). As the studies of whisker conductivity showed [9], the concentration of an impurity growth initiator (Pt, in our case) becomes greater upon an increase in the crystal diameter. Along with this, the concentration of a dopant (in our case, diamagnetic boron with $\chi^{dia}(B) = -70 \times 10^{-8}$ cm^3 g^{-1}) decreases with increasing diameter. These data explain the dimensional dependence of the susceptibility of needle-like Si whiskers (Fig. 3).

The appearance of paramagnetism and its increase with decreasing submicron-whisker size cannot be explained by the paramagnetism of Pt atoms since, according to the mass-spectroscopy data, the content of platinum drops with decreasing the whisker diameter [10]. The dimensional dependence of the susceptibility of submicron whiskers seems to be related to the specific features of their crystal structure. As is well known [11], such crystals consist of a central part of bulk silicon and a nanoporous envelope. We can attribute the magnetic behavior of submicron whiskers to a certain ordering of atoms in the porous envelope. Modification of the envelope occurs due to surface compression, the magnitude of which increases when the whisker diameter is decreased. One can assume that, in this case, the envelope structure changes with the formation of dangling bonds, which, as is well known, are paramagnetic centers [8]. It is this phenomenon that accounts for the

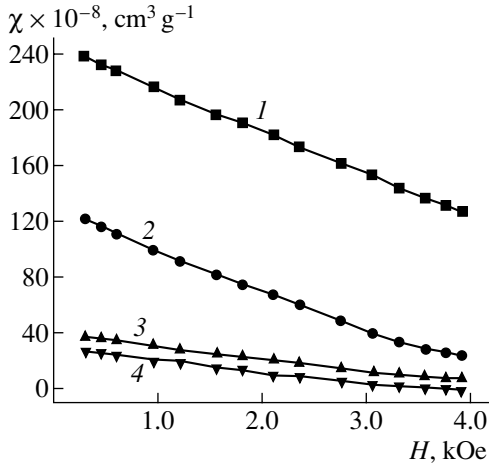

Fig. 3. Dependences of the magnetic susceptibility of needle-like Si whiskers with a diameter of (*1*) 1500, (*2*) 1000, (*3*) 700, and (*4*) 100 μm on the magnetic-field strength.

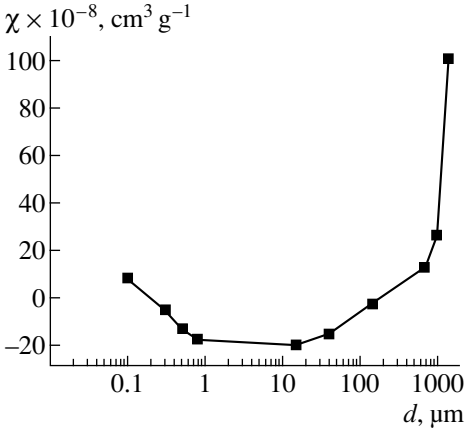

Fig. 4. Dependence of the magnetic susceptibility $\chi(6.0)$ on whisker diameter.

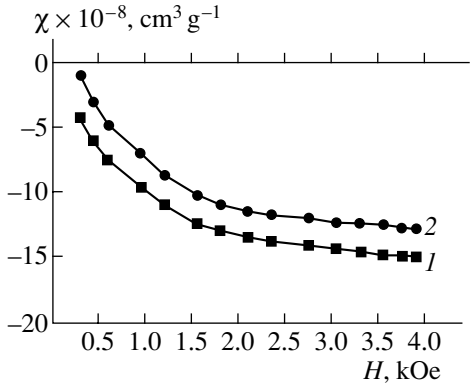

Fig. 5. Magnetic susceptibility of (*1*) unetched and (*2*) etched (for 10 min) Si whiskers 40 μm in diameter.

increase in the paramagnetic contribution when the diameter of submicron whiskers is increased.

Since the envelope deforms the central part of a whisker, the nonlinearity of the dependences $\chi(H)$ for Si whiskers can be related to either the elastic state of their cores or the deformation of whiskers caused by their gluing during the preparation of the sample [8].

To obtain additional information, the influence of etching on the susceptibility of Si whiskers was studied. The dependences $\chi(H)$ of etched and unetched samples 40 μm in diameter are shown in Fig. 5 (the etching time was 10 min). In our opinion, these data suggest the following: The values of χ of an unetched sample fit the results shown in Fig. 2 and expand them—the state of needle-like samples is changed from paramagnetic to diamagnetic with decreasing the whisker diameter. The etching of a needle-like sample leads to a decrease in the diamagnetic contribution, which, obviously, confirms that the crystal surface is enriched with diamagnetic impurities.

The Auger spectroscopy study revealed a significant bromine concentration on the whisker surface ($\sim 10^{14}$ cm^{-2}). Since bromine is diamagnetic, the etching of the surface should lead to a decrease in the diamagnetic contribution, which was observed experimentally.

Thus, the measured values of the susceptibility of Si whiskers are explained by the features of their crystal structure and chemical composition.

CONCLUSIONS

The results of the study of the dependences of the magnetic susceptibility of Si whiskers on magnetic-field strength allow us to conclude the following: Si whiskers from the first group (0.1–0.9 μm in diameter) change their state from paramagnetic to diamagnetic with increasing their diameter. Crystals of the third group (from 5 to 1500 μm in diameter) show a transition from a diamagnetic to a paramagnetic state with increasing their diameter. Both groups demonstrate the nonlinearity of the dependence of the magnetic susceptibility on magnetic-field strength, which enhances with increasing the sample paramagnetism. The susceptibility of crystals of the second group (twinned crystals 1–2 μm in diameter) is diamagnetic and close to the value of χ for bulk silicon; the nonlinearity of the $\chi(H)$ dependence is insignificant in this case. The measured values of the susceptibility of silicon whiskers are explained by the features of their crystal structure and chemical composition.

REFERENCES

1. E. I. Givargizov, *Growth of Whiskers and Plate-Like Crystals from Vapors* (Nauka, Moscow, 1977).
2. R. I. Baitsar, I. V. Kurylo, S. S. Varshava, and I. P. Ostrovskii, Funct. Mater. **8** (2), 398 (2001).
3. R. Baitsar, V. Voronin, E. Krasnogenov, and N. Bogdanova, Sens. Actuators A **30**, 175 (1992).
4. A. I. Klimovskaya, I. P. Ostrovskiĭ, and R. I. Baĭtsar, Izv. Ross. Akad. Nauk, Ser. Fiz. **57** (11), 210 (1993).
5. E. G. Gule, G. Yu. Rudko, A. I. Klimovskaya, *et al.*, Phys. Status Solidi B **161**, 565 (1997).
6. V. A. Voronin, I. L. Maryamova, and A. S. Ostrovskaya, Cryst. Prop. Prep. **36–38**, 340 (1991).
7. V. M. Tsmots', V. S. Shtym, M. Yu. Voĭtusik, and V. M. Mel'nik, Byull. Izobret., No. 11, 185 (1988).
8. V. M. Tsmots' and V. S. Shtym, Fiz. Tverd. Tela (Leningrad) **31** (9), 65 (1989) [Sov. Phys. Solid State **31**, 1511 (1989)].
9. A. I. Klimovskaya, I. P. Ostrovskii, and A. S. Ostrovskaya, Phys. Status Solidi A **153**, 465 (1996).
10. A. I. Klimovs'ka and I. P. Ostrovs'kiĭ, in *Abstracts of Scientific Conference Dedicated to the 40-Year Anniversary of Physical Faculty of Lviv State University* (Lviv, 1993), p. 120.
11. A. I. Klimovskaya, I. V. Prokopenko, and I. P. Ostrovskiĭ, J. Phys.: Condens. Matter **13**, 5923 (2001).

Translated by T. Dmitrieva

Crystallography Reports, Vol. 49, No. 2, 2004, pp. 206–210. Translated from Kristallografiya, Vol. 49, No. 2, 2004, pp. 257–261.

PHYSICAL PROPERTIES OF CRYSTALS

Water-Soluble Ferroelectric Crystals with Inhomogeneous Impurity Distribution[1]

V. N. Shut*, I. F. Kashevich*, and B. E. Watts**

** Institute of Technical Acoustics, National Academy of Sciences of Belarus, Vitebsk, Belarus*
e-mail: shut@vitebsk.by
*** Instituto Maspec/CNR, Parma, Italy*
e-mail: watts@imem.cnr.it

Received February 26, 2003

Abstract—Stabilization of the unipolar state via the formation of inhomogeneous impurity distribution in crystal bulk is considered. Possible growth of crystals with stable characteristics is demonstrated on triglycine sulfate (TGS) crystals with a regular inhomogeneous impurity distribution. The properties of TGS crystals with an inhomogeneous distribution of chromium ions grown above and below the Curie temperature T_C are studied. Inhomogeneous TGS crystals of three types are obtained: type-I crystals with a smooth variation of the concentration gradient along the growth direction, type-II crystals with a periodic layer variation of the impurity concentration, and type-III crystals with a sawtooth-like variation of the impurity concentration along the sample length. The TGS crystals with the regular inhomogeneous impurity distribution in the ferroelectric phase are characterized by higher values of the internal bias field E_b, unipolarity coefficient k, and pyroelectric coefficient γ than the inhomogeneous crystals in the paraelectric phase and the crystals with the statistic impurity distribution grown by the conventional method. © *2004 MAIK "Nauka/Interperiodica".*

INTRODUCTION

Stabilization of the spontaneous polarization necessary for the practical use of ferroelectric crystals is closely related to the creation of a unipolar state in these crystals. A natural weak unipolarity is observed in a considerable number of ferroelectric crystals. Therefore, recently, a great deal of attention has been paid to the improvement of the existing methods and development of new methods of creating unipolarity in crystals. The known data [1–3] lead to the assumption being made that unipolarity may be formed because of the existence of bulk or surface structural imperfections. Therefore, the creation of a unipolar state is associated with the interaction of structural defects and surface states with ferroelectric polarization.

The best-known methods of stabilizing spontaneous polarization in water-soluble ferroelectric crystals are the introduction of impurities into crystals and irradiation of already grown crystals [4, 5]. In both cases, the appearance of unipolarity is associated with the formation of internal fields in crystals, although the mechanism of their formation is not quite clear as yet. It has been shown both theoretically and experimentally [6, 7] that internal bias fields in impurity-containing crystals can be explained by the existence of the electric and mechanical stresses caused by the formation of a nonsymmetric impurity distribution during crystal growth. Therefore, it is important to develop methods for control of unipolarity and establish the factors governing this effect.

The present work is dedicated to the formation of regular inhomogeneous distribution of chromium ions in the bulk of TGS crystals grown both above (paraelectric phase) and below (ferroelectric phase) the Curie temperature T_C and its influence on the crystal properties and processes of spontaneous polarization in these crystals.

EXPERIMENTAL

We grew inhomogeneous TGS crystals with three types of profiles of the Cr^{3+}-ion distribution in the crystal bulk: type-I crystals with an impurity-concentration gradient in which the impurity concentration smoothly varied along the sample length from the set minimum value to the set maximum value during crystal growth; type-II crystals with a periodic layer variation of the impurity concentration (layers with an elevated impurity concentration alternated with layers with a lower impurity concentration); and type-III crystals with a sawtooth-like variation of the impurity concentration along the sample length. The choice of the Cr^{3+} impurity was dictated by active incorporation of chromium ions into the crystal lattice of TGS crystals and their considerable influence on crystal unipolarity [8].

In order to grow crystals with the preset impurity distribution, we developed an original method and designed a special crystallizer for growth of inhomogeneous crystals. Type-I crystals were grown in a crystal-

[1] This work was presented at the National Conference on Crystal Growth (NCCG-2002, Moscow).

lizer based on continuous feeding of the mother liquor with a solution of a modified composition [9]. In our case, the feeding solution was the supersaturated TGS solution with the set concentration of chromium ions. As a result of continuous feeding of the mother liquor with the initial impurity concentration C_{in} with a feeding solution with the impurity concentration C_{feed} during crystal growth, the impurity concentration in the mother liquor smoothly varied and, finally, attained the concentration C_{final}. The impurity-concentration gradient could be varied by setting different C_{in}, C_{feed}, and C_{final} values and varying the thermodynamic growth conditions. In order to compare the properties of inhomogeneous crystals with the composition gradient (type I) with the properties of the crystals with random impurity distributions, we also grew TGS crystals from the solutions with the impurity concentration equal to the average impurity concentration $(C_{final} - C_{in})/2$ in the static mode (hereafter, these are called the control or homogeneous crystals).

When growing inhomogeneous type-II and type-III crystals, we used the well-known fact that the impurity incorporation into a crystal depends on the growth rate. Since the coefficient of the interstitial-impurity distribution in TGS crystals is less than unity, an increase in the growth rate of these crystals results in a decrease in the impurity incorporation into crystals [10]. Type-II crystals were obtained by periodic application of low-frequency vibrations with the constant amplitude and frequency onto crystals growing from solutions. The period of their application was determined by the time of crystal growth in a certain (dynamic or static) mode. Type-III crystals with the sawtooth-like impurity distribution were also grown with the application of low-frequency vibrations but with the amplitude that varied in a sawtooth-like mode from 0 to 3 mm. The period for these crystals was set by the time of the amplitude change from the minimum to the maximum value. In addition to inhomogeneous crystals growing at a varying rate, we used the same solutions to grow homogeneous crystals at the minimum growth rate (in the static mode) and at the maximum growth rate (in the dynamic mode).

Both homogeneous and inhomogeneous crystals were grown by the method of temperature decrease, with the temperature being maintained within ±0.1°C. Growth of crystals at $T_{gr} < T_C$ was performed for 72 h by decreasing the growth temperature from 28 to 26.5°C and growth of crystals at $T_{gr} > T_C$, by decreasing the growth temperature from 60 to 59°C. Then, the crystals grown were used to cut the plates normally to the *b* axis; onto these plates, the aluminum electrodes were deposited.

Because of chromium impurity, the TGS crystals grown had a violet color, with the color intensity varying depending on the impurity concentration. The impurity distribution in type-I crystals was determined on an MF-2 microphotometer used for determining the darkening of the photographic plate by measuring the variation of the color intensity of the transmitted light along the plate length. The changes in the impurity concentration in the type-II and type-III samples were determined indirectly. We grew crystals using different modes by application of vibrations with the amplitude varying from 0 to 3 mm. The impurity content was determined on an MF-2 microphotometer, and the calibration curve was constructed for determining the impurity concentration in inhomogeneous crystals. Depending on the given gradient, the chromium-impurity concentration in type-I crystals almost smoothly varied from $C_{in} = 0$ to $C_{fin} = 5 \times 10^{-3}$–$2 \times 10^{-2}$ mol %. Type-II and type-III crystals were grown from the solutions with the maximum admissible concentration of chromium ions (up to 2 mol %). The impurity concentration between the layers grown in different modes varied within $(3–10) \times 10^{-3}$ mol %. It should be noted that the impurity concentration in the crystals also depended on the growth temperature—at a higher growth temperature, more impurities were incorporated into the crystal.

We studied the temperature dependence of the dielectric constant ε, spontaneous polarization P_s, internal bias field E_b, unipolarity *k*, and pyroelectric γ coefficients of the crystals grown. The data on E_b are listed in the table.

The dielectric constant ε along the direction normal to the (010) plane of TGS crystals with Cr^{3+} impurity was measured by an E7-8 bridge on samples with deposited ~0.8-mm-thick electrodes with the ~10 mm^2 area. The rate of temperature variation was 0.2 °C/min. The spontaneous polarization, internal bias field, and unipolarity coefficient were determined using the hysteresis loop [11]. The pyroelectric measurements were made using dynamic methods at a frequency of 20 Hz. The data obtained were compared with the pyroelectric

Average values of the internal bias field E_b and unipolarity coefficient *k* for inhomogeneous and homogeneous (control) crystals grown above and below T_C at T_{room}

Characteristic	Control crystals		Type-I crystals		Type-II crystals		Type-III crystals	
	$T_{gr} < T_C$	$T_{gr} > T_C$	$T_{gr} < T_C$	$T_{gr} > T_C$	$T_{gr} < T_C$	$T_{gr} > T_C$	$T_{gr} < T_C$	$T_{gr} > T_C$
E_b, kV/cm	0.9	0.7	1.6	0.8	2.0	1.1	2.3	1.2
k, %	36	12	67	28	91	34	105	40

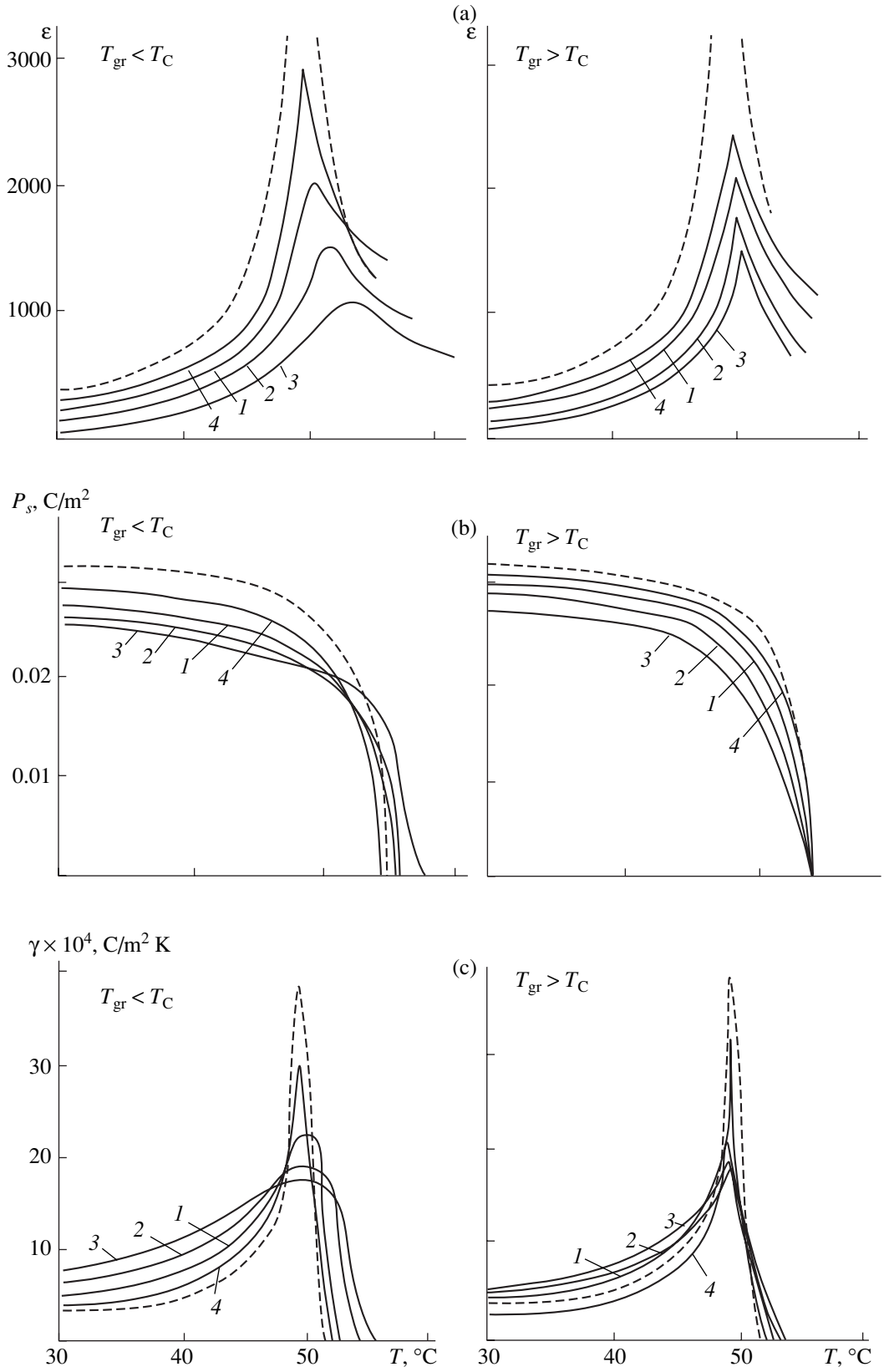

Fig. 1. Temperature dependences of (a) ε, (b) P_s, and (c) γ of TGS crystals with different distributions of Cr^{3+} impurity grown below and above the Curie point. Curves *1*, *2*, and *3* are obtained for crystals of types I, II, and III with inhomogeneous impurity distributions; curve *4* is obtained for a crystal with homogeneous impurity distribution (dashed line corresponds to an undoped crystal).

coefficient γ_0 of the reference pyroelectric receiver—a plate cut out from a single-domain TGS crystals doped with *L*-α-alanine with the known properties.

RESULTS AND DISCUSSION

Figure 1a shows typical $\varepsilon(T)$ curves for homogeneous and inhomogeneous crystals grown below and above T_C (all the curves were constructed using experimental points averaged over at least five independent values). It is seen that the character of the temperature dependences $\varepsilon(T)$ of TGS crystals in the paraelectric phase with both homogeneous and inhomogeneous impurity distributions differ only in the ε_{max} values. For inhomogeneous crystals in the ferroelectric phase, the ε_{max} value is considerably lower, especially for type-III crystals, whereas their Curie temperature is shifted toward higher temperatures. The $\varepsilon(T)$ dependence in the region of the phase transition is rather diffuse. In crystals of the paraelectric phase, no such diffusion is observed (Fig. 1a, the right-hand curve). In the control crystals grown at $T_{gr} < T_C$ (Fig. 1a, the left-hand plot, curve *4*), the $T_{\varepsilon_{max}}$ values are displaced toward low temperatures in comparison with the analogous values for inhomogeneous and pure (undoped) crystals.

Different directions of the displacement of the Curie point for inhomogeneous and control crystals (Fig. 1a, left-hand plot) may be explained as follows. The displacement of $T_{\varepsilon_{max}}$ toward low temperatures for crystals with the statistical impurity distribution indicate considerable structural rearrangements caused by impurity incorporation. Inhomogeneous crystals are characterized by a certain regular impurity gradient which gives rise to considerable internal fields in the crystal. This factor seems to be more important than the structural rearrangements, and, therefore, the ε_{max} value of inhomogeneous crystals shifts toward high temperatures. This may also explain the diffusion of the phase transition, because the diffusion in the ferroelectric systems is usually attributed to structural inhomogeneity and the influence of the internal and external fields [12].

The studies of $P_s(T)$, E_b, and k of inhomogeneous crystals confirm the existence in these crystals of considerable internal fields in the ferroelectric phase. The study of the $P_s(T)$ dependence (Fig. 1b) showed that the inhomogeneous impurity distribution can differently influence the value and the run of the $P_s(T)$ curves in crystals grown at different temperatures. Thus, in crystals grown at $T_{gr} < T_C$, a considerable decrease in the P_s value was observed that was especially pronounced at room temperature. For inhomogeneous crystals of types II and III, the P_s value at the Curie point had a nonzero value. For inhomogeneous type-I crystals, the differences between P_s and P_s of control crystals are much lower, whereas at $T_{gr} > T_C$ these differences are negligible. A decrease in P_s and the existence of the ferroelectric state above T_C are explained by the fact that the existence of the impurity gradient in type-I crystals gives rise to considerable mechanical and electric stresses along the gradient. These stresses produce a polarizing effect on the domain structure formed that is similar to the action of external mechanical and electric fields [13, 14]. Considerable internal fields arising in crystals with the impurity gradient (see table) exceed the equivalent fields due to external factors, and the fraction of the repolarizing volume of the crystal (i.e., the reverse part of P_s) decreases.

The existence of a gradient in a microlayer of the crystalline plate (inhomogeneous type-III crystals) makes this effect more pronounced because of an increase in the impurity gradient in the microlayer in comparison with the extended gradient. The above reasons also lead to an increase in the unipolarity coefficient of inhomogeneous crystals, and, therefore, also to an increase in the pyroelectric coefficient (Fig. 1c).

Since the inhomogeneous crystals grown differed only in the growth temperature, the effects arising in these crystals seem to be associated with the fact that the defects formed in these crystals interact with the formed domain structure of the crystal and polarize this structure. Moreover, the formed stable unipolar state arising during inhomogeneous incorporation of the impurity is also confirmed by the fact that a number of heating–cooling cycles with the transition through the point T_C practically do not change the unipolarity coefficient of inhomogeneous crystals. At the same time, the k value of conventionally doped crystals decreases after sample annealing.

CONCLUSIONS

Creating a regular inhomogeneous impurity distribution in a crystal, one can obtain unipolar ferroelectric single crystals with pronounced internal bias fields stabilizing the domain structure of crystals and, thus, also spontaneous polarization.

REFERENCES

1. J. C. Burfoot and I. G. W. Taylor, *Polar Dielectrics and Their Applications* (Univ. of California, Berkeley, Calif., 1979; Izd. Akad. Nauk SSSR, Moscow, 1981).
2. B. Brezina and M. Havrankova, Ferroelectr. Lett. Sect. **4**, 81 (1985).
3. G. T. Galstyan, I. S. Rez, and M. Yu. Reĭzer, Fiz. Tverd. Tela (Leningrad) **24** (7), 2186 (1982) [Sov. Phys. Solid State **24**, 1244 (1982)].
4. N. D. Gavrilova, V. K. Novik, E. A. Sorokina, *et al.*, Fiz. Tverd. Tela (Leningrad) **23**, 1775 (1981) [Sov. Phys. Solid State **23**, 1032 (1981)].
5. Ch. Pavlyachik, A. Pavlovski, and B. Hilcher, Kristallografiya **24** (5), 1076 (1979) [Sov. Phys. Crystallogr. **24**, 616 (1979)].

6. A. Yu. Kudin, S. P. Yudin, and T. V. Panchenko, Fiz. Tverd. Tela (Leningrad) **19**, 1218 (1977) [Sov. Phys. Solid State **19**, 713 (1977)].
7. I. I. Naumova, N. F. Evlanova, and S. A. Blokhin, J. Cryst. Growth **187**, 102 (1998).
8. N. D. Gavrilova, T. A. Derbeneva, and M. F. Koldobskaya, Kristallografiya **26** (2), 413 (1981) [Sov. Phys. Crystallogr. **26**, 236 (1981)].
9. V. V. Mikhnevich, I. F. Kashevich, and D. N. Minakov, in *Advances in Science and Technology* (VIMI, 1991), Vol. 1, p. 43.
10. V. V. Mikhnevich and I. F. Kashevich, Fiz. Tverd. Tela (St. Petersburg) **34**, 24 (1992) [Sov. Phys. Solid State **34**, 12 (1992)].
11. M. V. Tsedrik, *Physical Properties of the Crystals of the Triglycine Sulfate Family* (Nauka i Tekhnika, Minsk, 1986).
12. Yu. É. Lorents, B. N. Rolov, and A. B. Panteleev, Izv. Akad. Nauk LSSR, No. 3, 56 (1988).
13. M. S. Tsedrik and G. A. Zaborowski, Krist. Tech. **11** (4), 373 (1976).
14. O. M. Serdyuk, L. N. Kamysheva, S. N. Drozhdin, *et al.*, Fiz. Tverd. Tela (Leningrad) **30**, 540 (1988) [Sov. Phys. Solid State **30**, 308 (1988)].

Translated by L. Man

Crystallography Reports, Vol. 49, No. 2, 2004, pp. 211–214. Translated from Kristallografiya, Vol. 49, No. 2, 2004, pp. 262–265.

PHYSICAL PROPERTIES OF CRYSTALS

High-Temperature Raman Spectroscopy and Phase Transformations in Phosphates and Vanadates $Ca_{3-3x}Nd_{2x}(AO_4)_2$ (A = P, V; $0 \le x \le 0.14$)[1]

S. A. Kovyazina, L. A. Perelyaeva, O. N. Leonidova, I. A. Leonidov, and A. L. Ivanovskiĭ

Institute of Solid-State Chemistry, Ural Division, Russian Academy of Sciences, ul. Pervomaĭskaya 91, Yekaterinburg, 620219 Russia

e-mail: florid@rambler.ru

Received January 31, 2003

Abstract—The phases of variable composition $Ca_{3-3x}Nd_{2x}(AO_4)_2$ (A = P, V; $0 \le x \le 0.14$) based on calcium orthophosphate or orthovanadate are studied by Raman spectroscopy. The influence of the composition and temperature on the structural features of these compounds is considered. The changes observed in the Raman spectra at high temperatures are associated with the reversible phase transition due to the redistribution of calcium over different positions and partial reorientation of the AO_4 tetrahedra. *© 2004 MAIK "Nauka/Interperiodica".*

INTRODUCTION

In [1–4], it has been shown that the phases of variable composition $Ca_{3-3x}R_{2x}(AO_4)_2$ (R is a rare-earth element; A = P, V) based on alkaline-earth orthophosphates or orthovanadates are solid electrolytes and have a whitlockite-like structure. In the whitlockite-like structure of $Ca_3(AO_4)_2$, one of the five nonequivalent calcium positions [Ca(4)] is initially only half occupied by Ca^{2+} cations [5]. Vacancies at the Ca(4) positions are responsible for large values of calcium conductivity and diffusion coefficients of calcium isotopes [4]. The replacement of calcium ions by neodymium ions according to the scheme $3Ca^{2+} = 2Nd^{3+} + \square$ results in the depopulation of the Ca(4) positions. At high temperatures, structural disordering of these compounds leads to phase transitions and increases ionic conduction significantly [4]. Upon the $\beta \longrightarrow \beta'$ phase transition in whitlockite-like phases, part of the calcium positions become equivalent and one half of the $A(1)O_4$ tetrahedra changes orientation [6]. Since vibrational spectroscopy is very sensitive to short-range order, the application of this method makes it possible to reveal local structural distortions arising upon introduction of impurities and to observe the nucleation of fragments of high-temperature phases in the course of structural transitions; moreover, this technique is an efficient tool for studying the structure of compounds containing a large amount of structural defects [3, 7–9].

In this paper, the effect of temperature on the structural disordering of the phases of variable composition $Ca_{3-3x}Nd_{2x}(AO_4)_2$ (A = P, V; $0 \le x \le 0.14$) based on calcium orthophosphate and orthovanadate is studied by Raman spectroscopy.

EXPERIMENTAL

The samples were grown by the solid-phase synthesis. Certified calcium and neodymium phosphates and vanadates $Ca_3(AO_4)_2$ and $NdAO_4$ (A = P or V) were used as starting materials. The synthesis was conducted at temperatures of 1070–1520 K. The intermediate products were homogenized. The phase composition of the products was checked using X-ray diffraction on a DRON-2 diffractometer (CuK_α radiation).

The Raman spectra were recorded in the temperature range 298–1273 K at a heating rate of 50 K/min on a Renishaw-1000 spectrometer (Ar^+ laser, λ = 514.5 nm) equipped with a TS high-temperature attachment and a TMS program device.

RESULTS AND DISCUSSION

The Raman spectra of the variable-composition phases at room temperature are similar to the spectra of the starting compounds (Tables 1, 2): the shifts of the Raman lines are insignificant. This suggests that the crystal structure is distorted only slightly and the symmetry of the VO_4 and PO_4 tetrahedra remains unchanged, which agrees with the IR spectral data for vanadates based on $Ca_3(VO_4)_2$ [4].

[1] This work was presented at the National Conference on Crystal Growth (NCCG-2002, Moscow).

Table 1. Frequencies of optically active modes (ν, cm^{-1}) in the Raman spectra of $Ca_{3-3x}Nd_{2x}(VO_4)_2$ crystals at room temperature

$Ca_{3-3x}Nd_{2x}(VO_4)_2$								Assignment
$x = 0$	$x = 0.02$	$x = 0.04$	$x = 0.06$	$x = 0.08$	$x = 0.1$	$x = 0.12$	$x = 0.14$	
928	937	937	937	937	936	936	920	$\nu_1(A_1)$
865	871	873	872	872	871	871	867	
850	858	858	859	859	857	858	857	
826	834	838	836	840	837	839	834	$\nu_3(F_2)$
799	801	801	799	801	797	801		
766	779	780	778	778	778	778	778	
		622	624	625	621	622	619	$\nu_3(F_2) + \delta_4(F_2)$
		571	563	566	563	563	558	
451	459	458	457	458	457	455	455	$\delta_4(F_2)$
419	419	418	417	419	417	417	417	
357	363	363	364	363	360	362	357	$\delta_2(E)$
343	348	345	346	347	346	346	342	

Table 2. Frequencies of optically active modes (ν, cm^{-1}) in the Raman spectra of $Ca_{3-3x}Nd_{2x}(PO_4)_2$ crystals at room temperature

$Ca_{3-3x}Nd_{2x}(PO_4)_2$							Assignment
$x = 0$	$x = 0.02$	$x = 0.04$	$x = 0.06$	$x = 0.08$	$x = 0.10$	$x = 0.12$	
1089	1089	1088	1089	1089	1091	1094	$\nu_3(\nu_{as})$
1016	1016	1018	1015	1015	1011	1005	
969	969	970	969	969	969	969	$\nu_1(\nu_s)$
948	948	947	946	946	945	941	
		900	901	898	895	896	
		854	852	854	854	856	
		760	754	754	754	746	
630	629	632	630	629	632	634	$\nu_4(\delta_{as})$
613	611	611	611	611	613	611	
548	546	546	545	545	545	548	
		515	515	515	514	514	
476	476	476	476				$\nu_2(\delta_s)$
441	441	441	442	441	441	441	
405	405	405	403	405	403	403	
		342	342	344	344	344	Other lattice vibrations
280	280	278	277	275	275	280	
170	170	172	171	170	170	170	

The Raman lines of calcium vanadate are observed in two ranges of wave numbers, which correspond to the V–O stretching modes (950–750 cm^{-1}) and a combination of the V–O–V bending modes with the translational and rotational modes of the VO_4 groups and displacements of calcium cations (450–50 cm^{-1}) [8]. As the composition of the $Ca_{3-3x}Nd_{2x}(VO_4)_2$ vanadates changes, the number and position of the Raman lines remains virtually unchanged. A decrease in the amount of Ca^{2+} ions at the Ca(4) position results in a significant

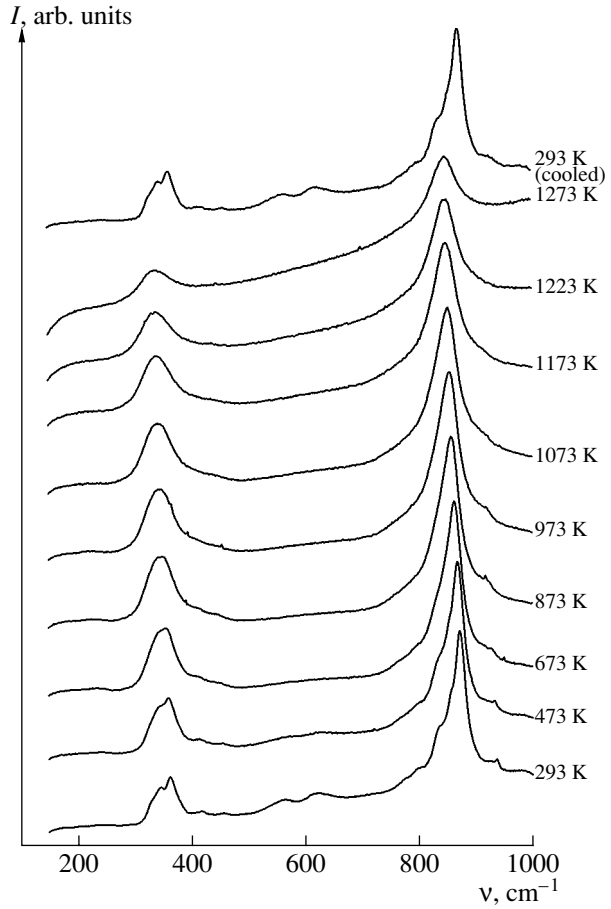

Fig. 1. Raman spectra of the $Ca_{2.64}Nd_{0.24}(VO_4)_2$ crystal in the temperature range 293–1273 K.

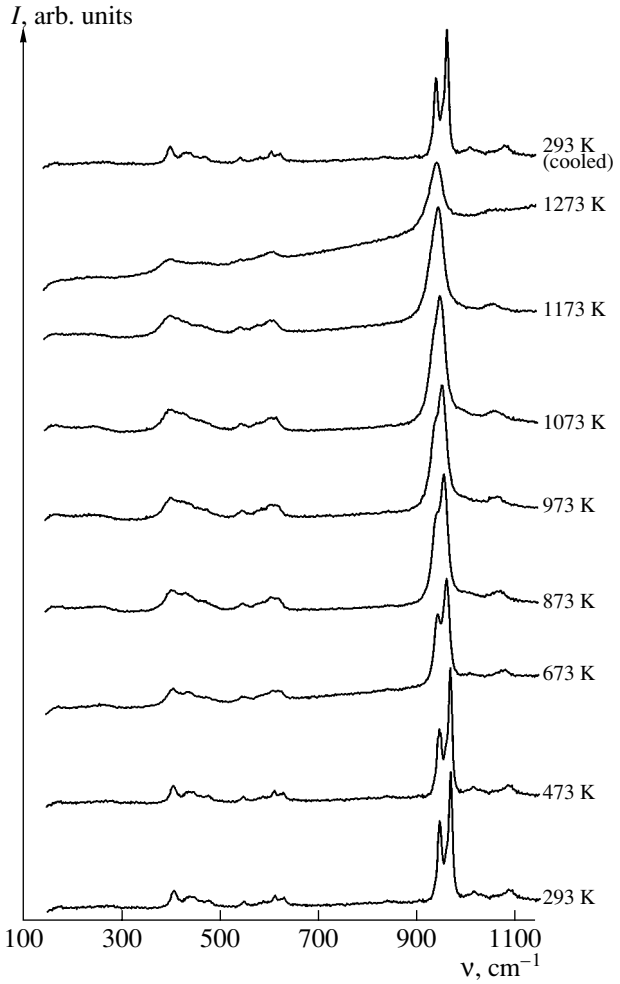

Fig. 2. Raman spectra of the $Ca_3(PO_4)_2$ crystal in the temperature range 293–1273 K.

decrease in the intensity of the line at 858 cm^{-1} due to a weakening of the V^{5+}–O–$Ca(4)^{2+}$ interaction.

The Raman lines of β-$Ca_3(PO_4)_2$ are located in five distinctly separate ranges, which correspond to the internal modes [1005–1094 cm^{-1} (ν_3), 940–970 cm^{-1} (ν_1), 545–634 cm^{-1} (ν_4), and 403–476 cm^{-1} (ν_2)] and lattice vibrations of the PO_4 polyhedra (170–345 cm^{-1}) [9]. In the $Ca_{3-3x}Nd_{2x}(PO_4)_2$ phosphates, the replacement of calcium by neodymium results in the formation of vacancies at the Ca(4) position, which decreases the intensity of the line at 948 cm^{-1}. The appearance of new lines in the range 850–900 cm^{-1} is due to the formation of longer P–O bonds of the P^{5+}–O^{2-}…Nd^{3+} type.

The structural disordering of $Ca_{3-3x}Nd_{2x}(VO_4)_2$ and $Ca_{3-3x}Nd_{2x}(PO_4)_2$ crystals and the reorientation of the $V(1)O_4$ and $P(1)O_4$ tetrahedra at high temperatures are reflected in the Raman spectra (Figs. 1, 2). For comparison, we chose the $Ca_{2.64}Nd_{0.24}(VO_4)_2$ and $Ca_3(PO_4)_2$ crystals, which are characterized by close values and similar temperature dependences of the calcium conductivity. The expansion of the crystal lattice (increase in the interatomic distances) leads to a decrease in the vibration frequencies. The changes in the Raman spectra of the calcium orthovanadate and the variable-composition phases based on calcium orthovanadate are observed at lower temperatures in comparison with those in the phosphate phases: part of the lines disappear already at 773 K. We attributed the changes observed in the Raman spectra in the temperature range 873–1273 K to structural disordering and a reversible phase transition. The Raman spectra of the samples cooled to room temperature are similar to the initial spectra, and the wave numbers of the lines coincide with the initial values.

According to the data of thermal analysis and measurements of cation conductivity, the $Ca_{2.64}Nd_{0.24}(VO_4)_2$ and $Ca_3(PO_4)_2$ crystals transform into the high-temperature β' modifications at a temperature of ~1200 K. The temperature dependences of the electrical conductivity in the Arrhenius coordinates (Figs. 3, 4) exhibit a kink near this temperature. A sharp decrease in the electrical conductivity below 1200 K in

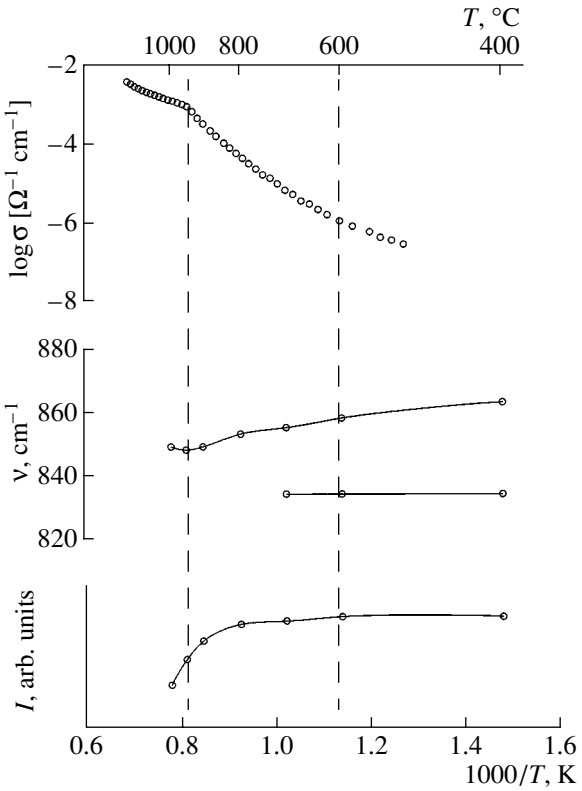

Fig. 3. Temperature dependences of the electrical conductivity σ, the wave number ν, and the intensity I of the ν_1 (A_{1g}) lines of the $Ca_{2.64}Nd_{0.24}(VO_4)_2$ vanadate.

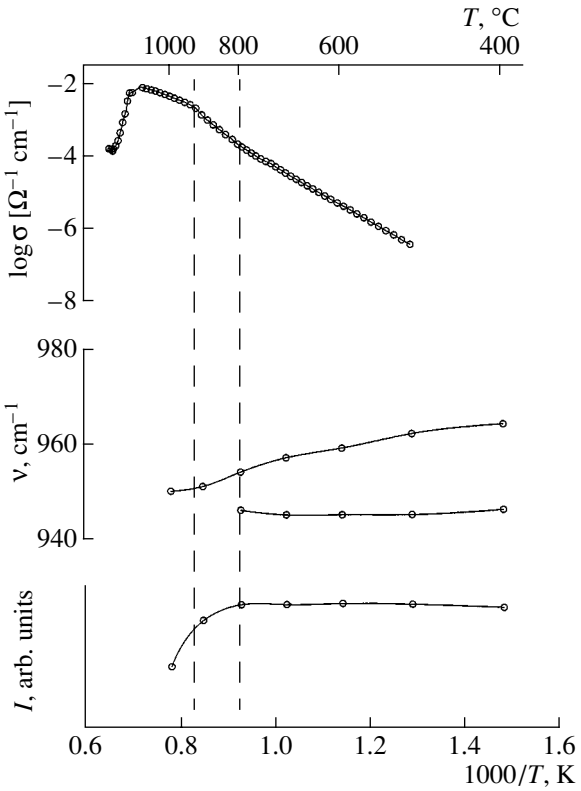

Fig. 4. Temperature dependences of the electrical conductivity σ, the wave number ν, and the intensity I of the ν_1 (A_{1g}) lines of the $Ca_3(PO_4)_2$ phosphate.

both samples indicates an ordering of cationic vacancies in the β phase of the whitlockite structure. A decrease in the electrical conductivity of the $Ca_3(PO_4)_2$ crystal at 1408 K is associated with the transformation of the β' phase into the high-temperature α modification. The $\nu_1(A_{1g})$ line is very sensitive to structural ordering. In disordered structures, its intensity decreases dramatically [7]. A decrease in the intensity of the $\nu_1(A_{1g})$ lines (Figs. 3, 4) above the temperature of the β ⟶ β' phase transition suggests that the β' phase is more structurally disordered than the β phase. The structural disordering of the whitlockite-like phases due to the reorientation of the $A(1)O_4$ tetrahedra and the redistribution of calcium over the $M(4)$ and $M(6)$ positions [6, 10] becomes noticeable at a temperature approximately 200–300 K below the phase transition point. An increase in the calcium conductivity by a factor of 100, the observed decrease in the number of lines in the Raman spectra, and the onset of the decrease in the intensity of the $\nu_1(A_{1g})$ lines can be attributed to the formation of the β' phase fragments, which are built into the structure of the low-temperature β modifications of whitlockite-like vanadates and phosphates. Probably, the structural transformation of the β phase of the whitlockite-like compounds studied nears completion slightly below the temperature of the β ⟶ β' transition, because the positions of the ν_1 (A_{1g}) lines before and after the phase transition differ insignificantly and the thermal effects of these phase transitions are very weak.

REFERENCES

1. I. A. Leonidov, M. Ya. Khodos, and A. A. Fotiev, Izv. Akad. Nauk SSSR, Neorg. Mater. **24** (1), 97 (1988).
2. I. A. Leonidov, M. Ya. Khodos, A. A. Fotiev, *et al.*, Izv. Akad. Nauk SSSR, Neorg. Mater. **24** (2), 347 (1988).
3. L. V. Kristallov, I. A. Leonidov, O. N. Leonidova, *et al.*, Zh. Neorg. Khim. **44** (10), 1699 (1999).
4. I. A. Leonidov, O. N. Leonidova, L. L. Surat, *et al.*, Zh. Neorg. Khim. **46** (2), 317 (2001).
5. R. Gopal and C. Calvo, Z. Kristallogr. **137**, 67 (1973).
6. A. A. Belik, F. Izumi, S. Yu. Stefanovich, *et al.*, Chem. Mater. **14**, 3197 (2002).
7. M. M. Sushchinskiĭ, *Raman Scattering and the Structure of Matter* (Nauka, Moscow, 1981).
8. A. Grzechnik, Chem. Mater. **10**, 1034 (1998).
9. P. N. de Aza, C. Santos, A. Pazo, *et al.*, Chem. Mater. **9**, 912 (1997).
10. B. I. Lazoryak, A. A. Belik, S. Yu. Stefanovich, *et al.*, Dokl. Akad. Nauk **384** (6), 780 (2002).

Translated by I. Polyakova

Crystallography Reports, Vol. 49, No. 2, 2004, pp. 215–216. Translated from Kristallografiya, Vol. 49, No. 2, 2004, pp. 266–267.

PHYSICAL PROPERTIES OF CRYSTALS

Optical and Electro-Optical Properties of ZnMgSe Single Crystals[1]

V. M. Puzikov, Yu. A. Zagoruiko, O. A. Fedorenko, and N. O. Kovalenko

Institute of Single Crystals, National Academy of Sciences of Ukraine, pr. Lenina 60, Kharkov, 61001 Ukraine

e-mail: zagoruiko@isc.kharkov.com

Received March 3, 2003

Abstract—The optical and electro-optical properties of large-sized (diameter, 20 mm; length, 70 mm) single crystals of $Zn_{1-x}Mg_xSe$ ($x \sim 0.5$) semiconductor solid solutions are investigated. The crystals are grown by the vertical Bridgman–Stockbarger method. It is found that, for ZnMgSe single crystals with a magnesium content up to 25 at. %, the modulus of the difference between the electro-optical coefficients $|r_{13} - r_{33}|$ at a wavelength of 0.63 μm is equal to $(1.1 \pm 0.22) \times 10^{-12}$ m/V, which is comparable in order of magnitude to the difference in the electro-optical coefficients for classical hexagonal $A^{II}B^{VI}$ compounds, such as CdS and CdSe. It is shown that single crystals of ZnMgSe solid solutions are promising materials for use in the fabrication of electro-optical modulators, λ/4- and λ/2-wavelength plates, and multifunctional optical elements operating in the range of high-intensity radiation of CO and CO_2 lasers. © *2004 MAIK "Nauka/Interperiodica".*

INTRODUCTION

In [1–3], crystals of $Zn_{1-x}Mg_xSe$ ($0.03 \le x \le 0.55$) substitutional solid solutions were synthesized, their structures were determined, the lattice parameters were measured, and the dependences of the mechanical, photoelectric, and dielectric properties on the Mg content were studied. Upon introduction of Mg into ZnSe, the crystals undergo structural transformations: first, the content of the hexagonal phase increases and, then, the crystal structure transforms into a hexagonal wurtzite structure. It has been established that, at $x > 0.14$, the $Zn_{1-x}Mg_xSe$ crystals have a hexagonal wurtzite structure.

At present, the optical properties of $Zn_{1-x}Mg_xSe$ crystals are partially understood only at a low Mg content ($0.03 \le x \le 0.18$). The $Zn_{1-x}Mg_xSe$ solid solution is transparent in the visible, near-IR, and middle-IR ranges and has a small absorption coefficient at a wavelength of 10.6 μm [1]. At $x > 0.14$, the solid solution is a uniaxial crystal, which renders this material promising for use in IR optics. Therefore, the study of the optical properties of $Zn_{1-x}Mg_xSe$ at a high Mg content ($x \sim 0.5$) is of current interest. In this work, we investigated the optical and electro-optical properties of $Zn_{1-x}Mg_xSe$ crystals and measured the refractive indices and moduli of the difference between the electro-optical coefficients.

[1] This work was presented at the National Conference on Crystal Growth (NCCG-2002, Moscow).

EXPERIMENTAL

The refractive indices were measured using a $Zn_{0.52}Mg_{0.48}Se$ sample prepared in the form of a trigonal prism with a refraction angle of 40°. The optic axis of the crystal was parallel to the short edge of the prism. Since the crystal is uniaxial, the incident radiation can separated into two components, namely, ordinary and extraordinary waves with the refractive indices n_o and n_e, respectively. It is known that the critical angle of incidence (the angle corresponding to the total internal reflection) is related to the refractive index as follows:

$$\theta_{crit} = \arcsin(1/n),$$

where θ_{crit} is the critical angle of incidence and n is the refractive index. By increasing the angle of incidence gradually and measuring its value at the instant of total internal reflection, we can calculate the refractive index from the formula

$$n = \sqrt{\frac{(\cos A \sin\alpha_{crit} + 1)^2}{\sin^2 A} + \sin^2\alpha_{crit}},$$

where n is the refractive index, A is the refraction angle of the prism, and α_{crit} is the critical angle of incidence of the radiation onto the prism.

The dispersion of the refractive indices n_o and n_e was measured in the visible range and at wavelengths of 1.064 and 10.6 μm. The modulus of the difference between the electro-optical coefficients $|r_{13} - r_{33}|$ was measured using a sample in the form of a prism. The base of the prism was an equilateral trapezoid, and the angle at the larger base was equal to 45°. The optic axis of the crystal was parallel to the short edge of the prism.

1063-7745/04/4902-0215$26.00 © 2004 MAIK "Nauka/Interperiodica"

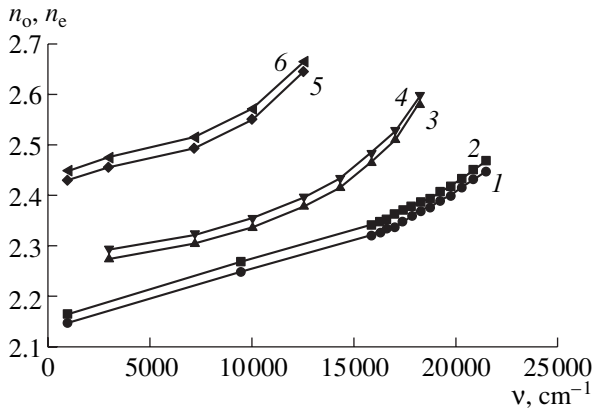

Frequency dependences of the (*1*, *3*, *5*) ordinary n_o and (*2*, *4*, *6*) extraordinary n_e refractive indices of (*1*, *2*) $Zn_{0.52}Mg_{0.48}Se$, (*3*, *4*) CdS, and (*5*, *6*) CdSe crystals.

It is known that, for wurtzite (symmetry class 6*mm*), the tensor of electro-optical coefficients has the following form:

$$\begin{bmatrix} 0 & 0 & r_{13} \\ 0 & 0 & r_{23} \\ 0 & 0 & r_{33} \\ 0 & r_{42} & 0 \\ r_{51} & 0 & 0 \\ 0 & 0 & 0 \end{bmatrix},$$

where $r_{13} = r_{23}$ and $r_{51} = r_{42}$ [4]. Hence, the expression for the optical indicatrix takes the form $(a_1 + r_{13}E_3)x^2 + (a_1 + r_{13}E_3)y^2 + (a_3 + r_{33}E_3)z^2 + 2r_{51}E_{2yz} + 2r_{51}E_{1xz} = 1$. The efficiency of electro-optical modulators based on the materials belonging to this class of symmetry is characterized by the quantity $|r_{13} - r_{33}|$. The modulus of the difference between the electro-optical coefficients $|r_{13} - r_{33}|$ was calculated according to the procedure used for CdS crystals in [5]. The external electric field was applied along the optic axis, and the radiation was directed perpendicular to this axis. In this case, the modulus of the difference $|r_{13} - r_{33}|$ satisfies the relationship

$$|r_{13} - r_{33}| \cong (n_o + n_e)\delta\varphi\lambda d/(n_o^2 n_e^2 \pi V l),$$

where V is the voltage applied to the crystal, λ is the wavelength of the radiation incident on the crystal, d is the distance between the electrodes, and $\delta\varphi$ is the additional phase difference acquired by the ordinary and extraordinary rays upon passing through the crystal of length l in response to an external electric field.

RESULTS

The frequency dependences of the ordinary and extraordinary refractive indices measured for the $Zn_{0.52}Mg_{0.48}Se$ crystal are shown in the figure. The dispersion curves for CdS and CdSe [6] are also shown in this figure for comparison. The results of the measurements demonstrate that the solid solution studied is a positive uniaxial crystal. The analysis of the curves depicted in the figure revealed that the ordinary n_o and extraordinary n_e refractive indices for $Zn_{0.52}Mg_{0.48}Se$ are smaller than those for CdS and CdSe, whereas the value of Δn for $Zn_{0.52}Mg_{0.48}Se$ is larger than that for CdS but is comparable to the value for CdSe.

The modulus of the difference between the electro-optical coefficients $|r_{13} - r_{33}|$ for the $Zn_{0.63}Mg_{0.37}Se$ crystal was measured at a wavelength of 0.633 μm. The mean value of $|r_{13} - r_{33}|$ is 1.1 ± 0.22 pm/V, which is smaller than that for CdS (3.6 pm/V).

CONCLUSIONS

The optical and electro-optical properties of $Zn_{1-x}Mg_xSe$ solid solutions with $x \sim 0.5$ were studied. The ordinary and extraordinary refractive indices n_o and n_e were determined in the visible, near-IR (λ = 1.064 μm), and middle-IR (λ = 10.6 μm) ranges. The comparison with classical anisotropic II–VI semiconductors showed that the anisotropy of the optical properties (the difference between n_o and n_e) of $Zn_{1-x}Mg_xSe$ is stronger than that of CdS and is comparable in magnitude to the anisotropy of the optical properties of CdSe, whereas the refractive indices are smaller. The $Zn_{1-x}Mg_xSe$ single crystals exhibit considerable birefringence and transparency in the near- and middle-IR ranges. Therefore, these materials can be used in fabricating control elements for IR optics. The modulus of the difference between the electro-optical coefficients $|r_{13} - r_{33}|$ for the $Zn_{0.63}Mg_{0.37}Se$ single crystal is 1.1 ± 0.22 pm/V.

REFERENCES

1. M. P. Kulakov and A. V. Fadeev, Neorg. Mater. **22** (3), 392 (1986).
2. Yu. A. Zagoruiko, O. A. Fedorenko, N. O. Kovalenko, *et al.*, Proc. SPIE **3794**, 96 (1999).
3. Yu. A. Zagoruiko, O. A. Fedorenko, N. O. Kovalenko, *et al.*, Semicond. Phys. Quantum Optoelectron. **3** (2), 165 (2000).
4. M. P. Shaskol'skaya, *Crystallography: A Textbook for Higher Technical Educational Schools* (Vysshaya Shkola, Moscow, 1976).
5. D. J. Gainon, J. Opt. Soc. Am. **54** (2), 270 (1964).
6. *Booklet of the Cleveland Crystals Firm* (1999).

Translated by I. Polyakova

Crystallography Reports, Vol. 49, No. 2, 2004, pp. 217–219. Translated from Kristallografiya, Vol. 49, No. 2, 2004, pp. 268–270.

PHYSICAL PROPERTIES OF CRYSTALS

Determination of the Parameters of Vector OOE Phase Matching in $LiNbO_3$[1]

A. A. Blistanov, V. V. Geras'kin, Zh. A. Goreeva, and Yu. V. Klyukhina

Moscow Institute of Steel and Alloys, Leninskiĭ pr. 4, Moscow, 117936 Russia

e-mail: goreeva_j@mail.ru

Received March 3, 2003

Abstract—Regularities in changes in the dimension of the ring of the second-harmonic radiation upon the rotation of a $LiNbO_3$ sample have been studied experimentally and confirmed by calculations for the case of vector ooe phase matching. It is shown that the angle δ of the external cone of the second-harmonic radiation in the case of vector ooe phase matching can be determined from the change in the ring dimension upon the rotation of an arbitrarily oriented crystal, provided that second-harmonic radiation is observed. © *2004 MAIK "Nauka/Interperiodica".*

INTRODUCTION

Deviations of the blend composition from congruent, volatility of Li_2O during the growth of lithium niobate from melt [1], and a change in the Nb oxidation state [2] result in a change in composition (the degree of nonstoichiometry) along the crystal length. The deviation from stoichiometry significantly affects the physical properties of lithium niobate [1, 3]. Knowledge of the composition allows a more effective use of single crystals for the development of crystalline elements. For optical applications of lithium niobate crystals, the dependence of the refractive indices on stoichiometry is of primary importance. This dependence, in turn, determines the influence of stoichiometry on the phase-matching conditions for nonlinear optical interactions.

Various methods can be used to determine the ratio $\eta = [Li_2O]/[Nb_2O_5]$ [4–6]. However, these methods have a number of drawbacks, such as the necessity for heating, complexity of instrumentation, and insufficient accuracy. The simplest and method, which is relatively accurate, is determining η from the angle δ of the external cone of the second-harmonic (SH) radiation in the case of vector ooe phase matching [7]. In so doing, the SH parameter for determining the Li/Nb ratio is the angle of the external SH cone when the wave normal of the fundamental-frequency radiation is perpendicular to the optical axis of the crystal. Thus, there is a general problem of finding this parameter in the case of an arbitrary orientation of the optical axis and nonparallel working faces of a crystalline element under study.

[1] This work was presented at the National Conference on Crystal Growth (NCCG-2002, Moscow).

THEORETICAL ANALYSIS

Nonlinear interaction of electromagnetic radiation with an anisotropic crystal gives rise to various phenomena, including frequency doubling (the second harmonic generation (SHG)). The phase-matching condition ($\mathbf{k}_1 + \mathbf{k}_2 = \mathbf{k}_3$) (following from the conservation of the energy and momentum of interacting photons) provides a relationship between the wave vectors of the fundamental-frequency radiation, $\mathbf{k}_1$ and $\mathbf{k}_2$, and the wave vector of the double-frequency radiation, $\mathbf{k}_3$. The vector ooe phase matching (when two ordinary rays of fundamental frequency interact with each other and the double-frequency radiation is extraordinary) is described by the relation

$$\mathbf{k}_1^o(\omega) + \mathbf{k}_2^o(\omega) = \mathbf{k}_3^e(2\omega). \quad (1)$$

The vector ooe phase matching can be observed experimentally for only one incident ray with the fundamental frequency ω. In this case, the entrance face of the sample should partially scatter the incident laser radiation (the entrance face being dull or its polished surface coated with a thin layer of talc). In addition to the principal ray, which is parallel to the incident ray and has up to 20% of its intensity, a cone of scattered rays, with an intensity much lower than that of the incident ray, also propagates in the crystal. In this case, because a multitude of rays with different wave-vector directions propagate in the crystal, the ooe phase-matching condition holds true for many rays. Theoretically, a cone of rays of SH radiation should be observed. Since the SH radiation intensity is proportional to the product of the intensities of the interacting rays [8], the actually observed pattern is formed by only those rays that propagate along the generatrix of the cone. The reason for this is that the SH radiation that is generated due to the interaction of the unscattered prin-

1063-7745/04/4902-0217$26.00 © 2004 MAIK "Nauka/Interperiodica"

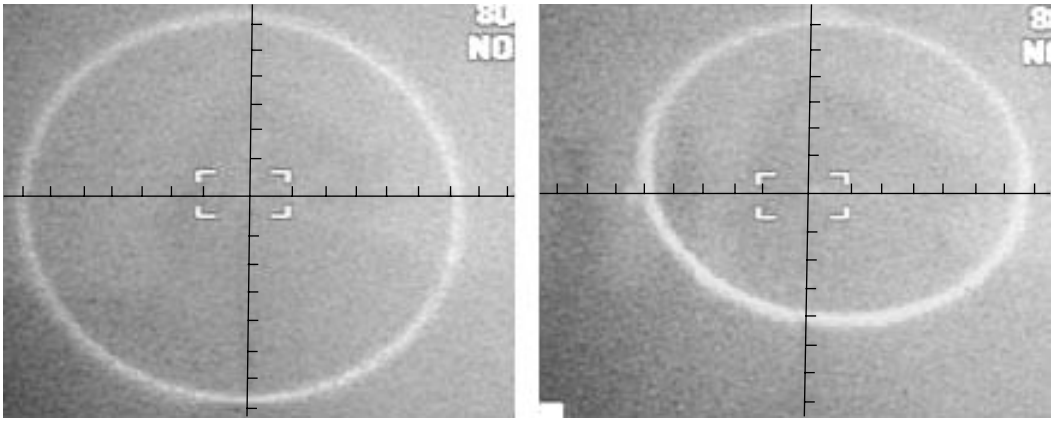

Fig. 1. Photographs of the rings of the SH radiation in a lithium niobate crystal.

cipal ray (with a high power density) with a scattered ray has the highest intensity.

EXPERIMENTAL

The dimensions of the SH radiation ring were measured using a setup based on an OSK-2 optical bench on which the elements of the optical system were mounted on riders. A lithium niobate sample was mounted on a rotary table that made it possible to rotate it about the vertical axis (the accuracy of measuring the rotation angle being 0.2°) and adjust it with respect to the incident radiation of frequency ω using an LGN-203 helium–neon laser. Radiation with a frequency of ω (an ILTI-237 yttrium–aluminum garnet laser with a wavelength of 1.079 μm, pulse width of 7 ns, pulse energy of 8 mJ, and beam diameter of 1 mm) enters an IKS-14 optical filter— with laser radiation with a wavelength of 1.079 μm passing through the filter, while the light of the pump lamp is absorbed—and falls on the sample. SH radiation with a frequency of 2ω and a wavelength of 0.54 μm passes through an SZS-22 optical filter (that cuts off light with a frequency of ω) and falls on a screen located at the distance L from the exit face of the sample. A ring of SH radiation and a bright spot are observed on the screen (Fig. 1). As the sample is rotated (the angle φ being varied), the ring dimensions change, and the bright spot shifts away from the ring center. Depending on the observation conditions, the ring of SH radiation may differ significantly from a circle. The maximum ring radius R is observed when the wave normal of the radiation of frequency ω is perpendicular to the optical axis C of the crystal. In this case, the bright spot is in the ring center.

Using the rulers on the screen, we determined the positions of the outermost (on the horizontal axis) points of the ring and the spot position. Then, we calculated the values of r_1 and r_2 (the distances from the bright spot to the ring edges), the ring radius $r = (r_1 + r_2)/2$, and the displacement of the bright spot from the ring center, $\Delta r = (r_1 - r_2)/2$. The dependence $\Delta r = f(\varphi)$ is linear; hence, one can plot the dependence $r = f(\Delta r)$ (Fig. 2), which can be approximated by a portion of an ellipse. This makes it possible to calculate the value of $R = r_{max}$ for each pair of experimental points and, with the known value of l, determine the angle δ:

$$\delta = \arctan(R/L). \tag{2}$$

Furthermore, it is possible to calculate the ratio η with the empirical formula obtained in [7] for the angle δ measured (or given) at $t = 21$°C:

$$\eta = 49.86 + 5.734 \times 10^{-3}\delta + 4.915 \times 10^{-4}\delta^2 + 8.671 \times 10^{-4}\delta^3 - 2.012 \times 10^{-5}\delta^4 \text{ mol \%}. \tag{3}$$

The experiment was performed with a single element, the geometry of which was changed as follows. First, the element had a rectangular shape and a ray was incident on its entrance face, the C axis being horizontal. Then, the entrance face was slanted at an angle of 5.7°. In the first stage, we evaluated the effect of the tilt of the C axis with respect to the horizon (with the working faces being parallel to the C axis). In the second

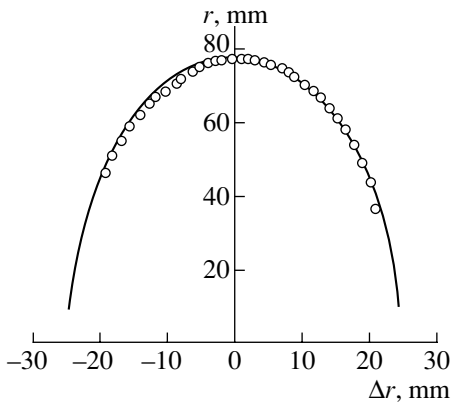

Fig. 2. Experimental (open circles) and calculated (solid curve) dependences of the radius r of the SH-radiation ring on the displacement Δr of the bright spot from the ring center (the optical axis of the crystal is horizontal).

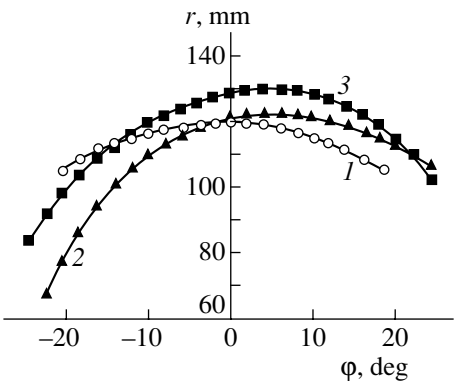

Fig. 3. Experimental dependences of the radius *r* of the SH-radiation ring on the rotation angle of the lithium niobate sample: (*1*) the optical axis of the crystal is horizontal, (*2*) a slant at an angle of 5.7° on the side of the incidence of the ray with frequency ω, and (*3*) a slant on the side of the screen.

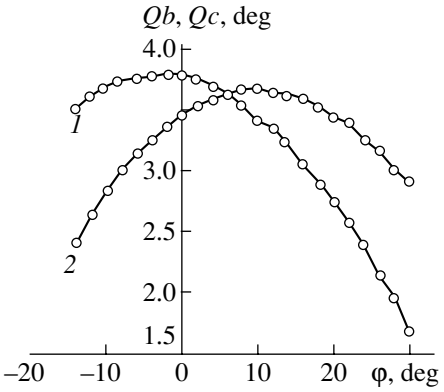

Fig. 4. Calculated dependences of the angles (*1*) *Qb* and (*2*) *Qc* on the angle of the rotation of the lithium niobate element, φ.

stage, we determined the effect of the slant on the working faces on the SH radiation parameters.

RESULTS AND DISCUSSION

It was found that the tilt of the *C* axis does not affect the dependences of *r* on Δ*r* and that the angle δ can be determined with formula (2). The slant on the working faces of the sample causes (i) the displacement of the SH radiation ring relative to the point of incidence of the radiation with the frequency of ω observed on the screen in the absence of the crystal and (ii) a change in the magnitude of the maximum. Figure 3 shows the results of measurements on the LN element slanted at an angle of 5.7°. The measurements were performed for two element positions: the slanted face was located (i) on the side of the incidence of the ray with frequency ω and (ii) on the side of the screen. The same situation occurs when the *C* axis is not parallel to the working faces of the element.

The analysis of the dependences $r = f(\Delta r)$ and $r = f(\varphi)$ measured (or calculated) for various wedge angles *g* showed that the angle δ cannot be determined from the maximum value of *r*. In order to find δ in these cases, we used the fact that the angles *Qb* and *Qc* between the SH rays and the ray of frequency ω are equal at the maximum value of *r*. From the dependences shown in Fig. 4, we determined the value of φ for *Qb* = *Qc*. Then, we calculated *Qb* and Q*c* for these values of φ and determined the angle of refraction *Fc* of the ray with frequency ω at the exit face of the sample, which equals the angle δ, using the formula

$$Fc = \delta = \arcsin[(\sin Qb)n_e(2\omega)]. \quad (4)$$

The calculated values of *R* (118.6 mm for the slant on the entrance face and 119.2 mm for the slant on the side of the screen) are in good agreement with the experimental value (118.1 mm, measured on the same sample before the slant was made, with the working faces being parallel and the *C* axis horizontal). The discrepancy in the calculated and experimental values of *R* is less than 1%, which supports the validity of the proposed calculation procedure.

CONCLUSIONS

Thus, the above calculation procedure can be used to determine the angle δ of the external cone of SH radiation in the case of vector ooe phase matching for samples with nonparallel working faces and an arbitrary optical-axis orientation (within the SH observation). The found value of δ can be used to determine the ratio η for $LiNbO_3$ crystals.

REFERENCES

1. Yu. S. Kuz'minov, *Lithium Niobate Crystals* (Cambridge Int. Sci., 1999), p. 126.
2. Yu. S. Kuz'minov and V. V. Osiko, Kristallografiya **39** (3), 530 (1994) [Crystallogr. Rep. **39**, 471 (1994)].
3. Yu. S. Kuz'minov, Kristallografiya **43** (5), 939 (1998) [Crystallogr. Rep. **43**, 884 (1998)].
4. P. Terner, C. Legras, and J. P. Dumas, J. Cryst. Growth **3–4** (1), 696 (1968).
5. Yu. S. Kuz'minov, Kristallografiya **40** (6), 1034 (1995) [Crystallogr. Rep. **40**, 959 (1995)].
6. M. D. Serrano, V. Bermúdez, L. Arizmendi, and E. Diéguez, J. Cryst. Growth **210**, 670 (2000).
7. A. A. Blistanov, V. V. Geras'kin, A. V. Dobriyan, and N. G. Sorokin, RF Patent No. 2061280 (1996).
8. V. G. Dmitriev and L. V. Tarasov, *Applied Nonlinear Optics. Second Harmonic Generators and Parametric Lasers* (Radio i Svyaz', Moscow, 1982).

Translated by A. Zolot'ko

Crystallography Reports, Vol. 49, No. 2, 2004, pp. 220–224. Translated from Kristallografiya, Vol. 49, No. 2, 2004, pp. 271–276.

SURFACE, THIN FILMS

Pyrolysis Kinetics of Silicon Hydrides on a Si(100) Surface[1]

A. V. Potapov

Institute of Physics of Microstructures, Russian Academy of Sciences, Nizhni Novgorod, Russia
e-mail: potapov@ipm.sci-nnov.ru; avpotapov@vvpaa.vvags.ru

Received February 26, 2003

Abstract—Specific features of the decomposition of silicon hydrides on a Si(100) surface have been considered. Simulation of thermodesorption hydrogen spectra revealed three possible ways of hydrogen desorption from the surface and the occurrence of only one bimolecular decomposition reaction of SiH_2 molecules. All the kinetic parameters were unambiguously determined from the comparison of the simulated and experimental spectra. The influence of the initial surface coverage on the thermodesorption spectra is also studied. © *2004 MAIK "Nauka/Interperiodica".*

INTRODUCTION

Hydride methods of epitaxy are widely used for manufacturing various devices for silicon microelectronics. The laws of growth of silicon and germanium layers and solid solutions on their basis from molecular flows of silicon and germanium hydrides have been studied in detail experimentally. However, a number of theoretical problems related to pyrolysis on the surface of a growing film are still open despite the fact that the properties of the deposited films and the potentials of the hydride technology are determined, to a large extent, by the elementary physical–chemical processes of hydride decomposition. There is still no one opinion on the ways of hydride decomposition on surfaces. There are no models that can describe hydride pyrolysis in detail and explain a number of experimental facts. The main problem here is associated with the possible occurrence of a large number of unknown reactions and the existence of a number of the corresponding kinetic constants. Below, we suggest an exhaustive model of the decomposition kinetics of SiH_4 and Si_2H_6 molecules on a Si(100) surface.

MODEL

The specific features of the technology of molecular-beam epitaxy from gas sources are such that the probability of molecule collisions in the reactor volume is negligible. In this case, the gas pressure determines the density of the molecular flux on the substrate surface, where various physicochemical processes determining the growth characteristics take place. In growth of Si films from the flow of mono- (SiH_4) or disilane (Si_2H_6) molecules, the surface contains SiH_n (n = 1, 2, 3) molecules and also Si and H atoms. We consider the averaged surface concentration of the particles of the ith type, θ_i. The latter is determined by the technological conditions (partial gas pressure, temperature of the substrate surface T) and the rates of occurring chemical reactions.

The initial stage of pyrolysis of mono- and disilane molecules on the Si(100) surface is studied quite well [1]. The collision of a molecule with the surface results in dissociative chemisorption occurring with the probability S. The process requires the existence of two dangling bonds

$$SiH_4 + \underline{2} \xrightarrow{S_{SiH_4}} \underline{Si}H_3 + \underline{H}, \quad (1)$$

$$Si_2H_6 \xrightarrow{S_{Si_2H_6}} 2\underline{Si}H_3. \quad (2)$$

Underlines indicate that the particle is bonded to a surface atom. The decomposition of $\underline{Si}H_3$ molecules is accompanied by a liberation of one hydrogen atom

$$\underline{Si}H_3 + \underline{1} \xrightarrow{\nu_{SiH_3}} \underline{Si}H_2 + \underline{H}. \quad (3)$$

The further stages of pyrolysis are studied in less detail. It is assumed [1] that the decomposition of $\underline{Si}H_2$ molecules can proceed via two competing reactions—mono- (4) and bimolecular (5) ones. The model suggested in [2] is based only on bimolecular reaction (5). In the present study, we take into account both reactions:

$$\underline{Si}H_2 + \underline{1} \xrightarrow{\nu^{(1)}_{SiH_2}} \underline{Si}H + \underline{H}, \quad (4)$$

$$2\underline{Si}H_2 \xrightarrow{\nu^{(2)}_{SiH_2}} \underline{Si_2}H_2 + H_2. \quad (5)$$

The decomposition of $\underline{Si_2}H_2$ molecules is accompanied by the formation of two surface $\underline{Si}$ atoms and a hydrogen molecule

$$\underline{Si_2}H_2 \xrightarrow{\nu_{Si_2H_2}} 2\underline{Si} + H_2, \quad (6)$$

whereas the $\underline{Si}H$ molecules interact with a dangling sur-

[1] This work was presented at the National Conference on Crystal Growth (NCCG-2002, Moscow).

face bond and liberate one hydrogen atom

$$\underline{\mathrm{Si}}\mathrm{H} + \underline{1} \xrightarrow{v_{\mathrm{SiH}}} \underline{\mathrm{Si}} + \underline{\mathrm{H}}. \quad (7)$$

Chemisorbed $\underline{\mathrm{H}}$ atoms formed in the course of reactions (1), (3), (4), and (7) are desorbed from the surface via the monomolecular reaction [1–3]

$$\underline{\mathrm{H}} \xrightarrow{v_{\mathrm{H}}} \frac{1}{2}\mathrm{H}_2. \quad (8)$$

The liberated Si adatoms are either incorporated into the epitaxial layer or desorbed:

$$\underline{\mathrm{Si}} \xrightarrow{r} \mathrm{Si(layer)}, \quad (9)$$

$$\underline{\mathrm{Si}} \xrightarrow{v_{\mathrm{Si}}} \mathrm{Si}. \quad (10)$$

This model takes into account three possible ways of hydrogen desorption from the film surface characterized by different "transmission capacity." Reactions (5) and (6) yield 25% of the total amount of desorbed hydrogen each, reaction (8) is responsible for the removal of the remaining 50% of adsorbed hydrogen. The proportion of the contributions made by reactions (5), (6), and (8) agrees with the experimentally obtained thermodesorption hydrogen spectra from the Si(100) surface subjected to the action of a monosilane flow [1].

Now, construct a mathematical model. In the case of monomolecular adsorption, the following equation is valid:

$$\theta_{\mathrm{SiH_3}} + \theta_{\mathrm{SiH_2}} + \theta_{\mathrm{SiH}} + \theta_{\mathrm{Si_2H_2}} + \theta_{\mathrm{H}} + \theta_{\mathrm{Si}} + \theta_V = 1, \quad (11)$$

where θ_V is the fraction of dangling surface bonds. A specific feature of monosilane chemisorption is that each $\underline{\mathrm{Si}}\mathrm{H_3}$ molecule blocks three surface bonds and, thus, hinders adsorption of $\mathrm{SiH_4}$ molecules [1, 4]. Thus, all the dangling bonds can be divided into blocked and unblocked ones:

$$\theta_V = \theta_{bl} + \theta_{nbl}, \quad (12)$$

$$\theta_{bl} = 3\theta_{\mathrm{SiH_3}}. \quad (13)$$

The estimation of the stationary rate of disilane pyrolysis on the Si(100) surface based on the data obtained in [5] shows that $\mathrm{Si_2H_6}$ molecules experience no blocking effect.

The continuation equations for the surface concentrations θ_i with due regard for the combinatorial multipliers have the form

$$\partial\theta_{\mathrm{SiH_3}}/\partial t = 2S_{\mathrm{SiH_4}}J_{\mathrm{SiH_4}}\theta_{nbl}^2 + 4S_{\mathrm{Si_2H_6}}J_{\mathrm{Si_2H_6}}\theta_V^2 - 2v_{\mathrm{SiH_3}}\theta_{\mathrm{SiH_3}}\theta_V, \quad (14)$$

$$\partial\theta_{\mathrm{SiH_2}}/\partial t = 2v_{\mathrm{SiH_3}}\theta_{\mathrm{SiH_3}}\theta_V - 2v^{(1)}_{\mathrm{SiH_2}}\theta_{\mathrm{SiH_2}}\theta_V - 4v^{(2)}_{\mathrm{SiH_2}}\theta^2_{\mathrm{SiH_2}}, \quad (15)$$

$$\partial\theta_{\mathrm{SiH}}/\partial t = 2v^{(1)}_{\mathrm{SiH_2}}\theta_{\mathrm{SiH_2}}\theta_V - 2v_{\mathrm{SiH}}\theta_{\mathrm{SiH}}\theta_V, \quad (16)$$

$$\partial\theta_{\mathrm{Si_2H_2}}/\partial t = 2v^{(2)}_{\mathrm{SiH_2}}\theta^2_{\mathrm{SiH_2}} - v_{\mathrm{Si_2H_2}}\theta_{\mathrm{Si_2H_2}}, \quad (17)$$

$$\partial\theta_{\mathrm{Si}}/\partial t = 2v_{\mathrm{Si_2H_2}}\theta_{\mathrm{Si_2H_2}} + 2v_{\mathrm{SiH}}\theta_{\mathrm{SiH}}\theta_V - r_{\mathrm{Si}}\theta_{\mathrm{Si}} - v_{\mathrm{Si}}\theta_{\mathrm{Si}}, \quad (18)$$

$$\partial\theta_{\mathrm{H}}/\partial t = 2S_{\mathrm{SiH_3}}J_{\mathrm{SiH_3}}\theta^2_{nbl} + 2v_{\mathrm{SiH_3}}\theta_{\mathrm{SiH_3}}\theta_V + 2v^{(1)}_{\mathrm{SiH_2}}\theta_{\mathrm{SiH_2}}\theta_V + 2v_{\mathrm{SiH}}\theta_{\mathrm{SiH}}\theta_V - v_{\mathrm{H}}\theta_{\mathrm{H}}. \quad (19)$$

Equations (11)–(19) form the complete system of equations for calculating all the surface concentrations θ_i.

The rate of layer growth is

$$V = r\theta_{\mathrm{Si}}N_S/N_0, \quad (20)$$

where N_S is the reticular density of the face and N_0 is the volume concentration of Si atoms. In the general case, the probability R of condensation of adatoms depends on their surface concentration. In this study, we used the semiempirical dependence described in [4].

The density of the flow of desorbed hydrogen adatoms is defined as

$$J_{\mathrm{H}} = 4v^{(2)}_{\mathrm{SiH_2}}\theta^2_{\mathrm{SiH_2}} + 2v_{\mathrm{Si_2H_2}}\theta_{\mathrm{Si_2H_2}} + v_{\mathrm{H}}\theta_{\mathrm{H}}. \quad (21)$$

The numerical coefficients in Eq. (21) also take into account the combinatorial multipliers and the number of hydrogen atoms evaporated in the course of an elementary reaction.

RESULTS AND DISCUSSION

To test the suggested model and determine its quantitative parameters, we considered the experimental thermodesorption hydrogen spectra obtained in [1]. These spectra have several peaks, which allowed us to relate the spectrum characteristics to the individual reactions and to reduce the ambiguity in the determination of the kinetic constants in elementary reactions (1)–(10). The experimental spectrum shown in Fig. 1 has two pronounced peaks at the temperatures 700 and 820 K. The peak areas are equal to one fourth and three fourths of the total spectrum area, respectively. It was established [1] that the first peak (at 700 K) is associated with the decomposition of $\underline{\mathrm{Si}}\mathrm{H_2}$ molecules by reaction (5). The second asymmetric peak (at 800 K) is associated with reactions (6) and (8) and is characterized by a steep leading edge and a flat trailing edge. This can be explained by the superposition of two peaks, one of which has a relatively small width and has a somewhat lower temperature, whereas the second has a large width and a somewhat higher temperature. The shape and size of a narrow peak allow one to attribute it to reaction (6). Then, the broader peak should be attributed to reaction (8).

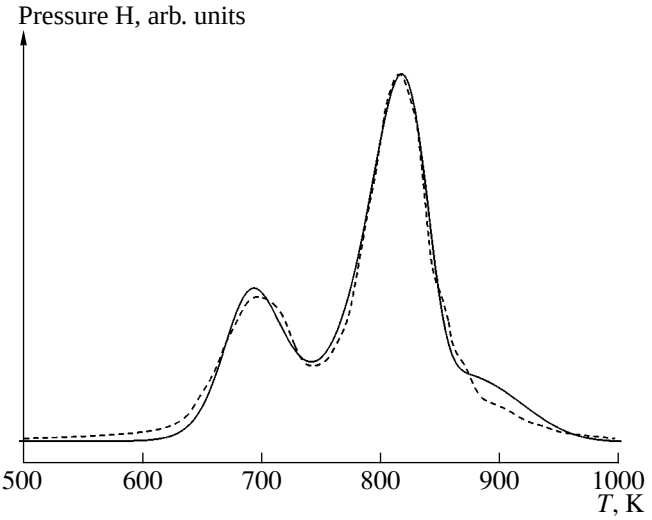

Fig. 1. Thermodesorption hydrogen spectrum obtained from the Si(100) surface under the action of a monosilane flow. Dashed curve indicates the experimental spectrum [1]; solid curve, the simulated one. Heating rate is 11 K/s.

The spectrum in Fig. 1 changes its shape with the change of the initial coverage: a decrease in the initial concentration of $\underline{Si}H_3$ molecules and $\underline{H}$ atoms results in a disproportional decrease in the peak at 700 K with respect to the peak at 820 K [1]. This may be explained by the competition between reactions (4) and (5) [1] or by lateral interactions between the particles at the surface, which can considerably influence the pyrolysis kinetics and the form of the thermodesorption spectrum [6]. Making allowance for all possible interactions in the multicomponent system studied is a rather complex problem. In the simplified variant, we took into account the lateral interactions only between the $\underline{Si}H_2$ molecules in the quasi-chemical approximation [6], which resulted in the appearance of an additional parameter E_{lat} (the energy of lateral interactions between molecules).

To simulate the thermodesorption spectrum, we integrated the system of equations (14)–(19) with due regard for Eqs. (11)–(13) under the initial conditions

$$\theta_{SiH_3} = \theta_H = 1/5, \quad \theta_V = 3/5. \qquad (22)$$

The initial surface temperature was 150 K and the constant heating rate was 11 K/s. The intensity of hydrogen desorption was calculated by Eq. (21). The criterion of the optimum model parameter was the minimum sum of the squared differences between the experimental and calculated spectra. The quantities to be optimized are indicated in the table. A large number of parameters (altogether 11), the existence of several extrema, and an ambiguous relief of the goal function dictated the refusal to use the traditional local–gradient methods of optimization. To solve the problem, we designed special software based on the classical genetic algorithm with selection of priorities. This method allowed us to use the uniform 12-digit discretization of the 11-dimensional space of parameters and determine the optimum solution with respect to each coordinate within the admissible time (from 1 to 10 h, 900 MHz Athlon processor).

The results of the performed optimization are indicated in Fig. 1 and in the table. Thermodesorption spectra (Fig. 1) demonstrate the qualitative and rather close quantitative correlations between the simulated and experimental data and confirm our assumption on three possible ways of hydrogen desorption from the film surface (Fig. 2). The allowance make for the contribution of the reaction described by Eq. (6) to the total spectrum resulted in a good agreement between the calculated and experimental spectra. The neglect of the process described by Eq. (6) would have resulted in the appearance of a narrower and higher peak at about 820 K, which would not allow us to model its asymmetric shape with an extended trailing edge.

The assumption about two competing reactions of $\underline{Si}H_2$ decomposition, (4) and (5), was not confirmed. All the numerical experiments yielded a zero rate of reaction (4). The attempts to increase this rate resulted in almost complete disappearance of the first peak and an increase in the second peak irrespective of the initial surface coverage. Thus, one can state that $\underline{Si}H_2$ mole-

Model parameters

E_{lat}, eV	0	3.16×10^{-2}
ν_{SiH_3}, s^{-1}	$7.00\exp(-0.08/k_BT)$	$7.00\exp(-0.08/k_BT)$
$\nu^{(1)}_{SiH_2}$, s^{-1}	0	0
$\nu^{(2)}_{SiH_2}$, s^{-1}	$5.35 \times 10^{16}\exp(-2.33/k_BT)$	$3.24 \times 10^{19}\exp(-2.69/k_BT)$
$\nu_{Si_2H_2}$, s^{-1}	$1.66 \times 10^{5}\exp(-1.02/k_BT)$	$1.66 \times 10^{5}\exp(-1.02/k_BT)$
$\nu_{SiH} = \nu_H$, s^{-1}	$8.22 \times 10^{13}\exp(-2.31/k_BT)$	$8.22 \times 10^{13}\exp(-2.31/k_BT)$

Note: Activation energies are indicated in eV.

cules can decompose only according to bimolecular reaction (5). The question about disproportional change of the spectrum with an increase in the initial coverage [1] is still open. Possibly, this phenomenon can be explained by the repulsion of $\underline{Si}H_2$ molecules, which decreases the probability of interaction between two molecules, broadens the thermodesorption peak, and shifts it to higher temperatures. The data on the simulation with allowance for lateral interactions are indicated in the table and in Fig. 3. The weak repulsion (with energy of about 0.03 eV) really changes the spectrum along the indicated direction. However, we failed to considerably suppress the first peak (at 700 K). All the attempts to increase the repulsion energy enhanced the suppression effect, but, at the same time, worsened the correspondence between the simulated and experimental spectra at the maximum surface coverage (22). At high and low surface coverages, the spectra can be successfully simulated only by varying the interaction energies (with an increase of coverage, one has to increase the parameter E_{lat}).

The calculated model parameters are consistent with the known experimental data. The unusually low activation energy of the decomposition of Si_2H_2 molecules (1.02 eV) is explained by the necessity to simulate the broad extended trailing edge of the spectrum. The lack of information on the decomposition of Si_2H_2 molecules does not allow one to draw a final conclusion about the reliability of the result obtained. The introduction of lateral interactions into the model does not change the optimum values of the parameters except for the activation energy and the preexponential multiplier characterizing the rate of reaction (5). An increase in the activation energy is explained by the necessity to compensate the broadening of the first peak (at 700 K) caused by particle repulsion. The reviewed experimental studies on film growth from monosilane show a considerable scatter in activation energies (2.00–2.80 eV) for the temperature dependence of the growth rate of the films at low temperatures. The value 2.69 eV is close to the upper limit of the above range.

Within the framework of the model considered, the scatter in the experimental data can phenomenologically be explained by the dependence of the energy of lateral interactions on the surface concentration of $\underline{Si}H_2$ molecules. An increase in the surface coverage should reduce the repulsion between $\underline{Si}H_2$ molecules by a value equal to the rate of the bimolecular reaction, which, in turn, should reduce the activation energy of molecule decomposition in order to preserve the width of the peak at 700 K. To verify this assumption experimentally, one has to perform a series of growth experiments from the flow of SiH_4 molecules under high and low gas pressures (at low and high surface coverages, respectively). Comparing the slopes of the Arrhenius dependences of growth rate on substrate temperature, it is possible either to prove or disprove the above assumption.

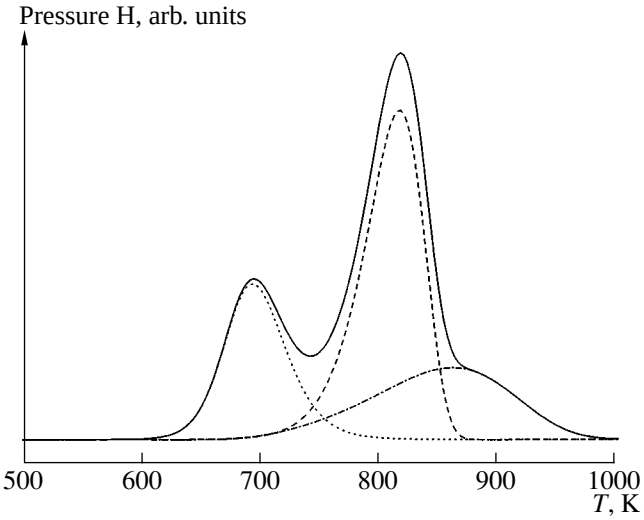

Fig. 2. Total thermodesorption spectrum (solid curve). Partial spectra indicated by dashed curves correspond to reactions (5) (peak at 696 K), (8) (peak at 817 K), and (6) (peak at 851 K). Heating rate is 11 K/s.

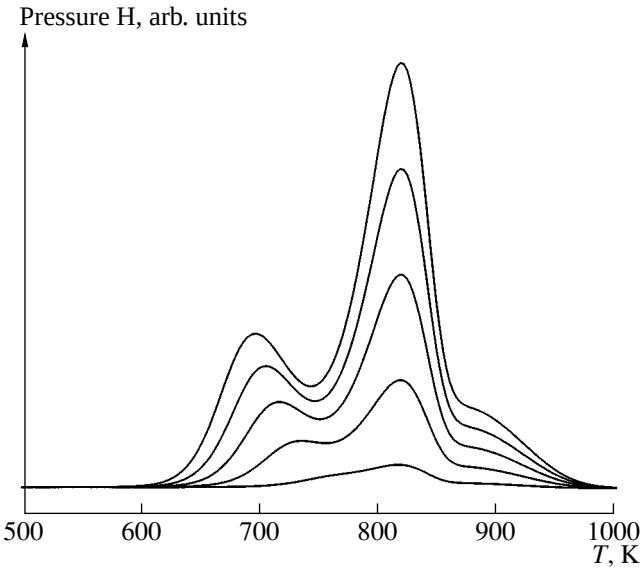

Fig. 3. Thermodesorption hydrogen spectrum from the Si(100) surface under the action of a monosilane flow. The initial coverage, $\theta_{SiH_3} = \theta_H = 0.20$, 0.15, 0.10, 0.05, and 0.01. Heating rate is 11 K/s.

The action of disilane molecules on the Si(100) surface differs from the action of monosilane molecules. Chemisorption of Si_2H_6 molecules results in the formation of two surface $\underline{Si}H_3$ molecules [see Eq. (2)]; therefore, at the initial moment, the surface contains no atomic hydrogen. Surface bonds are not blocked and, therefore, no limitation on the maximum surface concentration of $\underline{Si}H_3$ molecules is imposed, so that its value can exceed 0.2. The corresponding thermodesorption spectra are shown in Fig. 4. The equal contribu-

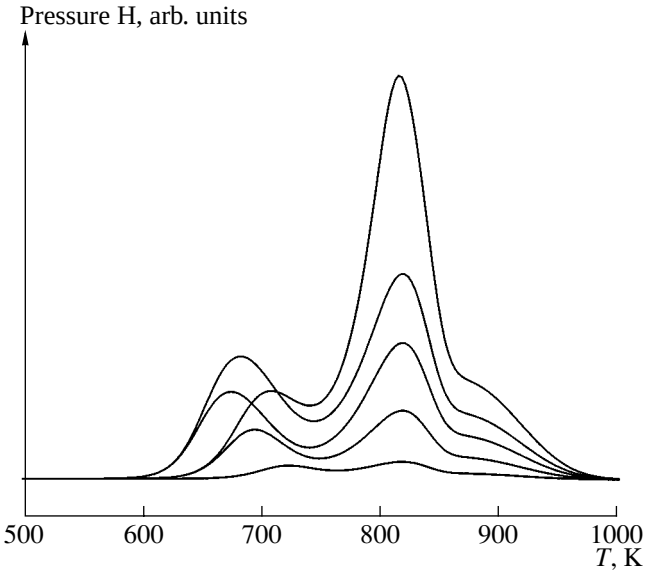

Fig. 4. Thermodesorption hydrogen spectra from the Si(100) surface under the action of a disilane flow. The initial coverage θ_{SiH_3} = 0.8, 0.6, 0.4, 0.2, and 0.05. Heating rate is 11 K/s.

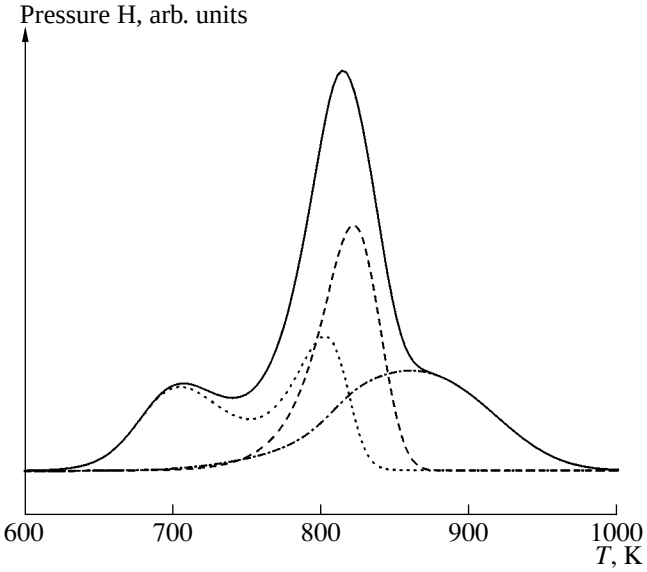

Fig. 5. Thermodesorption hydrogen spectrum from the Si(100) surface under the action of a disilane flow. The initial coverage θ_{SiH_3} = 0.8, θ_H = 0. Heating rate is 11 K/s. Partial spectra (dashed curves) correspond to reactions (5) (peaks at 704 and 803 K), (8) (peak at 823 K), and (6) (peak at 863 K).

tions that come from reactions (5), (6), and (8) to hydrogen desorption would result in considerable changes of the spectrum, which are well seen at the low initial coverages of the surface. An increase in the initial hydride concentration, first, shifts the peak due to reaction (5) toward lower temperatures because of the repulsion between $\underline{Si}H_2$ molecules. A further increase in the initial coverage results in a new effect—the peak caused by reaction (5) shifts back to higher temperatures. This phenomenon is explained by the fact that atomic hydrogen formed during reaction (3) fills practically the whole surface, which considerably hinders the pyrolysis. With an increase in the temperature, atomic hydrogen is desorbed more intensely, and the pyrolysis rate increases. Figure 5 shows the partial spectra at high initial concentrations. The spectrum caused by reaction (5) is split because of pyrolysis self-deceleration. This splitting results in a disproportional increase of the peak at 820 K on the general spectrum.

CONCLUSIONS

The detailed simulation of nonstationary pyrolysis kinetics of silicon hydrides on a Si(100) surface confirmed the adequacy of the scheme of hydride decomposition suggested above and allowed us to unambiguously determine all the kinetic parameters of the model (table) and establish the following:

—decomposition of surface $\underline{Si}H_2$ hydrides can proceed only by bimolecular reaction (5);

—surface hydrogen is desorbed according to three reactions—(5), (6), and (8);

—disproportional change of the thermodesorption hydrogen spectrum with a decrease in the initial coverage can be caused by lateral repulsion between $\underline{Si}H_2$ molecules;

—at high initial concentrations of $\underline{Si}H_3$ molecules, self-deceleration of surface pyrolysis is observed.

A further development of the theory of physical–chemical processes on the surface of silicon layers deposited from molecular flows of silicon hydrides should be directed to the study of molecular interactions and their effect on the growth rate of the films and their structure. It is also necessary to do some additional precision experiments in order to verify a number of theoretical assumptions.

REFERENCES

1. S. M. Gates, C. M. Greenlief, and D. B. Beach, J. Chem. Phys. **93**, 7493 (1990).
2. D.-S. Lin, T. Miller, and T.-C. Chiang, Phys. Rev. B **47**, 6543 (1993).
3. L. B. Lewis, J. Segall, and K. C. Janda, J. Chem. Phys. **102**, 7222 (1995).
4. A. V. Potapov, L. K. Orlov, and S. V. Ivin, Thin Solid Films **336**, 191 (1999).
5. T. R. Bramblett, Q. Lu, T. Karasawa, *et al.*, J. Appl. Phys. **76**, 1884 (1994).
6. V. P. Zhdanov, *Elementary Physical-Chemical Processes on Surface* (Nauka, Novosibirsk, 1988).

Translated by L. Man

Crystallography Reports, Vol. 49, No. 2, 2004, pp. 225–232. Translated from Kristallografiya, Vol. 49, No. 2, 2004, pp. 277–285.

SURFACE, THIN FILMS

The Effect of the Translational Symmetry of Crystalline Silicon on the Structure of Amorphous Germanium in the Interfacial Region[1]

N. I. Borgardt*, B. Plikat, M. Seibt**, and W. Schröter****

** Moscow Institute of Electronic Engineering, Moscow, 124498 Russia*

e-mail: lemi@lemi.miee.ru

*** IV Physikalishes Institut der Universität Göttingen und Sonderforschungsbereich 602, Tammannstr. 1, D-37077 Göttingen, Germany*

Received April 29, 2003

Abstract—The structure of an amorphous Ge layer near an interface with a Si(111) crystal was studied by quantitative high-resolution electron microscopy. It was found that the translational symmetry of a Si crystal leads to the crystal-like order in the positions of Ge atoms in the interfacial region, the width of which is about 1.4 nm. In this region, the average orientation of interatomic bonds tilted with respect to the interface compensates for the difference in the bond lengths in crystalline Si and amorphous Ge and is responsible for the tetragonal distortion of the most likely atomic positions. © *2004 MAIK "Nauka/Interperiodica".*

INTRODUCTION

The regularities in the atomic structure of amorphous materials near their interfaces with crystals are of both fundamental and practical interest. The reason is that interfaces play an important role in various physical processes, such as crystallization of amorphous materials, amorphization of crystals upon ion implantation [1], and low-temperature molecular-beam epitaxy [2]. For fundamental investigations, the question of the transformation of the long-range order of a crystal into the short-range order of an amorphous material is of much importance. Applied research is aimed at obtaining amorphous layers with specified properties. In particular, this problem is urgent for modern semiconductor technology [3], in which the interface between crystalline Si and amorphous SiO_2 plays a fundamental role.

The atomic structure of interfaces between different materials can be studied by high-resolution electron microscopy on the basis of quantitative comparison of experimental and simulated micrographs. The efficiency of this method for analysis of the structure of interfaces between crystalline materials was demonstrated in [4–8]. However, this approach cannot be used to study amorphous materials, since the exact positions of the atoms are unknown in this case and the structural properties of amorphous materials are characterized by a radial distribution function having spherical symmetry. In the interfacial region of an amorphous layer, this function is invalid, due to the violation of spherical symmetry in the atomic distribution. The reason for this violation is that the atoms occupying the lattice sites have an orientational effect on possible atomic positions in the amorphous material.

A new approach was developed in [9–11] on the basis of averaging high-resolution images of interfaces between a crystal and an amorphous layer, which makes it possible to find the two-dimensional distribution function for atoms in the interfacial region of the amorphous layer. This function is the projection of the three-dimensional atomic density onto the propagation direction of an electron beam.

We used the aforementioned approach to investigate the atomic structure of amorphous Ge near its interface with crystalline Si and determine the effect of the crystalline material on the atomic positions in the amorphous interfacial region.

METHOD OF INVESTIGATION

High-Resolution Images and Their Averaging

The effect of the translational symmetry of a crystal on the atomic structure of an amorphous layer can be analyzed most simply and unambiguously in the case of an atomically planar interface between two materials. In order to form such an interface, we used a single-crystal Si(111) wafer with a misorientation lower than 0.1° along the $[11\bar{2}]$ direction. According to the experimental procedure described in [12, 13], after the removal of a thermal oxide layer about 100 nm thick, the Si surface was chemically polished by etching in a 40% solution of NH_4F and then rinsed in deionized water. As was shown in [13] by atomic-force microscopy, such a treatment leads to the formation of a hydrophobic surface with atomically smooth nonrecon-

[1] This work was presented at the National Conference on Crystal Growth (NCCG-2002, Moscow).

1063-7745/04/4902-0225$26.00 © 2004 MAIK "Nauka/Interperiodica"

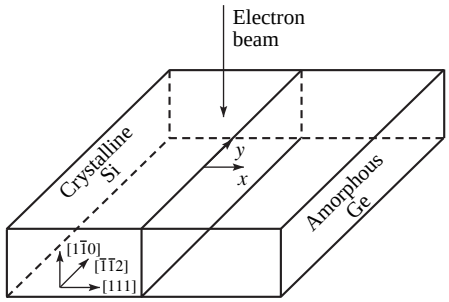

Fig. 1. Orientation of a sample with respect to the electron beam.

structed terraces more than 180 nm wide. Germanium evaporated from a crucible heated by an electron beam was deposited on this prepared substrate at room temperature. The growth rate of the Ge layer was 30 nm/min.

Cross-sectional samples with surfaces oriented perpendicularly to the [1$\bar{1}$0] direction were prepared for electron-microscopy measurements by mechanical thinning and subsequent etching by Ar ions with an energy of 3 keV incident at an angle of 10°. The measurements were performed using a Philips CM200-UT-FEG electron microscope with an accelerating voltage of 200 keV. The microscope point resolution and information limit were 0.19 and 0.11 nm, respectively. The sample was oriented with respect to an electron beam as shown in Fig. 1. Images were formed using an objective diaphragm with an angular aperture of 27.5 mrad, including the (111) and (200) reflections of Si. A series of 20 high-resolution micrographs obtained at different values of objective-lens defocus (the defocus series) was recorded by a GATAN SSC-CCD (Model 694) system. Signal drift during measurement of the defocus series was corrected using a cross-correlation function, the value of which was calculated for each pair of neighboring micrographs for the amorphous region in the images.

In order to obtain information on the structure and composition of materials, experimental and simulated high-resolution electron-microscopic images should be compared with each other. Such a comparison is a conventional procedure in the investigation of crystalline samples. However, it cannot be directly used for the analysis of the structural properties of an amorphous layer adjacent to a crystal, as the positions of the atoms in the amorphous material are only known with a certain probability. Even if the probability of the atomic distribution is known, the experimental and simulated images cannot be directly compared, due to the fact that an amorphous layer with a certain short-range order can be realized by a multitude of specific atomic positions.

In studying the crystal–amorphous-layer interface, quantitative comparison of the experimental data with the simulation results can be performed after averaging the high-resolution images over the interface [10, 11]. Such a procedure makes it possible to obtain a regular intensity distribution originating from the average distribution of atomic potentials projected on the electron-beam direction. The averaging can be performed in two ways.

In the first method, the average two-dimensional intensity distribution is calculated. The initial image (Fig. 2a) is divided into N bands of width d perpendicular to the interface, which correspond to the period of the intensity distribution in the image of the crystalline region along the interface (the 0y axis). Calculation of the average intensity at the equivalent points of the bands makes it possible to obtain the intensity distribution $I'(x, y)$ in the averaged image:

$$I'(x, y) = \frac{s_d(y)}{N} \sum_{-(N-1)/2}^{(N-1)/2} I(x, y + nd), \qquad (1)$$

where $I(x, y)$ is the intensity in the initial high-resolution image and $s_d(y)$ is the instrumental function, which is equal to unity at $-d/2 \le y < d/2$ and to zero at other values of y. The result of this image averaging is shown in the lower part of Fig. 2a.

In the second method of averaging high-resolution images, the average profile of the intensity $\bar{I}(x)$ is determined in the interval $A = Nd$ along the 0y axis:

$$\bar{I}(x) = \frac{1}{A} \int_{-A/2}^{A/2} I(x, y). \qquad (2)$$

Using the intensity profiles is convenient in the visual comparison of simulation and experiment results.

On the basis of expressions (1) and (2), averaged images and intensity profiles were obtained for all 20 micrographs of the defocus series. The averaging range amounted to 15.6 nm and included $N = 47$ bands. In order to prove the equality of the periods of the intensity distributions in the crystalline and amorphous parts of the images, the Fourier transforms of the intensity profiles along the directions noted by arrows *1* and *2* in Fig. 2a were calculated. Comparison of these Fourier transforms showed that the intensity varies with the period d in the interfacial amorphous region in the micrographs.

Some averaged images and intensity profiles of the defocus series are shown in Figs. 2b and 3b. The defocuses and the sample thickness, which is 13.8 nm, were determined on the basis of the well-known procedure of iterative fitting of images [14]. The experimental and simulated intensity distributions for the crystalline regions in the images were quantitatively compared with each other for all the micrographs of the defocus series at different defocuses and sample thicknesses until the best set of parameters was found.

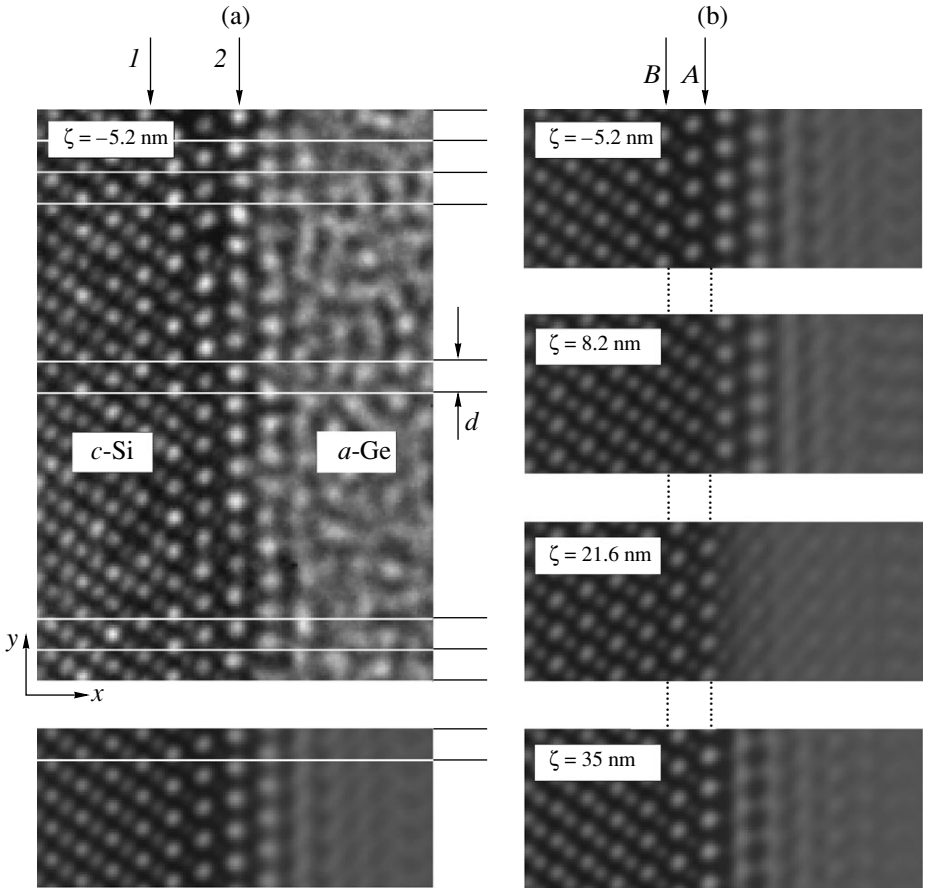

Fig. 2. (a) High-resolution micrograph of the interface between the crystal and the amorphous layer (with the averaging method shown) and (b) the averaged experimental images from the defocus series. An averaged image, repeated five times for better visualization, is shown in the lower part of (a). Arrows *1* and *2* in (a) show the directions along which the Fourier transform of the intensity distribution in the interface plane was calculated, and arrows *A* and *B* in (b) indicate the intuitive and calculated positions of the interface between the crystal and the amorphous layer.

Simulation of Averaged Images

High-resolution electron-microscopy images can be simulated by the so-called sheet method, which implies specification of the atomic positions in a sample, partition of the sample into thin layers perpendicular to the electron beam, and calculation of the projected atomic potentials for each layer. In this case, the passage of a fast electron through the sample can be considered to be successive scattering by a set of two-dimensional potentials. The sheet method is a well-developed procedure for calculating the intensity in the images of crystalline samples; hereinafter, we will refer to this method as the atomistic simulation.

The projected potential $\varphi_j(x, y)$ for the jth layer of the sample can be written as

$$\varphi_j(x, y) = \frac{1}{\Delta z}\sum_l \int_{z_{j-1}}^{z_j} V(\mathbf{r} - \mathbf{r}_{jl})dz, \qquad (3)$$

where $V(\mathbf{r})$ are the atomic potentials in the jth layer and $\mathbf{r}_{jl}$ are the atomic coordinates. If a sample contains atoms of different types, the potentials $V_l(\mathbf{r})$ are different.

In principle, the atomistic simulation can be used for modeling images of interfaces between crystals and amorphous materials. In this case, for correct comparison of calculatory and experimental results, the simulation should consider 10^4–10^5 atoms, a task which practically cannot be performed on the computers that are available, in particular, due to the complexity of the interatomic-interaction potentials that must be used in determining atomic positions in the amorphous layer.

As an alternative to the atomistic simulation, an approach was developed in [10, 11] that employs an approximation of averaged projected potential (an APP approximation) in a simulation using the sheet method. In this approach, the averaged potential $\varphi_j(x, y)$ is used for the amorphous region instead of the potential $\varphi_j(x, y)$. The potential $\varphi'_j(x, y)$ is calculated on the basis of the two-dimensional distribution function of atoms in the amorphous layer, $\rho(x, y)$. This function describes the average density of atoms within a band of width d

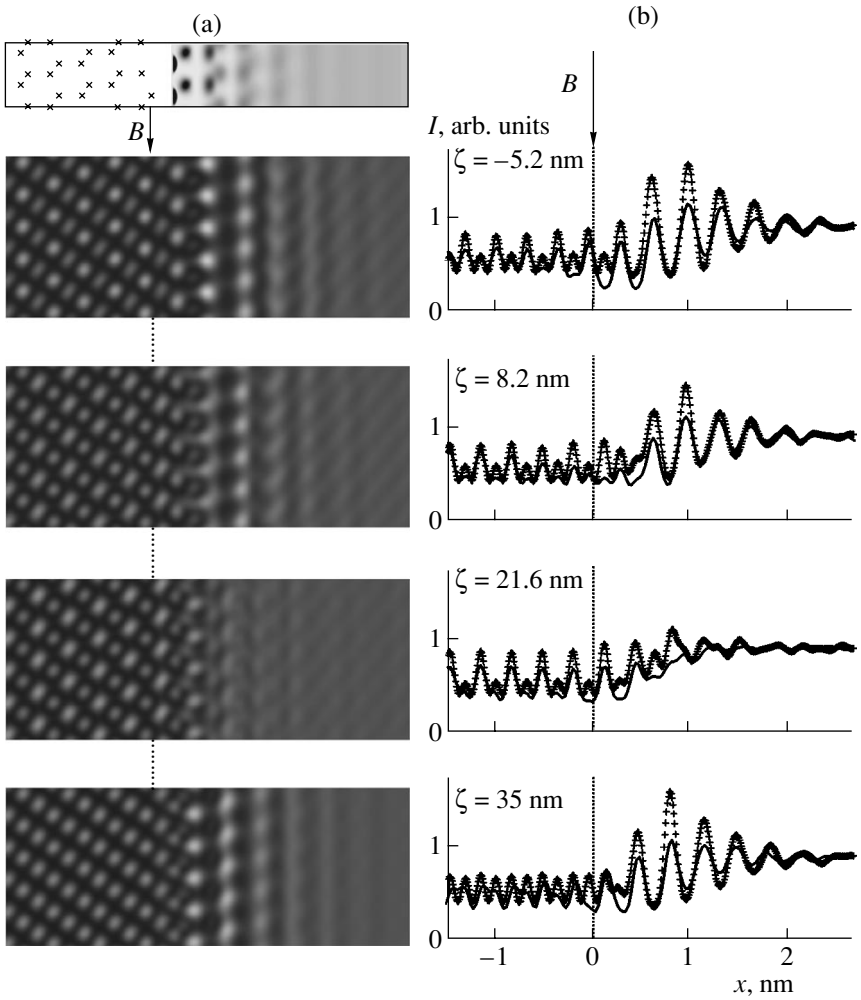

Fig. 3. (a) Averaged simulated images from the defocus series and (b) the intensity profiles corresponding to the experimental (solid line) and simulated (symbol (+)) images. The average two-dimensional distribution of atoms in a supercell, where the positions of atoms in the crystal are indicated by the symbol ×, is shown in the upper part of (b). Arrows *B* indicate the position of the interface between the crystal and the amorphous layer.

in the amorphous region. The quantity $\rho(x, y)dxdy$ determines the average number of atoms the positions of which are within the area $dxdy$ near the point (x, y). In this case, the potential $\varphi'_j(x, y)$ can be written as

$$\varphi'_j(x,y) = \frac{s_d(y)}{\Delta z}\sum_n \int_{z_{j-1}}^{z_j} \tilde{V}\left(p_x, \frac{n}{d}, 0\right)\rho\left(p_x, \frac{n}{d}\right) \times \exp\left[2\pi i\left(p_x x + \frac{n}{d}y\right)\right]dp_x, \quad (4)$$

where $\tilde{V}(p_x, p_y, 0)$ and $\tilde{\rho}(p_x, p_y)$ are the Fourier transforms of the atomic potential $V(\mathbf{r})$ and the two-dimensional distribution function $\rho(x, y)$, respectively.

To check the accuracy of the APP approximation, a simulation of high-resolution images of two test samples made of ordered and unordered materials was performed in [11]. The first sample was made of crystalline Si, and the second contained Si and Ge atoms randomly distributed according to the Gauss law in the vicinity of Si lattice sites. It was shown that, for typical values of the sample thickness, the APP approximation provides satisfactory calculation accuracy. In particular, this approximation makes it possible to correctly determine the positions of maxima and minima in the images.

Comparison of Experimental and Simulated Images

The atomic structure of an amorphous layer near its interface with a crystal can be revealed using an iterative fitting of images, this including the simulation of images and comparison of the calculational and experimental results. This approach has been well-appreciated and has been used to analyze the structure of inter-

faces between crystals and the atomic structure of defects [14].

As a measure of the difference between the intensity distributions in experimental and simulated micrographs, we chose the squared difference between the averaged experimental (I_{exp}) and simulated (I_{sim}) intensities, normalized by a weighting factor:

$$R(I_{exp}, I_{sim}) = \sum_{ij} \frac{[(I_{exp})_{ij} - (I_{sim})_{ij}]^2}{[(I_{exp})_{ij}]^2}, \quad (5)$$

where the subscripts i and j enumerate points in the images.

The introduced quantity $R(I_{exp}, I_{sim})$, which characterizes the difference between images, looks like the well-known R factor. The use of a weighting factor dependent of I_{exp} in calculating $R(I_{exp}, I_{sim})$ is justified, because noises are eliminated from the intensity in the experimental images after averaging of the initial high-resolution images. The use of the difference factor $R(I_{exp}, I_{sim})$ in the iterative fitting of images makes it possible not only to compare the positions of the maxima and minima of the intensity but also to take into account the character of the changes in the intensity in the transition region of the amorphous layer. In carrying out the fitting of images, the value of $R(I_{exp}, I_{sim})$ is minimized using the simplex method.

MODEL FOR CONSTRUCTING THE TWO-DIMENSIONAL DISTRIBUTION FUNCTION

To simulate averaged images, the average two-dimensional distribution of atoms in an amorphous layer near its interface with a crystal needs to be obtained. This distribution can be calculated directly by modeling the atomic structure in the interfacial region using the methods of random grids or molecular dynamics. Although the number of atoms involved in such modeling is much smaller than in the case of the atomistic simulation of high-resolution images, it is still very large for carrying out iterative fitting of images.

As a step preceding direct simulation of the interfacial-region structure, we will consider an approximate method of calculating the two-dimensional distribution function of atoms in an amorphous layer based on a simple model. This model takes into account the translational symmetry of the boundary atoms of the crystal and the orientation of the interatomic covalent bonds. The model suggests that the average spatial orientation of the bonds between Ge atoms is set by the sites of a lattice constructed in the amorphous region. The positions of these sites correspond to the tetragonally distorted Ge lattice, which is coherently matched with the Si crystal. The average spatial orientation of the interatomic bonds is not ideal, and the angle between the [111] direction and the average direction of the covalent bonds tilted with respect to the interface is about 65° instead of 70.5° (in the case of an ideal lattice). At this average orientation of the bonds in the interfacial region, the difference in their length in the crystalline Si and amorphous Ge is compensated.

After determining the average spatial orientation of the bonds, we will assume that the distribution of possible deviations of the interatomic bonds $\Delta\theta_i$ from these orientations obeys the Gauss law:

$$W_{\theta i}(\Delta\theta_i) = \frac{1}{\sqrt{2\pi}\sigma_{\theta i}} \exp\left[-\frac{1}{2}\frac{\Delta\theta_i^2}{\sigma_{\theta i}^2}\right], \quad (6)$$

where the subscript i enumerates the atomic Ge layers parallel to the interface and $\sigma_{\theta i}$ is the standard deviation for the ith layer.

Since the orienting effect of Si atoms on the positions of Ge atoms in the amorphous layer weakens with increasing distance from the interface, the deviation of possible directions of the bonds between Ge atoms from the average orientations increases as well. As a result, the standard deviation $\sigma_{\theta i}$ should increase from layer to layer with increasing i. We will restrict our consideration to a linear approximation for the dependence of the standard deviation on the layer number and represent $\sigma_{\theta i}$ in the form

$$\sigma_{\theta i} = \sigma_{\theta 1} + \alpha(i-1). \quad (7)$$

The quantity $\sigma_{\theta i}$ increases until the translational symmetry of the boundary Si atoms affects the positions of Ge atoms. The value of $\sigma_{\theta i}$ at $i = 1$ can be directly interpreted: it determines the standard deviation from the ideal orientation of the bonds between the boundary Si atoms and Ge atoms.

When determining the bond length between Ge atoms, we will assume that its possible values near the interface are the same as far from it. Then, taking into account [15], we can write $W_r(r)$ as

$$W_r(r) = \frac{1}{\sqrt{2\pi}\sigma_r} \exp\left[-\frac{1}{2}\frac{(r-r_0)^2}{\sigma_r^2}\right], \quad (8)$$

where $r_0 = 0.2463$ and $\sigma_r = 0.0074$ nm, which corresponds to their values for amorphous germanium [15]. For the layer of Ge atoms closest to the interface, the average bond length r_{01}, calculated as the average between r_0 and the bond length in crystalline Si, is equal to 0.2408 nm.

The introduced functions $W_r(r)$ and $W_{\theta i}(\Delta\theta_i)$ describe, respectively, the distribution of the lengths of interatomic bonds in the amorphous layer and their angular distribution with respect to the average directions set by the lattice constructed in the amorphous region. These functions can be used to find the average distribution of Ge atoms in the interfacial region. In this case, the possible positions of atoms in the ith layer are

calculated on the basis of the atomic distributions in the $(i-1)$th layer. Let us assume that an atom belonging to the $(i-1)$th layer is located at the point $\mathbf{r}_{j'}$, which coincides with some site of the lattice constructed in the amorphous region. Then, the function $f_{ij}(\mathbf{r})$, which describes the average distribution density for the atoms bound with the chosen atom, can be written as

$$f_{ij}(\mathbf{r}) = W_i'(\mathbf{r}, \mathbf{r}_{j'}), \quad (9)$$

where $W_i'(\mathbf{r}-\mathbf{r}')$ is the response function, which determines the distribution of atoms in the ith layer (with respect to the atomic positions) at the point $\mathbf{r}_{j'}$ in the $(i-1)$th layer. This function is calculated on the basis of the introduced functions W_{ri} and $W_{\theta i}$ as

$$W_i'(\mathbf{r}, \mathbf{r}') \equiv W_i'(\mathbf{r}-\mathbf{r}') = CW_r(|\mathbf{r}-\mathbf{r}'|)W_{\theta i}(\Delta\theta_i), \quad (10)$$

where $\Delta\theta_i$ is the angle between the vector $(\mathbf{r}-\mathbf{r}')$ and the corresponding average orientation of the bonds along the [111] direction and the constant C is determined from the normalization condition:

$$\int W_i'(\mathbf{r}-\mathbf{r}')d\mathbf{r} = 1. \quad (11)$$

Let us assume that the response function $W_i'(\mathbf{r}-\mathbf{r}')$ remains constant for all possible atomic positions in the vicinity of the point $\mathbf{r}_{j'}$. Then, the average distribution of the atomic density for the jth atom in the ith layer, bound with the j'th atom in the $(i-1)$th layer, is described by the expression

$$f_{ij}(\mathbf{r}) = \int f_{i-1j'}(\mathbf{r}')W_i'(\mathbf{r}-\mathbf{r}')d\mathbf{r}' = f_{i-1j'}(\mathbf{r}^*)W_i'(\mathbf{r}), \quad (12)$$

where $f_{i-1j'}(\mathbf{r})$ is the density of the average atomic distribution in the vicinity of the point $\mathbf{r}_{j'}$.

When an atom of the ith layer is bound with three atoms of the $(i-1)$th layer, the function $f_{ij}(\mathbf{r})$ is determined by the expression

$$\begin{aligned} f_{ij}(\mathbf{r}) &= \frac{1}{3}\sum_{j'=1}^{3}\int f_{i-1j'}(\mathbf{r}')W_{ij'j}''(\mathbf{r}-\mathbf{r}')d\mathbf{r}' \\ &= \frac{1}{3}\sum_{j'=1}^{3} f_{i-1j'}(\mathbf{r}^*)W_{ij'j}''(\mathbf{r}), \end{aligned} \quad (13)$$

where the functions $W_{ij'j}''(\mathbf{r})$ differ from the functions $W_i'(\mathbf{r})$ introduced above in that the subscripts j and j' are now used to enumerate three possible average spatial orientations of the bonds, with respect to which the deviations $\Delta\theta_i$ are measured.

The density of the average distribution of atoms in the interfacial region can be obtained by summing the functions $f_{ij}(\mathbf{r})$:

$$f(\mathbf{r}) = \sum_i\sum_j f_{ij}(\mathbf{r}). \quad (14)$$

Calculation of the average atomic distributions in the amorphous layer begins with the boundary atoms of the crystal. According to (12) and (13), the atomic positions in the first layer of Ge atoms, which is parallel to the interface, are determined by the functions $f_{ij}(\mathbf{r})$ at $i = 0$. These functions have the form

$$f_{0j}(\mathbf{r}) = \delta(\mathbf{r}-\mathbf{r}_{bj}), \quad (15)$$

where $\mathbf{r}_{bj}$ are the positions of the boundary Si atoms.

The above expressions can be used to calculate the average distribution of atoms in the amorphous layer in a cell with dimensions a, b, and c. The values $b = 0.665$ and $c = 0.384$ nm correspond to the dimensions of a unit cell in Si constructed along the $[1\bar{1}0]$ and $[\bar{1}\bar{1}2]$ directions. The cell dimension a along the [111] direction (normal to the interface) depends on the width of the transition interfacial region; the latter parameter is varied in the simulation.

After determining the average distribution of atoms in the amorphous layer, the two-dimensional distribution function is found to be

$$\rho(x, y) = \int_0^c f(\mathbf{r})dz. \quad (16)$$

The function $\rho(x, y)$ serves as a basis for simulating averaged high-resolution images using the APP approximation. The form of this function depends on the values of the variable parameters $\sigma_{\theta 1}$ and α.

IDENTIFICATION OF THE SHORT-RANGE ORDER IN THE AMORPHOUS INTERFACIAL REGION

In order to find the optimal values of the parameters $\sigma_{\theta 1}$ and α, which determine the two-dimensional distribution function of atoms in the amorphous layer, we performed an iterative fitting of the simulated and experimental images. The images were simulated using the APP approximation for 20 values of objective-lens defocus and crystal thickness, which corresponded to the experimental series of micrographs.

According to the experimental conditions, a simulation was performed for cross-sectional samples oriented along the $[1\bar{1}0]$ direction and irradiated with electrons having an energy of 200 keV. A supercell with the dimensions a, b, and c was used, with $a = 9.406$ nm. The interface between the crystal and the amorphous layer was located at $x = 0$ near the center of the supercell. The following calculation parameters were chosen: spherical-aberration coefficient 0.5 mm; semiangle of divergence of the electron beam 0.5 mrad; aperture

of the objective diaphragm 27.5 mrad; and spread of the focal length 2.4 nm. Electron absorption was described by the imaginary part of the potential, which was assumed to be proportional to its real part. The ratios of the imaginary and real parts of the potential were assumed to be equal to 0.05 for crystalline silicon and 0.04 for amorphous germanium. Such a relation between the noted ratios provided a proportion between the intensities in the crystalline and amorphous parts of a simulated image corresponding to the experimental micrographs. The influence of the transfer function of the digital-micrograph recording system was taken into account in the simulation using the results of [16]. The intensity in the recorded micrographs was normalized so as to ensure the same average level in the amorphous parts of the images obtained experimentally and simulated ones.

The optimal values of the parameters $\sigma_{\theta 1}$ and α obtained by the iterative fitting of images were equal to 0.154 and 0.0215 rad, respectively. The averaged simulated images corresponding to these values and the averaged intensity profiles are shown in Figs. 3a and 3b, respectively. In the calculation of $R(I_{exp}, I_{sim})$ by formula (5), the intensities in the interfacial region of the crystal and the amorphous region were compared for the values of x from $x_1 = -0.48$ to $x_2 = 2.02$ nm and all the values of y from $y_1 = 0$ to $y_2 = b = 0.665$ nm.

As can be seen from Figs. 2 and 3, the two-dimensional distribution function of atoms in the amorphous layer (Fig. 4), obtained on the basis of the model described above, makes it possible to adequately simulate averaged experimental images. The positions of the maxima and minima of intensity coincide in the simulated and experimental images, while the calculated and measured intensities change in a similar way. This result indicates that the function $\rho(x, y)$ determines the positions of the maxima of atomic density along the direction perpendicular to the interface quite precisely and correctly describes the main features of the distribution of Ge atoms in the interfacial region. The value of $\sigma_{\theta 1} \approx 8.8°$ that was found, which determines the standard deviation from the ideal orientation of the bonds between the boundary Si and Ge atoms, is in agreement with the value characteristic of amorphous germanium, which is 9.7° [15].

The form of the function $\rho(x, y)$ shown in Fig. 4 suggests that the positions of atoms in the amorphous layer near the interface are determined by the periodic arrangement of Si atoms and the spatial orientation of the covalent bonds between Ge atoms introduced into the model. The distribution function in the amorphous region changes more and more gradually as the distance from the interface increases. The calculations show that variations in the function $\rho(x, y)$ at $x \gtrsim 1.4$ nm almost do not affect the intensity distribution in averaged images. Therefore, the width of the transition region within which the translational symmetry of the crystal noticeably affects the positions of Ge atoms is about 1.4 nm along the direction perpendicular to the interface. This value significantly exceeds that found in [17] for the interface between crystalline and amorphous silicon with the use of the random-grid model, but is close to the value of 1.1 nm obtained for the same interface using the Monte Carlo method [18].

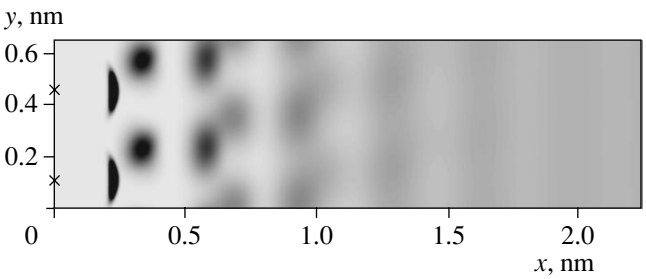

Fig. 4. Two-dimensional distribution function of atoms in the amorphous part of the interfacial region. The positions of the boundary Si atoms are indicated by the symbol ×.

The iterative fitting of images made it possible not only to found the optimal values of the model parameters for the interface structure, but also to correctly determine the position of the interface between the crystal and the amorphous layer. As can be seen from Fig. 2b, the interfacial layer of Si atoms is noticeably shifted to the left as compared to the position obtained from intuitive consideration based on the qualitative analysis of averaged images with a minimum contrast at $\zeta = 21.6$ nm (Fig. 2b). The appearance of the contrast typical of the crystal in the amorphous part of the image is primarily due to the ordering of the atomic positions in the interfacial region of the amorphous layer. The Fresnel diffraction effects are also responsible for the appearance of the contrast characteristic of the crystal in the bulk of the amorphous region. The degree of this "penetration" of the contrast into the bulk depends on the defocus and is at its minimum at $\zeta = 21.6$ nm in the image, with a minimum contrast in the amorphous part.

Although the intensity distributions in the calculated and experimental images are qualitatively similar, it can be seen from Fig. 3b that the magnitudes of intensities in these images are different. The main reasons for this are:

(1) insufficient accuracy of modern methods of simulating high-resolution electron-microscopy images [19];

(2) some error determining the sample thickness and the defocus values for the images of the defocus series;

(3) limitations of the APP approximation;

(4) limitations of the model used in the calculation of the two-dimensional distribution function of atoms in the interfacial amorphous region; and

(5) the possible presence of steps on the Si surface in the interfacial region between Si and Ge.

It is noteworthy that, although some features of the distribution function $\rho(x, y)$ may change due to the

above reasons, especially near the interface, the main regularities of the obtained distribution remain intact.

CONCLUSIONS

The structure of amorphous germanium grown on an atomically smooth Si(111) surface was studied using the methods of high-resolution electron microscopy. In order to obtain quantitative information on the atomic structure in the interfacial region, the experimental electron-microscopy images were averaged over the interface and then simulated using the APP approximation and an iterative comparison of calculatory and experimental results. Such an approach in terms of the proposed structural model made it possible to derive the optimal two-dimensional distribution function of atoms of the amorphous layer.

It is shown that the average distribution of interatomic bonds in the amorphous layer near the interface is determined by the sites of a tetragonally distorted Ge lattice, which is coherently matched with the Si crystal. Such an interatomic-bond orientation compensates for the difference in their lengths in the crystalline silicon and amorphous germanium. The width of the transition interfacial region, within which the translational symmetry of the Si crystal affects the positions of Ge atoms, is about 1.4 nm. The standard deviation from the ideal orientation of the bonds between Si and Ge atoms was found to be 8.8°, which is somewhat lower than the corresponding value for amorphous germanium, which is 9.7° [15].

REFERENCES

1. F. Priolo and E. Rimini, Mater. Sci. Rep. **5**, 319 (1990).
2. A. G. Cullis, N. G. Chew, H. C. Webber, and D. J. Smith, J. Cryst. Growth **68**, 624 (1984).
3. R. Hull, A. Ourmazd, W. D. Rau, *et al.*, in *Handbook of Semiconductors*, Ed. by K. A. Jackson and W. Schröter (Wiley–VCH, Weinheim, 2000), p. 453.
4. G. Möbus and M. Rühle, Ultramicroscopy **56**, 54 (1994).
5. W. E. King and G. H. Campbell, Ultramicroscopy **56**, 46 (1994).
6. H. Hoffman and F. Ernst, Ultramicroscopy **53**, 205 (1994).
7. C. Kisielowski, P. Schwander, F. H. Baumann, *et al.*, Ultramicroscopy **58**, 131 (1995).
8. A. N. Kisilev, F. Sarrazit, and N. A. Kisilev, Philos. Mag. A **76**, 633 (1997).
9. N. I. Borgardt, B. Plikat, M. Seibt, and V. Schröter, Izv. Ross. Akad. Nauk, Ser. Fiz. **61**, 1980 (1997).
10. N. I. Borgardt, B. Plikat, M. Seibt, and V. Schröter, Izv. Ross. Akad. Nauk, Ser. Fiz. **65**, 1238 (2001).
11. N. I. Borgardt, B. Plikat, M. Seibt, and W. Schröter, Ultramicroscopy **90**, 241 (2002).
12. U. Neuwald, H. E. Hessel, A. Felty, *et al.*, Appl. Phys. Lett. **60**, 1307 (1992).
13. M. Suhren, D. Graf, R. Schmolke, *et al.*, Inst. Phys. Conf. Ser. **149**, 301 (1996).
14. G. Möbus, R. Schweinfest, T. Gemming, *et al.*, J. Microsc. **190** (1/2), 109 (1998).
15. G. Etherington, A. C. Wright, J. T. Wenzel, *et al.*, J. Non-Cryst. Solids **48**, 265 (1982).
16. J. M. Zuo, Ultramicroscopy **66**, 21 (1996).
17. Y. Tu, J. Tersoff, G. Grinschtein, and D. Vanderbilt, Phys. Rev. Lett. **81**, 4899 (1998).
18. C. R. S. Da Silva and A. Fazzio, Phys. Rev. B **64**, 075301 (2001).
19. C. B. Boothroyd, J. Microsc. **190** (1/2), 99 (1998).

Translated by Yu. Sin'kov

Crystallography Reports, Vol. 49, No. 2, 2004, pp. 233–239. Translated from Kristallografiya, Vol. 49, No. 2, 2004, pp. 286–293.

SURFACES, THIN FILMS

Modern Preparation Methods of Oriented Thick Films of Superconducting Cuprates[1]

Yu. D. Tret'yakov*, E. A. Gudilin*, E. S. Reddy, and G. J. Schmitz****

** Faculty of Chemistry, Moscow State University, Vorob'evy gory, Moscow, 119992 Russia*

e-mail: goodilin@inorg.chem.msu.ru

*** ACCESS e. V., Intzest. 5, D-52072, Aachen, Germany*

Received March 27, 2003

Abstract—Modern trends in the development of methods of manufacturing biaxially textured large-grained coatings ~100 μm thick based on superconducting rare-earth–barium cuprate elements, as well as bismuth-containing high-temperature superconductors, are considered. It is shown that the formation of a symmetric artificial surface relief makes it possible to control the mutual orientation of crystallites on polycrystalline metal substrates with high efficiency. In this case, the fraction of superconductor crystallites with an angle of mutual misorientation <5% may be as high as 75–90%. The high efficiency of this method of forming oriented films of multicomponent oxide phases indicates that it can be used to fabricate new-generation superconducting composite materials. © *2004 MAIK "Nauka/Interperiodica".*

INTRODUCTION

High-temperature superconducting (HTSC) cuprates may have unique applications in various fields, such as magnetic levitation and shielding, detection of weak magnetic fields, medicine, energy-saving and ecologically pure technologies, microelectronics, and fault-current limiters. HTSC cuprates are a striking example of modern functional materials with structurally sensitive properties [1–7]. In view of anomalously low values of coherence length in HTSC phases, the prime task is to develop effective methods to allow obtaining highly oriented films, as well as to perform fundamental investigation of film-growth mechanisms [8–15]. Deposition of textured superconducting coatings with high critical currents (I_c) on long-length substrates and surfaces with complex geometry is of particular interest [8, 9]. In this study, a new approach to fabrication of such films, based on the use of an artificial surface relief, is proposed, and some aspects of oriented growth of crystallites in complex oxide systems are considered.

PRINCIPLES OF TEXTURING

Significant progress has been made recently in obtaining superconducting films. In particular, the following problems have been solved:

(i) Methods of continuous chemical-vapor deposition of oriented thin films of superconducting rare-earth–barium cuprates on biaxially textured metal ribbons made of nickel-containing alloys or silver [8, 9], liquid-phase epitaxy from cuprate–fluoride melts at low partial oxygen pressures and temperatures in the range 800–850°C [12–15], and pyrolysis of aerosols [11] were developed.

(ii) HTSC fabric cuprates with a developed system of regular pores having improved contact with liquid nitrogen, high resistance in the normal state, and high values of I_c (up to 55000 A/cm^2) were obtained, which makes it possible to design prototypes of superconducting fault-current limiters. In this case, the specific microstructure of samples is obtained using mutually oriented seeds and infiltration of an Y_2O_3 fabric with a cuprate melt at a high temperature with the formation of the $YBa_2Cu_3O_z$ superconductor, the initial sample shape being conserved [16–19].

(iii) Artificial gradients of concentrations of rare-earth elements were created that lead to directional crystallization of rare-earth–barium cuprates [20].

The texture (or mutual orientation of crystallites) (Fig. 1) may result from nucleation on the surface, due to which both the position and orientation of nuclei are determined by short-range molecular forces (the saturation of uncompensated bonds on the surface) or by the motion and mutual adjustment of crystallites caused by external fields and forces.

The former principle is realized in the aforementioned processes of vapor- or liquid-phase heteroepitaxy of thin films on single-crystal or biaxially textured substrates. Although these methods are very popular, they have a number of significant constraints, including the critical film thickness (at which the required morphology and orientation are still retained), a complex film-deposition procedure, low output, and so on [19].

[1] This work was presented at the National Conference on Crystal Growth (NCCG-2002, Moscow).

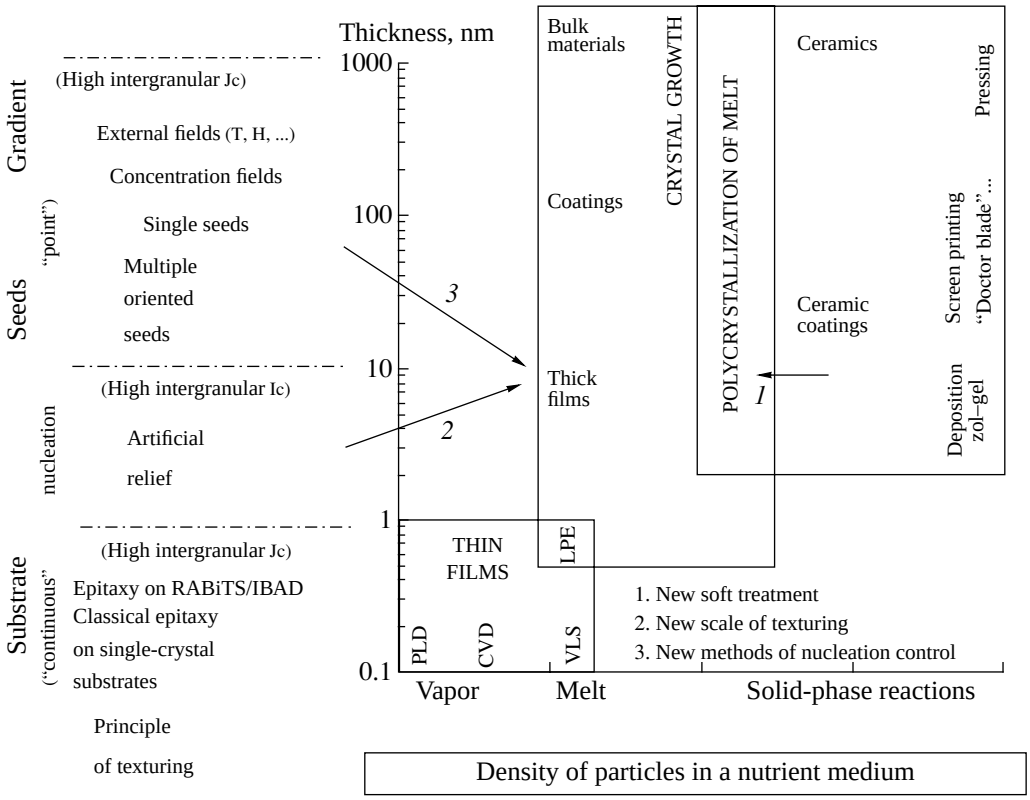

Fig. 1. General scheme of methods of texturing polycrystalline HTSC materials, depending on the thickness of a superconducting layer.

The latter principle (motion and adjustment) has practically no constraints on film thickness, as these processes are independent of the nature of the substrate and involve external factors [2–7] such as temperature gradients or magnetic fields and single or multiple seeds (Fig. 1). Methods of this group require the presence of a melt providing fast growth and mutual adjustment of crystallites. Bulk ceramic materials obtained by these methods are characterized by high values of functional parameters. At the same time, due to a low texture quality and the presence of various macrodefects, the specific characteristics turn out to be rather poor. Obviously, the necessity of either transferring samples through a zone with a gradient of external fields or ordering a number of artificial crystallization centers significantly limits the applicability of this group of methods for texturing long-length samples or samples with a large surface area.

Thick films are a reasonable compromise for obtaining high values of both specific and absolute functional properties [19]. Conventional methods of fabricating thick films (screen printing, zol–gel, spinning, dipping, electrophoresis, pyrolysis of aerosols, magnetron deposition, and so on [21]) are simple but inefficient for biaxial texturing because epitaxial effects are significantly reduced for films thicker than 1 μm.

HTSC coatings with improved superconducting properties can be formed using a combined approach based on both of the aforementioned concepts: the orienting effect of a substrate (thin films) and the formation of large grains from melt (bulk materials). For texturing polycrystalline layers of multicomponent functional materials, the use of self-assembly principles [22–24], which make mutually correlated growth of all the components simultaneously possible, is also rather promising. Such concepts are now typical of nanotechnology, where self-assembly of monolayers leads to the spontaneous formation of complex structures from the necessary constructional units. This phenomenon involves energy interactions at different levels and constraints for a number of degrees of freedom of a system [22]. For semiconductor films, filters for grain orientation have been developed that would control the preferential growth direction [23]. Thus, the search for alternative texturing principles remains urgent for HTSC coatings, especially those formed on nontexturated substrates of a complex shape.

GRAPHOTEXTURING

In order to obtain thick superconducting biaxially textured films, a method of graphotexturing was developed [25, 26] that consists in the use of polycrystalline metal substrates on which a submillimeter surface relief

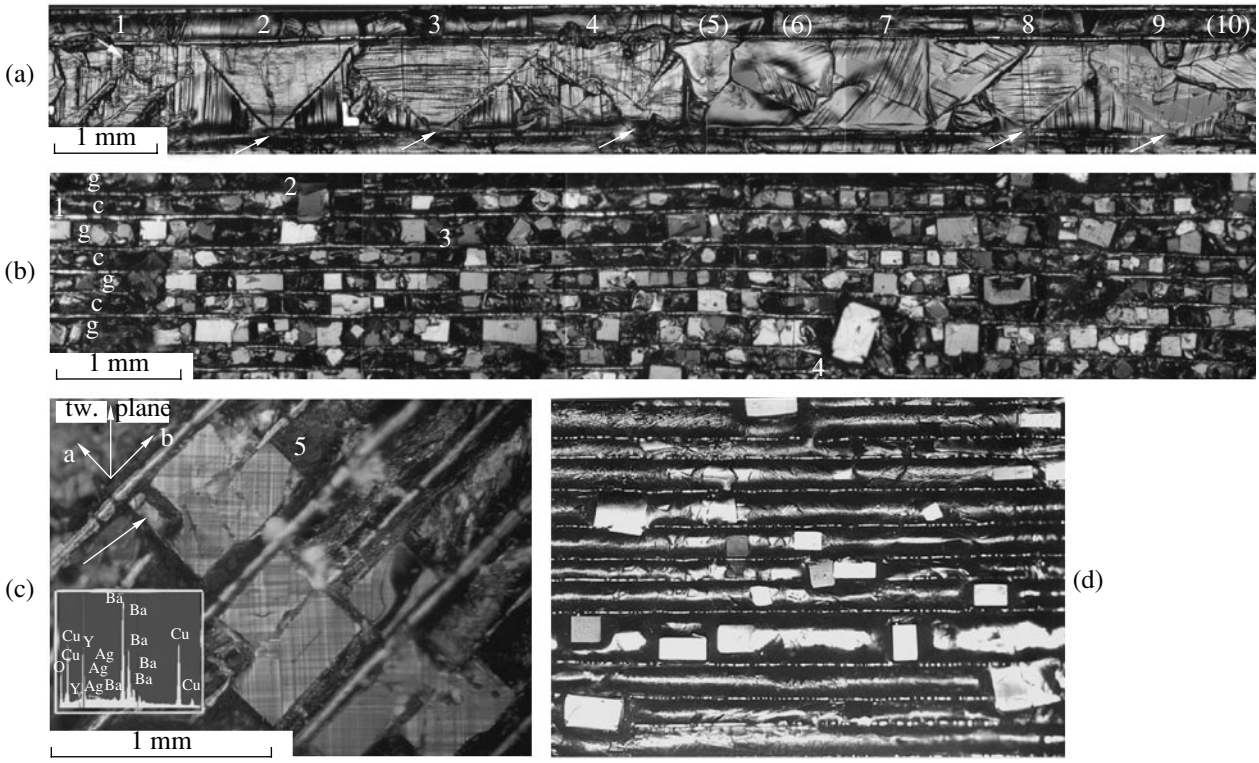

Fig. 2. Biaxial texturing of a polycrystalline layer of yttrium–barium cuprate using a symmetric surface relief: (a) crystallites oriented between two grooves due to the formation of crystallization centers near the relief elements (crystallites *5*, *6*, and *10* formed far from the walls distort the general orientation of the ensemble of crystallites); (b) about 220 crystallites, 75% of which are misorientated with respect to the stripe relief by less than 5°; (c) the twin defect pattern shows the biaxial orientation of crystallites; (d) oriented single crystallites of neodymium–yttrium–barium cuprate with a higher (in comparison with $YBa_2Cu_3O_z$) temperature of peritectic decomposition.

is formed (Fig. 1). For thin films, this approach is well-known as artificial epitaxy [27]. In the case of HTSC materials, there are only a few publications on the use of special substrates, atomic graphoepitaxy, or the formation of surface microrelief by photolithography [28, 29]. It is generally accepted that graphoepitaxy is effective only for thin (~1 μm) layers and, hence, only for small crystallites with sizes no larger than ~(1–10) μm. As was shown in [25], large (submillimeter) HTSC crystallites can also take the desired orientation with corresponding geometric constraints on their growth. As an example, Figs. 2–5 show micrographs of thick films for three widely spread superconducting systems obtained by different methods (see table).

An artificial relief has a relatively complex effect on the orientation of crystallites of superconducting cuprates [25]. Relief elements impose necessary constraints on the development of ensembles of crystal-

Specific features of manufacturing thick superconducting films on substrates with a surface relief in different systems

System, phase	Method of film deposition	Habit and size of crystallites	Relief	Symmetry	Mobility of a medium	Mobility of crystallites
K–Ba–Bi–O, (K, Ba)BiO_3	electrochemical deposition from molten alkali hydroxides [30]	cubic crystallites, ~(10–30) μm	Stripe or square mesh ~(100–500) μm	corresponding	high	absent
Y–Ba–Cu–O, $YBa_2Cu_3O_z$	infiltration of a Y_2BaCuO_5 layer with melt [25]	lamellar crystallites, ~(100–200) μm	Stripe, ~100 μm		intermediate	intermediate
Bi–Sr–Ca–Cu–O, $Bi_2Sr_2CaCu_2O_8$	peritectic decomposition [31]	needle-like crystallites, ~50–100 × 1000 μm^2	Stripe, ~100 μm, two mutually perpendicular sets of grooves		high	high

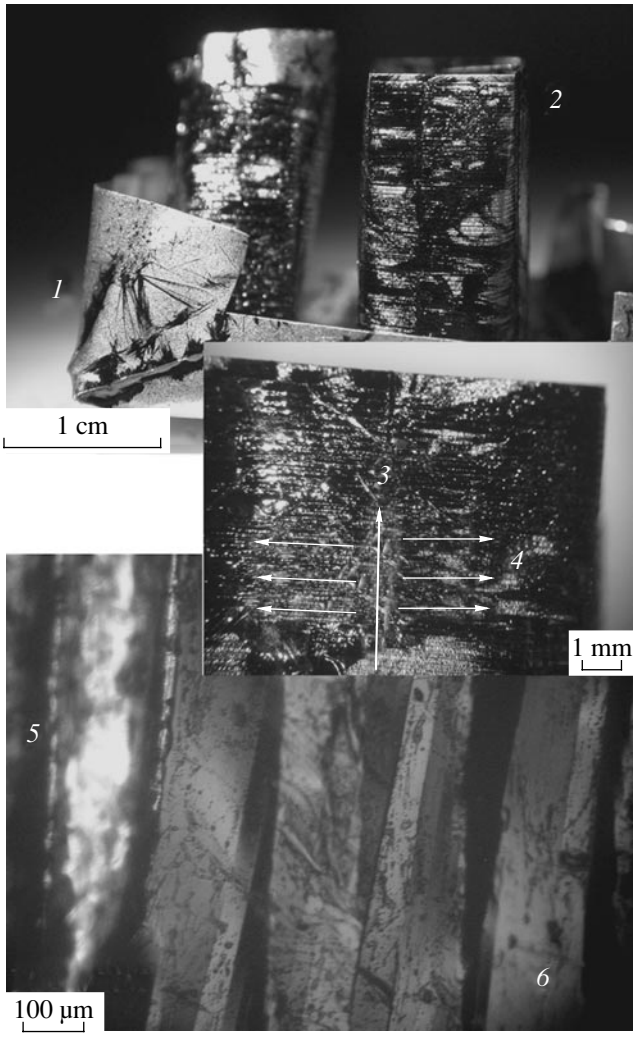

Fig. 3. Biaxially textured superconducting $Bi_2Sr_2CaCu_2O_8$ samples, manufactured using silver ribbons with an artificial surface relief: (*1*) a silver bath with a peritectic melt of the HTSC phase; (*2*) a cylinder coated with a textured HTSC layer; (*3*) grooves through which a melt rises along the sample surface due to capillary forces; (*4*) perpendicular grooves distributing the melt over the surface and forming the mutual orientation of HTSC grains upon crystallization; (*5*) a groove; and (*6*) an ensemble of oriented crystallites with a higher magnification.

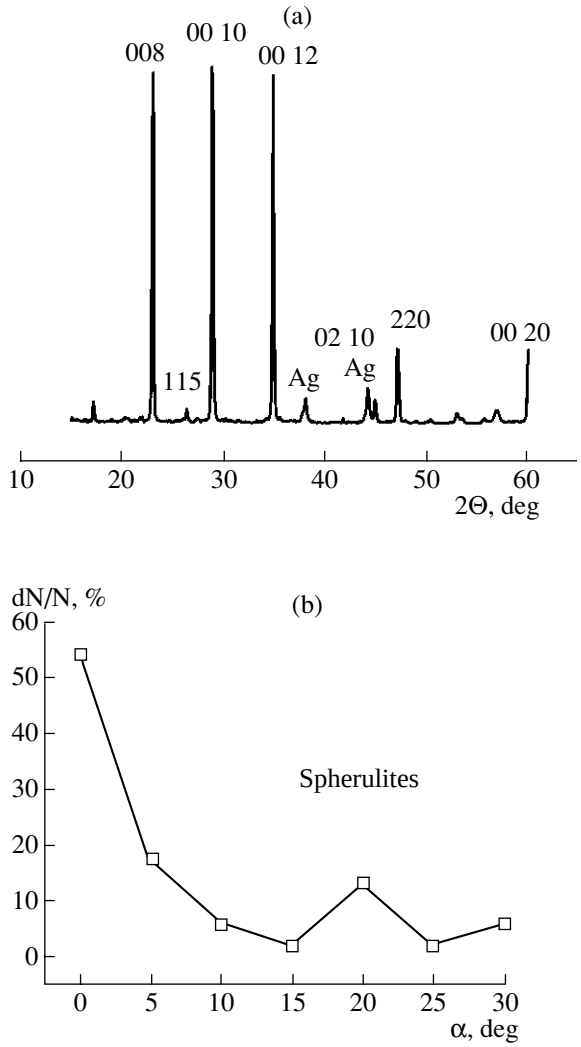

Fig. 4. Biaxial texturing of $Bi_2Sr_2CaCu_2O_8$ samples having T_C = 89 K on silver ribbons with an artificial surface relief: (a) spontaneously appearing uniaxial 00*l* texture of needle-like $Bi_2Sr_2CaCu_2O_8$ crystallites on the substrate surface; (b) the distribution of needle-like $Bi_2Sr_2CaCu_2O_8$ crystallites over the misorientation angle α (the angle between the crystallite axis and the walls of the stripe relief in the substrate plane).

lites. The elements form a geometric mask, the static effect of which distorts the isotropy of a crystallizing system and, finally, facilitates the required orientation of the crystallites (Fig. 6). It was found in [25, 26] that an artificial relief should satisfy the following requirements in the case of HTSC materials: (i) consist of only the most effective elements that give rise to oriented growth of crystallites, with inefficient elements being excluded; (ii) ensure necessary geometric constraints on crystallite growth when the symmetry of the position of the relief elements corresponds to the habit of the grown crystallites; and (iii) facilitate the formation of centers of crystallite growth near the elements of the artificial relief (since, in the opposite case, the efficiency of the latter significantly decreases).

The presence of a relief is a necessary but, unfortunately, insufficient condition for the formation of biaxially textured layers. For example, the stochastic occurrence and random growth of many crystallites may be unfavorable factors impeding the growth and motion of those crystallites that, in the opposite case, would be oriented by the artificial relief [25]. Hence, the number of crystallites per artificial-relief element depends on both the density of the nucleation probability and on the characteristic sizes of the relief elements (Figs. 2, 6).

The effect of the factors leading to the misorientation of crystallites was minimized by controlling nucleation [25], in particular, by introducing mobile floating microseeds (Fig. 2) and controlling cell size. Ideally, it is desirable to have only one crystallite in each cell of the artificial relief. The reduction in size of the cells of a square mesh (up to 0.5 mm) [25] seems a convenient method for improving the mutual orientation of HTSC crystallites. In this case, only one (or, less frequently, two) crystallite is formed in a cell, since space for nucleation and subsequent growth is physically limited. The nucleation of the first crystallites significantly reduces the supersaturation in the entire cell, thus preventing the formation of other crystallites. Therefore, the reduction of cells eliminates the main reason for misorientation—interaction with neighboring crystallites [25].

A simple stripe relief formed by narrow parallel grooves is most effective for orientation of HTSC crystallites [25, 26]. Such a relief geometry provides the following: effective geometric limitation of crystal growth by parallel walls of narrow grooves; the required relief symmetry corresponding to the habit of the growing crystals; and a crystallite-ensemble density that is almost independent of the cooling rate (as the size of the crystallites is limited physically by the width of the channels) (Figs. 2, 3). To date, about 75–85% of submillimeter crystallites can be fairly easily and reproducibly oriented with an angle of misorientation smaller than 10° on substrates with the noted artificial relief. In experiments with floating seeds, this parameter was as high as ~90% (Figs. 2–4).

In graphoepitaxy, the epitaxial relations for the orientation of crystallites are not used, because this method is based on the topographic effect of the surface relief, specific nucleation features, anisotropic wetting of the substrate surface by melt, local temperature gradients, capillary and surface-tension forces, and so on [27]. In this context, the most important factor is high particle mobility, which ensures the adjustment of grown nuclei floating on the melt surface in accordance with the position of the relief elements (Fig. 6). Comparison of the microstructures of different samples gives convincing evidence of this (Figs. 2, 3, 5; table). For example, an electrochemically obtained film of substituted potassium bismuthate consists of randomly oriented crystallites. The reason is that the growth of crystallites in this case requires direct contact with an electrode, which prevents crystallites from changing their fixed positions, despite the process occurring in the presence of a large amount of liquid (molten potassium hydroxide). The inconsistency between the characteristic sizes of the relief and the crystallites formed may also be a negative factor, although the stripe relief and cubic crystallites have the same symmetry (see table).

The surface tension and the presence of a free liquid between the crystallites and geometric structures of the substrate make crystallite motion and rotation possible,

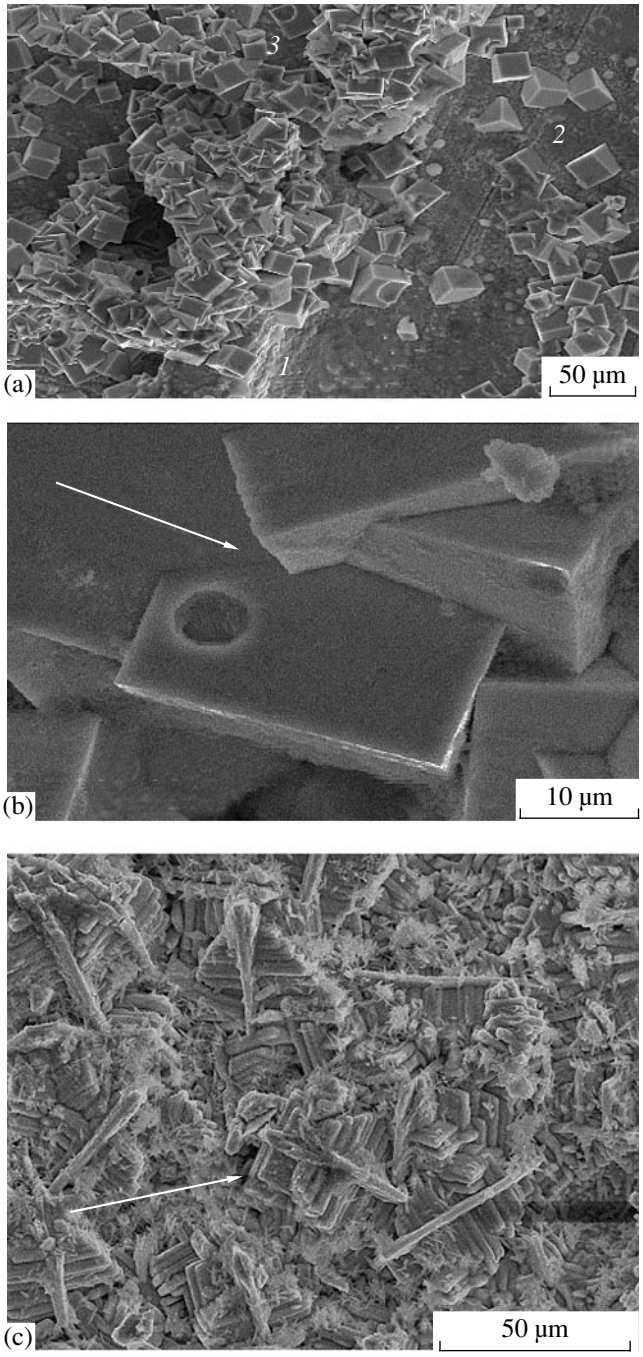

Fig. 5. Absence of texturing in a polycrystalline $(K,Ba)BiO_3$ layer deposited on a silver substrate with an artificial surface relief by electrocrystallization: (a) general view; (b) layer microstructure; and (c) formation of dendritic crystals at high deposition rates.

and they therefore change their position and orientation. The rotational degrees of freedom of crystallites are very important for adjustment of their mutual orientation. In this case, three-phase boundaries (crystal–substrate–melt and crystal–melt–gas) may play the most important role during the graphotexturing. In particular, the presence of a meniscus near the relief walls

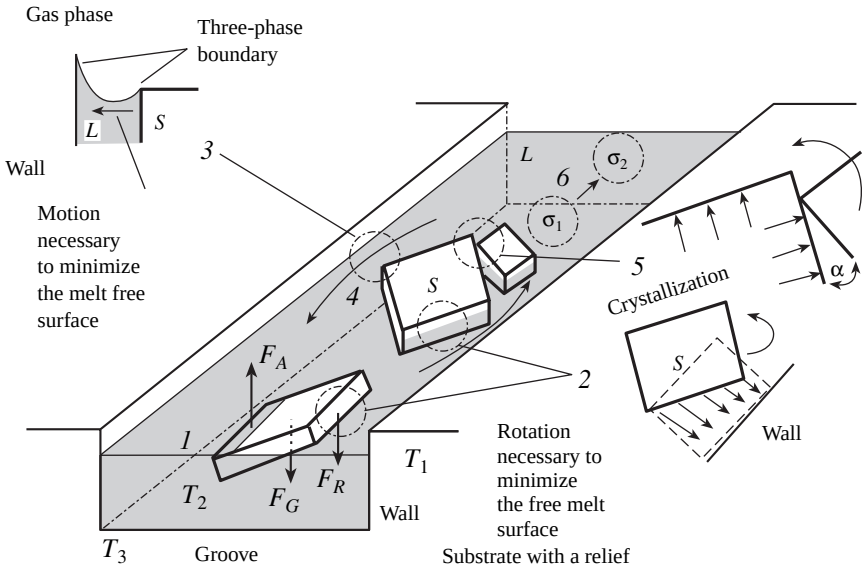

Fig. 6. Proposed model of orientation of growing crystallites of HTSC phases (*S*) with an artificial surface relief in the presence of a liquid phase (*L*). T_1 is the temperature of the substrate surface contacting with the gas phase and reemitting heat; T_2 is the temperature of melt (*1*) inside the elements of the artificial relief; and T_3 is the temperature of the substrate bulk (differences between these temperatures—including in the case of dynamic cooling/heating, with different specific heats and thermal conductivities of the substrate, melt, and surrounding gas phase—give rise to local temperature gradients). F_A, F_G, and F_R are the buoyant, gravity, and surface-tension forces, respectively, in the film of a melt (*2*) near crystallites (these forces balance small crystallites in horizontal positions on the melt surface). (*3*) The region of meniscus, where, due to the surface-tension force minimizing the free surface of the liquid, crystallite (*4*) rotates and approaches the relief wall. Interacting crystallites (*5*) may affect the orientation of each other due to the crystallization pressure or a change in the meniscus shape. The dependence of the surface-tension coefficient on the concentration of components is expressed in the form of gradient σ, which leads to the appearance of additional forces (Marangoni effects), facilitating the migration of crystallites.

and the minimization of the free melt surface near the meniscus lead to crystallite rotation and the alignment of one of their faces along the wall (Fig. 2). In narrow channels, the meniscus is bilateral, relatively symmetric, and has a large curvature radius. Hypothetically, this may stabilize the primary crystallite nuclei at the center of the channels due to the balance of surface-tension effects; in this case, the shape of the crystallites will correspond to the channel width during their growth (Fig. 2).

The redistribution of melt over the substrate surface and the anisotropic wetting of the substrate are also very important factors in crystallite orientation. For example, the capillary rise of a melt along a vertically positioned substrate, its distribution over the substrate surface, and the spontaneously appearing mutual orientation of superconducting cuprate grains that are formed forming upon cooling make it possible to obtain, even now, the biaxial texturing of the prototypes of some articles that can be used in practice—in particular, HTSC ribbons in the form of coils (Fig. 3). This method is effective for mass production of thick-film HTSC composites on relatively inexpensive metal substrates of complex shape in a uniform thermal field.

Looking back through history, we should note that it is probably only now that an object has been found (HTSC films) for which vitally important large-area texturing can be performed, as N.N. Sheftal' expected in his time from his discovery of graphoepitaxy [27].

CONCLUSIONS

The results of this study show that the universal principle of controlling the mutual orientation of crystallites, consisting in the artificial violation of the isotropy of a crystallizing system on substrates with a surface mesorelief, which leads to the self-assembly of biaxially textured layers with improved superconducting properties, can be used in the fabrication of large-grained coatings based on superconducting cuprates.

ACKNOWLEDGMENTS

We are grateful to E.I. Givargizov for the idea of writing this paper and fruitful discussion of the results.

This study was supported by the Russian Foundation for Basic Research, project no. 01-03-32828; the program "Support of Leading Scientific Schools," grant no. 00-15-97435; and the program "Universities of Russia," grant no. 015.06.02.008.

REFERENCES

1. B. J. Batlogg, R. Buhrman, J. R. Clem, *et al.*, J. Supercond. **10**, 583 (1997).

2. Y. Shiohara and A. Endo, Mater. Sci. Eng. R **19**, 1 (1997).
3. Y. Shiohara and E. A. Goodilin, in *Handbook on the Physics and Chemistry of Rare-Earths*, Ed. by K. A. Gschneidner *et al.* (Elsevier Sci., Amsterdam, 2000), Vol. 30, Chap. 189, pp. 67–221.
4. J. L. MacManus-Driscoll, Annu. Rev. Mater. Sci. **28**, 421 (1998).
5. Yu. D. Tret'yakov and E. A. Gudilin, Usp. Khim. **69** (1), 3 (2000).
6. Y. D. Tretyakov and E. A. Goodilin, Physica B (Amsterdam) **321**, 249 (2002).
7. Y. D. Tretyakov, N. N. Oleynikov, and E. A. Goodilin, Z. Metallkd. **92** (2), 121 (2001).
8. A. Goyal, D. P. Norton, D. K. Christen, and E. D. Specht, Appl. Supercond. **4** (10–11), 403 (1996).
9. D. K. Finnemore, K. E. Gray, M. P. Maley, *et al.*, Physica C (Amsterdam) **320**, 1 (1999).
10. A. Goyal, P. D. Funkenbusch, and D. M. Kroeger, Physica C (Amsterdam) **182** (1/3), 203 (1991).
11. R. L. Meng, D. Pham, Y. Q. Wang, *et al.*, Physica C (Amsterdam) **341**, 2315 (2000).
12. Y. Yamada, Y. Niiori, I. Hirabayashi, and S. Tanaka, Physica C (Amsterdam) **278**, 180 (1997).
13. Y. Yamada, T. Suga, and I. Hirabayashi, J. Cryst. Growth **236**, 221 (2002).
14. Y. Niiori, Y. Yamada, I. Hirabayashi, *et al.*, Physica C (Amsterdam) **301**, 104 (1998).
15. X. Qi and J. L. MacManus-Driscoll, J. Cryst. Growth **213**, 312 (2000).
16. J. G. Noudem, E. S. Reddy, E. A. Goodilin, *et al.*, Physica C (Amsterdam) **372–376**, 1631 (2002).
17. E. S. Reddy, E. A. Goodilin, M. Tarka, *et al.*, Physica C (Amsterdam) **372–376**, 1200 (2002).
18. J. G. Noudem, E. S. Reddy, M. Tarka, *et al.*, Physica C (Amsterdam) **366** (2), 93 (2002).
19. G. J. Schmitz, E. S. Reddy, and E. A. Goodilin, Physica C (Amsterdam) **378–381**, 607 (2002).
20. G. J. Schmitz and O. Kugeler, Physica C (Amsterdam) **275**, 205 (1997).
21. N. McAlford, S. J. Penn, and T. W. Button, Supercond. Sci. Technol. **10**, 169 (1997).
22. F. Schreiber, Prog. Surf. Sci. **65**, 151 (2000).
23. H. Tanabe, C. M. Chen, and H. A. Atwater, Appl. Phys. Lett. **77**, 4325 (2000).
24. A. B. Rodriguez-Navarro, Thin Solid Films **389**, 288 (2001).
25. E. A. Goodilin, E. S. Reddy, J. G. Noudem, *et al.*, J. Cryst. Growth **241**, 512 (2002).
26. E. A. Goodilin, E. S. Reddy, J. G. Noudem, *et al.*, Physica C (Amsterdam) **372–376**, 842 (2002).
27. E. I. Givargizov, in *Handbook of Crystal Growth*, Ed. by D. T. J. Hurle (Elsevier, Amsterdam, 1994), Part 3b, Chap. 21, pp. 941–995.
28. S. Miyazawa and M. Mukaida, Appl. Phys. Lett. **64**, 2160 (1994).
29. W. D. Dozier and C. E. Platt, Appl. Phys. Lett. **62**, 2048 (1993).
30. S. N. Barilo, N. M. Olekhnovich, N. S. Orlova, and A. V. Pushkarev, Cryst. Res. Technol. **1** (31), 107 (1996).
31. R. R. Schartman, R. Sakidja, and E. E. Hellstrom, J. Am. Ceram. Soc. **76** (3), 724 (1993).

Translated by Yu. Sin'kov

Crystallography Reports, Vol. 49, No. 2, 2004, pp. 240–245. Translated from Kristallografiya, Vol. 49, No. 2, 2004, pp. 294–299.

CRYSTAL GROWTH

The Mechanism of Formation of Light-Scattering Centers in Sapphire Crystals Grown in Gas Atmospheres[1]

A. Ya. Dan'ko, N. S. Sidel'nikova, G. T. Adonkin, A. T. Budnikov, S. V. Nizhankovskiĭ, and S. I. Krivonogov

Institute for Single Crystals, National Academy of Sciences of Ukraine, pr. Lenina 60, Kharkov, 61001 Ukraine
e-mail: danko@isc.kharkov.com

Received February 26, 2003

Abstract—The mechanism of the formation of light-scattering centers in sapphire crystals grown by horizontal directed crystallization in gas atmospheres reducing with respect to the Al_2O_3 melt was studied. The experimental regularities here significantly differ from those observed upon formation of other conventional defects in sapphire crystals (vacancy pores, gas bubbles, and so on). It is shown that the known formation mechanisms of macroscopic (≥1 μm) inclusions in crystals are not acceptable in this case. Using the model of bulk crystallization is proposed to describe the obtained regularities. *© 2004 MAIK "Nauka/Interperiodica".*

INTRODUCTION

The use of protective-gas atmospheres containing the reducing components H_2 and CO for growing sapphire crystals by horizontal directed crystallization (HDC) has made it possible to replace expensive construction materials (W and Mo) with less-expensive graphite ones. As a result, the profitability of this method has increased significantly, and, now, it is very widely used in mass production of large sapphire elements [1]. However, a deviation from stoichiometry of a melt related to the presence of a reducing component in the atmosphere during its crystallization leads under certain conditions to the formation of microparticles 1–5 μm in size—light-scattering centers—in the grown crystals [2, 3]. When the concentration of such defects exceeds a certain limit (10^5 cm^{-3}), the material becomes unfit for optical applications.

Previously, on the basis of experimental data and theoretical estimates [4], it has been suggested that there must be a degree of deviation from stoichiometry critical for the Al_2O_3 lattice (when the deviation exceeds the critical value, second-phase microparticles precipitate in the crystal). However, there have been no direct experimental data that would confirm this suggestion and make it possible to estimate the critical oxygen-vacancy concentration. Nor have the size, shape, and distribution of particles been studied. As a result, the question of the origin of these defects (which are either formed in the melt and then captured by the crystallization front or due to solid-phase reactions in a crystal supersaturated with oxygen vacancies) remains open.

[1] This work was presented at the National Conference on Crystal Growth (NCCG-2002, Moscow).

The aim of this study was to obtain experimental data that would make it possible to explain the formation mechanism of light-scattering centers in sapphire crystals grown in reducing-gas atmospheres.

A STUDY OF THE DEPENDENCE OF THE CONCENTRATION OF OXYGEN VACANCIES AND MICROPARTICLES IN LEUCOSAPPHIRE CRYSTALS ON THE PROTECTIVE-ATMOSPHERE PRESSURE

Crystals were grown by the HDC method in a graphite thermal unit in a protective atmosphere (Ar + CO) in the pressure range P = 10–800 Torr. Raising the temperature and premelting the blend were performed under conditions of dynamic pumping at $P \sim 0.1$ Torr. After premelting, pure Ar was supplied to the chamber up to a fixed pressure, after which crystals were grown in the closed volume. The fraction of impurities (O_2, H_2O, N_2, and so on) in the supplied Ar did not exceed 10^{-2} vol %. As control measurements by a GAZOKhROM-3101 gas chromatograph showed, the fraction of the reducing component CO in the gas atmosphere was ≥1 vol %, increasing from the beginning to the end of the crystallization process by a factor of about 1.5. The reason seems to be the formation of CO due to the interaction of oxygen emerging from the evaporating melt and the atmospheric air leaking into the growth chamber during crystallization with the material of the thermal unit. In order to exclude the effect of foreign impurities on the formation of microparticles during crystal growth, we used a blend with a low impurity content (see table).

The experimental samples were cut parallel to the crystal surface ((0001) plane). Their transmission spec-

1063-7745/04/4902-0240$26.00 © 2004 MAIK "Nauka/Interperiodica"

tra were recorded on an SPECORD-UV-VIS spectrophotometer in the spectral range 200–800 nm. The absorption spectra $K(\lambda)$, cm^{-1}, were plotted after correcting for the reflection and reducing to unit thickness.

The concentration of *F* centers in the samples was estimated by the Smakula formula, using the values of the oscillator strengths obtained in [5]. The concentration of microparticles in the samples was estimated using an MIK-4 optical microscope. Measurements showed that the concentration of *F* centers in crystals increases with increasing the gas-atmosphere pressure, attaining values as high as $\sim 8 \times 10^{16}$ cm^{-3} for a crystal grown at $P \sim 30$ Torr. Further increase in pressure does not lead to a noticeable increase in the concentration of *F* centers but is accompanied by precipitation of second-phase microparticles, the concentration of which increases with increasing the pressure of the growth medium (Fig. 1). The theoretical estimates of the concentration of anion vacancies [4] (curve *2*) are in good agreement with the experiment (curve *1*) for crystals that were grown at $P \sim 10$–30 Torr (in which practically no microparticles were detected) and significantly exceed the experimental values for crystals grown at higher pressures, which contained microparticles. Let us assume that the second-phase microparticles have the composition $AlAl_2O_4$ (Al–Al spinel [6]). Then, as many as 1.2×10^{10}–3.25×10^{11} vacancies are required to form one microparticle 1–3 μm in size. The estimates of the average concentration of microparticles performed under these assumptions [3] (curve *4*) agree well with the experimental values (curve *3*).

It has also been ascertained that the concentration of microparticles C_{MP} increases from the beginning to the end of a crystal, according to the increase in the CO concentration in the growth medium during the crystallization, and that the character of the distribution of *F* centers depends significantly on the growth-medium pressure (Fig. 2). In crystals grown at $P \sim 10$–100 Torr, the concentration of *F* centers, C_F, decreases from the beginning to the end of a crystal simultaneously with an increase in C_{MP}. For example, in the beginning of a crystal grown at $P \sim 10$ Torr, $C_F \sim 6 \times 10^{16}$ cm^{-3} (microparticles being absent in this part of the crystal). In the end of the crystal, simultaneously with the appearance of microparticles, a noticeable decrease in C_F is observed (up to $\sim 1 \times 10^{16}$ cm^{-3}). A similar picture is observed for a crystal grown at 30 Torr: in the beginning of the crystal, $C_F \sim 7.5 \times 10^{16}$ cm^{-3} (there are almost no microparticles in this part of the crystal, and their concentration is about 10^4 cm^{-3}), while, in the end of the crystal, simultaneously with the precipitation of microparticles, a noticeable decrease in C_F is seen (up to $\sim 3 \times 10^{-16}$ cm^{-3}). In a crystal grown at $P \sim 100$ Torr, where $C_{MP} \sim 10^5$ cm^{-3} even in the beginning, this decrease is less significant. In crystals grown at higher pressures (400–800 Torr), the character of the distribution of *F* centers changes: their concentration increases in the same way as that of microparticles.

Contents of main impurities in the blend

Element	Ca	Cr	Fe	Ga	Mg	Na	Si	Ti
Concentration, ppm	<5	<1	<4	<11	<3	7	<18	2–5

The results obtained confirm the suggestion about the existence of a critical (limiting) deviation from stoichiometry for crystallization of Al_2O_3 (when the deviation exceeds the critical one, precipitation of microparticles occurs) and make estimation of the critical concentration of oxygen vacancies possible: $\sim 8 \times 10^{16}$ cm^{-3}. The fact that the precipitation of microparticles is accompanied by a decrease in the degree of deviation from stoichiometry of the grown crystal lends weight to the idea that these microparticles are inclusions of an oxygen-depleted phase.

STUDY OF THE SIZE, SHAPE, AND DISTRIBUTION OF MICROPARTICLES

The mechanisms of the formation of macroscopic (≥1 μm) inclusions in crystals have been widely studied [7]. Such inclusions can be formed due to both trapping of foreign particles by the crystallization front and precipitation of excess components and impurities in the solid phase when crystals are cooled or annealed [7]. Taking it as a given that these well-known regularities

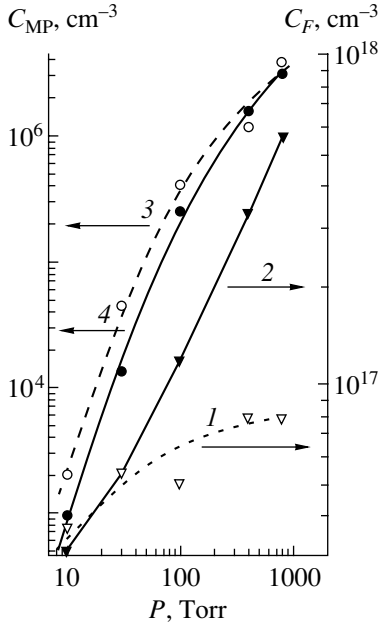

Fig. 1. Dependences of the concentrations of *F* centers and microparticles in sapphire crystals on the pressure *P* of the protective-gas atmosphere Ar + CO. (*1*) Concentration of *F* centers (experimental data); (*2*) concentration of oxygen vacancies in the Al_2O_3 melt (calculation for $P_{CO} = 0.01P_{Ar+CO}$); and (*3*) experimental and (*4*) calculated concentrations of microparticles.

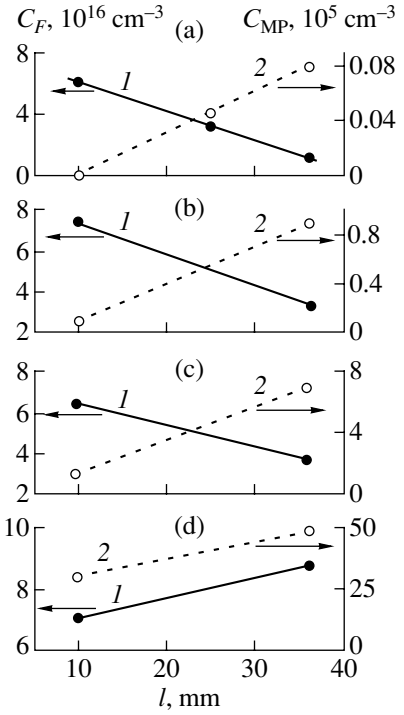

Fig. 2. Distribution of anion vacancies and microparticles over the crystal length. The crystals were grown in an Ar + CO atmosphere at P = (a) 10, (b) 30, (c) 100, and (d) 800 Torr. Concentrations of (*1*) F centers, C_F, and (*2*) microparticles, C_{MP}.

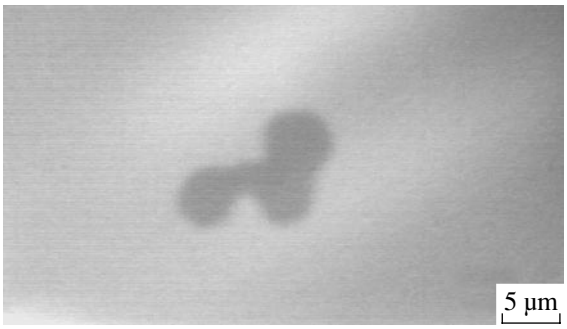

Fig. 3. Micrograph of a particle formed by the merging of several smaller ones.

are typical of the defects we are interested in—microparticles formed in sapphire crystals grown by the HDC method in a reducing-gas atmosphere—we investigated their sizes, shapes, and the character of their distribution over the crystal volume in detail.

The object of study was microparticles in leucosapphire single crystals grown at a rate of 1–60 mm/h in CO and Ar + CO atmospheres at pressures from 0.1 to 800 Torr. Crystals with (0001), $(10\bar{1}2)$, and $(11\bar{2}0)$ surfaces were analyzed.

The investigations revealed the following regularities:

Depending on the growth conditions, the concentration of microparticles in crystals is $\leq 10^4$–10^7 cm^{-3}. Depending on their size, microparticles can be divided into two groups: large (3–5 μm; less often, up to 10–15 μm) and small (~1 μm). With an increase in particle concentration, their average size decreases from 3–5 to 1–3 μm. Particles formed by the merging of several smaller ones were observed (Fig. 3). As a rule, particles are distributed in a statistically uniform manner. However, regions with higher microparticle density were observed in some cases. Microparticles also decorate block boundaries.

Microparticles have irregular shapes or are faceted (with a minimum size of ~2 μm). Faceting of smaller particles has not been reliably ascertained. If we assume that microparticles are vacancy pores (negative crystals), their faces should coincide with the crystallographic planes of the crystal itself, as was observed, for example, in [8] in studying sapphire crystals grown by the Stepanov method. However, we failed to establish such regularities. When a certain crystallographic plane of a sample was studied, the simultaneous existence of particles with different facetings was observed (Fig. 4).

These experimental data can be explained if we assume that the particles consist of $AlAl_2O_4$ and have a cubic spinel structure that determines their faceting. In this case, that particles with different facetings are observed in the same crystallographic plane can be explained as follows: Although these particles have a cubic faceting, they have different lengths in different directions and are inclined at different angles. Thus, observation of particles with different facetings is, apparently, only a visual effect related to the small size of the objects under investigation. The results of experiments in which crystal growth was stopped for a few hours and then renewed argue in favor of this idea. In this case, the crystallization front was decorated with larger (~10 μm) particles and chains of particles up to 50 μm long, located at the place where the front was stopped, in the front plane (Fig. 5). The large size of the particles quite reliably suggests that they are oriented parallel to the crystallization front and that their faceting is by and large similar to cubic.

Since the crystallization front has a convex shape and is tilted with respect to the crucible bottom, the shape of the projection of particles on the plane parallel or perpendicular to the crystal surface may change, depending on the particle position. As a result, particles with seemingly different facetings can be observed in the same crystallographic plane (Fig. 4). We should also note that no regularly shaped microparticles with sizes greater than 10–15 μm were observed. When microparticles greater than 3 μm in size merge, chains, rather than large particles of equilibrium shape, are primarily formed (Figs. 3, 5).

Thus, the investigation of the sizes, shapes, and distribution of microparticles did not allow an unambiguous assessment of their origin. The experimental data

obtained suggest their formation both in melt (for example, when crystals contain regions with higher particle densities that reproduce the shape of the crystallization front) and, it seems, due to solid-phase reactions (small faceted particles, see Fig. 4).

THE POSSIBILITY OF MICROPARTICLE FORMATION DUE TO SOLID-PHASE REACTIONS

The contradictory experimental data necessitated carrying out special investigations in order to determine the possibility of the formation of inclusions due to solid-phase reactions. It is well known that a high-temperature (~1900–1950°C) annealing of a crystal in an atmosphere with a high reducing potential may result in a high, in comparison with the as-grown crystal, concentration of anion vacancies in the crystal volume (up to ~10^{18} cm^{-3}), which exceeds the critical value of <10^{17} cm^{-3}. It was found that crystals grown under the aforementioned conditions always contain microparticles. At the same time, it is well known that a high concentration of anion vacancies (the result of annealing) does not lead to the precipitation of microparticles.

Therefore, if microparticles are formed due to solid-phase reactions, these reactions should occur at higher temperatures that are close to the melting temperature of α-Al_2O_3. To verify this idea, we performed the following experiments: In the first, crystal I was grown in a CO atmosphere at $P \sim 0.1$ Torr; in this case, no microparticles are formed. Argon was then fed into the growth furnace up to $P = 800$ Torr to form a reducing Ar + CO atmosphere—the conventional growth medium for crystals containing microparticles. A part of the grown crystal was melted, and the melt, together with the unmelted part, was kept in this atmosphere for 30 h, after which the growth of the remaining part was continued. In the second experiment, crystal II was grown in an Ar + CO atmosphere and, therefore, contained microparticles. The chamber was then evacuated to $P \sim 0.1$ Torr to form an atmosphere in which microparticles are not formed during crystallization. Part of the grown crystal was melted. Then, the melt, together with the unmelted part, was kept in the atmosphere for 30 h, after which growth of the remaining part of the crystal was continued.

The results of these experiments are shown in Fig. 6. The interface between the parts of the crystal grown under different conditions, which reproduces the shape of the crystal–melt interface (shown by an arrow), is an interesting object of study. It should be noted that the shape of the interface in the near-bottom part features an abrupt change in slope. It was suggested that, if microparticles are formed due to solid-phase reactions, because of the formation of microparticles in the unmelted part of crystal I, the region containing microparticles should shift to the beginning of the crystal within the time it is kept in the atmosphere (30 h). In crystal II, due to decomposition of microparticles in the unmelted part, the region that is free of microparticles should shift to the beginning of the crystal. Hence, in this case, we would observe a blurred interface between the parts grown under different conditions, as shown in Fig. 6 by the dotted line. If solid-phase reactions are not involved in the formation of microparticles, a clear interface should be retained.

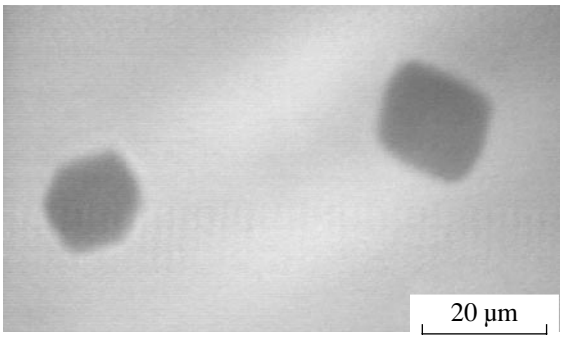

Fig. 4. Simultaneous existence of microparticles of different shapes in the same crystallographic plane ($11\bar{2}0$).

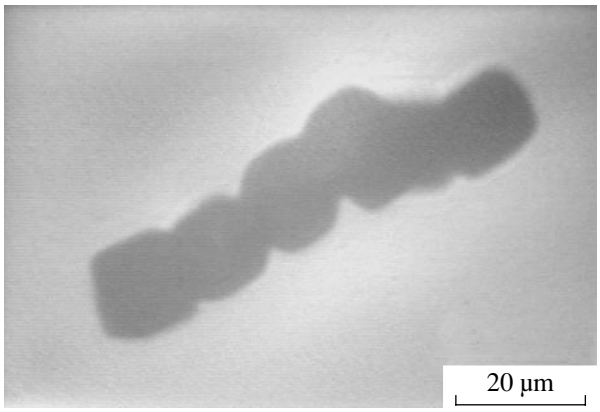

Fig. 5. Chain of large (~5–7 μm) particles located in the plane of the crystallization front (the crystallographic plane (0001)).

Microscopic studies showed the presence of a clear interface between the parts of a crystal grown under different conditions; no noticeable variations in the size and density of microparticles are observed near the interface (Fig. 6). Hence, microparticles are not formed in the solid phase. Moreover, they do not transform noticeably in the solid phase even at high (premelting) temperatures near the crystal–melt interface. For example, trends to neither decomposition, nor increase in size, nor merging of particles were observed in crystal II at the interface (Fig. 6c); i.e., the formation of these defects occurs in the melt or at the crystal–melt interface.

We may suggest that, when a deviation from stoichiometry occurs in the melt, the dissociation products

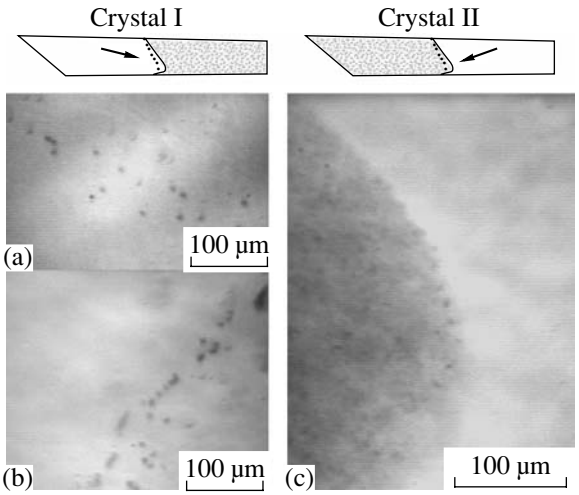

Fig. 6. Schematic diagrams of crystals with parts that were grown in atmospheres with different reducing potentials and the micrographs of interfacials between the parts grown under different conditions. (a) Top and (b) bottom parts of crystal I and (c) crystal II in the region where the slope of the crystallization front changes (individual particles are not visible).

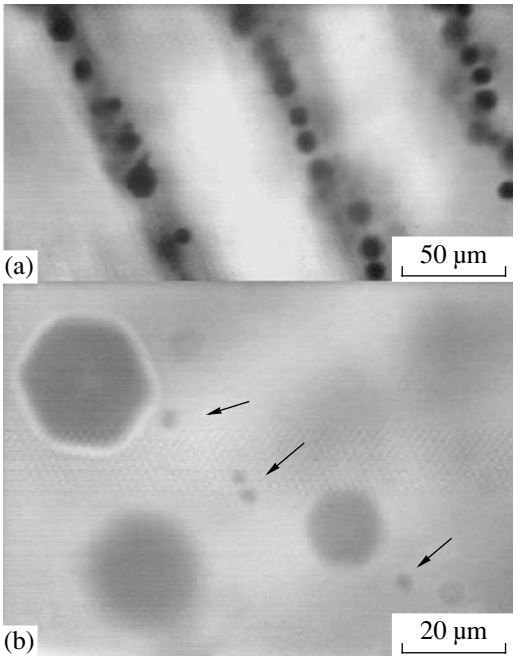

Fig. 7. (a) Chains of bubbles containing microparticles (individual particles are not visible) and (b) microparticles (shown by arrows) in the bubble chains; crystallographic plane ($11\bar{2}0$). The growth rate was 60 mm/h.

that are not involved in the formation of the stoichiometric grating of Al_2O_3 are "foreign" in the melt. If they are considered as impurities in the melt, an increase in their concentration should lead to supercooling of the concentration and the appearance of inhomogeneities at the crystallization front. In this case, the distribution of microparticles should be similar to that of the most conventional defects in sapphire crystals—ordered gas pores in the form of individual chains parallel to the direction of crystal growth [9]. However, our investigation showed that there are no fundamental differences in the size and distribution of microparticles in crystals grown in different crystallographic directions. Neither was ordering of particles revealed; random distribution was observed in the cases of both low (~10^4 cm^{-3}) and high (≤10^7 cm^{-3}) concentrations. Chains of microparticles were observed only when violations of the crystallization front occurred for other reasons, in particular, when the crystallization rate increased to 60 mm/h (Fig. 7). In this case, under conditions of concentration supercooling of the melt, chains of bubbles are formed in a crystal (Fig. 7a); the mechanism of this process was studied in detail in [9]. Small (~1 μm) microparticles are chaotically distributed between bubbles only within the chains (Fig. 7b), being absent in the gaps between. These experimental data indicate that the formation of microparticles occurs without significant violations at the crystallization front, which would lead to cellular crystal growth.

RESULTS AND DISCUSSION

These experimental regularities differ significantly from those observed upon formation of other conventional defects in sapphire crystals, for example, vacancy pores and gas bubbles. In such a case, the well-known mechanisms for the formation of macroscopic (≥1 μm) inclusions in crystals due to precipitation of an excess component both in the solid phase [8] and at the crystal–melt interface in depressions between cells [9] are not applicable. The model of bulk crystallization explains the mechanism of formation of light-scattering centers in crystals grown in reducing-gas atmospheres more reliably [10]. In this case, the mechanism of the formation of light-scattering centers can be represented as follows:

Due to the interaction with a reducing atmosphere, the composition of the Al_2O_3 melt deviates from stoichiometry: the melt becomes oxygen-depleted, and the composition of the dissociation products shifts to that of products having an excess of Al in comparison with the stoichiometric composition of Al_2O_3. The crystallization is bulk-type and begins even in the melt via the nucleation of clusters with a crystal-like structure. If the degree of deviation from the melt stoichiometry is low, the grown crystal captures vacancies. It seems that the limiting concentration of oxygen vacancies that can be captured does not exceed ~8×10^{16} cm^{-3}. If the deficit of oxygen in the melt exceeds this value, the dissociation products that are not involved in the formation of stoichiometric Al_2O_3 clusters are pushed to their boundaries. The accumulation of dissociation products with compositions that do not correspond to the stoichiome-

try of the Al_2O_3 lattice leads to the formation of clusters of another phase (depleted with oxygen). In fact, in the molten zone before the crystallization front, the melt separates into the Al_2O_3 phase and the phase depleted with oxygen, the trapping of which leads to the formation of microparticles in the grown crystal. At present, there are no direct data on the structure and composition of microparticles. However, the fact that small (~3–5 μm) microparticles are faceted and the independence of this faceting on the crystal structure suggest that the microparticles under study are neither vacancy clusters (negative crystal) nor gas-filled cavities. In our opinion, the most likely process is the formation of microparticles in the form of solid compound $AlAl_2O_4$ (Al–Al spinel), which is responsible for their cubic faceting.

REFERENCES

1. N. P. Katrich, A. Ya. Dan'ko, Yu. P. Miroshnikov, *et al.*, Ukr. Patent No. 18923A, Byull. Izobret., No. 6, 3.1.117 (1997).
2. A. L. Samsonov and S. V. Bodyachevskiĭ, Neorg. Mater. **24** (10), 1666 (1988).
3. A. Ya. Dan'ko, N. S. Sidel'nikova, G. T. Adonkin, *et al.*, *Functional Materials for Science and Engineering* (Inst. Monokrist., Kharkov, 2001), p. 200.
4. A. Y. Danko and N. S. Sidelnikova, Funct. Mater. **8** (2), 271 (2001).
5. B. D. Evans and M. Stapelbroek, Phys. Rev. B **18** (12), 7089 (1978).
6. N. E. Filonenko, I. V. Lavrov, O. V. Andreeva, and R. L. Pevzner, Dokl. Akad. Nauk SSSR **115** (3), 583 (1957).
7. A. A. Chernov, E. I. Givargizov, Kh. S. Bagdasarov, *et al.*, in *Modern Crystallography*, Vol. 3: *Crystal Growth*, Ed. by B. K. Vaĭnshteĭn, A. A. Chernov, and L. A. Shuvalov (Nauka, Moscow, 1980; Springer, Berlin, 1984).
8. T. N. Yalovets and V. A. Borodin, Neorg. Mater. **24** (6), 946 (1988).
9. N. P. Katrich, Yu. A. Borodenko, E. P. Solov'eva, and V. E. Kachala, *Single Crystals and Technology* (VNII Monokrist., Kharkov, 1975), No. 11, p. 20.
10. E. R. Dobrovinskaya, L. A. Litvinov, and V. V. Pishchik, *Corundum Single Crystals* (Naukova Dumka, Kiev, 1994), p. 139.

Translated by Yu. Sin'kov

Crystallography Reports, Vol. 49, No. 2, 2004, pp. 246–255. Translated from Kristallografiya, Vol. 49, No. 2, 2004, pp. 300–309.

CRYSTAL GROWTH

Phenomenon of Thermal-Field Jumps in Growth of Single-Crystal Sapphire Ribbons by the Stepanov and Horizontal Directional-Crystallization Methods[1]

P. I. Antonov*, S. I. Bakholdin*, L. L. Kuandykov*, and J. K. Linhart**

** Ioffe Physicotechnical Institute, Russian Academy of Sciences, Politekhnicheskaya ul. 26, St. Petersburg, 194021 Russia*

e-mail: pantonov@pop.ioffe.rssi.ru

*** Progressive Technologies, Benesovska, 10100 Prague 10, Czech Republic*

e-mail: prt@progtech.cz

Received May 16, 2003

Abstract—The phenomenon of thermal-field jumps in bulky single-crystal sapphire ribbons grown by the Stepanov and horizontal directional-crystallization methods is observed. Considerable jumps of thermal fields with up to 4-min duration and a 50°C amplitude were recorded at a distance of 40 mm from the crystallization front of ribbons grown by both methods. As a result, the crystals had considerable nonstationary thermoelastic stresses that could give rise to the formation of blocks and other structural defects. The jumps revealed considerably exceeded the noise level of the measuring system. Possible causes of oscillations of the radiative heat flow along an optically transparent sapphire crystal are considered. © *2004 MAIK "Nauka/Interperiodica"*.

INTRODUCTION

Growth of large single-crystal sapphire ribbons requires special control of the temperature distribution inside these ribbons [1]. Earlier, the thermal fields in crystals were studied mainly on sapphire single crystals with small transverse cross sections [2–4]. Growth of broad sapphire ribbons with a cross section of 50×6.5 mm and a low defect concentration by the Stepanov method [5] requires the measurement of the thermal fields in the ribbons (by the method of grown-in thermocouples). The first experiments [6] showed considerable jumps in thermocouple readings never observed in relatively thin crystals. Earlier, one of us (Linhart) observed similar jumps in growing crystals by the method of horizontal directional crystallization, but unfortunately did not published these results. Later, Linhart, Aronov, and Marchenko revealed and studied the phenomenon of thermal-field inversion in transparent crystals [7]. Below, we consider the phenomenon of thermal-field jumps in crystals grown by both above methods.

EXPERIMENTAL

Comparison of the Methods for Measuring Temperatures in Optically Transparent Sapphire Single Crystals

Temperature fields in growing sapphire single crystals can be measured either by a grown-in thermocouple [4] or by a pyrometer [8].

Optical pyrometer. Temperature fields in sapphire single crystals can precisely be measured by a special optical pyrometer operating in the IR range [9]. A pyrometer operates in a narrow spectrum range in the vicinity of $\lambda = 7.5$ μm, where a sapphire single crystal is not transparent irrespective of the temperature and where its effective blackness is close to unity, which allows one to avoid all the difficulties associated with the crystal transparency. The advantages of the pyrometer are high accuracy of measurements (0.7%), low inertia (0.2 s), and high resolution (0.5–0.6 K at the temperature of 2500 K). Before each scanning cycle, the pyrometer was tuned to the crystallization front, and the reference temperature was the temperature of the phase transition of sapphire. The pyrometer shortcomings are the complexity of its technical realization and the necessity of a slight "opening" of the thermal zone in order to let the pyrometer "see" a crystal, which somewhat distorts the thermal field. Moreover, the dimensions of the viewing windows of conventional setups for crystal growth are also limited. Therefore, in practice, such a pyrometer can be used for measuring temperatures only of some limited portions of the crystal. It was shown [8] that such a pyrometer can measure the temperature on shaped sapphire single crystals (thin-wall single-crystal sapphire tubes). However, this pyrometer is very attractive for studying temperature fields in sapphire plates grown by the method of horizontal directional crystallization.

Thermocouple. The method of a grown-in thermocouple is technically simple: a thermocouple is mounted at the end of a preliminarily grown crystal—a

[1] This work was presented at the National Conference on Crystal Growth (NCCG-2002, Moscow).

seed. During crystal pulling, the thermocouple is being incorporated into the crystal and, thus, "passes" all the regions of the hot zone and records the temperatures along the whole crystal length without changing screening. The shortcomings of the method are associated with the thermocouple inertia, losses in the electromotive force because of sapphire conductivity, and the influence of the electrodes and thermocouple junction onto the crystal temperature.

Thermocouple inertia does not allow one to make reliable measurements at a rate higher than one measurement per second. At a typical growth rate of shaped sapphire single crystals (1 mm/min), this measurement frequency is quite sufficient.

Additional difficulties are associated with different optical properties of the thermocouple junction and the corresponding volume of the single crystal. It is well known that the heat transfer in sapphire proceeds mainly due to the radiative heat flow along the crystal [10]. The thermocouple junction absorbs the heat radiation practically as an ideal black body, whereas the equivalent volume of a semitransparent sapphire crystal would absorb only a small fraction of the heat radiation determined by the absorption coefficient. In [11], the corresponding error was estimated for a cylindrical thin sapphire single crystal and a stationary temperature field. It was shown that, at the crystallization front, this error does not exceed 25°C and decreases along the crystal length. However, at fast variations of the radiative heat flow, some additional dynamical component of the error may arise because a semitransparent crystal is heated and cooled at a lower rate than the nontransparent thermocouple.

Stepanov Method

Growth of sapphire. The $\{11\bar{2}0\}\langle 10\bar{1}0\rangle$ oriented sapphire ribbons up to 200 mm in length and with a cross section of 50×6.5 mm (with the *c* axis being normal to the narrow side of the ribbon) were grown in the hot zone (resistive graphite heater) in the argon atmosphere. A molybdenum shaper was used. The pulling rate was constant in all the experiments (1 mm/min).

Thermocouple design. Thermal fields were measured by a built-in WR5/20 tungsten–rhenium thermocouple with electrodes 0.1 mm in diameter. Insulation was made of single-crystal sapphire with the electrodes in the hot zone being applied onto the opposite sides of a ribbon–seed and the insulating tubes touching neither the seed and nor one another. Only the horizontal end part of the thermocouple with the junction crossed the ribbon. This design minimizes both leakage current and heat removal along the thermocouple electrodes.

The thermocouple junction was placed into a transverse ~2-mm-deep notch. Upon the formation of a liquid column at the moment of seeding, the melt filled the notch, where it was instantaneously crystallized. Then, the seed was slightly melted, so that the thermocouple turned out to be incorporated into the ribbon (by 0.2–0.3 mm above the crystallization front) without having a contact with the shape former (in order to avoid welding).

Temperature measurements and noise evaluation. The emf of a thermocouple was measured by a 16-digit A/D converter with a preamplifier (National Instruments 6B11 input module) and was recorded by a computer. The same module also recorded the temperature of the cold ends of the thermocouple at the beginning and the end of the experiment. In the process of thermocouple incorporation into a crystal, the thermocouple readings were recorded every 5 s.

The nominal error in temperature readings in the vicinity of 2000°C was ±13°C. However, the real accuracy of temperature measurements was much higher because we measured not the absolute temperature, but its variation with respect to the melting point (2050°C, the reference temperature in all the measurements). In order to determine the measurement error, we recorded the thermocouple readings each second under the following conditions:

—the intrinsic noise of the thermocouple and the measuring system (in vacuum without heating) was ±0.3°C;

—the noise of a freely hanging thermocouple in the heated chamber filled with argon was ±0.5°C;

—the noise of a freely hanging thermocouple in the notch (at a seed connected with the shaper) was ±2–3°C.

Thus, the relative error in the thermocouple readings did not exceed ±3°C.

Horizontal Directional Crystallization

The (250–270) × 150 × (20–25)-mm sapphire plates were grown by the method of horizontal directional crystallization in a tungsten thermal unit at a rate of 4–8 mm/h. The setup had a CaF_2 window (100 mm in length and 20 mm in width) for tuning a special IR pyrometer.

At each scanning cycle, the pyrometer was tuned to the interface, and this point was used as the reference point, 2053°C. All the measurements, both in crystals and in melts, were made relative to this point, which excluded the influence of possible contamination of the CaF_2 window. Moreover, to increase the experimental accuracy, a specially designed multielement gradient transducer (described in detail in [12]) was used in some experiments. The characteristic feature of the gradient transducer allowed one to determine the position of the crystallization front automatically from the jump in the intensity in the visible range of the spectrum. Then, the measurements were made in the range of sapphire nontransparency with respect to the sapphire melting point. The diameter of the spot of the tuned pyrometer was 1 mm, and that of the gradient transducer, 0.7 mm. The pyrometer scanned the temperature

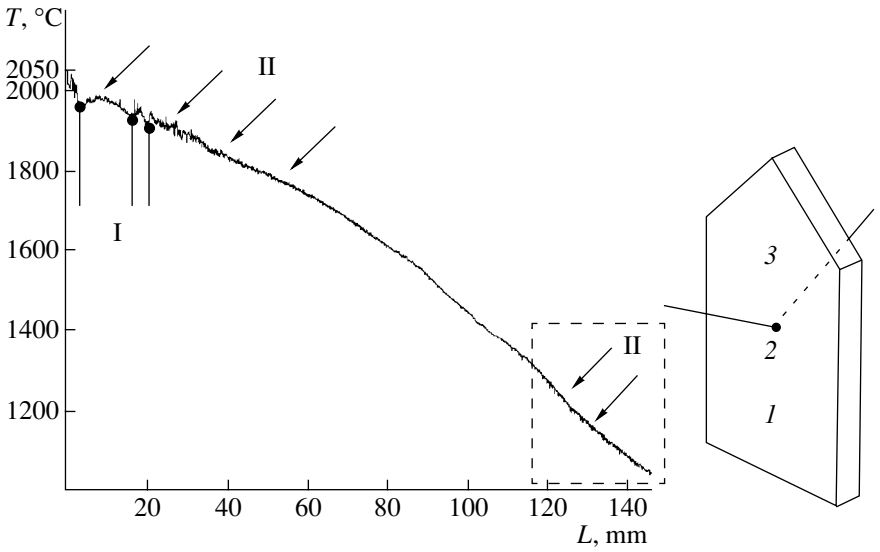

Fig. 1. Readings of a thermocouple grown into a 50×6.5-mm single-crystal sapphire ribbon at a distance of 50 mm from the upper end. (*1*) Single-crystal ribbon, (*2*) thermocouple junction, (*3*) seed. Pronounced temperature jumps (I) are observed within the first 30–40 mm of the crystal length in the high-temperature range (2050–1850°C). Usually, 3–4 jumps with an amplitude of 30–50°C are observed within 2–4 min and up to 10 low jumps with the amplitude of 10–20°C are observed within 1 min (II). Dashed line indicates the region of low jumps with increasing amplitudes outside the hot zone ($L > 120$ mm).

field along the crystal axis for a length of 150–180 mm within 20–30 s. The gradient transducer scanned automatically and almost instantaneously the phase-transition region from 0 to a length of 50 mm.

RESULTS

Stepanov Method

Altogether, we performed six experiments on temperature measurements in the ribbons, which can be divided into three groups.

I. Experiments with seeds having the same cross sections as the cross sections of growing ribbons. Seeding was made over the whole width. Ribbons–seeds were 10, 20, and 50 mm in length. In all the cases, the temperature distributions over the crystal length L (Fig. 1) were similar. All the curves obtained in this experimental series showed two types of jumps in the thermocouple readings. After seeding, pronounced jumps were observed in the high-temperature regions (2050–1850°C) of newly grown crystals within the first 30–40 mm of their length. Usually, we observed from three to four 30–50°C jumps with a duration from 2–4 min each. Moreover, these jumps were often accompanied by numerous small (10–20°C) jumps observed within several seconds.

In one of the experiments, after the passage of the region of large jumps, crystal pooling was stopped at a crystal length of 40 mm. However, we still observed small jumps of the same amplitude and duration even without crystal pulling.

II. In this experiment, point-like seeding was used with a thin $(0001)\langle 10\bar{1}0\rangle$ oriented ribbon with a cross section of 8×2 mm and the c axis being normal to the broad side of the ribbon. Before seeding, the ribbon was "sharpened up" to a cross section of 3×2 mm and was set with its broad side across the shaper (Fig. 2). The thermocouple was built-in directly under the thin seed. The general distribution of large and small jumps remained unchanged, but their amplitudes decreased.

III. In this experiment, the starting material contained an impurity, and the growing crystal was turbid because of a large number of small pores. By the end of this experiment, the heater power dramatically increased, which indicated an increase in the crystal transparency and radiative heat flow [13, 14]. The seed was 80 mm in length (Fig. 3). No pronounced jumps were observed, whereas small jumps were observed only after the crystal length attained 120–150 mm. The kinks of the curve at a crystal length of 50–100 mm are associated with the exit of the crystal from the zone of thermal screens.

In some experiments of series I, we also observed a slight increase in the amplitude of small jumps at the crystal lengths $L > 120$–150 similar to an increase in the jump amplitude observed in the experiment with a turbid crystal (Fig. 3).

Method of Horizontal Directional Crystallization

The measurements were performed directly in the technological process with the aid of both an IR pyrometer and a gradient transducer, which allowed us to measure the exact length of the crystallized part of the

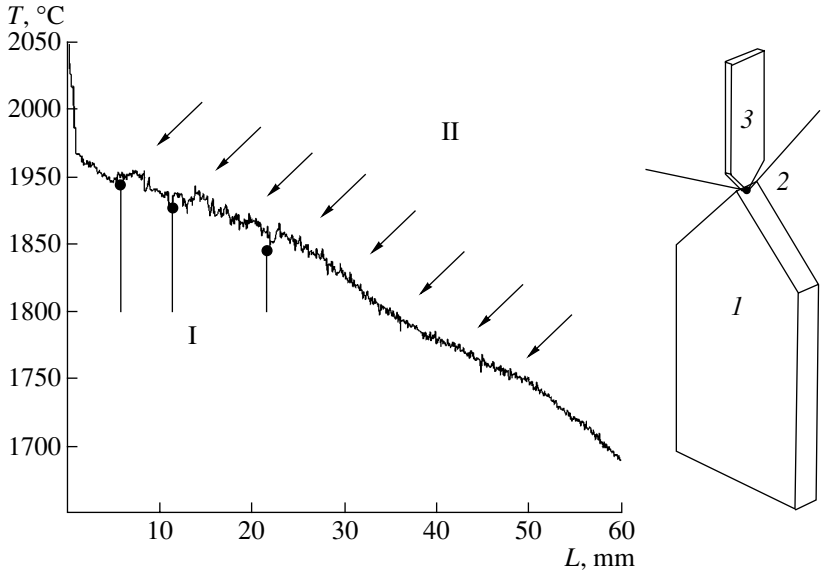

Fig. 2. Readings of a thermocouple built into a 50 × 6.5-mm single-crystal sapphire ribbon under a thin 8 × 2-mm (*3*) seed. For notation, see Fig. 1.

melt. The temperature jumps were recorded by both devices. It is seen from Fig. 4 that the temperature jumps arise almost in the same region of the crystal irrespective of its length, with the oscillation amplitude being 45–50°C.

POSSIBLE NATURE OF JUMPS

The jumps in the thermocouple and pyrometer readings can be interpreted as dramatic oscillations of the radiative heat flow in a crystal. Let us consider various possible sources of the radiation that arrives to the given point of the crystal and the causes giving rise to oscillations of these flows.

Heat flow from the crystallization front, the melt layer, and the shaper with due regard for its shape (Stepanov method). A radiative heat flow may oscillate because of variations in the melt-layer thickness, transparency, or periodic formation of a layer of gas bubbles in the liquid. Let us estimate possible oscillations in the temperature of a heat flow that enters the crystal. Assuming that the shaper and the melt layer are flat and have the same temperature, which is approximately equal to the melting point (for sapphire, T_m = 2323 K), one can introduce the effective temperature of a radiation flow entering the crystal, T_R. This temperature is equal to the temperature of an ideal black body emitting a radiation flow which is numerically equal to the sum of the flows from the melt layer and the shaper at a level of the crystallization front:

$$\sigma T_R^4 = \sigma T_m^4 (1 - e^{-kh}) + \sigma T_m^4 \varepsilon e^{-kh}, \qquad (1)$$

where $\sigma T_m^4 (1 - e^{-kh})$ is the radiation flow from the melt layer of the thickness h with the absorption coefficient k, $\sigma T_m^4 \varepsilon e^{-kh}$ is the radiation flow from a shaper with the efficient blackness ε partly absorbed by the melt layer, and σ is the Stefan–Boltzmann constant. We obtain from Eq. (1)

$$T_R = T_m \sqrt[4]{1 - (1 - \varepsilon) e^{-kh}}. \qquad (2)$$

Up to the melting point, a solid sapphire crystal is a weakly absorbing medium with the absorption coefficient $k \le 0.3$–0.5 cm^{-1}. However, the absorption coefficient of the melt is k = 25 cm^{-1} (0.6 μm) [15], and the characteristic absorption length is about 0.4 mm. Approximately, this corresponds to the thickness of the melt layer in the Stepanov method. Consider three possible cases of kh values.

$kh \ll 1$. If a melt layer is either rather thin (h is low) or is transparent (k is low), then $kh \ll 1$, and the radiation flow from the shaper is very weakly absorbed by the melt layer, and the melt layer almost does not emit any radiation flow. In this case, $T_R = \sqrt[4]{\varepsilon} T_m$ and, at ε = 0.7, Eq. (2) yields T_R^a = 2125 K.

$kh \gg 1$. This case is possible if the radiation flow from the shaper is almost completely absorbed in the melt (thick or low-transparency melt layer), whereas the melt itself emits the radiation flow almost as an ideal black body. In this case, $T_R^b = T_m$ = 2323 K. The difference $\Delta T_R = T_R^b - T_R^a$ = 198 K is the maximum estimate of possible jumps in the thermocouple readings.

$kh \sim 1$. It is this intermediate case that may be observed in practice. With the change of the parameter kh from 0.5 to 0.7, Eq. (2) shows the jump in the effective temperature of the radiation, ΔT_R = 27 K. This

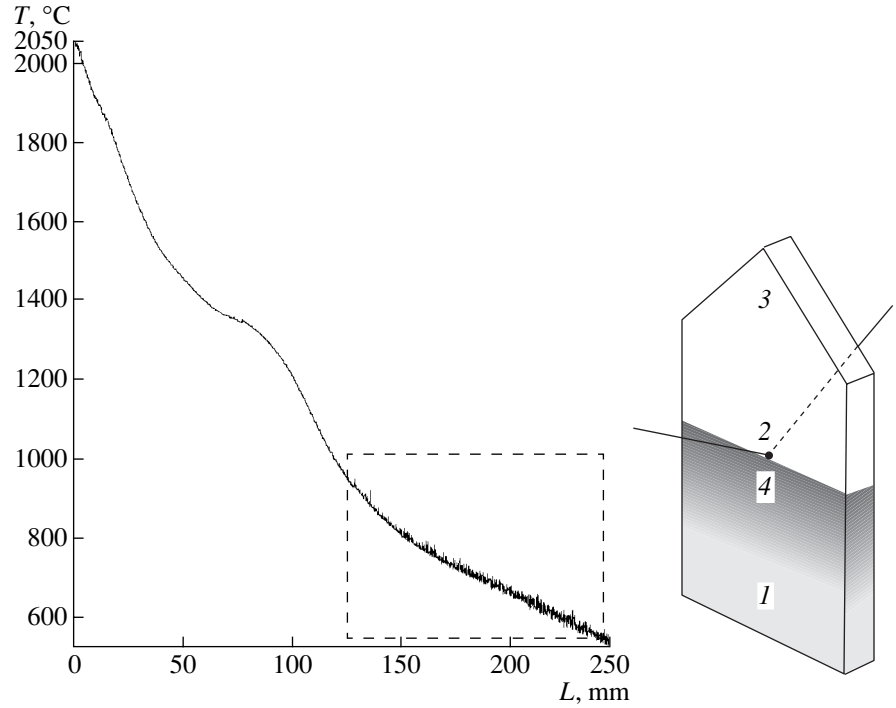

Fig. 3. Readings of a thermocouple grown into a 50×6.5 mm turbid single-crystal sapphire ribbon (*4*) whose transparency increases to the end of the growth process. The thermocouple was grown into a ribbon at a distance of 80 mm from the upper end. The region in the gray rectangle shows an increase in the low-jump amplitude for a crystal taken away from the hot zone ($L > 120$ mm). For notation, see Fig. 1.

change in kh may take place, e.g., if the melt-layer thickness h (i.e., the height of the crystallization front) with $k = 25$ cm^{-1} changes from 0.2 to 0.28 mm and, at $h = 0.2$, varies from 25 to 35 cm^{-1}.

These estimates agree with the experimental amplitudes of pronounced jumps, 30–50 K. The fact that no jumps were observed for thin crystals can be explained by oscillations in the melt transparency. It is possible to assume that the melt in the crucible is optically inhomogeneous. It can contain regions having different transparencies and, thus, different radiative powers. The jumps observed in the Stepanov method can be caused by the periodic arrival of such melt portions to the shaper. In this case, the dimension of the region with jumps depends on the rate of mass crystallization. The cross-section area of a tube with a diameter of 8 mm and a wall thickness of 1 mm is less (by a factor of 15) than for the ribbons under consideration, with the pulling rate being approximately the same. Thus, the rate of mass crystallization of a tube is also lower by a factor of 1.5, and the region of jumps should increase by 30–60 mm, i.e., should be extended over the whole high-temperature region. A jump of such a duration in a thin-wall crystal requires measurements of the crystal temperature at several points by one thermocouple, which is impossible. At the same time, the changes in the readings in different experiments could mistakenly be considered as thermocouple error.

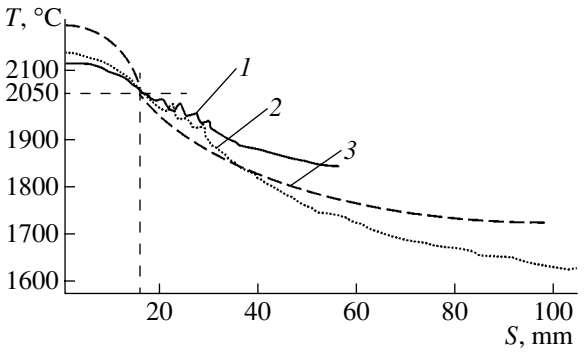

Fig. 4. Temperature variations behind the crystallization front measured by an IR pyrometer in a single-crystal sapphire plate obtained by horizontal directional crystallization. *1*, Crystal length 45 mm, *2*, crystal length 90 mm, *3*, crystal grown from a considerably overheated melt, *S* is the scanned region.

The fact that the pronounced jumps are observed only at the initial stage of growth also indicate an important role played by the oscillations of the flow coming to the crystal from the melt through the crystallization front. With an increase of the distance to the crystallization front in the flow recorded by the thermocouple, the flow components from the lower parts of the crystal start dominating, and the jumps of the radiation flow from the front stop being noticeable.

Possibly, the shape of the crystallization front also influences the formation of nonuniform temperature

distribution. Usually, a shaper in the Stepanov method has "skewed" edges. In growth of large crystals, this can change the character of the radiative-flow propagation, especially, at the crystallization front. In growth of thin crystals, curvature influences the character of the radiation-flow propagation to a considerably lesser degree.

Melt convection. In Czochralski growth of semiconductor crystals, the thermal flow from the melt to the crystallization front fluctuates because of the irregular free convection caused by the temperature gradient in the crucible [16, 17]. The oscillation amplitude equals several degrees centigrade and the oscillation frequency ranges from 0.5 to 0.01 Hz. Fluctuations increase with a decrease in viscosity. Moreover, depending on the Rayleigh number, a cellular convection may arise and disappear in different regions of the melt.

It has been established experimentally [18] that in Stepanov growth of Si ribbons, the temperature of the shaper contacting the melt oscillated with an amplitude of 0.5–5.0°C and a frequency of 0.5–0.005 Hz. These oscillations were explained [18] by fluctuations of the melt temperature in the crucible because of nonstationary convection.

It cannot be excluded that similar phenomena may also take place in our case, despite the fact that the properties of the melt and the shaper material and the mechanism of heat transfer in the present study considerably differ from those in growth of semiconductor crystals.

Thermal-field inversion. The phenomena of nonmonotonicity and inversion of the temperature field in optical materials described in detail elsewhere [15] allow one to interpret the temperature jumps revealed. Inversion can be observed in an optically transparent body with a diffusely scattering boundary. In the crystal–melt system, the role of such boundary can be played by the region of the crystallization front because of the accumulation of microbubbles in the adjacent melt layer and also because the front is diffuse.

Figure 5 shows nonmonotonic and inverse temperature distribution in a transparent body with varying optical thickness, which contains an internal diffusely transmitting boundary (flat layer). The phenomenon of inversion can arise both in a crystal–melt system (then the role of the diffuse boundary is played by the region of the crystallization front) and in the local portions of the crystal.

Formation of a diffuse boundary that gives rise to thermal-field inversion. Layer of microbubbles. Figure 6 illustrates the formation of a layer of microbubbles in the method of horizontal directional crystallization and in the Stepanov growth. At some moments, a layer of microbubbles can be accumulated at the crystallization front from the side of the melt. The dimensions of these microbubbles are comparable with the thermal-radiation wavelength, and, therefore, their transfer to the surface by convective flows is rather difficult. In this case, the crystallization front starts diffusely emitting a thermal flow into the crystal and also diffusively scattering the thermal flow that comes from the melt volume. These processes create the necessary prerequisites for the inversion of the temperature field in the crystal.

Consider three main acting forces that determine the velocity of floating-up of a microbubble to the surface (Figs. 6a, 6b). These are:

—the Archimedes force

$$F_1 = \rho g V, \tag{3}$$

where ρ is the melt density in the vicinity of a microbubble, g is the gravitation constant, V is the volume of a microbubble with the radius r equal to the volume of the sphere $V = 4\pi r^3/3$;

—the force F_2 related to inhomogeneity of the temperature field

$$F_2 = (\rho - \rho_0)gV = g\rho\beta V\Delta T, \tag{4}$$

where β is the volume expansion coefficient, ΔT is the difference between the temperatures under and above the microbubble, and ρ_0 is the melt density in the region with a higher temperature;

—and the reactive force acting onto a microbubble moving in the liquid with the viscosity η at a velocity U (Stokes formula)

$$F_3 = 6\pi\eta r U. \tag{5}$$

In horizontal directional crystallization, the forces F_2 and F_3 are directed opposite to the Archimedes force F_1 (Fig. 6a) ($F_1 = F_2 + F_3$), whereas in the Stepanov method, the situation is opposite; floating-up of a bubble to the surface is hindered only by the viscous- friction force F_3 (Fig. 6b) ($F_1 + F_2 = F_3$). However the crystallization rate is higher by an order of magnitude, and, with an increase in a crystal thickness, a microbubble has not enough time to float up to the surface.

It is seen from Eq. (5) that the lower the melt viscosity, the higher the velocity of a bubble floating up to the surface. Thus, because of considerable overheating of the sapphire melt, some convective flows arise, which are rather intense because of the low sapphire viscosity at high temperatures [19] (Fig. 7). However, in the direct vicinity of the crystallization front, the melt viscosity increases, and the velocities of these laminar convective flows dramatically decrease. Obviously, floating-up of microbubbles to the surface in a highly viscous melt becomes very difficult, and the necessary buoyancy can be created only if the microbubbles coalesce into larger formations; otherwise they will be captured by a growing crystal. Because of low growth rates, the diffuse character of the crystallization front can be preserved for a rather long time and can periodically be changed.

The curves in Fig. 4 obtained in crystal scanning by a pyrometer in the horizontal directional crystallization differ from the curves measured by a thermocouple

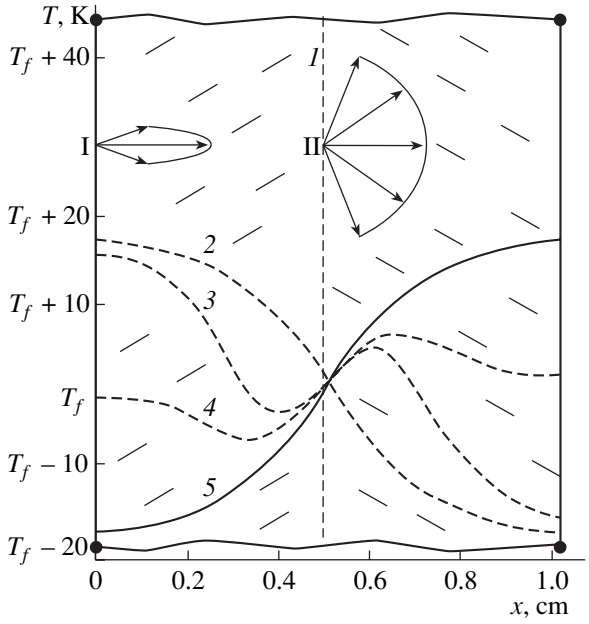

Fig. 5. Formation of temperature inversion in a transparent body (or in two contacting bodies with different optical thicknesses in the presence of an internal diffusely transmitting boundary in the shape of a flat layer (dashed line *1*). The radiation source is at the point $x = 0$, the absorber is at the point $x = 1$ cm. I is the radiation from the boundary $x = 0$, II is the radiation scattered by a diffuse boundary, and T_f is a certain characteristic temperature. If the diffuse boundary is a crystallization front, the T_f is the phase- transition temperature. *2* is the conventional temperature distribution in the absence of a diffuse layer, *3, 4* show the nonmonotonic temperature distribution, and *5* is the inverse temperature distribution.

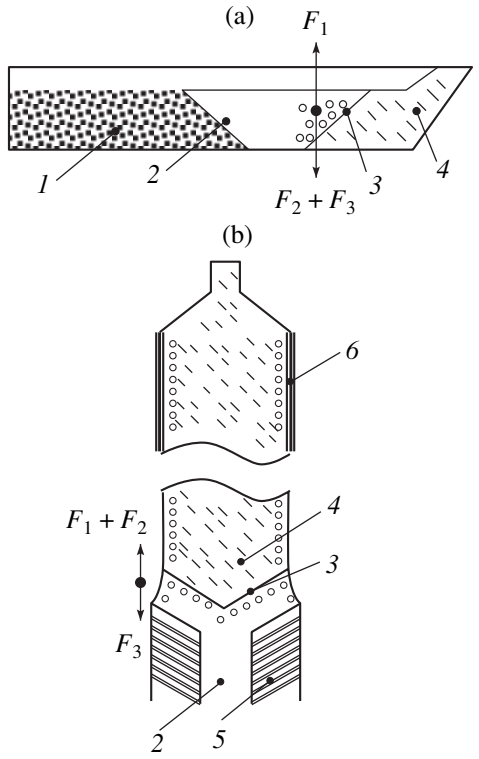

Fig. 6. Distributions of microbubbles and the force determining microbubble floating-up to the surface. (a) Horizontal directional crystallization, (b) the Stepanov method. (*1*) Starting material, (*2*) melt, (*3*) crystallization front, (*4*) crystal, (*5*) shaper, (*6*) graphite film, (F_1) Archimedes force, (F_2) force caused by an inhomogeneous temperature field, and (F_3) viscous-friction force.

because, in fact, they represent the instantaneous temperature distribution over the crystal. Therefore, the scanned region in which jumps were observed can be compared with a concrete region in a crystal grown. Analysis of the crystals grown by the method of horizontal directional crystallization showed that a layer of microbubbles (1–2 μm in size) arise approximately at the sites of temperature jumps. The size of the microbubbles approximately equals the wavelength of the intensity maximum of the radiative flow at these temperatures. Under melt overheating to 2600–2650 K, no temperature jumps were observed in the crystal. This is explained by the fact that a decrease in the temperature gradient over the crystal thickness and an increase in melt overheating, i.e., the narrowing of the weak-convection region before the crystallization front, considerably reduces the probability of microbubble capture by the crystallization front.

Side surface of a crystal and subsurface bubble layer. When growing shaped sapphire single crystals by the Stepanov method, one always observes the formation of a subsurface microbubble layer (tens of microns) at distances of 0.1–0.3 mm from the side surface (Fig. 7b). This is associated with the specific features of the melt flow in the melt column [20]. Possibly, in addition to the individual macrobubbles, a layer of microbubbles also forms in this region, which diffusely scatters the radiation coming to the crystal from the screens and the heater via its side surface. This can give rise to the formation of a nonmonotonic temperature distribution having the form of small jumps at considerable distances from the crystallization front.

Moreover, in the graphite zone, the crystals grown are always coated with a finely dispersed film of graphite particles deposited onto the crystal during its removal from the hot zone (at $L > 120$ mm). Graphite films were observed on the crystals in all the growth experiments by the Stepanov method. This film can play the role of a diffuse boundary necessary for the appearance of temperature jumps. Since this film becomes thicker with time, whereas the layer becomes more and more diffuse, the amplitude of small jumps should also increase. The increase in the small-jump amplitudes in Figs. 1 and 3 corresponds to the exit of the crystal from the hot zone and beginning of the formation of a graphite film on the crystal. These experiments clearly show the relation between the formation of a diffuse boundary and the appearance of thermal-

field inversion that gives rise to small temperature jumps.

Crystallization front. An interface has a rather complex structure and, mathematically, cannot be considered as a smooth surface. The crystallized part of the material is always preceded by a very thin material layer whose nature (liquid or solid) cannot be determined. In other words, it is a layer with a partially ordered structure (crystal) and chaotic mobility of some molecules. It is this layer that may capture microbubbles that later may enter the crystal.

The formation of a microbubble layer is not a necessary condition for the manifestation of inversion—this layer only substantially enhances the effect. The radiative flow from the melt arrives, and, because of the considerable difference between the absorption coefficients of the melt and the crystal, it is practically black with respect to the crystal, i.e., in accordance with the Planck function, the melt emits a radiative heat flow to the crystal. It should also be noted that the radiative flow passing through the crystallization front is diffusely scattered by a growing crystal because, as was already noted, the interface is not smooth. In the same way, the interface, or a rather thin layer before the crystallized phase, emits the heat flow also somewhat diffusely. In any case, we consider here a diffusely transmitting and emitting boundary. Moreover, in sapphire, the crystallization front is always diffuse because of the jump in absorption.

Thermal-field inversion as a cause of nonmonotonic temperature distribution in a crystal. Microbubbles with dimensions comparable with the thermal-radiation wavelength increase scattering and the degree of diffusion can attain unity; in other words, the radiation in the crystal is of a diffuse nature. The surfaces of the elements surrounding a growing crystal show mainly specular reflection. In horizontally directed crystallization, specular reflection is observed from mirror-smooth walls of a molybdenum container; in the Stepanov method, from the heating elements, the smooth surface of a growing crystal, the thermal insulating screens, etc. As a result, at a certain optical thickness, a certain part of the heat radiation is "closed" in a growing crystal and gives rise to the formation of a nonmonotonic thermal field. The inversion radiation from a cool part of the crystal is less intense and, moreover, with the arrival at the crystallization front, this radiation is diffusely scattered back into the crystal. As is seen from Fig. 5 (curves *3* and *4*), the inversion is not necessarily complete. The complete inversion is the limiting case and may arise only under certain conditions. Nonmonotonic temperature distribution results in the fact that the temperature drops in some regions of the growing crystal, whereas, in some other regions, it increases.

Earlier, we performed the model calculations for calcium fluoride in which the absorption coefficient, contrary to its jumpwise increase in sapphire, smoothly increases with temperature. The nonmonotonic temperature distribution can arise only in some rare cases where the crystallization front captures impurities. As soon as the crystallization front stops being diffusely transmitting and radiative, nonmonotonicity disappears, and the hot radiation stops "being closed" in the crystal. This effect was also calculated theoretically for the thinnest strongly absorbing germanium and silicon layers [21].

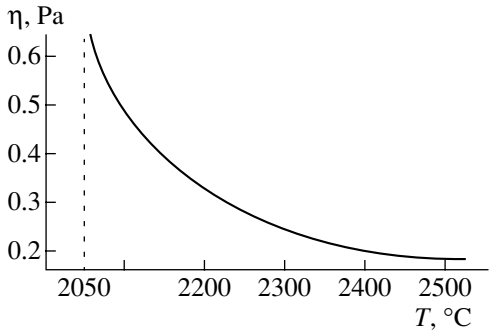

Fig. 7. Viscosity η of a sapphire melt as a function of temperature *T*.

Because the nonmonotonicity is uniquely related to the optical thickness (ranging within certain limits), this phenomenon should be observed in the direct vicinity of the crystallization front. At low optical thicknesses (thin crystals), the key part in the formation of the temperature gradient in the vicinity of the crystallization front is played by the molecular heat conductivity of the crystal. The thermal radiation passes through the crystal as in a light guide and, therefore, the reverse flows cannot play any important role in the formation of the temperature field. Therefore, the temperature curve of thin crystals remains smooth and shows no jumps in temperature.

TEMPERATURE-FIELD JUMPS AND REAL STRUCTURE OF A CRYSTAL

Evaluation of the maximum possible thermoelastic stresses. The temperature jumps up to 50°C can give rise to nonstationary temperature stresses in a crystal which influence the structure formation. We evaluated the maximum thermoelastic stresses by calculating stresses in a 50 × 130-mm isotropic two-dimensional sapphire ribbon in a thermal field (a curve analogous to the curve of thermocouple readings shown in Fig. 2 (using the Cosmos/M 2.6 package of programs based on the finite-element method [22]). Thus, assuming that the crystal temperature varies in a way similar to the temperature of the thermocouple junction, the temperature oscillations should give rise to the thermoelastic stresses as large as 60–100 MPa for pronounced jumps. These values considerably exceed the critical shear stresses at these temperatures (~1 MPa). However, the volume of a semitransparent sapphire would have a considerably higher thermal inertia than the volume

occupied by the thermocouple junction. It is difficult to say whether fast oscillations (compared to the pronounced 2–4-min-long jumps) would be able to heat a sapphire crystal. However, even a certain fraction of the stresses caused by the pronounced jumps are sufficient to give rise to plastic deformation. Cyclic jumps should accelerate the motion and rearrangement of the dislocations formed. The dislocation density exceeds the critical value, which, in turn, leads to the formation and development of a block structure [23].

It should be noted that, even under the assumption that there are no temperature jumps, the general character of the temperature distribution in thick ribbons differs from that observed in thin crystals. Therefore, the character of the stress fields should also change. At present, it is difficult to establish the structural characteristics of thick ribbons caused by temperature jumps.

Effect of orientational twisting. In thin-walled single-crystal sapphire tubes, the so-called twisting effect was revealed—the gradual change of the crystallographic orientation of a crystal via its rotation about the pulling direction coinciding with the optic axis [24]. Twisting was observed during the formation of a block structure from somewhat misoriented blocks. Misorientation of the blocks was not random and the blocks were "accumulated" along the crystal length, which resulted in a change of the crystal orientation as a whole with an average rate of ~0.5 deg/cm (up to 100 at a length of 200 mm). It was assumed that twisting is the result of the adaptation of the crystal to the growth medium. However, the driving force giving rise to the change of orientation is unknown. Usually, the formation of a block structure is observed at the initial stage of crystal growth under pronounced nonstationary thermal conditions. If the level of thermal stresses in the crystal during its further growth is low, only one block may survive, e.g., as in narrow sapphire ribbons [25]. At a higher stress level, the processes of tapering of the blocks with unfavorable orientations and formation of new dislocation boundaries due to plastic deformation in the hot zone result in the formation of a relatively stable block structure (Verneuil method [26], broad ribbons and other shaped crystals [27]). However, no rotation of the average crystal orientation is observed. The situation is quite different if continuous thermal-field jumps are observed in the hot zone. Then, in accordance with the above evaluation, the passage of a jump results in high stresses and intense generation of new dislocations. In the intervals, the stresses between the jump fronts decrease, and the crystal turns out to be under conditions of high-temperature annealing. This gives rise to the fast changes in the lengths of the block boundaries and the angles of their misorientations [28]. These nonstationary conditions may give rise to continuous development of the block structure and a gradual change of the crystal orientation.

CONCLUSIONS

The phenomenon of thermal-field jumps is observed in bulk single-crystal sapphire ribbons grown by the Stepanov (50 × 6.5 mm) and horizontal directional crystallization (150 × 20–25 mm) methods. Within the first 30–40 mm of the crystal length, 3–4 jumps with the amplitude 30–50°C are observed within 2–4 min, which are accompanied by up to ten low jumps with the amplitude 10–20°C observed for 1 min along the whole crystal length.

The jumps observed considerably exceed the noise of the measuring system and seem to be caused by the oscillations of the radiative flow propagating along the optically transparent sapphire crystal.

The following most probable causes of the jumps are considered:

—oscillations of the radiative thermal flow that enters the crystal through the crystallization front. This flow is formed by the shaper and a thin layer of the melt in a liquid meniscus (Stepanov method) or by a relatively thick layer of the melt (horizontal directional crystallization). The flow oscillations can be caused by variations in the optical properties of the melt (absorption or scattering by a layer of microbubbles) and small variations of the shaper temperature (Stepanov method);

—periodic temperature-field inversion in a semitransparent crystal. The role of a diffuse boundary (necessary for the appearance of the inverse temperature distribution) can be played by a layer of gas microbubbles in the melt formed before the crystallization front, a rough side surface of the crystals coated with a graphite film, a layer of subsurface microbubbles in the crystal (this assumption is confirmed by the experiments performed in this study), a rough crystallization front, and the microbubbles accumulated in the crystal bulk. All the above phenomena may be nonstationary and give rise to an inverse temperature distribution in the hot zone of the crystal and jumps in the radiative heat flow.

Of course, there are also some other factors that may cause temperature jumps, such as change in the conditions of formation of a light-guide flow in a crystal because of small variations in the cross-section dimensions and temperature variations resulting from melt convection in the crucible.

In all the cases, the jumps in the radiative heat flow can result in a nonstationary temperature distribution and the corresponding thermal stresses. Pronounced jumps can give rise to considerable plastic deformation inhomogeneous with respect to time and crystal volume. This deformation may manifest itself in generation of dislocations and acceleration of their rearrangement. In this connection, the phenomenon of the temperature jumps may influence the formation of the defect structure of the crystal grown and, therefore, requires further detailed study.

REFERENCES

1. P. I. Antonov, E. V. Galaktionov, V. M. Krymov, *et al.*, Izv. Akad. Nauk SSSR, Ser. Fiz. **40** (7), 1419 (1976).
2. P. I. Antonov, S. I. Bakholdin, E. A. Tropp, and V. S. Yuferev, J. Cryst. Growth **50**, 62 (1980).
3. P. I. Antonov, S. I. Bakholdin, M. G. Vasil'ev, *et al.*, Izv. Ross. Akad. Nauk, Ser. Fiz. **58** (9), 72 (1994).
4. V. M. Krymov, V. N. Kurlov, P. I. Antonov, *et al.*, J. Cryst. Growth **198–199**, 210 (1999).
5. P. I. Antonov, S. I. Bakholdin, A. S. Vlasov, *et al.*, in *Abstracts of X National Conference on Crystal Growth* (Moscow, 2002), p. 149.
6. S. I. Bakholdin, L. L. Kuandykov, and P. I. Antonov, in *Abstracts of X National Conference on Crystal Growth* (Moscow, 2002), p. 254.
7. B. I. Aronov, J. K. Linhart, and N. V. Marchenko, Teplofiz. Vys. Temp. **27** (4), 737 (1989).
8. A. L. Alishoev, L. M. Zatulovskiĭ, J. K. Linhart, and D. L. Shur, Izv. Akad. Nauk SSSR, Ser. Fiz. **52** (10), 1985 (1988).
9. J. K. Linhart and V. A. Petrov, Teplofiz. Vys. Temp. **18**, 174 (1980).
10. V. S. Yuferev, Prikl. Mekh. Tekh. Fiz., No. 4, 31 (1978).
11. V. S. Yuferev, Zh. Tekh. Fiz. **51**, 190 (1981) [Sov. Phys. Tech. Phys. **26**, 112 (1981)].
12. J. K. Linhart, USSR Inventor's Certificate No. 1333013 (1987).
13. S. F. Burachas, O. D. Kolotiĭ, and B. L. Timan, Kristallografiya **43** (5), 949 (1998) [Crystallogr. Rep. **43**, 894 (1998)].
14. A. V. Moskalev, S. I. Bakholdin, V. M. Krymov, *et al.*, in *Abstracts of IX National Conference on Crystal Growth* (Moscow, 2000), p. 192.
15. J. Linhart, Cryst. Res. Technol. **37** (8), 849 (2002).
16. V. V. Krapukhin, I. A. Sokolov, and G. D. Kuznetsov, *Physical-Chemical Principles of Technology of Production of Semiconductor Materials* (Metallurgiya, Moscow, 1982), p. 334.
17. V. N. Lozovskiĭ, S. Yu. Knyazev, and A. S. Nefedov, in *Abstracts of IX National Conference on Crystal Growth* (Moscow, 2000), p. 220.
18. B. N. Evtodiĭ, L. P. Egorov, A. F. Karpukhin, *et al.*, Izv. Akad. Nauk SSSR, Ser. Fiz. **47** (2), 342 (1983).
19. M. A. Maurakh and B. S. Mitin, *Liquid Refractory Oxides* (Metallurgiya, Moscow, 1979).
20. V. A. Borodin, A. V. Zhdanov, and D. N. Frantsev, in *Abstracts of IX National Conference on Crystal Growth* (Moscow, 2000), p. 192.
21. B. I. Aronov, J. K. Linhart, and N. V. Marchenko, Teplofiz. Vys. Temp. **25** (6), 1187 (1987).
22. *Cosmos/M Documentation Revision v.2.6* (Structural Research and Analysis Corp., 2002); www.cosmosm.com.
23. Yu. S. Bagdasarov, E. P. Dobrovinskaya, L. A. Litvinov, and V. V. Pishchik, Izv. Akad. Nauk SSSR, Ser. Fiz. **37**, 2362 (1973).
24. P. I. Antonov, S. I. Bakholdin, V. M. Krymov, and I. L. Shul'pina, Izv. Ross. Akad. Nauk, Ser. Fiz. **63** (9), 1790 (1999).
25. P. I. Antonov, S. I. Bakholdin, V. M. Krymov, *et al.*, Poverkhnost **10**, 21 (2001).
26. *Ruby and Sapphire*, Ed. by M. V. Klassen-Neklyudova and Kh. S. Bagdasarov (Nauka, Moscow, 1974).
27. P. I. Antonov, I. L. Shul'pina, S. I. Bakholdin, *et al.*, Izv. Ross. Akad. Nauk, Ser. Fiz. **58** (9), 42 (1994).
28. E. P. Dobrovinskaya, *Growth and Defects of Single Crystals* (Naukova Dumka, Kiev, 1972), p. 284.

Translated by L. Man

Crystallography Reports, Vol. 49, No. 2, 2004, pp. 256–260. Translated from Kristallografiya, Vol. 49, No. 2, 2004, pp. 310–314.

CRYSTAL GROWTH

Curved-Face Growth of $NaNO_3$ Crystals[1]

Yu. O. Punin and V. D. Franke

St. Petersburg State University, Universitetskaya nab. 7/9, St. Petersburg, 199164 Russia

e-mail: franke@ag2460.spb.edu

Received May 20, 2003

Abstract—Curved-face growth of $NaNO_3$ crystals under the action of the $(NH_4)_2Mo_2O_7$ impurity is studied experimentally and possible causes of face bending are analyzed. Selective impurity adsorption on the basal pinacoid results in growth of platelike crystals with spherically bent faces. Growth-rate measurements show that the impurity decelerates pinacoid-face growth by the Bliznakov kink-poisoning mechanism. Face bending can be explained by gradual deceleration of step growth by the impurities accumulated before step fronts. A model of step deceleration is suggested that is based on the assumption of slow impurity adsorption resulting in the instability of a step train. The model allows one to qualitatively interpret the experimental data. © *2004 MAIK "Nauka/Interperiodica".*

INTRODUCTION

Crystals of many minerals (such as gypsum, calcite, quartz, and diamond) are characterized by the formation of curved (antiskeletal) growth shapes [1]. Rounded diamond crystals have been the subject of lively discussion of whether their curved shape is explained by their growth or dissolution. The possible formation of rounded crystals during growth has long been known and confirmed by numerous experimental data (see, e.g., [2]). It has been shown that curved-face growth is provoked by the presence in solutions of strongly adsorbing impurities. However, the concrete mechanism of this process is still unclear. Numerous examples show that adsorption is decelerated by impurities and is accompanied by dramatic changes of the crystal habit but without face bending. Thus, impurity adsorption alone cannot explain curved-face growth, so that some additional factors should be taken into account. Below, we describe the experimental study of curved-face growth of sodium nitrate crystals and analyze possible reasons for face bending.

METHODS AND EXPERIMENTAL RESULTS

Sodium nitrate, a structural analogue of calcite, belongs to the trigonal system and has the symmetry $\bar{3}m$. Sodium nitrite crystals grown from pure aqueous solutions are uniquely faceted by the faces of the $\{10\bar{1}1\}$ rhombohedron. The introduction into the solution of the ammonium dimolybdate impurity $(NH_4)_2Mo_2O_7$ results in the development of curved $\{0001\}$ pinacoid faces on $NaNO_3$ crystals. Despite the fact that we also found a number of other impurities giving rise to the formation of pinacoid faces on $NaNO_3$ crystals (KH_2PO_4, $KHSO_4$, KF, LiCl, and KIO_8), only the presence of the $(NH_4)_2Mo_2O_7$ impurity resulted in growth of curved faces.

The $NaNO_3$ crystals were obtained by spontaneous crystallization from aqueous solutions at the fixed initial supersaturations in the absence of solvent evaporation at 20°C. The concentration of the $(NH_4)_2Mo_2O_7$ impurity varied from 0.0 to 7.5 g per 100 g H_2O, the initial supersaturation, from 1.2 to 5.0 g per 100 g H_2O. Special experiments showed that $(NH_4)_2Mo_2O_7$ almost does not affect $NaNO_3$ solubility in water and, thus, also the solution supersaturation.

We determined the degree of the development of the (0001) pinacoid face and the degree of its bending. The development of the pinacoid can be characterized by the quantity $K = [d^R_{[0001]} - d_{(0001)}]/d_{(0001)}$, where $d_{(0001)}$ and $d^R_{[0001]}$ are the distances from the crystal center to the pinacoid face and rhombohedron vertex, respectively, and $d^R_{[0001]}/d_{(0001)}$ is the ratio of the average growth rates of the rhombohedron and the pinacoid face along the [0001] direction, i.e., $V^R_{[0001]}/V_{(0001)}$. The coefficient K was calculated from the measured linear dimensions of the crystal faces and was averaged over 20–25 crystals. The K curves as functions of impurity concentration and supersaturation are shown in Fig. 1a.

Bending of the pinacoid face was determined from the measured curvature depth h/a of a bent edge between the rhombohedron face and the pinacoid surface (Fig. 1b). Special measurements of the edge shape on the coordinate table of a microscope showed that these edges can be closely approximated by the arcs of circumferences, from whence it follows that the pinacoid surface should be spherically bent. In this case, the

[1] This work was presented at the National Conference on Crystal Growth (NCCG-2002, Moscow).

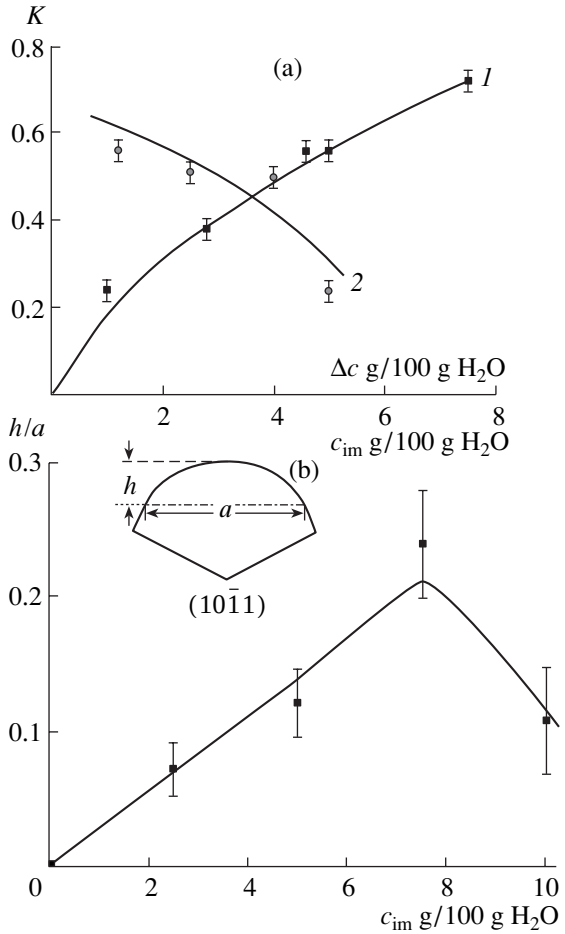

Fig. 1. Influence of growth conditions on morphology of $NaNO_3$ crystals: (a) development of a pinacoid as a function of the (*1*) $(NH_4)_2Mo_2O_7$ concentration at constant supersaturation Δc = 1.2 g/100 g H_2O and (*2*) supersaturation Δc at the impurity concentration c_{im} = 4.6 g/100 g H_2O and (b) pinacoid bending as a function of the $(NH_4)_2Mo_2O_7$ concentration at Δc = 5 g/100 g H_2O and the schematic of measurement of the curvature depth of the pinacoid edge.

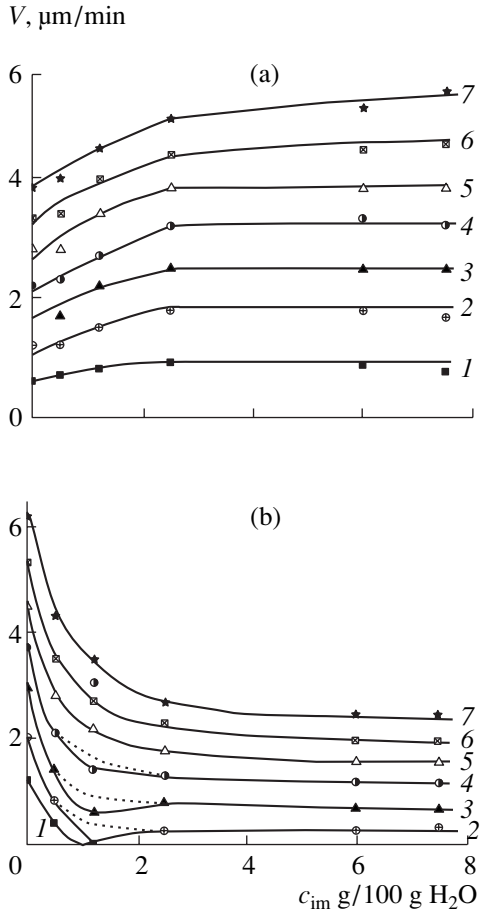

Fig. 2. Growth rate of $NaNO_3$ crystals as a function of $(NH_4)_2Mo_2O_7$ concentration in the solution: (a) faces of an obtuse (10$\bar{1}$1) rhombohedron, (b) faces of a (0001) pinacoid at the supersaturations Δc: (*1*) 0.50, (*2*) 1.00, (*3*) 1.50, (*4*) 2.00, (*5*) 2.45, (*6*) 2.90, and (*7*) 3.45 g/100 g H_2O

h/*a* value is an adequate characteristic of the bending degree. Figure 1b shows the dependence of the bending degree on the $(NH_4)_2Mo_2O_7$ concentration in the solution.

Comparing Figs. 1a and 1b, we see that the curvature of the pinacoid surface increases with the deceleration of growth of this face by the ammonium dimolybdate impurity. Thus, one can state that it is the selective adsorption of impurity on the pinacoid that gives rise to face bending.

In order to establish the mechanism of growth deceleration by impurity in the system under consideration, we studied the growth kinetics of the (10$\bar{1}$1) and (0001) faces of $NaNO_3$ crystals at six different values of $(NH_4)_2Mo_2O_7$ content in the solution: 0, 0.5, 1.2, 2.5, 6.0, and 7.5 g per 100 g H_2O. The growth rates were measured by the standard method described elsewhere [3]. The growth rates of three to five seeds were measured at each solution composition. The averaged results are shown in Figs. 2a and 2b for the (10$\bar{1}$1) and (0001) faces, respectively. It is seen that the $(NH_4)_2Mo_2O_7$ impurity does not decelerate growth of rhombohedron faces; on the contrary, the impurity slightly increases the growth rate, and, vice versa, the impurity dramatically decreases the growth rates of pinacoid faces. At elevated supersaturations, $\Delta c >$ 2 g/100 g H_2O, the shape of the curves of growth rate as functions of impurity concentration, $V(c_{im})$, indicates poisoning of the step kinks (Chernov–Bliznakov mechanism [4, 5]). At low supersaturations, $\Delta c \le 2$ g/100 g H_2O, the curves show a minimum at the impurity concentration (1–2) g/100 g H_2O. At $\Delta c < 1.5$ g/100 g H_2O, the growth rate of a pinacoid in the above range of the solution composition drops to zero; in other words, a so-called dead zone is formed [3]. This may indicate poisoning with impurity of ledges between the steps

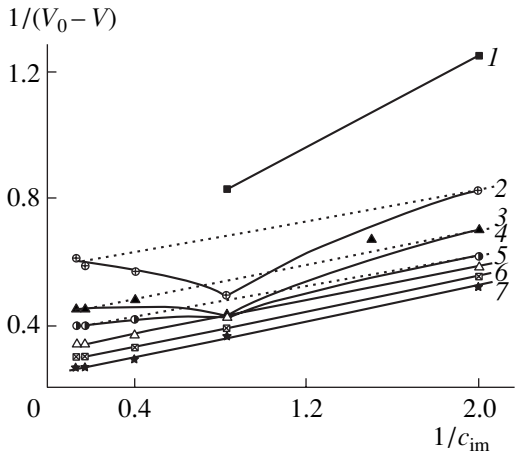

Fig. 3. Linearization of the data on growth rates of pinacoid faces in accordance with the Bliznakov equation. (*1*)–(*7*) The same as in Fig. 2.

(Cabrera mechanism [3, 4]) superimposing with kink poisoning and resulting in an additional contribution to a decrease in the growth rate. The limited range of impurity concentrations that can give rise to ledge poisoning is still unclear. One may think that this unusual behavior is associated with the change in the impurity state in the solution, namely, with polymerization of $(NH_4)_2Mo_2O_7$ with an increase in its concentration. This is confirmed by precipitation of small amounts of fine and almost insoluble precipitate from the solutions containing more than 15 g/100 g H_2O of $(NH_4)_2Mo_2O_7$. X-ray diffraction analysis of the ammonium polymolybdate precipitate showed that its composition is $(NH_4)_6Mo_7O_{24} \cdot 4H_2O$. We also observed a similar effect of the Cabrera mechanism in the NH_4Cl–carbamide–water system and explained it by the change of the impurity state in the solution [6].

The contribution of ledge poisoning to the total growth deceleration is rather low; the impurity mainly decelerates growth of pinacoid by the mechanism of kink poisoning. This can be demonstrated by transforming the experimental data to satisfy the Bliznakov equation [5]:

$$1/(V_0 - V) = [b/(V_0 - V_\infty)]*1/c_{im} + 1/(V_0 - V_\infty), \quad (1)$$

where b is the constant, V_0, V, and V_∞ are the growth rates of the face in the absence of impurity, at the given impurity concentration, c_{im}, and at the complete kink poisoning (which corresponds to the horizontal portion of the $V = V(c_{im})$ curves in Fig. 2b), respectively. The $1/(V_0 - V)$ dependence on c_{im} is shown in Fig. 3. It is seen that at the supersaturations $\Delta c \geq 2$ g/100 g H_2O, the points satisfactorily fit the straight lines, which corresponds to Eq. (1). At $\Delta c < 2$ g/100 g H_2O, these dependences are substantially nonequilibrium. However, smoothing the minima on the curves (dashed lines) in Fig. 2b, we managed to attain a good correspondence to Eq. (1) also at low supersaturations.

Thus, deceleration of a pinacoid because of kink poisoning at the steps is confirmed by the experimental data. Now, consider how poisoning with an impurity can lead to bending of pinacoid faces. Obviously, this can be caused by a gradual decrease in the growth rate of steps during their motion from the crystal center to its periphery. The dependence of the step growth rate v on the distance x from the face center determines the bent-surface profile. We have already noted that surface bending is close to spherical. Then, measuring the curvature depth of the pinacoid edge, h/a, one can calculate the slope of the surface to the (0001) plane, $p(x) = dz/dz$, at any point. Then, assuming that the curved-face shape is stationary (i.e., constant along the surface of the normal growth rate $\partial V/\partial x = 0$), we obtain the change of the growth rate of steps along the face, $v(x) \sim V/p(x)$. For a spherical surface of radius R, the slope in the central section $x^2 + z^2 = R^2$ under the condition that $x \ll R$ (which takes place for real curved-face crystals) is $p(x) = p_0 + x/(R^2 - x^2)^{-1/2} \sim p_0 + x/R$. Here, p_0 is the surface slope at the point of emergence of the dislocation source of layers, which is assumed to be located at the face center (this is confirmed by the face microrelief). Then $v(x) \sim V/(p_0 + x/R)$, i.e., the velocity of step motion decreases inversely proportionally to their distance from the source.

It is reasonable to assume that deceleration of growth steps is associated with accumulation of impurities before the step fronts during their propagation. According to the above kinetic data, the steps are decelerated by the mechanism of kink poisoning. Then the fraction θ of poisoned kinks at the step end increases with the distance of the step from the source according to the hyperbolic law

$$\theta \approx V_0/(V_0 - V_\infty)(1 - p_0/(p_0 + x/R)). \quad (2)$$

At $x \longrightarrow R$, the above expression becomes invalid.

DISCUSSION

Thus, the curved-face growth forms can be associated with the accumulation of impurities before moving steps, which decelerates step propagation. The most probable cause of this effect seems to be a slow attainment of the adsorption equilibrium at the surface of the growing crystal. In growth from solutions, slow impurity adsorption is encountered rather often and results in such nontrivial phenomena as hysteresis of the morphological rearrangements of the surface microrelief [7] and growth rates of crystals [8] and the instability of an equidistant train of growth steps [9–12]. It is this instability that gives rise to impurity accumulation in front of the steps and, in the final analysis, to curved-face growth. Consider this problem in more detail.

In the case of slow impurity adsorption, the impurity concentration at the surface in front of the end of a

moving step depends on the exposure time of the step-separating ledge to the solution, $\tau = d/v$, where d is the ledge width and v is the step velocity. The amount of impurity adsorbed per unit area of the surface for this time is

$$n = n_e[1 - \exp(-k\tau)] = n_e[1 - \exp(-kd/v)], \quad (3)$$

where n_e is the equilibrium surface concentration of the adsorbed impurity at the given impurity concentration in the solution, c_{im}, and k is the desorption constant. The impurity concentration in front of the step determines the step velocity, v. In the case of kink poisoning, this dependence is given by the Bliznakov equation [4, 5]

$$v(\theta) = v_0 - (v_0 - v_\infty)\theta, \quad (4)$$

where the fraction of the poisoned kinks, θ, is determined by the impurity concentration at the step front, n, and v_0 and v_∞ are the step velocities at $\theta = 0$ and 1, respectively. In the case of an equidistant train of steps separated by the distance d (dependent on supersaturation alone), Eqs. (3) and (4) yield the stationary velocity of the step train. However, this state is unstable. Any perturbation in the step density at the source would give rise to step coalescence that is more intense the larger their distances from the source [9–12]. The step coalescence leads to an increase in the interstep distance, and, therefore, also in the exposure time of the ledges to the solution. In accordance with [9], the exposure time τ logarithmically increases with the time of step motion, t,

$$\tau = 1/k(\ln t/t_0), \quad (5)$$

where t_0 is the transient time prior to the beginning of step coalescence. This result does not depend on the concrete mechanism of step deceleration by impurities [9, 10]. An increase in the exposure time with the distance from the source results in impurity accumulation in front of the steps and their gradual deceleration. In particular, in the Bliznakov mechanism, Eqs. (3)–(5) yield a decrease in the step velocity with time

$$v(t) = v_0 - (v_0 - v_\infty)\theta_e(1 - t_0/t), \quad (6)$$

where θ_e is the equilibrium fraction of the kinks filled with impurities that corresponds to n_e and c_{im}.

The surface slope at the distance x from the layer source (corresponding to the time t of step motion) is $p = h/d$, where $d = v(t)\tau$, and, according to [9], the step height is $h = A\ln t/t_0$. The proportionality coefficient A can be roughly estimated as $A \sim p_0 v_0 k$, where p_0 is the surface slope in the vicinity of the step source determined, as usual, by the supersaturation and the source power. Then, using Eqs. (5) and (6), we obtain

$$p = p_0/[1 - \theta_e(1 - v_\infty/v_0)(1 - (t_0/t))]. \quad (7)$$

The distance x corresponding to the given time t is found by integrating Eq. (6) from t_0 to t,

$$x = x_0/[\theta_e(1 + \ln t/t_0) + (1 - \theta_e)t/t_0], \quad (8)$$

where x_0 is the distance from the source at which the step coalescence begins.

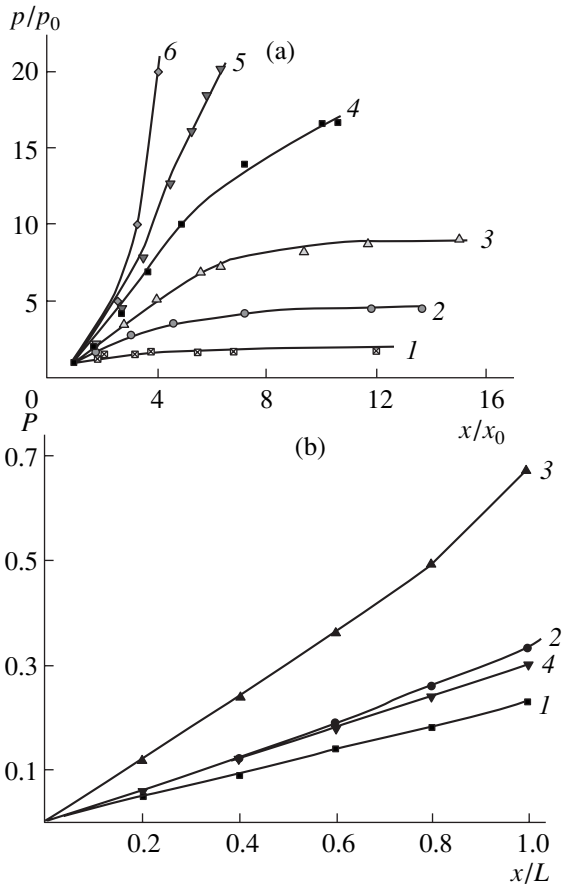

Fig. 4. Slope of the curved pinacoid surface to the (0001) plane as a function of the distance to the main layer source: (a) theoretical curves calculated by Eqs. (7) and (8) at $(1 - v_\infty/v_0)$: (*1*) 0.50, (*2*) 0.80, (*3*) 0.90, (*4*) 0.95, (*5*) 0.97, and (*6*) 1.00 and (b) experimentally observed change in the slope in the direction from the face center to its edge at the $(NH_4)_2Mo_2O_7$ concentration c_{im}: (*1*) 2.5, (*2*) 5.0, (*3*) 7.5, and (*4*) 10.0 g/100 g H_2O.

Equations (7) and (8) yield the change in the slope of the curved face to the rational plane depending on its distance to the layer source. Figure 4a shows similar dependences at different values of the parameter $\theta_e(1 - v_\infty/v_0)$ determining the degree of kink poisoning. It is seen that at slight poisoning, the surface slope attains a constant value shortly after the beginning of step coalescence. This corresponds to the equilibrium impurity concentration at the step front, $n = n_e$. On the contrary, at pronounced poisoning, $\theta_e(1 - v_\infty/v_0) \longrightarrow 1$, the curves are flattened-out only slightly, and the surface curvature $\partial p/\partial x$ is quite pronounced. The real picture for a curved pinacoid face of a $NaNO_3$ crystal (Fig. 4b) shows the variation of the surface slope to the (0001) plane with an increase of the reduced distance $\rho = x/L$ between the face center and its periphery. As was noted above, the surface is almost spherical, and, therefore, the curves $p(\rho)$ are not flattened-out. In accordance with the Fig. 4a, this corresponds to pronounced poi-

soning of the growth points with the impurity. Indeed, at the impurity concentrations used, the fraction of the kinks filled with impurity almost equals unity, and $v_\infty \ll v_0$ (Fig. 2). The nonmonotonic dependence of the degree of pinacoid curvature on the impurity content in the solution is rather surprising (Figs. 1b, 4b). At first sight, this does not correspond to the theoretical positions of the curves in Fig. 4a at different θ_e, because, in accordance with the Langmuir equation, θ_e monotonically increases with the impurity content in the medium. Nevertheless, even visual observations show that at high $(NH_4)_2Mo_2O_7$ concentrations in the solution, the $NaNO_3$ crystals grown are pronouncedly flattened along the pinacoid and are only slightly curved. This behavior is explained by a dramatic deceleration of the step velocity at high impurity concentrations. This considerably increases the transitional time t_0 in Eqs. (7) and (8). Assuming that the derivative $\partial p/\partial x$ is a measure of the surface curvature, we obtain from Eqs. (7) and (8)

$$\partial p/\partial x = p_0\theta_e t_0 t/v_0[t(1-\theta_e) + t_0\theta_e]^3. \quad (9)$$

At high degrees of kink poisoning, θ_e tends to unity and only weakly depends on the impurity concentration in the solution (the "saturation" effect characteristic of adsorption along the Langmuir isotherm). Then, Eq. (9) yields an inverse dependence of the surface curvature on the transient time t_0. The transient time t_0 is determined by the impurity flux at the surface, i.e., by the volume impurity concentration in the solution, c_{im}. According to [12], the dependence of t_0 on c_{im} is nonmonotonic and has the minimum. The analogous behavior of x_0 (which is proportional to t_0) also follows from [11]. Then, in virtue of Eq. (9), with an increase of the impurity content in the solution, the surface curvature should pass through the maximum, which was observed experimentally. It should be noted that we also observed a similar nonmonotonic change in the face curvature with an increase in the impurity concentration in potassium sulfate crystals in the K_2SO_4–K_2WO_4–H_2O system [14].

Thus, the model of formation of crystals with curved faces based on slow impurity absorption reflects qualitatively correctly the main experimental dependences of the curved-face growth. Of course, the model suggested above is mainly of heuristic importance. Since the model is rather crude, one cannot expect that it would describe the experiment quantitatively correctly. It should be noted that the model is also valid (with a corresponding change of formalism) in the case of growth poisoning by the Cabrera mechanism.

ACKNOWLEDGMENTS

The study was supported by the Russian Foundation for Basic Research, project no. 02-05-65279.

REFERENCES

1. I. I. Shafranovskiĭ, *Crystals of Minerals. Curved-Face, Skeleton, and Granular Forms* (Gosgeoltekhizdat, Moscow, 1961).
2. H. Buckley, *Crystal Growth* (Wiley, New York, 1951; Inostrannaya Literatura, Moscow, 1954).
3. T. G. Petrov, E. B. Treĭvus, and A. P. Kasatkin, *Crystal Growth from Solutions* (Nedra, Leningrad, 1983, 2nd ed.; Consultants Bureau, New York, 1969).
4. A. A. Chernov, E. I. Givargizov, Kh. S. Bagdasarov, *et al.*, in *Modern Crystallography*, Vol. 3: *Crystal Growth*, Ed. by B. K. Vaĭnshteĭn, A. A. Chernov, and L. A. Shuvalov (Nauka, Moscow, 1980; Springer, Berlin, 1984).
5. E. B. Treĭvus, *Kinetics of Crystal Growth and Dissolution* (Leningr. Gos. Univ., Leningrad, 1979).
6. Yu. O. Punin and V. D. Franke, Cryst. Res. Technol. **33** (3), 449 (1998).
7. J. W. Noor and B. Damm, J. Cryst. Growth **76** (2), 243 (1986).
8. Yu. O. Punin and O. I. Artamonova, Kristallografiya **34** (5), 1262 (1989) [Sov. Phys. Crystallogr. **34**, 760 (1989)].
9. J. P. van der Eerden and H. Müller-Krumbhaar, Electrochim. Acta **31** (8), 1008 (1986).
10. J. P. van der Eerden and H. Müller-Krumbhaar, Phys. Rev. Lett. **57** (19), 2431 (1986).
11. S. V. Moshkin, *Physics of Crystallization* (Tver. Gos. Univ., Tver, 1989), p. 56.
12. D. G. Vlachos and K. F. Jensen, Surf. Sci. **262** (3), 359 (1992).
13. A. Adamson, *The Physical Chemistry of Surfaces* (Wiley, New York, 1976; Mir, Moscow, 1979).
14. Yu. O. Punin, V. D. Franke, and D. S. Kenunen, Zap. Vseross. Mineral. O–va, No. 1, 110 (2000).

Translated by L. Man

Crystallography Reports, Vol. 49, No. 2, 2004, pp. 261–265. Translated from Kristallografiya, Vol. 49, No. 2, 2004, pp. 315–319.

CRYSTAL GROWTH

Hydrodynamic Conditions for Growth of Large KDP Crystals[1]

V. I. Salo, A. P. Voronov, M. I. Kolybaeva, I. M. Pritula, V. F. Tkachenko, and V. M. Puzikov

Scientific Technological Association Institute of Single Crystals, National Academy of Sciences of Ukraine, Kharkov, Ukraine

e-mail: salo@isc.kharkov.com

Received March 3, 2003

Abstract—Three-dimensional mass transfer is simulated. The factors determining the hydrodynamic conditions for efficient mass transfer in growth of large KDP single crystals (cross sections up to 45×45 cm^2) from solutions in a real 300-l-crystallizer are established. The conditions for the motion of the supersaturated solution to the surface of a growing crystal in the direction opposite to that of gravitation are attained. The growth mode developed provides growth rates that are five times higher of large high-quality optical KDP crystals. © *2004 MAIK "Nauka/Interperiodica".*

INTRODUCTION

It is well known that the hydrodynamics of the medium around a growing crystal influence the occurring growth processes. However, the fact that the hydrodynamic conditions may play the key role in growth control is often ignored. Varying the hydrodynamic conditions, with all the other parameters being the same, one can considerably change the growth rate, the quality of the crystal, and its final dimensions [1–5].

Taking into account the relation between heat and mass transfer and solution motion, it is important to study the solution kinetics in the zone adjacent to the crystallization front and the interaction between this part of the solution with its main part.

Comparison of the influence produced by diffusion, convection, and forced stirring on the boundary-layer thickness and the maximum linear growth rate of the crystal, v, showed [1, 4] that the average velocity of solution particles at the surface of a growing crystal in the case of the diffusion mechanism of stirring is $R = 5 \times 10^{-5}$ cm/s at $v = (0.5–3) \times 10^{-8}$ cm/s. Under the conditions of thermal convection at the solution velocity $R = 4 \times 10^{-2}$ cm/s, the maximum linear growth rate is $v = (20–80) \times 10^{-8}$ cm/s. At the same time, forced stirring may create the conditions under which the solution particles at the crystal surface would move with the velocity R = (1–100) cm/s at v = (100–5000) $\times$ 10^{-8} cm/s.

The present study is aimed at better understanding of the kinetics of the flow of a liquid and material transport in a real crystallizer used for growth of large KDP-type crystals.

[1] This work was presented at the National Conference on Crystal Growth (NCCG-2002, Moscow).

APPARATUS AND EXPERIMENTAL METHODS

We studied the kinetics of liquid flows in growth of large potassium dihydrogen phosphate (KDP) and deuterated potassium dihydrogen phosphate (DKDP) crystals with sections up to 45×45 cm^2. Growth of these large crystals was performed by the method of solvent recirculation in the crystallizer illustrated by Fig. 1. This method reduces to the following. Supersaturation in the growth chamber necessary for growth occurs due to solvent evaporation, whereas a constant supersaturation is attained by the control of the evaporation rate, condensate accumulation, dissolution of an additional amount of the initial raw material by the condensate in the feeding chamber, and the return of the supersaturated solution to the growth chamber.

Hydrodynamics was studied by three-dimensional simulation of the heat and mass flows under the conditions of forced convection caused by rotation of a crystal on a flat holder and the use of additional stirrers. The model liquid was water because its parameters (viscosity, density, heat conductivity, etc.) were close to those of real solutions. The flows of the model liquid were visualized with the aid of indicators—$KMnO_4$ or color granulated polyethylene present in the solution in the suspended state. The additional rodlike stirrers used for creating better mixing conditions were of an aerodynamic shape or had square cross sections.

The hydrodynamic conditions corresponded to the processes occurring in a real 300-l crystallizer with a diameter of 65 cm and a height of 90 cm. Of all the methods that can enable the solution motion, we selected stirring because the best hydrodynamic conditions for heat and mass transfer could be expected in the case where a crystal is rotated whereas the main part of the solution remains still. Under these conditions, the solution circulation is not limited to the zone adjacent to the crystal and proceeds over the whole volume.

1063-7745/04/4902-0261$26.00 © 2004 MAIK "Nauka/Interperiodica"

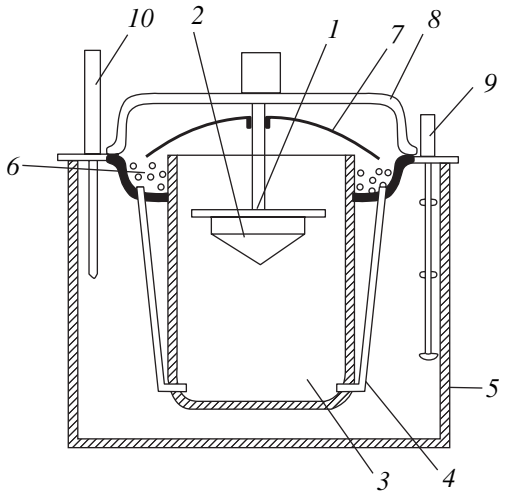

Fig. 1. Schematic of a crystallizer: (*1*) crystal holder with rotating drive, (*2*) crystal, (*3*) growth chamber, (*4*) tube for pouring the solution, (*5*) thermostat, (*6*) feeding chamber, (*7*) umbrella, (*8*) refrigerator cover, (*9*) stirrer, (*10*) thermometer.

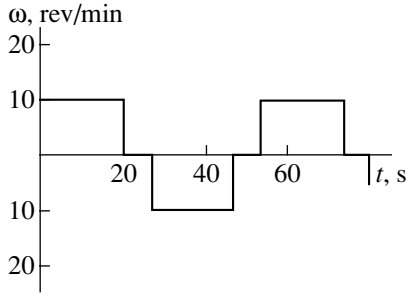

Fig. 2. Illustrating the typical mode of crystal rotation at a constant velocity.

Moreover, the rotating crystal forces the liquid to flow to the crystal. If the solution stirring is provided by the rotation of the growth chamber, the flat stirrer located close to the bottom of a platform on which a large crystal is fixed, then under the growing crystal a flow arise which is directed from the crystal. In a real crystallizer, the feeding holes are located close to the bottom, and, therefore, in our experiments, the conditions were created for the upward motion of the supersaturated solution to the growing-crystal surface in the direction opposite to that of gravitation.

RESULTS AND DISCUSSION

The conditions for solution stirring were simulated based on the natural-size model of a KDP crystal, with the crystal dimensions being comparable with the crystallizer dimensions. The diagonal of the crystal grown was up to 63 cm, with the inner diameter of the growth chamber being 65 cm. Rotation with a constant velocity of $\omega > 25$ rev/min gave rise to turbulent flows, formation of rather high waves at the surface of the liquid, and splashing of the liquid out from the growth chamber during growth cessation or the beginning of the rotation in the opposite direction. Therefore, in our experiments, we used the rotation velocity $\omega = 20$ rev/min.

Three stirring modes were used: reverse rotation of a crystal with a constant velocity, reverse rotation of a crystal with a constant velocity with the aid of additional rodlike stirrers, and accelerating-decelerating reverse rotation of a crystal with the aid of additional aerodynamic-shape stirrers.

To obtain more detailed information on the influence of the velocity of the reverse crystal rotation on the stirring conditions, we studied the flows of the model liquid inside the growth chamber at the velocities 5, 8, 10, 15, and 20 rev/min with and without growth cessation. Figure 2 illustrates this rotation mode.

At $\omega = 5$ rev/min, the weak motion liquid is observed with stirring occurring only in the region adjacent to the crystal. The motion proceeds along the circle; no motion of the liquid from below to the growing crystal is observed. The state of the liquid in the crystallization volume only slightly differs from its state in the case of the absence of any crystal rotation.

In the case of crystal rotation with the velocity $\omega = 10$ rev/min, twisting of the liquid layers is observed. The maximum velocity of the model-liquid motion is observed in the rotation plane of the pyramidal growth sectors; the liquid moves from the crystal to the side walls of the chamber in the plane normal to the rotation axis (Fig. 3). Above and below this region, the liquid only starts to be involved into the motion. This is well seen from the curved bands. After some time, the moving flows reach the walls of the growth chamber and start moving along these walls. These flows are twisted in the direction toward the rotation axis. Thus, the crystal rotation gives rise to the formation of some toroidal regions with the resulting helical motion of the liquid inside them. The motion of the liquid flows in the toroidal regions is much more intense than in other regions. Above and below the toroidal regions, the liquid is weakly stirred, especially in the vicinity of the chamber bottom. At the very beginning of the cycle of the crystal rotation, the flows proceed from the chamber bottom. However, 15 s later (formation of the rotating toroidal region), no flows from the chamber bottom are observed, and the whole liquid starts rotating over a circle. The indicator particles fix the pattern being arranged over the circles at the chamber bottom.

At the crystal rotation with the velocity $\omega = 15$–20 rev/min, the pattern of the liquid-flow motion is the same as was considered above with the only difference being—the motion of the liquid flows inside the toroidal regions becomes more intense and the rotation velocity of the liquid as a whole becomes higher.

In the mode of stirring of the liquid with additional rodlike stirrers, the flow-motion pattern of the model liquid is similar to that considered above, but the pene-

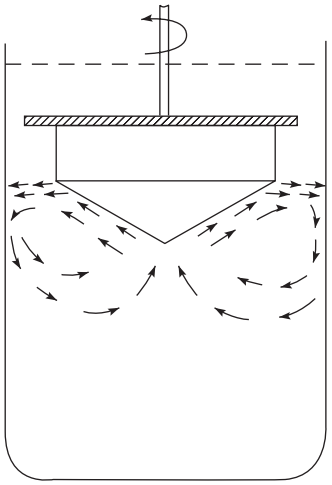

Fig. 3. Flow pattern in the growth chamber with a crystal rotating at a constant velocity of 10 rev/min.

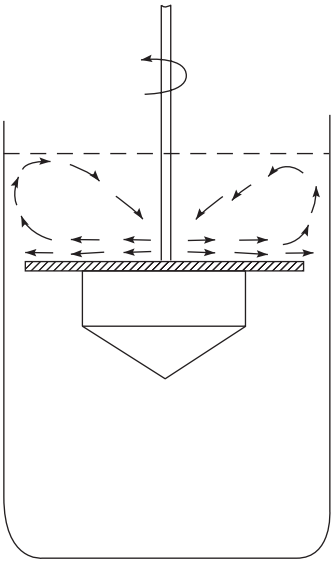

Fig. 4. Flow pattern formed above a flat crystal holder.

tration depth of the toroidal region reaches the chamber bottom. Moreover, the time necessary for the formation of the rotating toroidal region and setting in rotation of the whole liquid volume decreases to 10 s. It is also established that the cessation of the rotation of the whole liquid volume takes at least 180 s. At shorter pause in the rotation (switching-off time of the motor rotating the crystal), the beginning of the motion in the opposite direction changes the symmetry of the flow motion, and almost the whole half-period of the crystal rotation is "spent" to stop the rotation of the whole liquid in the opposite direction and to set this volume to the rotation in the direction of the crystal rotation. In the following half-period, rotation direction is changed, and the pattern of the liquid motion is repeated. As a result, uncontrolled chaotic motion of the liquid inside the growth chamber is observed, which is accompanied by formation of turbulent flows.

It is well known that, within a narrow horizontal layer between the hydrodynamic medium and the solid surface normal to the rotation axis (where the rotation velocities are different), a radial flow is formed [3], the so-called "flow in the Eckman layer." This flow is observed in vessels with heights comparable with their diameters. According to [3], the Eckman layers are formed both above and below of a suspended seeding crystal. As is seen from Fig. 4, a fast radial flow in the Eckman layer in our experiments is formed in the vicinity of the surface of a crystal holder.

As is shown in [6], the Eckman-layer thickness is determined from the equation

$$d = (\eta/\rho\omega)^{1/2}, \quad (1)$$

where η is the viscosity, ρ is the density, and ω is the rotation velocity.

Inside the layer, the radial velocity of the flows has the maximum value

$$v = \omega L, \quad (2)$$

where L is the characteristic length.

The vertical velocity of liquid flows in the larger part of the vessel is considerably lower

$$W = (\eta\omega/\rho)^{1/2}. \quad (3)$$

The flow pattern in the Eckman layer is preserved only within the transient process. The flow is gradually decelerated with an increase of the fraction of the liquid participating in the uniform rotation. The flow in the Eckman layer ceases with the whole liquid volume being set in rotation. We often observed this effect in our experiments. The evaluation of the hydrodynamic parameters using Eqs. (1)–(3) yields the following values: the Eckman-layer thickness is of about 0.1 cm, the velocity of the liquid in the Eckman layer is 20–25 cm/s, and the velocity of the vertical liquid flow is of the order of 0.1 cm/s.

The design of the crystallization chamber (Fig. 1) enables the supply of the supersaturated solution from the feeding chamber to the lower part of the growth chamber with the subsequent stirring of the solution. As was shown above, the stirring modes considered above cannot provide a uniform supply of the supersaturated solution to a growing crystal. We designed and constructed the stirrers with cross sections of the aerodynamic shape intensifying the downward liquid flow along the walls of the immobile crystallizer. As was noted above, the Eckman flow is preserved if the transient process of the liquid motion is maintained as constant. Obviously, this can be achieved by rotating the crystal with an acceleration up to a certain optimum rotation velocity. When searching for the optimum con-

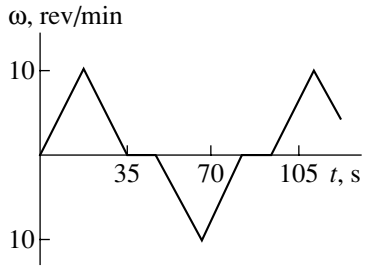

Fig. 5. Mode of accelerated–decelerated rotation of a growing crystal.

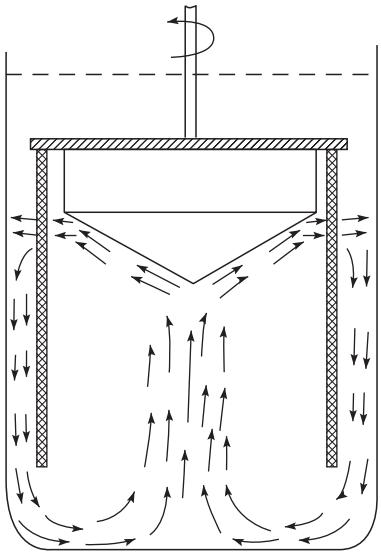

Fig. 6. Flow pattern obtained in accelerated-decelerated rotation of a crystal with the aid of additional stirrers of aerodynamic shape fixed along the same rotation axis.

ditions for growth of large KDP-type crystals, we also studied the stirring process of the supersaturated solution using the accelerating–decelerating rotation of a crystal with the use of additional stirrers along the common rotation axis. Stirring was first accelerated from zero to the maximum rotation and then decelerated to zero. In this case (Fig. 5), a radial flow in the Eckman layer arises within a narrow layer at the crystal–liquid interface at the stage of accelerated rotation and the pattern; the liquid motion is of the same nature as in the transient process during rotation with a constant velocity.

With an increase in rotation velocity from zero to the maximum value, a rarefaction above the rotation crystal is observed, which is caused by centrifugal forces. As a result, the flow from the chamber bottom arises; this flow becomes more intense also because of the pressure of the liquid layers created by additional stirrers along the walls (Fig. 6). The use of rotation deceleration from the maximum value to zero allowed us to avoid twisting of the whole liquid volume and its circular rotation. This pattern of the liquid motion is also confirmed by the arrangement of the indicator particles on the growth-chamber bottom. Thus, at the accelerated–decelerated rotation of the crystal with the use of additional stirrers fixed along the same rotation axis, a closed cycle of the liquid motion inside the growth chamber is observed with a fast laminar flow in the vicinity of a rotating crystal and with a slower reverse flow through the main part of the liquid volume. This pattern of the liquid motion takes place only if the whole volume of the liquid is not rotated. With the formation of rotating toroidal regions, the radial flow (radial flow in the Eckman layer) in the vicinity of the growing crystal and the flow from the growth-chamber bottom are decelerated and, finally, disappear when the whole liquid starts rotating.

The most efficient stirring conditions are attained at the maximum rotation velocity 10 rev/min, the duration of the cycle of reverse rotation 80 s, and the pause between the opposite directions of rotation 12 s. In the reverse rotation, the liquid flows are symmetric. The vertical liquid flow and the closed cycle of the flow motion are observed during both half-periods of rotation. Under our conditions, the average velocity of the vertical flow from the chamber bottom to a growing crystal was 4 cm/s. An increase in the minimum number of revolutions or the time of the rotation cycle resulted in the formation of vortices, appearance of toroidal regions, and uniform circular rotation of the liquid. A decrease in the maximum number of revolutions and duration of the cycle resulted in a considerable decrease in stirring efficiency. The pause resulted in the complete cessation of the liquid motion. Now, the conditions for motion of the supersaturated solution to the growing surface of the crystal along the direction opposite to that of gravitation are achieved. At the characteristic length of 50 cm, the Reynolds number is $\mathrm{Re} = 10^4$–10^5, and the velocity of the flows washing the crystal faces is 20–25 cm/s. Under these conditions, mainly the kinetic mode of growth takes place. At such high Reynolds numbers, turbulent flows may arise along the crystal edges. The digital simulation of the hydrodynamic flows [7, 8] confirmed their formation.

It should be noted that it is necessary to study in detail the formation of vortex flows at the vertices and side faces of the crystal and determine shear stresses of the liquid at the side faces of the crystal resulting in local morphological instabilities of growth steps and capture of liquid inclusions.

CONCLUSIONS

The factors determining the hydrodynamic conditions for efficient mass transfer in a real crystallizer during growth of large KDP crystals from solutions have been studied. The mode of solution stirring by the accelerated–decelerated reverse rotation of the crystal with the use of additional stirrers of an aerodynamic shape is developed. Under these conditions, a fast lam-

inar flow of a liquid arises in a thin Eckman layer at the solution–crystal interface and the closed cycle of the motion of the supersaturated solution to the faces of the growing crystals inside the growth chamber is observed. The velocity of the liquid flow in the Eckman layer is higher by an order of magnitude than the velocity of the solution flow in the crystallizer volume.

A fast laminar flow of the solution along the face of a growing crystal ensures efficient mass transfer and creates the conditions for high growth rates at the crystallization front (kinetic growth modes) and growth of large defect-free crystals. The hydrodynamic growth modes developed here, with all the other growth parameters remaining unchanged (temperature, supersaturation, etc.), allowed us to grow large KDP crystals with cross sections up to 40×40 cm^2 at the growth rate 4.1×10^{-6} cm/s. The experimental optical absorption of the crystals ranges from 0.03 to 0.04 cm^{-1} at λ = 1.06 μm and is consistent with the results obtained earlier in [9, 10].

REFERENCES

1. H. J. Scheel, J. Cryst. Growth **13–14**, 560 (1972).
2. H. J. Scheel and E. O. Schulz-DuBois, J. Cryst. Growth **8**, 304 (1971).
3. E. O. Schulz-DuBois, J. Cryst. Growth **12**, 81 (1972).
4. V. I. Salo, Candidate's Dissertation in Chemistry (Inst. of Single Crystals, Kharkov, 1979).
5. W. A. Tiller, J. Cryst. Growth **2**, 69 (1968).
6. R. Hide and C. W. Titman, J. Fluid Mech. **29**, 39 (1967).
7. Y. Zhou and J. J. Derby, J. Cryst. Growth **180**, 497 (1998).
8. H. F. Robey and D. Maynes, J. Cryst. Growth **222**, 263 (2001).
9. V. I. Salo, Semicond. Phys. Quantum Electron. Optoelectron. **3** (2), 200 (2000).
10. V. I. Salo, M. I. Kolybayeva, V. F. Tkachenko, and I. M. Pritula, Semicond. Phys. Quantum Electron. Optoelectron. **3** (2), 200 (2003).

Translated by L. Man

Crystallography Reports, Vol. 49, No. 2, 2004, pp. 266–270. Translated from Kristallografiya, Vol. 49, No. 2, 2004, pp. 320–324.

CRYSTAL GROWTH

Growth of Large KDP Single Crystals for UV Spectrum Range[1]

M. I. Kolybaeva, V. I. Salo, I. M. Pritula, Yu. N. Velikhov, A. P. Voronov, V. F. Tkachenko, and V. M. Puzikov

Scientific Technological Association Institute of Single Crystals, National Academy of Sciences of Ukraine, Kharkov, Ukraine

e-mail: salo@isc.kharkov.com

Received March 3, 2003

Abstract—The influence of various technological parameters of crystallization (acidity of growth solutions, crystallization temperature, growth rate, degree of solution purification) on the optical absorption of large KDP single crystals has been studied in the UV range of the spectrum. It is shown that the method of solvent recirculation with the use of the starting material with the microimpurity content not exceeding 5×10^{-5} wt % and solution ultrafiltration under the optimum crystallization conditions (t_{cr} = 80°C, V_{cr} ~ (0.8–1.6) × 10^{-6} cm/s, pH 4) enables one to grow KDP single crystals with cross sections up to 300 × 300 mm^2 and the transmission in the vicinity of the fundamental absorption edge (λ = 200 nm) equal to 86%. © *2004 MAIK "Nauka/Interperiodica".*

INTRODUCTION

At present, potassium dihydrogen phosphate (KDP) crystals are among a few widespread nonlinear optical materials efficiently used as laser-radiation modulators and frequency amplifiers in industrial laser systems. Since the short-wave boundary of the optical transparency band of KH_2PO_4 crystals lies in the range of vacuum UV (176 nm), it is possible to use these crystals for efficient conversion of powerful laser radiation (YAG : Nd laser, λ = 1.064 μm) into the third (λ = 0.353 μm) and fourth (λ = 0.266 μm) harmonics. An important factor limiting applicability of KDP crystals for higher-harmonics generation of a neodymium laser is the optical absorption of crystals in the near UV range of the spectrum. As has been shown by numerous researchers, radiation absorption in the UV range is caused mainly by the impurities of polyvalent Fe^{3+}, Cr^{3+}, Al^{3+}, Sb^{3+}, Bi^{3+}, Cu^{2+}, and Hg^{2+} metals [1–3], organic compounds such as fatty acids, phthalates, and phenols [4], NO_3^- impurity [5], and metastable (at room temperature) intrinsic defects such as $(HPO_4)^-$, $(H_2PO_4)^0$, and electron center H^0 arising in crystals under the action of powerful laser radiation [6, 7].

The present work is dedicated to study of the effect of Ca, Si, and Pb impurities on the optical properties of KDP crystals, since these impurities are present in the starting material in amounts up to 1×10^{-3} wt % and can considerably increase the absorption of crystals in the spectral range from 200 to 400 nm [8]. We also analyzed the influence of a number of technological factors (acidity of growth solution, crystallization temperature, growth rate, degree of solution purification) on the transmission spectra of KDP crystals at λ = 200–400 nm.

EXPERIMENTAL

The crystals studied were grown by the method of solvent recirculation, which allows one to create stable crystallization conditions within the whole cycle of single crystal growth. We studied potassium dihydrogen phosphate crystals with the controllable impurity (Fe, Cr, Al, Sb, Bi, Cu, Hg, Ag, Pb, Mg, Mn, and Ca) level (5×10^{-5}) wt %. The crystals were grown on a prismatic seed along the [001] direction. The mother-liquor temperature was maintained within an accuracy of ±0.05 K. All the solutions were subjected to microfiltration through polymer membrane filters with a pore size of 0.05 μm. Before filtration, the solutions were overheated by 10 K above the saturation point and then were kept for 24 h at this temperature. The filtration process was performed under a rarefaction of 0.8 kgf/cm^2 with the aid of a special device for solution filtration by the method described elsewhere [9]. When varying one of the parameters, we kept all the other parameters intact. To maintain the constant growth rate 0.8 × 10^{-6} cm/s at elevated temperatures (70–80°C), we decreased the evaporation-mirror area with the aid of an aperture fixed at the central rod of the crystal holder [10].

The optical measurements were made on a series of 20 × 20 × 20 mm specimens cut out from various regions of the grown crystals with polished surfaces normal to the crystallographic *c* axis. The transmission spectra in the UV range were measured on an SF-56 (LOMO) spectrophotometer at room temperature. To

[1] This work was presented at the National Conference on Crystal Growth (NCCG-2002, Moscow).

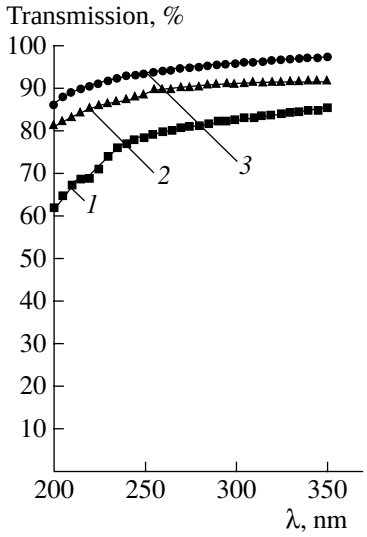

Fig. 1. Transmission spectra of KH_2PO_4 single crystals grown at various pH: (*1*) 5.5, (*2*) 2, and (*3*) 4 ($V_{cr} = 0.8 \times 10^{-6}$ cm/s, $t_{cr} = 55°C$).

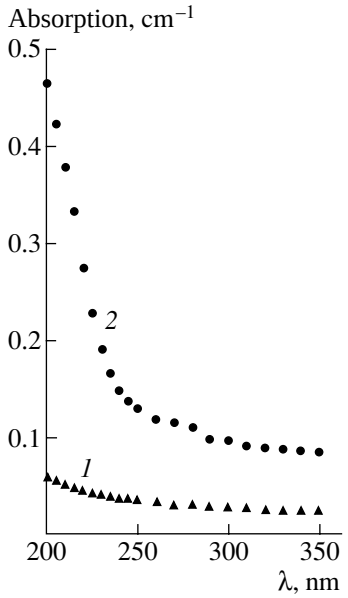

Fig. 2. Absorption spectra of KH_2PO_4 single crystals grown from filtered solutions (filter with (*1*) 0.05 and (*2*) 0.15 μm pores) at pH 4, $V_{cr} = 0.8 \times 10^{-6}$ cm/s, and $t_{cr} = 55°C$.

visualize the scattering centers in the crystals, we used a special setup consisting of a 30 mW He–Ne laser, an optical microscope, a CCD imaging chamber, and a computer to process the data obtained. The specimens were fixed on a crystal holder which enabled specimen motion along the directions normal to the incident radiation. The measuring optical devices were arranged at an angle of 90° to the laser beam.

RESULTS AND DISCUSSION

Mother-liquor acidity. The variation of pH of the solution and, therefore, also of the solution composition is one of the methods used to control growth of crystals and their quality [11].

It is widely believed [12] that the effect of acidity on the optical characteristics of crystals is explained mainly by the change in the state of impurities in the solution. In solutions, all the impurities can be divided into two groups—extrinsic ones (microamounts of other elements, suspended particles) and impurities that arise as a result of dissociation, association, and polymerization of the starting components or are their solvates (hydrates). In this connection, the influence of solution acidity on the crystal quality should be considered both in terms of the impurity interaction with the main substance and in terms of the structural changes in the solution determined by the acid–base equilibria. Thus, the variation in pH changes the state of extrinsic

Analysis of precipitates on filters after solution filtration (wt %)

	Experiment	Na	Ca	Mg	Al	B	Si	Ti	Cu	Ag	Fe	Cr	Ni	Mn	Pb	Sr
Filter with the pore size 0.05 μm	1	10^{-3}					$>10^{-2}$	10^{-3}	$>10^{-5}$	10^{-4}			10^{-5}			
	2						$>10^{-2}$	10^{-3}	$>10^{-5}$							
	3						$>10^{-2}$	10^{-4}	$>10^{-5}$							
Filter with the pore size 0.15 μm	4	10^{-4}						10^{-5}	10^{-4}	10^{-4}	10^{-5}					
	5							10^{-5}	10^{-4}	10^{-4}	10^{-5}	10^{-5}		10^{-5}		
	6						10^{-4}	10^{-5}	10^{-5}	10^{-5}	10^{-5}			10^{-4}		
	7								10^{-5}	10^{-5}	10^{-5}					
	8							10^{-5}	10^{-4}	10^{-4}	10^{-5}	10^{-5}				10^{-5}
	9							10^{-5}	10^{-5}	10^{-4}	10^{-4}	10^{-4}		10^{-4}	10^{-5}	10^{-4}
	10							10^{-4}	10^{-5}	10^{-4}	10^{-4}	10^{-4}		10^{-4}	10^{-5}	10^{-4}

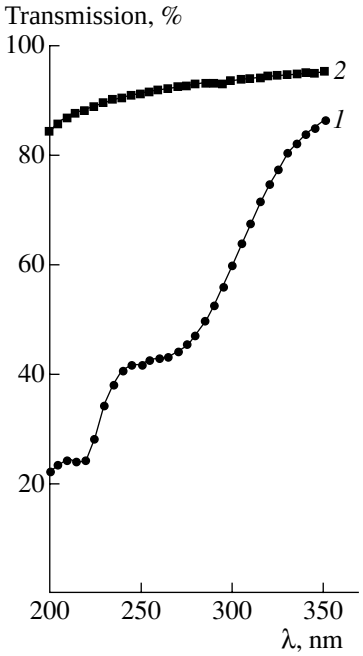

Fig. 3. Transmission spectra of KH_2PO_4 crystals grown at two growth rates V_{cr}: (*1*) 4.1×10^{-6} and (*2*) 0.8×10^{-6} cm/s (pH 4, t_{cr} = 55°C).

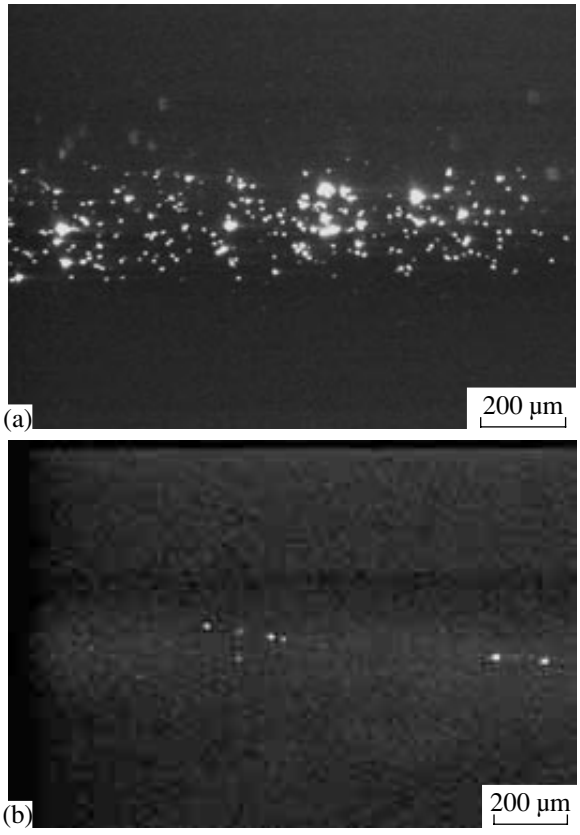

Fig. 4. Light scattering in KH_2PO_4 single crystals grown at two V_{cr}: (a) 4.1×10^{-6} and (b) 0.8×10^{-6} cm/s.

impurities and the concentration of the structural units of the crystals [13].

Figure 1 shows the transmission spectra of KH_2PO_4 crystals grown at various pH (2, 4, 5.5) and $V_{cr} = 0.8 \times 10^{-6}$ cm/s at the temperature t_{cr} = 55°C. It is seen that the pH value of the mother liquid considerably influences the optical properties of crystals. The lowest transmission is observed for crystals grown from an alkali solution with pH 5.5. In the vicinity of the fundamental absorption edge, transmission does not exceed 60%; moreover, one can clearly see the band of anomalous absorption at the wavelength λ = 220 nm. The spectra of crystals grown from acid solutions show no specific characteristics in the whole wavelength range and their transmission is lower than transmission of crystals grown from the stoichiometric solutions. The crystals grown at pH 4 are characterized by high transmission (85% at λ = 200 nm) and the absence of transmission bands. It should be noted that the impurity distributions in the crystals grown from acid, neutral, and alkali solutions are considerably different. Thus, for crystals grown from acid solutions, the impurity distribution over the crystal bulk is the most uniform. The impurity content in crystals growing from neutral solutions dramatically decreases with the growth time. The crystals grown from alkali solutions are characterized by a more complex impurity distribution in comparison with the crystals grown from neutral solution—here the impurities are nonuniformly distributed over the crystal. The character of the impurity distribution in crystal seems to be confirmed by their spectra. Thus, the deviation of the solution composition from the stoichiometry both toward acidity or to alkalinity results in deterioration of crystal transmission in the UV spectrum range.

Solution filtration. It is well known [14] that absorption of radiation by crystals is related to the purity of the initial growth solutions, which, in turn, depends on the concentration of mechanical impurities and their composition. Mechanical purification of the solution from impurities is usually performed with the aid of various filters. The shortcomings of most filters are their inability to filtrate particles whose size does not exceed 1 μm; moreover, some of these filters can themselves deteriorate solution purity [15].

The influence of the solution filtration on the quality of the crystals grown from these solutions was studied with the use of MMFK-type membranes with a pore size of 0.15 and 0.05 μm.

The use of purified solutions enabled us to grow the crystals whose study is illustrated by Fig. 2. It is seen that the crystals grown from the solution purified with the aid of the filters with the pore size 0.05 μm show the fivefold higher transmission than the crystals grown from the solutions purified by filters with the pore size 0.15 μm. The qualitative chemical analysis of the precipitates on the filters showed that the filters with the pore size 0.05 μm filter away much larger amounts of

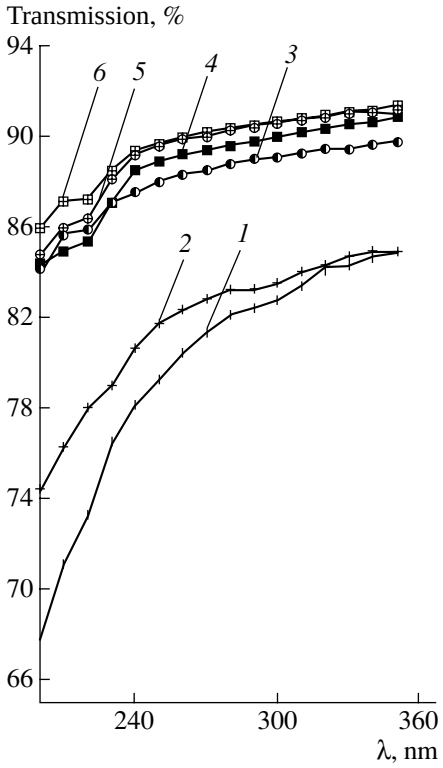

Fig. 5. Transmission spectra of KH_2PO_4 single crystals grown at various temperatures: (*1*) 35, (*2*) 45, (*3*) 55, (*4*) 60, (*5*) 70, and (*6*) 80°C.

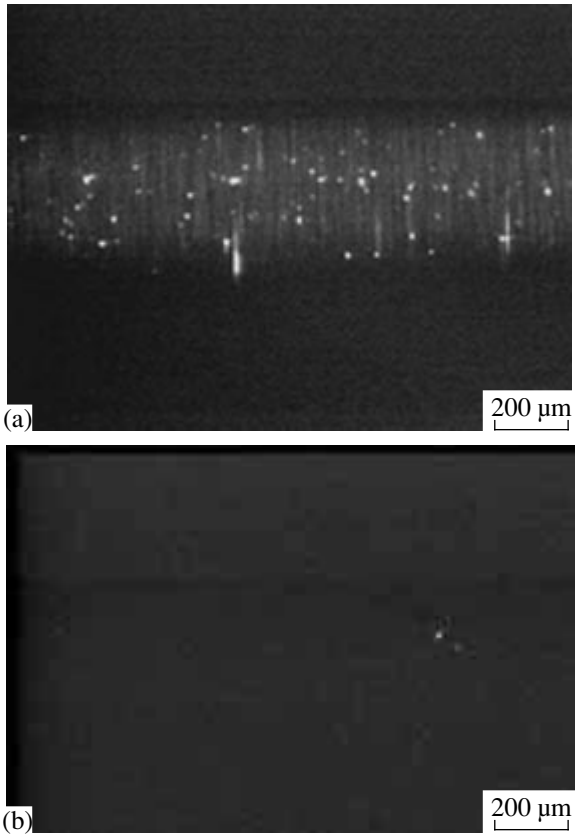

Fig. 6. Light scattering in KH_2PO_4 single crystals grown at two temperatures *t*: (a) 35 and (b) 80°C.

Na, K, Al, B, Si, Ti, Fe, and Cr impurities than the filters with 0.15 μm pores (table). The filters with 0.05 μm pores also retained water-insoluble particles of an unknown nature.

Growth rates. It is well known [16–18] that with an increase in supersaturation and, thus, also in growth rate, the probability of defect formation in crystals also increases. The appearance of inhomogeneities is not directly related to an increase in the growth rate. However, the sectorial, vicinal–sectorial, and zonal inhomogeneities arising because of nonstationary growth conditions manifest themselves more pronouncedly in fast grown crystals than in crystals grown under the traditional conditions, which is reflected in the optical characteristics of the crystals.

The study of the growth-rate influence on the transmission spectra of the crystals showed than an increase in V_{cr} up to $(0.8–4.1) \times 10^{-6}$ cm/s reduces the transmission in the UV spectrum range at $\lambda = 230$ nm by a factor of 15 (Fig. 3). The low transmission in rapidly grown crystals seems to be explained by a high concentration of liquid-phase inclusions. Crystals grown at a rate of $V_{cr} = 4.1 \times 10^{-6}$ cm/s have the maximum concentrations of liquid-phase inclusions and solid particles of various shapes and sizes. Figures 4a and 4b show the photographs of scattering centers in crystals grown at various growth rates.

Moreover, the measurements of the concentration of free water in liquid-phase inclusions of rapidly grown crystals ($V_{cr} = 4.1 \times 10^{-6}$ cm/day) showed that its content is several times higher than in crystals grown at a rate of $V_{cr} \sim 0.8 \times 10^{-6}$ cm/s [19].

Crystallization temperature. An increase in growth temperature considerably influences the quality of the crystals grown [19] for several reasons: the change of the structure and properties of the growth solution (density and viscosity, thermal motion and degree of ion hydration, the work of nucleus formation, etc.) [20], less intense formation of the boundaries between the crystal sectors [21], the change in the surface structure of the crystal and, in particular, of the kink concentration at the growth steps [22], and a decrease of impurity adsorption by the crystal surface because of the displacement to the right of the adsorption–desorption equilibrium [3].

The analysis of the influence of the crystallization temperature on the optical quality of the crystals is considered on specimens grown from solutions at $t_{cr} = 35$, 45, 55, 60, 70, and 80°C (Fig. 5). It is shown that a decrease in the crystallization temperature to 35 and

45°C increases the absorption in the UV spectrum range; in the vicinity of the fundamental absorption edge, the transmission of the crystals grown at these temperatures is about 70%. With an increase in the crystallization temperature up to 80°C, the transmission in the UV range also increases up to 86%. This effect seems to be explained by the fact that an increase in the crystallization temperature facilitates the desorption of impurities adsorbed on the face. At lower temperatures, the effective capture of impurities by a growing crystal results in the formation of various defects (Figs. 6a, 6b) and, as a result, in a lower transmission. The anomalous absorption band at λ = 220 nm is observed in the spectra of all the crystals studied.

CONCLUSIONS

The studies considered above show that the method of solvent recirculation with the use of the starting material with a microimpurity content not exceeding 5×10^{-5} wt %, microfiltration of the solution, and the optimum crystallization conditions (t_{cr} = 80°C, $V_{cr} \sim (0.8–1.6) \times 10^{-6}$ cm/s, pH 4) results in growth of KDP single crystals with cross sections up to 300×300 mm^2 and transmission at the wavelength λ = 200 nm of about 86%.

REFERENCES

1. E. Diegues, A. Cintas, P. Hernandez, and J. M. Cabrera, J. Cryst. Growth **73** (1), 193 (1985).
2. V. I. Bredikhin, N. V. Kiseleva, and V. V. Korolikhin, Izv. Akad. Nauk SSSR, Neorg. Mater. **22** (1), 112 (1986).
3. Yu. N. Velikhov, I. M. Pritula, V. I. Salo, *et al.*, Izv. Ross. Akad. Nauk, Neorg. Mater. **36** (7), 880 (2000).
4. F. M. Singelton, J. F. Cooper, B. D. Andersen, and F. P. Milanovich, Appl. Phys. Lett. **52** (11), 857 (1988).
5. É. P. Lokshin, Kristallografiya **41** (6), 1115 (1996) [Crystallogr. Rep. **41**, 1061 (1996)].
6. C. D. Marshall, S. A. Payne, M. A. Henesian, *et al.*, J. Opt. Soc. Am. B **11**, 774 (1994).
7. N. Y. Garces, K. T. Stevens, L. E. Halliburton, *et al.*, J. Appl. Phys. **89** (1), 47 (2001).
8. I. M. Pritula, V. I. Salo, and M. I. Kolybaeva, Neorg. Mater. **37** (2), 237 (2001).
9. V. V. Azarov, L. I. Bespalova, and M. I. Kolybaeva, in *Single Crystals and Scintillators* (VNIIM, Kharkov, 1978), p. 3.
10. V. V. Azarov, M. I. Kolybaeva, and Ya. A. Obukhovskiĭ, in *Single Crystals and Scintillators* (VNIIM, Kharkov, 1981), p. 134.
11. C. Belouet, E. Dunia, and J. Petroff, J. Cryst. Growth **23**, 243 (1974).
12. N. S. Stepanova and A. V. Belyustin, Izv. Akad. Nauk SSSR, Neorg. Mater. **11**, 1457 (1975).
13. Yu. N. Velikhov, Candidate's Dissertation in Chemistry (Khar. Gos. Univ., Kharkov, 1993).
14. K. E. Montgomery and F. P. Milanovich, J. Appl. Phys. **68**, 3979 (1990).
15. A. G. Gusachenko and N. F. Obukhova, Khim. Tekhnol., No. 2, 70 (1988).
16. Y. Kvapil, V. John, and J. Novak, in *Proceedings of II Seminar on Single Crystals* (Turnov, 1967).
17. J. W. Mullin, J. Appl. Chem. **17**, 151 (1967).
18. I. V. Gavrilova, Acta Crystallogr. **21**, 258 (1966).
19. L. V. Atroshchenko, A. B. Blank, L. M. Nikitina, *et al.*, Izv. Akad. Nauk SSSR, Neorg. Mater. **25**, 1402 (1989).
20. Yu. N. Velikhov, I. M. Pritula, V. I. Salo, *et al.*, Izv. Ross. Akad. Nauk, Neorg. Mater. **33** (7), 867 (1997).
21. I. V. Gavrilova, in *Crystal Growth* (Nauka, Moscow, 1965), Vol. 5, p. 197.
22. S. S. Fridman, N. S. Stepanova, and A. V. Belyustin, in *Crystal Growth* (Nauka, Moscow, 1972), Vol. 9, p. 79.

Translated by L. Man

Crystallography Reports, Vol. 49, No. 2, 2004, pp. 271–274. Translated from Kristallografiya, Vol. 49, No. 2, 2004, pp. 325–328.

CRYSTAL GROWTH

The Growth and Structure of $Pb_3Ga_2Ge_4O_{14}$ and $Ba_3Ga_2Ge_4O_{14}$ Single Crystals[1]

L. N. Bezmaternykh, A. D. Vasil'ev, I. A. Gudim, and V. L. Temerov

Kirensky Institute of Physics, Siberian Division, Russian Academy of Sciences, Akademgorodok, Krasnoyarsk, 660036 Russia

e-mail: bezm@iph.krasn.ru

Received March 3, 2003

Abstract—Conditions for the flux synthesis of $Pb_3Ga_2Ge_4O_{14}$ and $Ba_3Ga_2Ge_4O_{14}$ single crystals and their solid solutions $Pb_{3-x}Ba_xGa_2Ge_4O_{14}$ are studied. Structural analysis showed that the Ga^{3+}- and Ge^{4+}-cation positions in flux-grown $Pb_3Ga_2Ge_4O_{14}$ and $Ba_3Ga_2Ge_4O_{14}$ single crystals are not mixed. © *2004 MAIK "Nauka/Interperiodica".*

INTRODUCTION

More than a hundred crystalline compounds belonging to the $Ca_3Ga_2Ge_4O_{14}$ structural family have been synthesized, many of them in the form of single crystals [1]. Their piezoelectric, photorefractive, and laser properties have attracted much attention [1, 2]. Many of these crystals surpass quartz, which is widely used in microelectronics, in piezoelectric properties. Some have the lowest excitation thresholds among all the known solid-state matrices doped with Nd^{3+} ions [3]. In single crystals of compounds of this structural type, which demonstrate a wide variety of compositions, the cation distribution not only depends on the individual characteristics of single crystals [1, 4], but also may be sensitive to growth conditions. Hence, the properties of single crystals may acquire specific features upon being subsequently subjected to external influences.

Among synthesized compounds of this type, lead and barium gallogermanates are distinguished primarily by having the largest cations. Based on extrapolation, the single crystals of these compounds are expected to have record-high values of piezoelectric constants [1]. However, these compounds melt with decomposition, and only a fine-grained aggregate of $Sr_3Ga_2Ge_4O_{14}$ has been grown by the Czochralski method using $Pb_3Ga_2Ge_4O_{14}$ seed crystals [5].

In this study, we examined the possibilities of the flux synthesis and investigated the structural characteristics of flux-grown single crystals of lead and barium gallogermanates.

THE SEARCH FOR FLUX COMPOSITIONS

Because of the low decomposition temperature of $Pb_3Ga_2Ge_4O_{14}$ (980 ± 5°C), we first studied the crystal formation in fluxes based on $PbO + 0.2WO_3$. According to [6], this mixture has a low melting temperature (t_m = 800 ± 5°C). In these fluxes containing crystal-forming oxides in both stoichiometric and nonstoichiometric ratios, we did not detect trigonal $Pb_3Ga_2Ge_4O_{14}$. In all cases, gallogermanate $PbGa_{10}Ge_2O_{20}$ was obtained as a high-temperature phase.

Then, we studied fluxes containing nothing but the crystal-forming components

$$(100 - n)\ \text{wt \%}\ (PbO + kGeO_2) + n\ \text{wt \%}\ Pb_3Ga_2Ge_4O_{14}. \quad (1)$$

For a flux with k = 1.42, the trigonal phase of

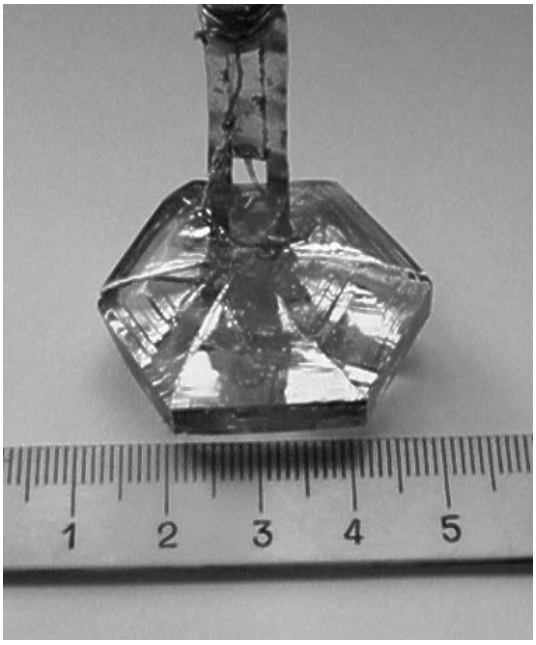

Fig. 1. $Pb_3Ga_2Ge_4O_{14}$ single crystal.

[1] This work was presented at the National Conference on Crystal Growth (NCCG-2002, Moscow).

Table 1. X-ray diffraction data

Composition of single crystals		$Pb_3Ga_2Ge_4O_{14}$	$Ba_3Ga_2Ge_4O_{14}$
Number of measured reflections		709	860
Number of independent reflections (Friedel pairs are not averaged)		402	493
Number of independent reflections (complete averaging)		242	296
$2\theta_{max}$, deg		52	54.2
hkl range		$0 \le h \le 10$	$-9 \le h \le 10$
		$-10 \le k \le 8$	$-10 \le k \le 0$
		$0 \le l \le 6$	$-6 \le l \le 0$
Lattice parameters, Å	*a*	8.405(1)	8.367(2)
	c	5.0112(7)	5.4397(8)
Extinction coefficient		0.008(2)	0.028(3)
Reliability factor *R*1 calculated against $\|F\|$		0.038	0.055
Reliability factor *wR*2 calculated against $\|F^2\|$		0.098	0.126
Goodness-of-fit, GOOF		1.095	1.125

$Pb_3Ga_2Ge_4O_{14}$ is crystallized in a wide (~100°C) temperature range. At n = 70 wt %, the saturation temperature t_{sat} = 920 ± 10°C, which is 60°C lower than the decomposition temperature of gallogermanate. The slope of the concentration dependence dt_{sat}/dn = 7.2 K/wt %. The metastability range is Δt_{met} ~ 10 K. One of the drawbacks of this flux is its relatively high viscosity. Therefore, we tested also fluxes containing lead fluoride:

$$(100 - n)\text{ wt \% } [(1 - q)PbO + qPbF_2 + 1.42GeO_2] + n\text{ wt \% } Pb_3Ga_2Ge_4O_{14}. \quad (2)$$

Even at q = 1, $Pb_3Ga_2Ge_4O_{14}$ remains to be a high-temperature phase in a wide (~100 K) temperature range, retaining high solubility (at n = 70 wt %, t_{sat} = 900 ± 10°C). For this flux, dt_{sat}/dn = 1.4 K/wt % and the metastability range is also about 10 K.

Flux (1) was used to study the formation of gallogermanate crystals $Pb_3Ga_2Ge_4O_{14}$ with a partial replacement of lead by barium ($Pb_{3-x}Ba_xGa_2Ge_4O_{14}$). In a test experiment, single crystals were grown by spontaneous crystallization from a flux with the composition

$$30\text{ wt \% } (PbO + 1.42GeO_2) + 70\text{ wt \% } Pb_{2.1}Ba_{0.9}Ga_2Ge_4O_{14} \quad (3)$$

with t_{sat} = 920 ± 10°C. X-ray diffraction analysis showed that the lattice parameters of these single crystals are a = 8.445 Å and c = 5.042 Å. The grown crystals had the composition $Pb_{2.75}Ba_{0.25}Ga_2Ge_4O_{14}$, as evidenced by an evaluation of the Ba content based on the linear interpolation of the lattice parameters of $Pb_3Ga_2Ge_4O_{14}$ and $Ba_3Ga_2Ge_4O_{14}$. We failed to prepare crystals with a higher Ba content because of the appearance of another high-temperature phase.

$Ba_3Ga_2Ge_4O_{14}$ single crystals were grown from a flux with the composition

$$25\text{ wt \% } (BaO + 0.62B_2O_3) + 75\text{ wt \% } Ba_3Ga_2Ge_4O_{14} \quad (4)$$

with t_{sat} ~ 855°C. The slope of the solubility curve was

Table 2. Fractional coordinates and equivalent thermal parameters of atoms

Atom	Coordinates			Occupancy of the position, *q*	U_{eq}, Å^2
	x	*y*	*z*		
Pb Ba	0.5943(2) 0.5836(3)	0	0	1/2	0.0158(4) 0.0252(6)
Ga	2/3	1/3	0.4872(7) 0.4878(6)	1/3	0.0054(8) 0.0046(7)
Ge(1)	0	0	0	1/6	0.010(1) 0.048(2)
Ge(2)	0.2406(3) 0.2435(4)	0	1/2	1/2	0.0077(7) 0.042(1)
O(1)	2/3	1/3	0.826(5) 0.796(4)	1/3	0.016(5) 0.020(5)
O(2)	0.715(2) 0.703(2)	0.547(2) 0.541(2)	0.345(3) 0.355(3)	1	0.019(3) 0.022(3)
O(3)	0.207(2) 0.207(3)	0.119(2) 0.118(3)	0.773(3) 0.751(5)	1	0.017(4) 0.060(10)

about 11 K/wt %. Single crystals up to 4 mm in size were grown by spontaneous crystallization in the temperature range 830–805°C.

GROWTH OF $Pb_3Ga_2Ge_4O_{14}$ SINGLE CRYSTALS

$Pb_3Ga_2Ge_4O_{14}$ single crystals were grown from fluxes (1) and (3) using a seeding technique. Fluxes (150 g) were prepared at $t = 950 \pm 2$°C in a platinum crucible with diameter $D = 40$ mm and height $H = 65$ mm by smelting a mixture of oxide powders. Homogenization was also carried out at $t = 950 \pm 2$°C. The temperature in the flux decreased as the distance from the crucible bottom increased, and the magnitude of the vertical component of the temperature gradient along the axis of the crucible was ~3 K/cm.

The saturation temperature was determined with an accuracy of ±2 K using a trial crystal. Then, a seed was immersed in a flux at $t = t_{sat} + 20$°C. The crystallographic threefold axis of the seed coincided with the normal to the flux surface. The immersion depth was 1 mm. Immediately after seeding, the temperature was reduced to $t = t_{sat} - 2$°C. During the first ten days, the temperature was reduced at a rate of 1 K/day, after which the cooling rate amounted to 1.5 K/day until the growth process was completed. The total growth time was four weeks. When grown, the crystal was pulled from the flux and cooled in the furnace after it has been switched off. The weight of the $Pb_3Ga_2Ge_4O_{14}$ single crystal grown from flux (3) in the range $t = 910$–870°C was 42 g (Fig. 1). The weight loss of the flux during the crystal growth was 2%, and the weight loss during the growth from flux (1) was no larger than 0.7%. After replenishment with crystal-forming oxides, these fluxes were used repeatedly.

$Pb_3Ga_2Ge_4O_{14}$: Nd^{3+} single crystals were grown from a flux to which SiO_2 was added in order to increase the distribution coefficient of Nd^{3+} ions. The seeding technique was not used for growing either $Ba_3Ga_2Ge_4O_{14}$ or $Pb_{3-x}Ba_xGa_2Ge_4O_{14}$ single crystals.

STRUCTURAL CHARACTERISTICS

X-ray diffraction studies were carried out with ellipsoidal samples with linear sizes of 0.12–0.15 mm that were prepared from $Pb_3Ga_2Ge_4O_{14}$ and $Ba_3Ga_2Ge_4O_{14}$ single crystals. The X-ray diffraction intensities were measured on an automated KM-4 diffractometer (MoK_α radiation, a graphite monochromator, and a $\theta/2\theta$ scan at a variable rate). The details of the X-ray diffraction studies and the results of structure refinement are listed in Table 1.

The absorption corrections were calculated and applied using a ψ scan of 15 reflections with a step of 10°. The structures were solved and anisotropically refined (for Pb (Ba), Ga, and Ge atoms) using the SHELX97 program package (Table 2). Both compounds belong to the langasite structural type with the sp. gr. $P321$. Oxygen atoms form Thomson cubes around large Pb^{2+} and Ba^{2+} cations (the distances are listed in Table 3). Small Ga^{3+} and Ge^{4+} cations in the crystals grown by us, unlike cations in the structures studied in [5], are not mixed and occupy strictly separated positions: Ga^{3+} cations occupy tetrahedral

Table 3. Interatomic distances in $Pb_3Ga_2Ge_4O_{14}$ and $Ba_3Ga_2Ge_4O_{14}$ crystals (Å)

$Pb_3Ga_2Ge_4O_{14}$		$Ba_3Ga_2Ge_4O_{14}$	
Pb–O	2 × 2.42(2) 2 × 2.697(9) 2 × 2.82(2) 2 × 2.84(2)	Ba–O	2 × 2.60(2) 2 × 2.748(9) 2 × 2.84(2) 2 × 3.03(2)
Ga–O	3 × 1.78(2)		3 × 1.76(2)
	1.70(3)		1.67(3)
Ge(1)–O	6 × 1.89(1)		6 × 2.03(1)
Ge(2)–O	2 × 1.80(2) 2 × 1.81(2)		2 × 1.80(2) 2 × 1.81(2)

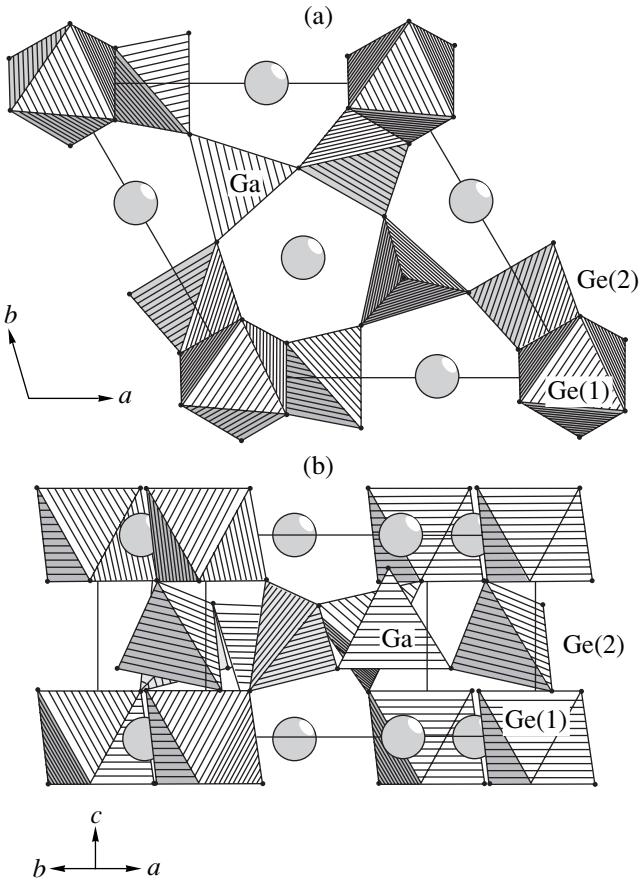

Fig. 2. Unit cell of $Pb_3Ga_2Ge_4O_{14}$ and $Ba_3Ga_2Ge_4O_{14}$ single crystals projected onto the (a) *ab* and (b) *ac* planes. The Pb and Ba atoms are represented by circles.

2*d* positions and Ge^{4+} cations are in the 3*f*-tetrahedral (Ge2) and 1*a*-octahedral (Ge1) oxygen environments (Fig. 2).

In both cases, attempts to refine the inverted structural models indicated the correctness of the model parameters listed in Table 2.

CONCLUSION

We developed a flux method for growing $Pb_{3-x}Ba_xGa_2Ge_4O_{14}$ single crystals ($0 \le x \le 0.3$) with dimensions sufficient for investigation of piezoelectric, photorefractive, and nonlinear optical properties. $Ba_3Ga_2Ge_4O_{14}$ single crystals up to 4 mm in size were grown from barium borate fluxes. The structure of this compound was studied for the first time. $Ba_3Ga_2Ge_4O_{14}$ and $Pb_3Ga_2Ge_4O_{14}$ single crystals are characterized by a strictly positional distribution of Ga^{2+} and Ge^{4+} cations. Studies by laser spectroscopy and investigation of the lasing characteristics were performed using $Pb_3Ga_2Ge_4O_{14}$ single crystals doped simultaneously with Nd^{3+} and Si^{4+} ions. The results of studies of the elastic and piezoelectric properties of $Pb_3Ga_2Ge_4O_{14}$ single crystals in the ordered state will be published elsewhere.

REFERENCES

1. B. V. Mill and Y. V. Pisarevsky, in *Proceedings of International Frequency Control Symposium and Exhibition* (IEEE/EIA, 2000), p. 133.
2. A. A. Kaminskiĭ, S. É. Sarkisov, B. V. Mill', *et al.*, Izv. Akad. Nauk SSSR, Neorg. Mater. **18**, 1396 (1982).
3. *Physics and Spectroscopy of Laser Crystals*, Ed. by A. A. Kaminskiĭ (Nauka, Moscow, 1986).
4. B. H. T. Chai, A. N. P. Bustamante, and M. C. Chou, in *Proceedings of International Frequency Control Symposium and Exhibition* (IEEE/EIA, 2000), p. 163.
5. E. L. Belokoneva, S. Yu. Stefanovich, Yu. V. Pisarevskiĭ, *et al.*, Zh. Neorg. Khim. **45** (11), 1786 (2000).
6. *Phase Diagrams of Silicate Systems*, Ed. by N. A. Toropov *et al.* (Nauka, Leningrad, 1969).

Translated by T. Safonova

Crystallography Reports, Vol. 49, No. 2, 2004, pp. 275–278. Translated from Kristallografiya, Vol. 49, No. 2, 2004, pp. 329–333.

CRYSTAL GROWTH

Use of a Fluorine-Containing Solvent in the Synthesis of $YBa_2Cu_3O_{7-\delta}$ Single Crystals[1]

P. P. Gorbik, I. V. Dubrovin, N. V. Abramov, and A. I. Nastasienko

Institute of Surface Chemistry, National Academy of Sciences of Ukraine, ul. Generala Naumova 17, Kiev, 03680 Ukraine

e-mail: div@wadev.com

Received March 3, 2003

Abstract—A laboratory technological procedure has been developed for the synthesis of high-temperature superconducting $YBa_2Cu_3O_{7-\delta}$ single crystals ($T_c \sim 90$ K, $\Delta T_c \sim 1.0$ K) up to 0.25 cm^2 in size from a nonstoichiometric fluorine-containing flux of $(YO_{1.5})(BaO)_{4-x}(BaF_2)_x(CuO)_{10}$, where $2 \geq x \geq 0$, using a combination of enhanced nucleation and directional crystallization by the Czochralski method. Studies using differential thermal analysis demonstrated that the addition of BaF_2 decreased the eutectic-crystallization temperature and increased the crystal-growth rate. The optimum concentration of BaF_2 in the starting melt composition was found ($x = 0.2$). The single-crystal surface was studied by atomic-force nanoscopy. The morphology of single crystals that have been synthesized from a melt of their own components differs substantially from that of crystals grown from a BaF_2-containing melt. © *2004 MAIK "Nauka/Interperiodica".*

INTRODUCTION

Study of the quasi-ternary system Y_2O_3–BaO–CuO demonstrated that the $YBa_2Cu_3O_{7-\delta}$ compound (123; hereinafter, phases existing in this system will be denoted similarly in accordance with the Y : Ba : Cu ratio) is formed by the peritectic reaction [1]. Single crystals of this compound cannot be grown from a stoichiometric melt. To reach the primary-crystallization field of $YBa_2Cu_3O_{7-\delta}$ on the liquidus surface upon cooling a melt, the growth is most commonly performed from a nonstoichiometric melt enriched in the intrinsic components of the compound crystallized (such as BaO and CuO) [2]. This approach allows one to carry out crystallization at temperatures below the decomposition temperature of yttrium–barium cuprate.

Adding foreign components with the aim of decreasing the crystallization-onset temperature of $YBa_2Cu_3O_{7-\delta}$ is not desirable, because foreign components, along with this positive effect, considerably influence the physical and structural properties of the crystals grown. The main requirements for the solvents are that they should readily dissolve the recrystallized material at relatively low temperatures, must not form compounds with either the material crystallized or its components, should have a low vapor pressure at growth temperatures, must not react with the container material, and should be negligibly soluble in the grown crystal.

At present, investigations are not only carried out with the use of solvents consisting of the components of compounds synthesized [2], but also using halides of the metals that are the components of the crystalline materials formed [3, 4]. Barium fluoride, on the whole, satisfies the above-mentioned requirements. Experiments have shown that BaF_2 can be used as a solvent component. However, the composition and morphology of the grown crystals and the effect of BaF_2 on their physical characteristics have not been adequately investigated, and the appropriate concentration range has not been studied completely.Elucidating the effect of small additives of BaF_2, not only on the decrease in the growth temperature of 123 single crystals, but also on the mass-transfer processes in the synthesis in the temperature range close to the temperature of decomposition of the 123 compound according to the peritectic reaction, is also of interest.

The aim of this work was to study the physicochemical characteristics of the growth of 123 single crystals from a BaF_2-containing melt with the composition $(YO_{1.5})(BaO)_{4-x}(BaF_2)_x(CuO)_{10}$, where $2 \geq x \geq 0$; develop an optimum procedure for the synthesis of 123 single crystals; and examine their chemical composition, morphology, and main electrophysical characteristics.

EXPERIMENTAL METHOD

$YBa_2Cu_3O_{7-\delta}$ single crystals were grown according to the procedure described previously [2]. In a fraction of the $(BaO)_2(CuO)_7$ mixture used as a solvent, BaO was replaced by BaF_2. Powdered Y_2O_3, $BaCO_3$, BaF_2, and CuO of high-purity grade were used as starting components. The mixture was pelletized and, then, decarbonized and sintered in an alundum container at

[1] This work was presented at the National Conference on Crystal Growth (NCCG-2002, Moscow).

1063-7745/04/4902-0275$26.00 © 2004 MAIK "Nauka/Interperiodica"

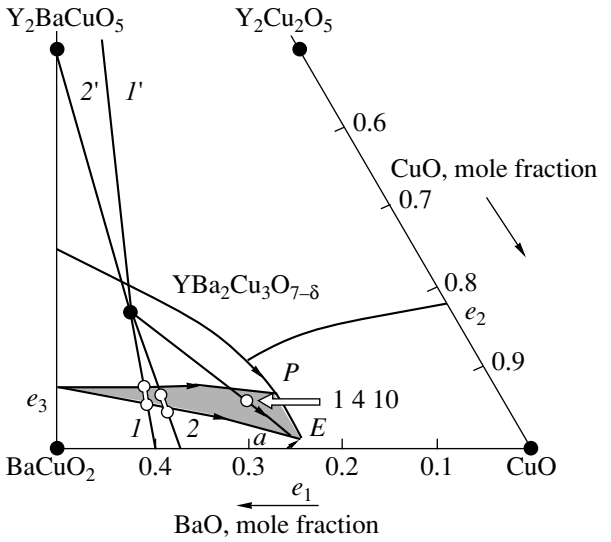

Fig. 1. Qualitative view of the fragment of the quasi-ternary phase diagram of $YO_{1.5}$–BaO–CuO in the vicinity of the superconducting phase $YBa_2Cu_3O_{7-\delta}$.

850°C for 20 h to prepare mixtures of the composition $(YO_{1.5})(BaO)_{4-x}(BaF_2)_x(CuO)_{10}$, where $2 \geq x \geq 0$, with the concentration increment $\Delta x = 0.2$. After grinding and repeated pelletization, a sample of each composition was annealed again as described above. The thermal characteristics were measured by differential thermal analysis (DTA) in air with linear heating and cooling at a rate of 3–5 K/min in the temperature range t = 500–1100°C.

The structures and phase compositions of the starting material and single crystals were studied on a DRON-3M diffractometer (CuK_α radiation). The chemical compositions and morphology of the grown single crystals were studied on a JAMP-10S Auger electron spectrometer (JEOL, Japan), an atomic-force nanoscope (Digital Instruments), and a scanning electron microscope equipped with an JCXA-733 electron-probe X-ray microanalyzer.

To transform single crystals from a tetragonal into an orthorhombic structure (which may undergo a transition to a superconducting state), saturation with oxygen was carried out in a flow system with linear cooling at a rate of 5 K/h at t = 500–420°C. Before use, the oxygen was dried and purified. In the synthesis and oxidation process, the heating and cooling temperatures were controlled to within an accuracy of ±0.1 K using a RIF-101 precision programmable controller. The temperature dependence of the surface impedance was studied at T = 77–200 K using an inductive method [5].

RESULTS AND DISCUSSION

Single crystals were synthesized using a previously tested technique that includes enhanced nucleation and directional crystallization from flux by the Czochralski method [2]. According to our results and analysis of the phase diagrams of the $YO_{1.5}$–BaO–CuO system [6], a melt with the composition $YBa_4Cu_{10}O_y$ reaches the upper region (with respect to temperature) of the primary-crystallization surface of $YBa_2Cu_3O_{7-\delta}$ upon cooling (Fig. 1). As the melt is depleted in the compound crystallized, the representative point of the melt composition moves towards the boundary curve e_3–E of the secondary formation of phases 011 + 123 and is tangential to this curve at the point a close to the point E, which corresponds to the tertiary formation of phases 123 + 011 + 001 (an invariant equilibrium). For this melt composition, the most substantial concentration range of the crystallization path is 1 4 10–a. Therefore, crystallization can also be performed in a wide temperature range because the point E is the lowest point of the liquidus and, hence, corresponds to the composition with the lowest melting point. Two polythermal sections *1* and *2* that were studied in [6] are shown in Fig. 1. The ranges of primary crystallization of phase 123 along these sections are indicated by open circles. It can be seen that these ranges are rather narrow. Upon cooling the system, a small part of the path a–E for the representative point of the melt coincides with the line of the secondary formation of two phases: 123 + 011 (see Fig. 1). The introduction of BaF_2 as an additional system component leads to an increase in the variance of the system. In this case, according to the phase rule, a multivariant equilibrium should exist in a ternary eutectic, due to which the temperature range of crystallization of $YBa_2Cu_3O_{7-\delta}$ can be increased by varying the BaF_2 concentration.

The starting samples of a mixture with the composition $(YO_{1.5})(BaO)_{4-x}(BaF_2)_x(CuO)_{10}$ ($2 \geq x \geq 0$, Δx = 0.2), with the fraction of the solvent $(BaO)_{2-x}(BaF_2)_x(CuO)_7$ ($2 \geq x \geq 0$), were studied by DTA and powder X-ray diffraction analysis at t = 500–1100°C. The cooling thermograms show two exothermic effects (Fig. 2). The exothermic effect at $t \sim 1020$°C corresponds to the phase transition $L \longleftrightarrow 123 + L$ (L is a liquid) and its temperature is close to the temperature of the peritectic reaction $123 \rightleftharpoons 211 + L$. The second exothermic effect at $t \sim 800$°C corresponds, it appears, to two phase transitions: $123 + L \rightleftharpoons 123 + 011 + L$ and $123 + 011 + L \rightleftharpoons 123 + 011 + 001$, because the individual exothermic effect related to the $123 + L \rightleftharpoons 123 + 011 + L$ transition was not observed. This circumstance may be associated with the narrow temperature range in which the phase region 123 + 011 + L for the $YBa_4Cu_{10}O_y$ (1 4 10) composition in the phase diagram of the $YO_{1.5}$–BaO–CuO system exists.

An increase in the BaF_2 concentration in the range $2 \geq x \geq 0$ leads to a decrease in the phase-transition temperature (Figs. 2, 3). Thus, a decrease in the liquidus temperature by ~10 K corresponds to a decrease in the crystallization temperature of a eutectic by ~35 K, which substantially extends the temperature range of crystallization of yttrium–barium cuprate 123. A powder X-ray diffraction study of samples annealed for

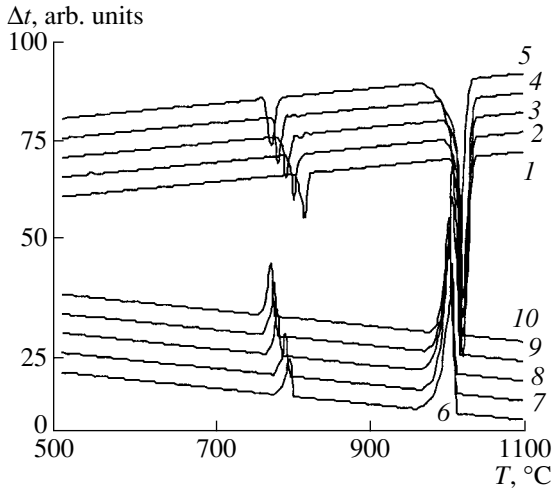

Fig. 2. DTA curves for samples with different BaF_2 contents; heating: x = (*1*) 0, (*2*) 0.2, (*3*) 0.4, (*4*) 1, and (*5*) 2; cooling: x = (*6*) 0, (*7*) 0.2, (*8*) 0.4, (*9*) 1, and (*10*) 2.

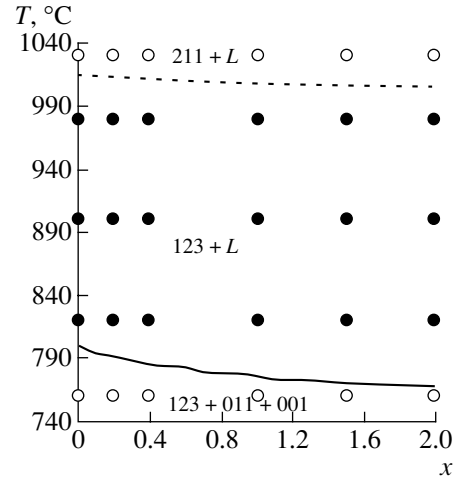

Fig. 3. Phase-transition temperatures of $(YO_{1.5})(BaO)_{4-x}(BaF_2)_x(CuO)_{10}$ samples vs. the BaF_2 content (x) and the phase composition.

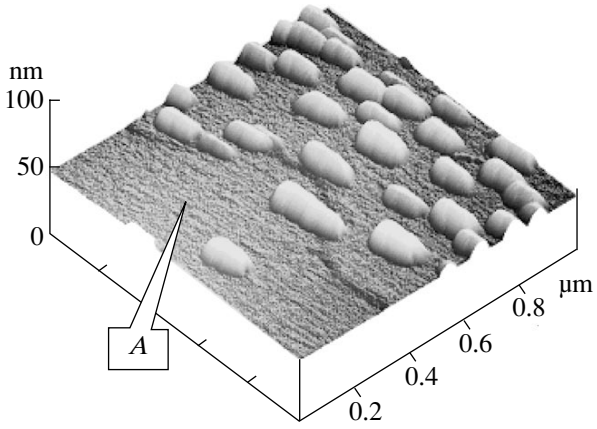

Fig. 4. Nanorelief of the surface of an $YBa_2Cu_3O_{7-\delta}$ single crystal.

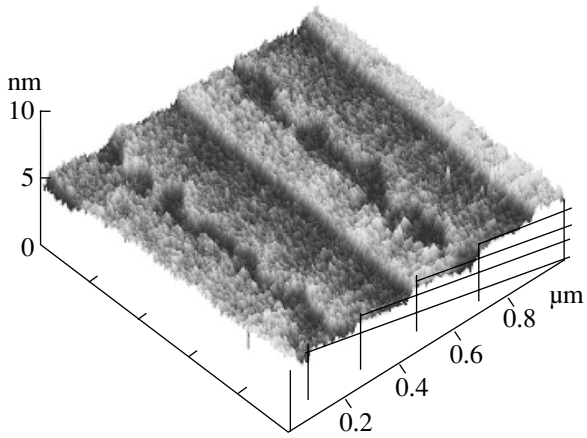

Fig. 5. Fragment *A* of the surface of an $YBa_2Cu_3O_{7-\delta}$ single crystal.

20 h and quenched in air confirmed the presence of the phase regions shown in Fig. 3. The BaF_2-containing composites $(BaO)_{2-x}(BaF_2)_x(CuO)_7$ ($2 \geq x \geq 0$, Δx = 0.2) are of interest as solvents that can be used in different methods of single-crystal growth. However, we were interested primarily in the possibility of decreasing the melt viscosity with the aim of raising the growth rate. Thus, the crystal-growth rate depends on the transfer rate of the compound components through the molten zone. In our synthesis method, diffusion to the growth zone of the material to be crystallized is, apparently, the rate-limiting factor. In the diffusion mode, the growth rate is determined by the equation $V = D \times dC/dT \times G$ [7], where V is the growth rate, D is the diffusion coefficient of the recrystallized compound, G is the temperature gradient in the molten zone, and dC/dT is the slope of the liquidus determined from the phase diagram. As can be seen from this equation, the crystal-growth rate in the diffusion mode depends on the properties of the compounds and the parameters of the technological equipment used.

We found that the sizes of the grown single crystals depend nonmonotonically on the initial concentration of BaF_2. Low BaF_2 concentrations (x = 0.2) were found to be most favorable for the growth of 123 single crystals. Solvent-free plate-like single crystals with a surface area of up to 0.25 cm^2 were obtained. At high values of x, the total amount of rapidly growing nuclei increases substantially, giving rise to a large number of small plate-like crystals.

The powder X-ray diffraction study of the grown single crystals demonstrated that barium fluoride is virtually insoluble in the 123 compound (<1 mol %). This fact was confirmed by studying the crystal surface and bulk (etching with Ar ions) by Auger electron spectroscopy. The results indicate enrichment of the near-sur-

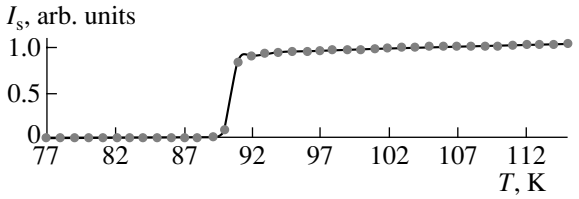

Fig. 6. Temperature dependence of the surface impedance (I_s) of $YBa_2Cu_3O_{7-\delta}$ single crystals.

face region in Ba and Cu atoms with respect to the stoichiometry observed in the crystal bulk. After oxidative annealing, local fluorine-rich regions at the grain boundaries and in dislocation clusters were found in mosaic crystals by electron-probe X-ray microanalysis.

The nanostructure of the single-crystal surface was studied by atomic-force nanoscopy. Approximately 25 follicle-like aggregates with heights of ~10 nm were observed on the surface within an area of 1×1 μm (Fig. 4). Their surface density amounted to $\sim 2.5 \times 10^9$ cm^{-2}. Presumably, these aggregates on the surface are very fine particles of solid phase 011 existing in the phase region 123 + 011 + *L*. In fact, as the system is cooled, crystallization of the 123 phase occurs virtually without supersaturation on the surface of the crystal formed in the previous phase region. Nuclei of the 011 phase are formed in the bulk while passing through the interface 123 + *L* $\rightleftharpoons$ 123 + 011 + *L* due to supersaturation of the melt with this component. Therefore, cooling of the melt leads to precipitation of the 011 phase on many nuclei distributed in the bulk. Upon cooling the melt, the 011-phase supersaturation decreases as these particles grow. Therefore, the stable single-crystal growth continues in the phase region 123 + 011 + *L*. However, this process is hindered due to the presence of particles of the solid phase 011 in the melt. As the melt recedes, individual particles of the 011 phase, remaining, it appears, at the active centers on the surface of the 123 single crystal (Fig. 4), take a spindle-like shape in accordance with the direction of the temperature gradient. We may assume that nanosized particles of the 011 phase interact with the surface of the 123 crystal and are fixed at its active centers. As a result, the crystal surface is "decorated" with nanosized particles. In particular, structural defects, such as dislocations, can serve as active centers. If this is the case, the number of active centers can be determined. This value is equal to the number of visible particles of the 011 phase per unit of surface area. According to the results of statistical calculations, the surface concentration of these centers is $\sim 2.5 \times 10^9$ cm^{-2}.

Taking into account that the rate of cooling is very low (~0.5 K/h), the two-dimensional nucleation of a new atomic layer in the course of the growth of the {001} face is unlikely. Growth appears to occur discontinuously, with the formation of growth steps to which adatoms migrating over the crystal surface attach. These adatoms form bonds with a larger number of the nearest neighbors. The steps on the vicinal face (indicated by straight lines; inset 1), with a height-to-length ratio of ~1 : 200, are clearly seen in Fig. 5. Thus, the surface of the plate-like single crystals grown by the technique described above is a nearly singular face. In the *ab* plane, the growth of a flat face was practically not observed. This is, most likely, associated with the growth of a nonsingular face (for example, {110}) containing a large number of active growth sites, due to which substantial supersaturation is not required. This is also evidenced for by the relatively high growth rate of this face.

Measurements of the temperature dependence of the surface impedance of the crystals highly saturated with oxygen ($\delta \sim 0$) yielded the value of the superconducting-transition temperature $T_C \sim 90$ K and the transition width $\Delta T \sim 1.0$ K (Fig. 6). It is well-known that dislocations are among the main types of structural defects that serve as pinning centers. In our case, the concentration of dislocations emerging onto the crystal-face surface ($\sim 2.5 \times 10^9$ cm^{-2}) is much lower than the dislocation density ($\sim 10^{11}$) in thin 123 films, which have a high critical current.

CONCLUSIONS

Crystallization of $YBa_2Cu_3O_{7-\delta}$ from a fluorine-containing flux was studied, and a method of synthesizing this compound was optimized. This method was used to prepare 123 single crystals of high structural quality with a surface area of ~0.25 cm^2. The solubility of BaF_2 in 123 single crystals does not exceed 1 mol %. The specific features of the nanostructure of the single-crystal surface were examined. The relationships between the structure of the single-crystal surface, (i) the character of phase transitions occurring during the crystallization, and (ii) a number of physical properties were ascertained. The solvent $(BaO)_{2-x}(BaF_2)_x(CuO)_7$, with a specified melting temperature, can be used for the synthesis of 123 single crystals by a number of other known methods.

REFERENCES

1. Yu. A. Bashkirov and L. S. Fleĭshman, Sverkhprovodimost: Fiz., Khim., Tekh. **5** (8), 1351 (1992).
2. P. P. Gorbik, I. V. Dubrovin, I. V. Laguta, *et al.*, Metallofiz. Noveĭshie Tekhnol. **21** (8), 1057 (2001).
3. K. Watanabe, J. Cryst. Growth **114**, 269 (1991).
4. Yamada, Yasuji, Niiori, *et al.*, US Patent No. 5817172 (October 6, 1998).
5. I. F. Voloshin, S. V. Gaponov, N. V. Il'in, *et al.*, Sverkhprovodimost: Fiz., Khim., Tekh. **2** (5), 93 (1989).
6. G. Krabbes, P. Schätzle, W. Bieger, *et al.*, Physica C (Amsterdam) **242**, 145 (1995).
7. V. N. Lozovskiĭ, *Floating-Zone Melting with a Temperature Gradient* (Metallurgiya, Moscow, 1972).

Translated by T. Safonova

Crystallography Reports, Vol. 49, No. 2, 2004, pp. 279–281. Translated from Kristallografiya, Vol. 49, No. 2, 2004, pp. 334–336.

CRYSTAL GROWTH

A New Optical Medium—$Cd_{0.75}Sr_{0.25}F_2$ Single Crystals[1]

I. I. Buchinskaya and P. P. Fedorov

Institute of Crystallography of the Russian Academy of Sciences, Moscow

e-mail: buchinskaya@rambler.ru

Received March 3, 2003

Abstract—For the first time, single crystals of the $Cd_{0.75}Sr_{0.25}F_2$ solid solution with the fluorite structure are grown from melt by the Bridgman–Stockbarger method. The composition of these single crystals corresponds to the composition congruently melting at the minimum point on the phase diagram. The maximum diameter of the crystal is 50 mm; the maximum height is 30 mm. The vickers microhardness of the semitransparent crystals equals 191 ± 43 kg/mm^2. The transmission cutoff in the IR range is ~10 μm. © *2004 MAIK "Nauka/Interperiodica".*

INTRODUCTION

Fluorides of divalent metals are valuable materials for structural optics. They can relatively easily be grown from melts by the Bridgman–Stockbarger method. One of the most important characteristics determining the use of these crystals in optics is their homogeneity. The difference between the liquidus and solidus temperatures during growth of single crystals of solid solutions from melt gives rise to changes of the composition both along the ingot length and normal to it (cellular substructure). In the general case, the liquid and solid phases have different compositions; in other words, the solid solutions are melted and crystallized incongruently everywhere except for the compositions at the stationary points, which considerably hinders growth of multicomponent single crystals. Therefore, the knowledge of the compositions of congruently melting solid solutions allows one to considerably increase the crystallization rate and improve the quality of the crystals grown. As a rule, the crystals of the compositions thus found form the basis for creating new materials.

THEORETICAL ANALYSIS

Binary systems have stationary points of two types—minima and maxima. Fluorides with the fluorite structure, CdF_2 and PbF_2, CdF_2 and SrF_2, form the continuous series of solid solutions with the minimum points on the liquidus lines [1] (Fig. 1a). In the CdF_2–SrF_2 system, the coordinates of the minimum are 25 mol % CdF_2 and 1025°C. The transition to the solid solutions with the compositions corresponding to the composition of the stationary points during crystal growth allows one to decrease the melting point of the material and, thus, to reduce the energy consumption and the losses of the material in evaporation and improve its mechanical characteristics (increase hardness and avoid cleavage). Earlier, we manage to grow single crystals of the composition $Pb_{0.67}Cd_{0.33}F_2$ corre-

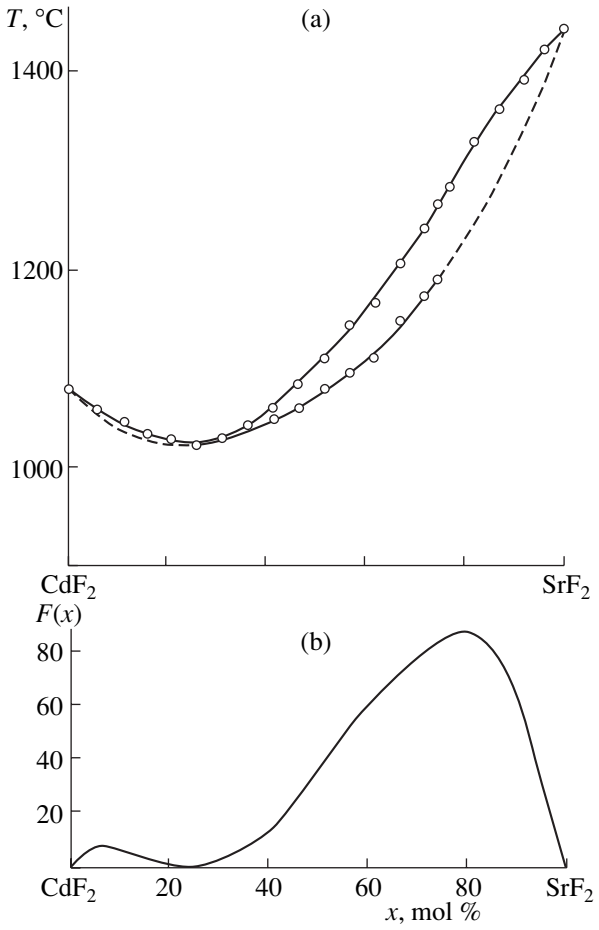

Fig. 1. (a) Phase diagram of the SrF_2–CdF_2 system [1] and (b) the stability function at the crystallization front of the solid solution in the SrF_2–CdF_2 system.

[1] This work was presented at the National Conference on Crystal Growth (NCCG-2002, Moscow).

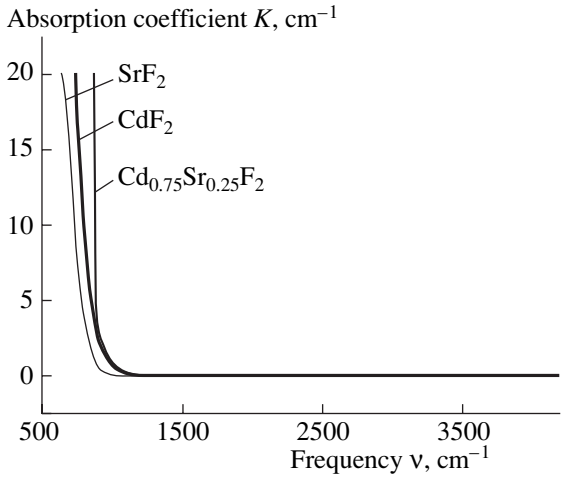

Fig. 2. Frequency dependence of transmission coefficient, $K = -(\ln T)/d$, where T is transmission, and d is the sample thickness.

sponding to the minimum point on the phase diagram of the CdF_2–PbF_2 system, which are a promising optical material [2, 3]. As a rule, the cellular substructure of multicomponent single crystals is a result of the loss of stability of the flat crystallization front because of the concentration supercooling of the melt. The conditions for stability of the flat crystallization front can be characterized by the stability function $F(x)$ [4–6], which is the right-hand part of the modified Tiller criterion,

$$GD/V > m\Delta x = F(x),$$

where m is the tangent of the tilt angle of the liquidus curve on the phase diagram, Δx is the difference of the concentrations in the liquid and solid phases at the crystallization front, G is the temperature gradient, D is the self-diffusion coefficient, and V is the crystallization rate. The physical sense of the stability function reduces to the following: If the above inequality is fulfilled, i.e., if the ratio GD/V of the growth parameters at the given concentration x exceeds the $F(x)$ value, then the flat crystallization front is stable.

The stability function for the CdF_2–SrF_2 system is determined from the experimental data on the phase diagram [1] and is shown in Fig. 1b. The coefficient of SrF_2 and CdF_2 distribution was evaluated as 0.40 [7]. At a low concentration of the second component, where m and the distribution coefficient k can be assumed to be constant, the $F(x)$ function is a straight line proceeding from the origin. The maximum $F(x)$ value is attained at the composition for which the difference between the liquidus and solidus lines is close to the maximum value. At the minimum point of the liquidus, $\Delta x = 0$ and $m = 0$, and, therefore, $F(x) = 0$ and $F'(x) = 0$. Therefore, in directional crystallization, the material with the composition corresponding to the composition of the minimum point is more advantageous than weakly doped materials, because, at small fluctuations in concentration of such a material, its crystallization front remains stable.

EXPERIMENTAL

Traditionally, fluoride single crystals were industrially grown from melts. At present, the Bridgman–Stockbarger method or the method of vertical directional crystallization are widely used [8, 9].

Single crystals of the composition $Cd_{0.75}Sr_{0.25}F_2$ (in charge) were grown by the Bridgman–Stockbarger method from melt in the Ar atmosphere and the products of tetrafluoroethylene pyrolysis. The starting materials were extra pure CdF_2 and SrF_2 preliminarily melted in the same atmosphere. A graphite heater created a 33 ± 5 K/cm temperature gradient in the crystallization zone. We used graphite crucibles with cells of various diameters. In order to attain a higher optical quality, the crucible was lowered rather slowly (3.5–4.0 mm/h) to a depth ranging from 40 to 70 mm depending on the height of the melt column; and the cooling rate was about 100 K/h. The material loss during growth amounted to 1 wt %. The maximum crystal diameter was 50 mm and the maximum height, 30 mm. X-ray phase analysis of single crystals grown was made on an AFV-202E diffractometer by the powder method (CuK_α radiation, Ni filter). Microhardness was measured by the Vickers method on mechanically polished plane-parallel plates cut out from the ingot normally to the growth axis by a manual PMT-3M hardmeter under an empirically selected load of $P = 50$ g. The microhardness measured allowed us to compare the strength of the solid-solution crystals with the strength of pure components. The transmission spectra in the visible IR range of the CdF_2, SrF_2, and $Cd_{0.75}Sr_{0.25}F_2$ samples were measured on an IKS-20 spectrometer.

RESULTS AND DISCUSSION

We grew 30-mm-high single crystals with a diameter ranging from 12 to 50 mm. The lattice parameter determined by the X-ray phase analysis was $a = 5.4778 \pm 0.0023$ Å. We refined the composition of the largest crystal. Assuming the validity of Vegard's law for the SnF_2–CdF_2 system (at the lattice parameters of cadmium and strontium fluorides equal to 5.388 and 5.800 Å, respectively), the composition of the crystal grown is $Cd_{0.77}Sr_{0.23}F_2$.

For this crystal, the microhardness is 191 ± 43 kg/mm^2, whereas the microhardness of pure CdF_2 is as low as 65 kg/mm^2. Similar hardening of solid-solution single crystals was also observed in the PbF_2–CdF_2 system, with the maximum microhardness being different from the composition of the minimum on the melting curve [2].

Figure 2 shows the frequency dependence of the absorption coefficients. It is seen that the transmission

range of $Cd_{0.75}Sr_{0.25}F_2$ single crystals is somewhat narrower than that of the pure starting components.

CONCLUSIONS

Both strontium and cadmium fluorides possess high heterovalent capacity with respect to metal fluorides MF_n [10]. One may assume that this property would also be characteristic of crystals of intermediate compositions (in other words, the ranges of solid solutions would not be tapered in the ternary SrF_2–CdF_2–MF_n systems). For the PbF_2–CdF_2–MF_n systems studied here, this statement is also valid [11]. The possibility of heavy doping of materials with both iso- and heterovalent impurities, in particular, with RE and transition metal fluorides, allows one to hope that it would also be possible to synthesize a broad spectrum of functional (lasing, magnetic, etc.) materials based on the matrix suggested here. For the SrF_2–CdF_2–RF_n systems (R are rare earths), one can expect the existence of triple saddlelike stationary points.

REFERENCES

1. A. Kozak and M. Samuel, Rev. Chim. Miner. **8**, 805 (1971).
2. I. I. Buchinskaya, Candidate's Dissertation in Chemistry (Moscow Inst. of Fine Chemical Technology, Moscow, 1996).
3. I. I. Buchinskaya, P. P. Fedorov, and B. P. Sobolev, Proc. SPIE **3178**, 59 (1996).
4. P. P. Fedorov, Doctoral Dissertation in Chemistry (Moscow Inst. of Fine Chemical Technology, Moscow, 1991).
5. P. P. Fedorov, T. M. Turkina, and B. P. Sobolev, Butll. Soc. Catalana Cien. Fis. Quim. Mat. **13** (1), 259 (1992).
6. P. P. Fedorov, Neorg. Mater. **37** (1), 95 (2001).
7. S. P. Ivanov, I. I. Buchinskaya, and P. P. Fedorov, Neorg. Mater. **36** (4), 484 (2000).
8. D. S. Stokbarger, Discuss. Faraday Soc. **394** (5), 299 (1946).
9. E. A. Krivandina, Butll. Soc. Catalana Cien. Fiz. Quim. Mat. **12** (2), 275 (1991).
10. P. P. Fedorov, M. A. Sattarova, Z. I. Zhmurova, *et al.*, Kristallografiya **31** (1), 194 (1986) [Sov. Phys. Crystallogr. **31**, 115 (1986)].
11. P. P. Fedorov, I. I. Buchinskaya, V. A. Stasyuk, and O. S. Bondareva, Zh. Neorg. Khim. **41** (3), 464 (1996).

Translated by L. Man

Crystallography Reports, Vol. 49, No. 2, 2004, pp. 282–287. Translated from Kristallografiya, Vol. 49, No. 2, 2004, pp. 337–342.

CRYSTAL GROWTH

Synthesis, Growth Conditions, and Crystal Structures of Alkali Metal Hypophosphites MH_2PO_2[1]

M. I. Naumova, N. V. Kuratieva, D. Yu. Naumov, and N. V. Podberezskaya

Institute of Inorganic Chemistry, Siberian Division, Russian Academy of Sciences, pr. Akademika Lavrent'eva 3, Novosibirsk, 630090 Russia

e-mail: m.i.naumova@ngs.ru

Received March 3, 2003

Abstract—Metal hypophosphites are widely used in various fields. However, their structures have not been adequately studied. The synthesis conditions (the temperature and precursors) were found and crystals of anhydrous Li, K, Rb, Cs, and NH_4 hypophosphites were grown. The structures of these compounds were established by X-ray diffraction analysis. These crystal structures can be described as packings of layers consisting of hypophosphite anions coordinated to metal cations. In all these salts, the hypophosphite anions serve as bridges between four cations belonging to the same layer. Each oxygen atom is bound to two cations. © *2004 MAIK "Nauka/Interperiodica".*

INTRODUCTION

Metal hypophosphites are widely used. However, data on their crystal structures, which could elucidate and provide deeper insight into the mechanisms of decomposition of these compounds, are scarce. We chose to investigate alkali metal hypophosphites. Although salts of hypophosphorous acid can be readily synthesized, it is rather difficult to prepare samples suitable for X-ray diffraction analysis.

In laboratory conditions, metal hypophosphites are generally prepared from sulfates [1], hydroxides and oxides [2], or nitrates of the corresponding metals by their reactions with aqueous solutions of hypophosphorous acid or its sodium or barium salts.

There are few studies on the crystal structures of anhydrous metal and ammonium hypophosphites [3–10]. Presumably, the reason is that it is difficult to pre-

[1] This work was presented at the National Conference on Crystal Growth (NCCG-2002, Moscow).

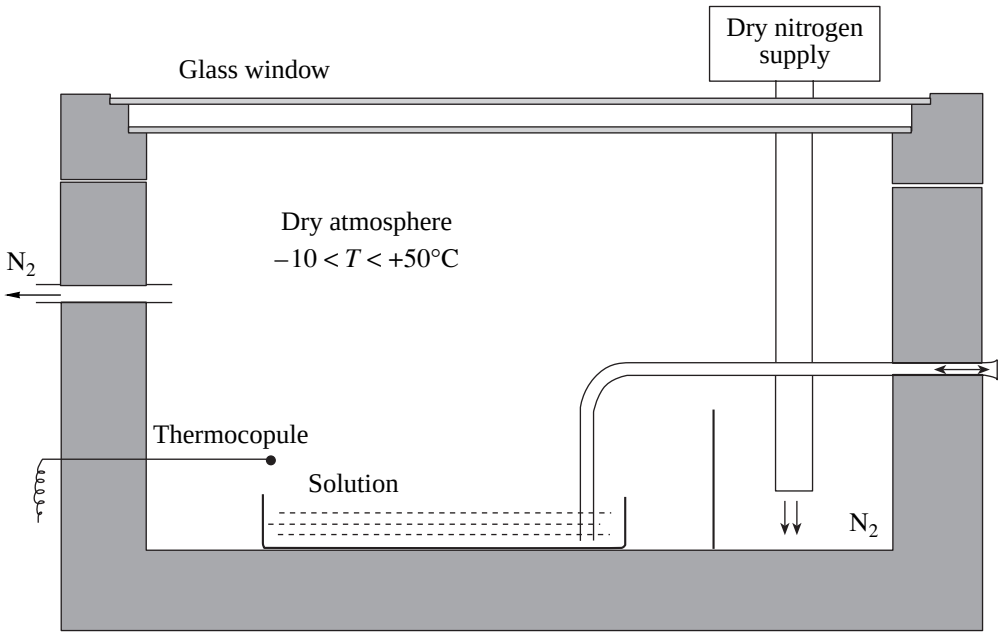

Fig. 1. Schematic diagram of an apparatus for crystal growth under special conditions.

1063-7745/04/4902-0282$26.00 © 2004 MAIK "Nauka/Interperiodica"

pare these compounds due to their high hygroscopicity and tendency to decompose.

EXPERIMENTAL

In this study, crystals of anhydrous potassium, rubidium, and cesium hypophosphites were grown from corresponding aqueous solutions that were prepared by reactions of equimolar amounts of hypophosphorous acid with alkali metal carbonates. At 25°C and a relative humidity of 80%, potassium, rubidium, and cesium hypophosphites represent saturated aqueous solutions because of their high hygroscopicity. Under such conditions, crystals cannot be grown. We succeeded in growing crystals of anhydrous potassium, rubidium, and cesium hypophosphites at 40°C using a specially designed apparatus filled with dry nitrogen as a drying agent (Fig. 1). Temperature was maintained using an Oxford CryoSystem cooler by feeding dry gaseous nitrogen at a given temperature. The thermal-insulating walls of the container and a double-glass window in its cover allow one not only to maintain the required temperature in the container but also to visually monitor the crystal-growth process. The use of this construction and an Oxford CryoSystem cooler make it possible to either maintain the preset temperature with high precision (0.5 K) in the range from –40 to +50°C or vary the temperature according to a specified algorithm. The use of dry nitrogen (inert atmosphere) for cooling accelerates the evaporation of the solvent (water). This system can also be used for growing crystals at low temperatures.

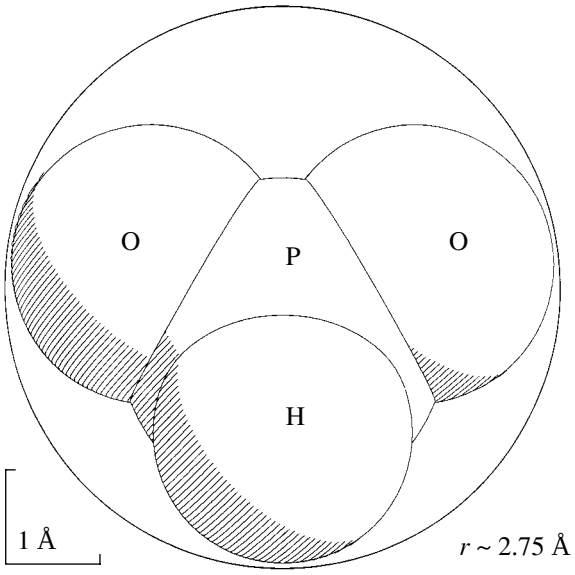

Fig. 2. Shape and size of the hypophosphite anion $H_2PO_2^-$.

Crystals of anhydrous lithium hypophosphite were grown at 20°C from an aqueous solution of lithium hypophosphite, which was prepared from lithium oxalate and calcium hypophosphite. Recrystallization

Crystallographic data for anhydrous alkali metal and ammonium hypophosphites

Formula	$NH_4H_2PO_2$	LiH_2PO_2	KH_2PO_2	RbH_2PO_2	CsH_2PO_2
Space group	*Cmma*	*C*2/*m*	*C*2/*c*	*Pnma*	*Pnma*
a, Å	7.5425(3)	9.3557(11)	7.3131(10)	7.9835(9)	8.3776(9)
b, Å	11.5204(5)	5.3107(7)	7.2952(8)	6.3678(7)	6.6271(6)
c, Å	3.9942(2)	6.5432(12)	7.1814(10)	7.5755(11)	7.9165(10)
β		108.259(11)	116.205(10)		
Volume, Å^3, *Z*	347.07(3), 4	308.73(8), 4	343.75(8), 4	385.12(8), 4	439.52(8), 4
ρ_{calcd}, g/cm^3	1.589	1.547	2.011	2.595	2.991
Coordination number (*M*)	**4 + 4**	**4**	**4 + 2 + 2**	**4 + 2 + 2**	**4 + 2 + 2**
Polyhedron	Tetrahedron (distorted cube)	Tetrahedron	Octahedron with split oxygen and hydrogen vertices		
M–O, Å	N–O_1 2.8460(10) × 4	1.933(4) × 2	2.7368(13) × 2	2.859(3) × 2	3.026(5) × 2
	N–O_2 3.5591(11) × 4	1.936(4) × 2	2.7747(14) × 2	2.932(3) × 2	3.094(5) × 2
			2.9220(15) × 2	3.063(3) × 2	3.221(7) × 2
M–H, Å			3.74(3)	4.06(4)	4.12(7)
P–O, Å	1.5010(12) × 2	1.478(2)	1.4914(12) × 2	1.478(3) × 2	1.487(6) × 2
		1.484(2)			
P–H, Å	1.33(2)	1.35(4)	1.28(3)	1.18(7)	1.37(11)

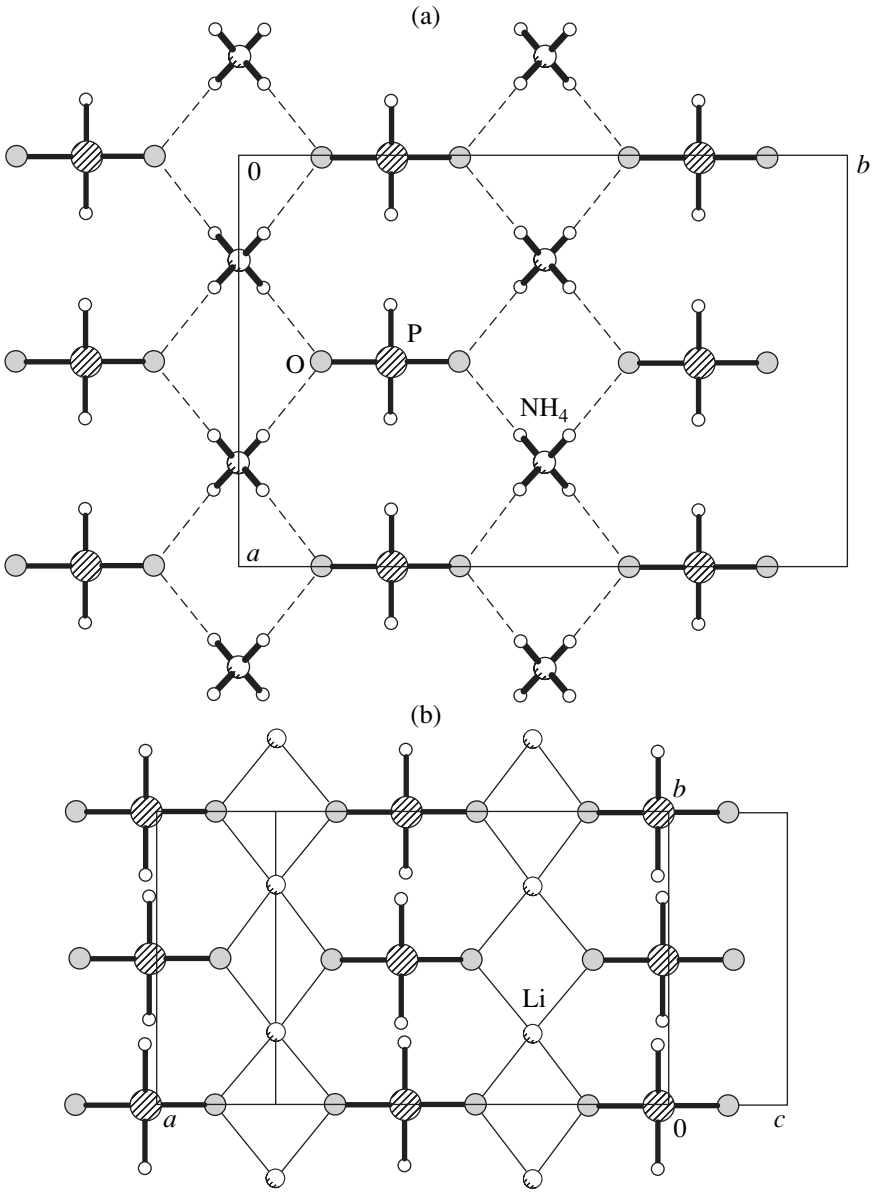

Fig. 3. Projections of the structures of (a) $NH_4(H_2PO_2)$ onto the (001) plane and (b) LiH_2PO_2 onto the (010) plane.

was carried out three times, the temperature being decreased to 10°C. Attempts to grow crystals of anhydrous sodium hypophosphite under similar conditions failed; instead, crystals of sodium hypophosphite hydrate with a known structure [11] were formed. Ammonium hypophosphite crystals were grown by recrystallization of the reagent from an aqueous solution.

The X-ray diffraction data for crystals of anhydrous Li, K, Rb, Cs, and NH_4 hypophosphites were collected on an automated Enraf-Nonius CAD-4 diffractometer using the standard method (MoK_α radiation, graphite monochromator, variable scan rate of from 1 to 16 deg/min, θ-scan range from 1° to 25°). Radiation damage in the crystals was monitored by measuring the intensities of check reflections every hour.

RESULTS AND DISCUSSION

We found the growth conditions for crystals of anhydrous Li, K, Rb, and Cs hypophosphites. It appears that a precursor used for the synthesis of aqueous solutions of hypophosphites of the corresponding metals influences the crystal growth of alkali metal hypophosphites, because the former may be present in solutions at concentrations lower than 3–5%. Such amounts of impurities in crystals are too small to be detected by X-ray diffraction methods.

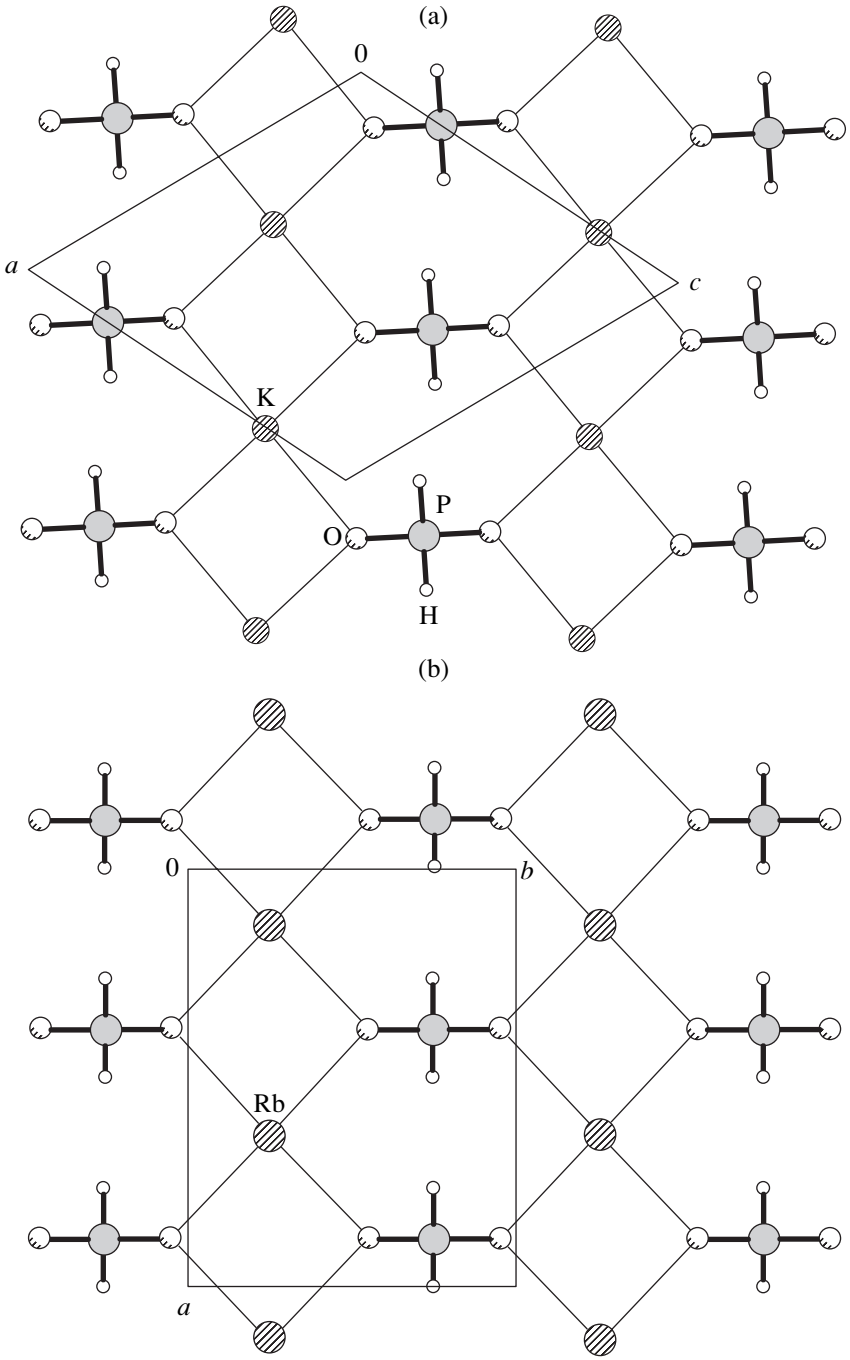

Fig. 4. Projections of the structures of (a) KH_2PO_2 onto the (010) plane and (b) RbH_2PO_2 onto the (001) plane.

Crystals of anhydrous Li, K, Rb, and Cs hypophosphites were prepared as well-faceted transparent plates with a maximum dimension of 3 mm and a thickness up to 0.5 mm. Due to rapid absorption of atmospheric moisture, the crystals swelled and then dissolved. We succeeded in conserving the crystals using a polymer coating (epoxide resin). The hygroscopicity of the crystals increases in the series of Li, K, Rb, and Cs.

The hypophosphite anion is a tetrahedron with a phosphorus atom at its center. The vertices of the tetrahedron are occupied by two oxygen atoms and two hydrogen atoms. The typical shape and size of the hypophosphite anion are shown in Fig. 2. The hypophosphite anion can be represented as a sphere with an effective radius of 2.75 Å. This anion may be linked with a metal cation by oxygen atoms in different ways (mono- or bidentately) and may serve as a bridge between two cations.

We carried out structural and crystal–chemical analysis of the compounds synthesized. The crystallo-

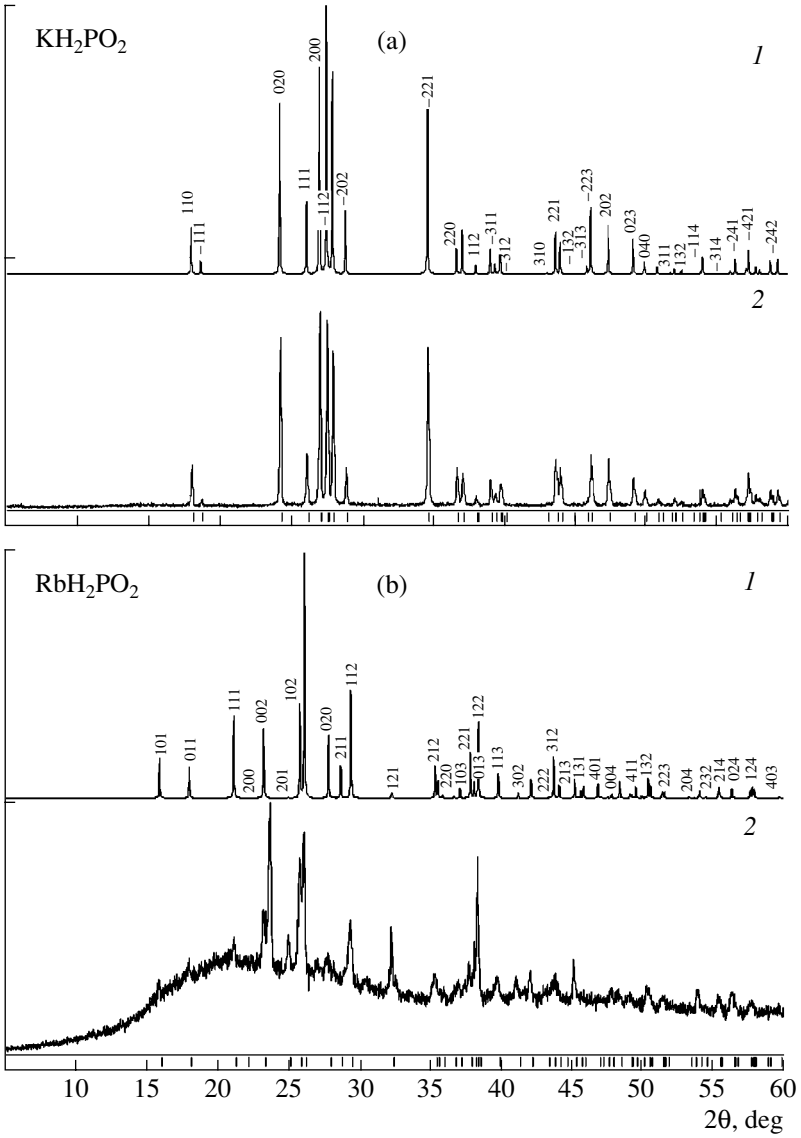

Fig. 5. (*1*) Calculated and (*2*) experimental X-ray diffraction patterns of (a) KH_2PO_2 and (b) RbH_2PO_2.

graphic data for anhydrous alkali metal and ammonium hypophosphites are given in the table. The crystal–chemical analysis demonstrated that these compounds can all be represented as packings of layers consisting of hypophosphite anions linked with metal cations. All the compounds under consideration are characterized by an identical packing motif of cations and phosphorus atoms. Let us consider the layer structure using the example of ammonium hypophosphite (Fig. 3a). A hypophosphite anion is bound to four ammonium cations, and each ammonium cation is bound to four hypophosphite anions. An analogous structure (with respect to metal and phosphorus atoms) is observed for the NaCl structure in the (100) layer. The structures consist of two alternating layers, the second being shifted with respect to the first in such a way that the hypophosphite ion of the second layer is located directly above the metal cation of the first layer.

The arrangement of the hypophosphite anions in the ammonium compound provides a tetrahedral oxygen environment for the ammonium cation. This arrangement is due to alternated orientations of hypophosphite anions (oxygen atoms are directed alternatively upwards and downwards with respect to the layer).

A similar layer structure is observed in lithium hypophosphite (Fig. 3b), differing from that of ammonium hypophosphite only in the distance between the oxygen atom of the hypophosphite anion and the lithium cations, because the ionic radius of lithium is 0.8 Å smaller than the radius of the ammonium cation.

A similar packing of phosphorus and potassium atoms is observed in potassium hypophosphite

(Fig. 4a). The tetrahedral environment in this salt is distorted due to corrugation of the cation sublayer and flattening of the hypophosphite sublayer in such a way that the local environment of the cation becomes almost square. The cation environment also involves two oxygen atoms belonging to the upper hypophosphite layer and two hydrogen atoms of the lower hypophosphite layer that form a polyhedron, which can be understood as an octahedron with two split vertices. The layer packing is similar to that in the structures of ammonium and lithium hypophosphites.

Rubidium and cesium hypophosphites are isostructural (Fig. 4b). The structure of the layers is similar to that in potassium hypophosphite. The difference is that hypophosphite anions are oriented along the [010] direction in rubidium salt and along the $[\bar{1}01]$ direction in potassium salt. The difference in the orientation of hypophosphite anions leads to a change in symmetry from monoclinic (in the structure of potassium hypophosphite) to orthorhombic (in the structures of rubidium and cesium hypophosphites).

The presence of additional peaks in the X-ray diffraction pattern of rubidium hypophosphite indicates the presence of an additional phase similar to that of potassium hypophosphite (Fig. 5).

CONCLUSION

We synthesized anhydrous lithium, potassium, rubidium, cesium, and ammonium hypophosphites and found conditions for growing crystals of anhydrous alkali metal hypophosphites (except for sodium hypophosphite) suitable for X-ray diffraction analysis. The crystal structures of these salts were established. For potassium and rubidium hypophosphites, the powder and single-crystal X-ray diffraction data were compared. The single-phase state of potassium hypophosphite and the two-phase state of rubidium hypophosphite were confirmed.

REFERENCES

1. N. V. Romanova and N. V. Demidenko, Usp. Khim. **44** (12), 2150 (1975).
2. G. Brun, A. Norbert, and M. Caucanas-Dumail, Rev. Chim. Miner. **9**, 581 (1972).
3. W. H. Zachariasen and R. C. L. Mooney, J. Chem. Phys. **2** (1), 34 (1934).
4. T. J. R. Weakley, Acta Crystallogr., Sect. B: Struct. Crystallogr. Cryst. Chem. **35** (1), 42 (1979).
5. P. A. Tanner, L. Yu-Long, and T. C. W. Mak, Polyhedron **16** (3), 495 (1997).
6. L. A. Aslanov, V. M. Ionov, M. A. Poraĭ-Koshits, *et al.*, Neorg. Mater. **11** (1), 117 (1975).
7. T. Matsuzaki and Y. Iitaka, Acta Crystallogr., Sect. B: Struct. Crystallogr. Cryst. Chem. **25** (10), 1932 (1969).
8. T. J. R. Weakley and W. W. L. Watt, Acta Crystallogr., Sect. B: Struct. Crystallogr. Cryst. Chem. **35** (12), 3023 (1979).
9. P. A. Tanner, T.-H. Sze, T. C. Mak, *et al.*, J. Cryst. Spectr. Res. **22** (1), 25 (1992).
10. P. A. Tanner, M. D. Faucher, and T. C. W. Mak, Inorg. Chem. **38** (26), 6008 (1999).
11. M. Catti, Acta Crystallogr., Sect. B: Struct. Crystallogr. Cryst. Chem. **35** (5), 1041 (1979).

Translated by T. Safonova

Crystallography Reports, Vol. 49, No. 2, 2004, pp. 288–293. Translated from Kristallografiya, Vol. 49, No. 2, 2004, pp. 343–349.

CRYSTAL GROWTH

Conditions for Single-Crystal Formation during Bridgman Growth[1]

V. I. Shtanov

Moscow State University, Vorob'evy gory, Moscow, 119992 Russia

e-mail: shtanov@inorg.chem.msu.ru

Received March 4, 2003

Abstract—The microstructure of IV–VI crystals grown by varying the shape of the conical bottom of a ampoule, the melt superheating ΔT^+ with respect to the liquidus temperature of a blend, the axial temperature gradient in a furnace ΔT, and the pulling rate of a ampoule v were studied. It was found that the nucleation of a single-crystal seed is most likely under the following conditions: $\Delta T \le 20$ K/cm, $\Delta T^+ < 30$ K, and $v < 0.4$ mm/h. The conical bottom of a ampoule should have walls of constant thickness. The principle of geometric selection of a single-crystal seed is not efficient. The obtained results are discussed with regard to data on the structure and behavior of IV–VI melts upon heating and cooling. *© 2004 MAIK "Nauka/Interperiodica".*

INTRODUCTION

For many practical purposes, semiconductor materials should be obtained in the form of single crystals of high structural quality. In scientific research (and, in some cases, commercial production), growing multicomponent crystals by the Bridgman method has a number of advantages. These are simplicity of experiment; conservation of calculated ratios of components due to the use of a closed system; reproducibility of composition at the synthesis of multicomponent crystals and solid solutions; and the possibility of obtaining large single crystals (of up to tens of cubic centimeters in volume) with good microstructural characteristics, which makes studying their physical properties easier. It should be noted that the realization of this possibility strongly depends on the formation of a high-quality single-crystal seed in the initial stage of growth, if the crystallization is carried out without a seed.

In contrast to the gas phase deposition, crystallization from melt is characterized by a long duration and the complexity of relaxation processes in the feeding medium. Since the structure of the liquid phase and its variations upon transition to the metastable (supercooled) state have not been studied in detail, experimental investigation of the influence of the precrystallization parameters of a melt on the microstructure and properties of the crystal grown from it is topical, especially for complex materials with compositions and structures that are substantially different in the solid and liquid states.

[1] This work was presented at the National Conference on Crystal Growth (NCCG-2002, Moscow).

Heterogeneous nucleation is affected by the nature of a crystallizing material, the state of ampoule walls, the preliminary treatment of a blend, the presence of liquid or solid inclusions in a melt and its thermal treatment, and the process parameters. The purpose of this study was to determine the conditions for the formation of single-crystal seeds by processing the available experimental data on crystals of binary compounds PbTe, PbSe, and SnTe and $Pb_{1-x}Sn_xTe$, $Pb_{1-x}Sn_xSe$, and $Pb_{1-x}S_xSe$ alloys grown by the Bridgman method from a stoichiometric blend or from flux. The shape of the ampoule bottom, the superheating of a melt with respect to the liquidus temperature ΔT^+, the axial temperature gradient in a furnace ΔT, and the pulling rate of a ampoule v were considered as variables.

The phase diagrams of binary compounds contain points of congruent melting, but the equality of compositions of the solid phase and the melt at this point can be considered only as arbitrary. Each binary compound dissociates upon transition from the solid state to melt even at the melting temperature. The degree of dissociation increases in the series PbS $\longrightarrow$ PbSe $\longrightarrow$ SnTe $\longrightarrow$ PbTe $\longrightarrow$ GeTe and with increasing temperature [1–5]. As a result, the equality of the compositions of the melt and solid phase at the point of congruent melting holds true for binary compounds only at the macroscopic level; at the microscopic level, it is violated due to fluctuations of the component concentrations under the action of different factors. The phase diagrams of ternary solid solutions generally contain no points of congruent melting. Hence, at the moment of solid phase nucleation in the microvolume of a melt, the composition of the solid phase always differs from that of the melt where the nucleation occurs. Therefore, the composition of the initial blend was excluded from the set of variables.

1063-7745/04/4902-0288$26.00 © 2004 MAIK "Nauka/Interperiodica"

EXPERIMENTAL METHODS

It is well known [6–8] that the presence of low-dispersion heterogeneous impurities in a melt reduces the activation energy of nucleation. The most conventional impurity that can be readily introduced into an initial blend are oxides of the blend components. Their amount and location in the melt at the moment of nucleation cannot be controlled. Therefore, the technique for preparing a blend should provide complete purification of it from metal oxides and remain invariable from process to process.

A ampoule made of S5-1 quartz with an inner diameter of 13–30 mm was first washed in a mixture of concentrated nitric and hydrofluoric acids (1 : 1) (this being the preferred regime) or in aqua regia at a temperature of 290–370 K for 0.3–0.5 h and then rinsed multiply in distilled water. Ampoules were degassed in the flame of an air or oxygen burner with continuous pumping.

Metals and chalcogens with a main-component content of no less than 99.998 wt % were used as initial components. Oxide phases were removed from the surfaces of metal ingots either mechanically with a knife or scalpel (Pb, Sn, In) or by etching (Pb, Sn, Ge). Lead and tin were additionally purified from the oxygen by heating in vacuum in a quartz funnel with continuous pumping and subsequent pouring of a molten metal into the growth ampoule through a capillary. In this stage, the last traces of metal oxides adhere to the funnel walls (forming silicates) and the purified metal is fed into the growth ampoule. The blend components were weighted to within an accuracy of ±0.005 g, and the total weight of the blend ranged from 50 to 150 g, depending on the ampoule size. Such a technique of blend preparation turned out to be more efficient than that described in [9] with respect to the degree of purification of metals from oxides.

After preliminary heating at 600–900 K, a sealed-off ampoule was placed (with the conical part facing downward) into the lower (low-temperature) part of the heated furnace, where the temperature was 50–100 K below the liquidus temperature of the blend T_{liq} and, then, raised at an average rate of 5 mm/h to the initial position for crystallization with periodic stirring of the melt. The ampoule was kept for 0.5–2 h in the initial position with periodic stirring of the melt (Fig. 1), after which the pulling mechanism was switched on. One should take into account that, the lower the ratio of the inner diameter of the furnace to the external diameter of the ampoule and the larger the value of ΔT, the larger the deviation of the real initial temperature of the melt T_{min} (Fig. 1) from the temperature at a given point in the furnace, determined by a thermocouple in the absence of a ampoule. The temperature in the furnace was maintained at a given value accurate to within ±0.5 K using VRT-2 and PIT-3 temperature controllers. The ranges of the variable parameters are listed in Table 1. When crystallization was over, either the ampoule with the grown crystal was taken out of the furnace and the uncrystallized melt was poured off from the crystal to monitor the shape of the crystallization front or the ampoule with the grown crystal was cooled together with the furnace at a rate of 3–10 K/h to relieve thermal stresses in the grown crystal. The cooled crystal could be freely moved in the ampoule, which indicated the absence of oxides on the crystal surface.

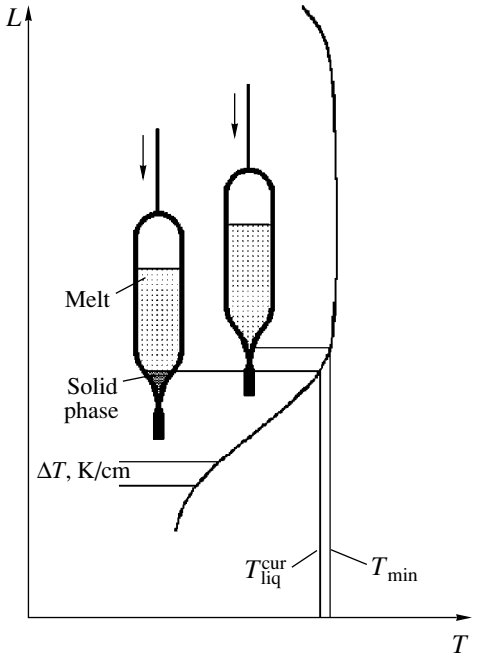

Fig. 1. Schematic diagram of crystal growth.

This technique makes it possible to obtain crystals with an impurity content determined by the purity of the initial components (see [10] and Table 2). The fact of the formation of single-crystal seeds and the appearance of secondary crystallization centers were established from the character of distribution of block-to-block interfaces over the crystal length using wafers cut perpendicular to the growth axis (the ampoule axis) or parallel to the (100) plane by the methods described in [11, 12]. Single-block crystals were used to study the physical properties and nature of point defects in these materials [13–16].

EFFECT OF THE CONSTRUCTION OF A GROWTH AMPOULE ON THE FORMATION OF SINGLE-CRYSTAL SEEDS

When crystals are grown without seeds, the construction of the growth container must provide supercooling of a small volume of the melt at the start of crystallization, which increases the probability that a single-crystal seed will be formed. In this case, the supercooling ΔT^- is the difference between the liquidus temperature of the blend T_{liq} and the actual temperature of the melt, which is below T_{liq}. The supercooling is

Table 1. Ranges of variable parameters in Bridgman growth of IV–VI crystals

Variable parameter	Range
Inner ampoule diameter	13–30 mm
Axial temperature gradient in a furnace ΔT	10–65 K/cm
Outer ampoule diameter/inner furnace diameter	0.9–0.5
Pulling rate of a ampoule (melt cooling rate)	0.19–2.0 mm/h (0.19–10 K/h)
Melt superheating ΔT^+	(1–2)–(50–60) K

Table 2. Contents of impurities (in at %) in different $Pb_{1-x}Sn_xTe$ crystals grown by the Bridgman method

Element	Neutron activation analysis		Spark mass spectrometry	
	detection limit	result	detection limit	result
Na	1×10^{-8}	2×10^{-4}	1×10^{-7}	4×10^{-5}
K	1×10^{-6}	$<1 \times 10^{-6}$		
Rb	1×10^{-6}	$<1 \times 10^{-6}$		
Cs	1×10^{-7}	$<1 \times 10^{-7}$		
Cu	2×10^{-8}	1×10^{-5}		
Zn	5×10^{-7}	2×10^{-4}	5×10^{-8}	4×10^{-4}
Cd	1×10^{-7}	3×10^{-5}		
Sc			5×10^{-8}	4×10^{-6}
La	1×10^{-8}	$<1 \times 10^{-8}$		
Ge			5×10^{-8}	4×10^{-6}
As	1×10^{-8}	3×10^{-6}		
Se			5×10^{-8}	4×10^{-2}
Cr			5×10^{-8}	2×10^{-4}
Mn	1×10^{-8}	2×10^{-4}	5×10^{-8}	3×10^{-4}
Cl			1×10^{-7}	2×10^{-4}
Br			5×10^{-8}	7×10^{-6}
Fe			1×10^{-7}	8×10^{-4}
Ni	1×10^{-6}	$<1 \times 10^{-6}$		

obtained by moving the ampoule in a furnace with a nonisothermal temperature profile and controlling the heat exchange between the ampoule and the surrounding medium via the radiative emission of the constructive elements of the ampoule. The simplest and most appropriate means for providing supercooling through radiative emission is the construction of a ampoule (crucible) with a bottom having a near-conical shape and a transferable heat-removing rod made of the same material for local additional cooling of the cone vertex. Convective gas fluxes in the furnace volume must be completely excluded in this case, since they lead to uncontrolled oscillations of temperature with time in different parts of the ampoule. It is believed that a geometric selection of single-crystal seeds from a polycrystalline nucleus is possible [17].

In this study, the constructions of ampoules based on the principle of geometric selection of the single-crystal part of a seed crystal [18] were of two types. In the first variant, a cylindrical extension 20–40 mm long and 5–8 mm in diameter with a conical vertex was attached to the conical part of a ampoule with an inner diameter of 18–25 mm (Fig. 2a). In the second variant, the conical part of the ampoule had a cylindrical narrowing 3–10 mm long, with the inner diameter varying from 3 to 7 mm (Figs. 2b, 2c). A heat-removing rod was occasionally welded to the vertex of the conical part of the ampoule (Figs. 2c, 2f, 2h). It was believed that, during the crystal growth in the extension (narrowing), the blocks of the nucleated block (polycrystalline) solid phase would be wedged out from the extension and a single-crystal seed would emerge into the main part of the ampoule. Study of crystallization in such ampoules allowed us to conclude the following:

(i) The ampoule volume designed for the formation of a seed crystal is not always completely filled with melt; notably, the longer the narrowing part and the smaller its diameter, the more difficult it is to fill it, even by removing the ampoule with a melt from the furnace for a short time and turning it over. The void in the extension inhibits the geometric selection and further growing of a seed into the main part of the ampoule (Fig. 3a).

(ii) The concentration and size of microinclusions increase abruptly in the narrowing due to the trapping of the mother melt by the grown crystal; i.e., the narrowing hinders the diffusion of the uncrystallized components from the zone of the crystallization front into the melt volume (Fig. 3b). When a metal flux is used as the initial blend, this trend is significantly enhanced due to the segregation of the flux components.

(iii) When the vertex angle of the main cone of the ampoule (Fig. 2, *1*) exceeds 80°–90°, new crystallization centers are often formed in both the transition region between the extension (narrowing) and the main cone and the region between the main cone and the cylindrical part of the ampoule (Fig. 3c). With an increase in the axial temperature gradient in the furnace ΔT, this trend becomes enhanced. The reason for this is a step deflection in the isotherm to lower temperatures at the air–ampoule-wall–melt boundaries, due to which zones of supercooled melt spatially separated from the crystallization front are formed in the ampoule (Fig. 3c).

We thus failed to geometrically select a single-crystal part from the block seed crystal. Therefore, we focused our efforts on improving the construction of a ampoule that would provide supercooling of a minimum melt volume at the vertex of the ampoule cone and prevent the formation of crystallization centers in other parts of the melt during the entire crystal-growth process.

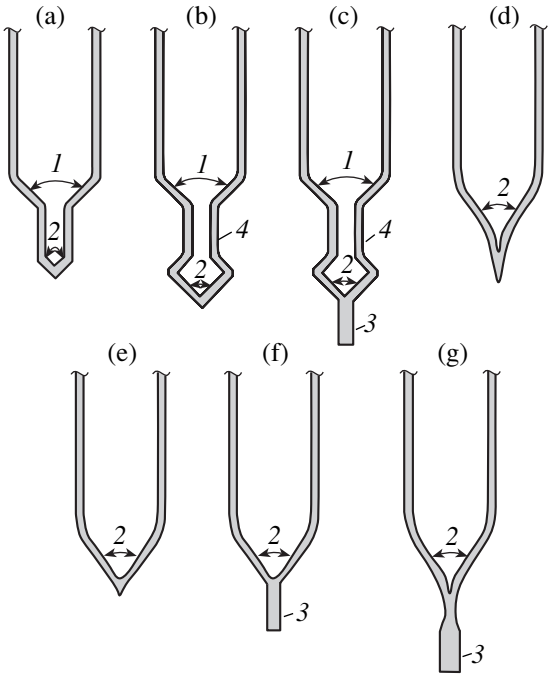

Fig. 2. Types of ampoules with different bottom constructions: (*1*) cone angle of the ampoule bottom, (*2*) angle at the cone vertex, (*3*) heat-removing rod, and (*4*) narrowing.

The use of conical-bottom ampoules with a constant ($1 \sim 2 = 60°$–$100°$ in Figs. 2e, 2f) or variable ($1 \neq 2$ in Fig. 2d) cone angle was far from always successful. A heat-removing rod 15–50 mm long and 4–8 mm in diameter did not improve the situation either (Fig. 2f). By the beginning of crystallization, such a large volume of melt was supercooled that seed crystals composed of several blocks were formed in it.

The construction of the ampoule bottom shown in Fig. 2h was found to be optimal. The cylindrical part of the ampoule gradually becomes conical, with a cone angle of 80°–60°. Within the last 7–8 mm, the cone angle decreases to 10°–20°. There is a waist 2–3 mm in diameter between the ampoule and the heat-removing rod, which is 30–40 long and 4–6 mm in diameter. The important factor in achieving success is the thickness of the ampoule walls, which should be constant in all the parts of the ampoule and rather small (no more than 2.5 mm).

EFFECT OF THE FURNACE TEMPERATURE PROFILE, MELT SUPERHEATING, AND THE AMPOULE PULLING RATE ON THE FORMATION OF SINGLE-CRYSTAL SEEDS

Two stages are generally distinguished in the formation of crystallization centers in melts: the induction period, during which the metastable supercooled state exists until the first crystallization center arises, and the period of dynamic nucleation occurring at a high rate in the presence of the solid phase formed [8]. A single-crystal seed will be formed if only one solid-phase nucleus is formed in the supercooled melt, while the formation of other nuclei in this volume is suppressed in one way or another. The probability of forming only one nucleus for the growth of a single-crystal seed increases with both a decrease in the volume of the supercooled melt (the number of nuclei being proportional to the total number of atoms in the volume where the nucleation occurs and with no melt for the stage of dynamic nucleation) and a reduction of supercooling. The first factor depends on the ampoule construction and the value of ΔT, while the second depends on the temperature prehistory of the melt. The expectation time for the appearance of the first crystallization center should be 10^3–10^4 s; in this case, the melt volume will not increase significantly due to the ampoule motion in the furnace during the interval from the beginning of supercooling to the appearance of the first nucleus.

Processing of the results of experiments aimed at determining the effect of the minimum melt temperature at the beginning of pulling T_{min}, the axial tempera-

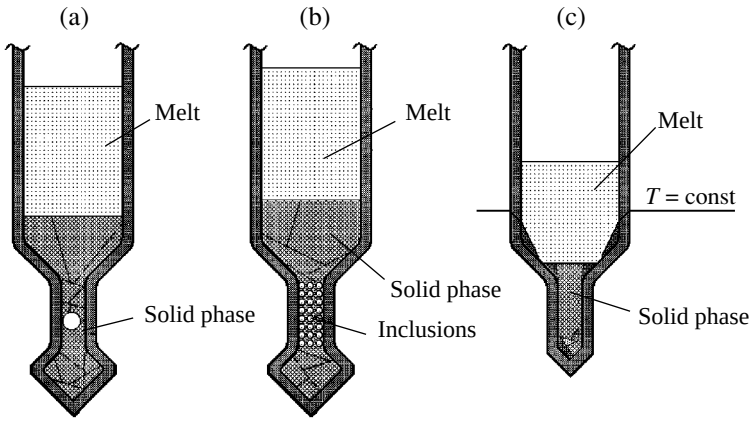

Fig. 3. Schematic diagrams of the formation of (a) voids, (b) microinclusions of the mother melt, and (c) secondary crystallization centers for ampoules based on the principle of geometric selection of a single-crystal seed.

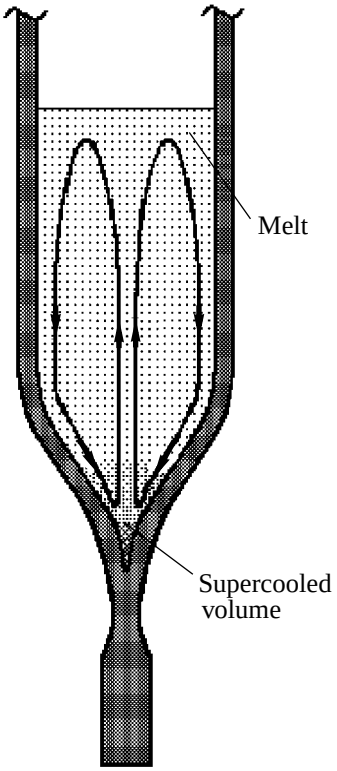

Fig. 4. Schematic of convective fluxes in a melt at the Bridgman growth.

ture gradient ΔT, and the pulling rate v on the probability of single-crystal seeds in the ampoules shown in Fig. 2h being formed yields the following results:

(i) If a ampoule is loaded into a furnace with ΔT = 10–40 K/cm and the value of T_{min} corresponding to the temperature profile of the furnace without a ampoule exceeds T_{liq} by 30 K or more, single-crystal seeds are not formed even at v = 0.19 mm/h.

(ii) If furnaces with ΔT > 40 K/cm are used, single-crystal seeds cannot be obtained even at $(T_{min} - T_{liq}) < 5$ K. In this case, it is likely that the convection in the melt (Fig. 4) will become so intense that the small volume of the supercooled melt necessary for the formation of a single-crystal seed will not be obtainable at the cone vertex without additional forced heat removal.

(iii) When the requirements for the optimal value of T_{min} and optimal ampoule construction for furnaces with ΔT = 12–20 K/cm are satisfied, the formation of single-crystal seeds at $v < 0.4$ mm/h occurs with a probability of 40–50%. At v = 0.9–1.1 mm/h, the probability is about 10%, and, at v > 1.6 mm/h, it is close to zero. For stoichiometric binary melts and concentrated fluxes, the probability of forming single-crystal seeds, all other factors being equal, always exceeds that in the case of fluxes with the solvent fraction initially exceeding 15 wt % of the initial blend, although it was believed in [2] that a solvent affects the melt structure up to concentrations about 30–35 wt % only insignificantly.

The regularities found in the formation of single-crystal seeds were verified and confirmed upon growing of GeTe, PbS, $Pb_{1-x}Se_xTe$, $Pb_{1-x}Ge_xTe$, $Pb_{1-x}Ga_xTe$, $Pb_{1-x}Ga_xSe$, $Pb_{1-x}In_xTe$, $Pb_{1-x-y}Sn_xGa_yTe$, $Pb_{1-x-y}Sn_xIn_yTe$, and $Pb_{1-x-y}Sn_xGe_yTe$ crystals. The behavior of melts of the quaternary alloys upon their crystallization is similar to that of melts of the ternary alloys.

The expectation time for the appearance of the first crystallization center at a given value of supercooling depends on the readiness of the melt to be crystallized. The readiness to be crystallized means the possibility of forming a solid particle, the size of which is equal to or exceeds the critical nucleus size and the composition of which corresponds to the equilibrium between the solid phase and the melt for a given temperature, at the interface between the melt and the ampoule wall. Several processes occurring simultaneously both in the melt and at the internal wall of the quartz ampoule are responsible for this readiness.

In the melt of a IV–VI compound, covalent bonds between atoms are retained, and a chain-like one-dimensional structure $-A-B-A-B-$ is formed with charge carriers at the chain ends. The structure of the melt is inhomogeneous at the microscopic level: it contains crystal-like groups of atoms, in which the packing of chains is similar to the solid-phase packing, and groups of statistically distributed atoms of different types [5]. The packing of structural units (chains) may be such that the short-range order structure will be close to the solid-phase structure in a wide temperature range or near the melting temperature only. In the latter case, heating should lead to the reconstruction of the short-range order structure with the formation of a configuration (statistical distribution of atoms) that varies with increasing temperature only insignificantly. The increase in the conductivity of all the IV–VI melts with increasing temperature indicates that the concentration of charge carriers increases, i.e., that bonds in structural units and molecules break. X-ray scattering curves for the surfaces of melts of binary systems [19–21] show that heating a melt by 50 K above T_{liq} leads to a strong broadening of the maxima in the radial distributions of atoms. This circumstance is indicative of the instability of a compound in the liquid phase. Hence, the structure of a IV–VI melt is very sensitive to its temperature. One should also take into account the fact that, at a temperature of (1.01–1.1) T_{liq}, the adsorption layer with the solid-phase structure that is located on the ampoule walls decays [8].

Obviously, if during the blend melting the temperature reaches the value at which crystal-like fragments of the melt structure decay, considerable time is required to reproduce this structure upon cooling. The variation in ΔT^- with varying ΔT^+ for a stoichiometric melt carefully purified from heterogeneous inclusions was

described in [22] for PbTe and SnTe. When the melt is superheated by 1–12 K above the melting temperature and then cooled at a rate of 2 K/min, mass crystallization occurs at $\Delta T^- \le 1$ K. Melts that are superheated by 13 K or more begin to crystallize under the same conditions at temperatures 40 K below T_{liq}. Melts that are supercooled by 1–2 K can remain in the metastable state for hundreds of hours. It is clear that, for fluxes and ternary or quaternary melts, the value of ΔT^+ is similar to that for binary melts, but the former are more prone to existing in the metastable state.

If a melt was superheated in the initial state and the crystal-like fragments in it were destroyed or if a ampoule moves at a high velocity, the time of melt cooling to the liquidus temperature turns out to be significantly smaller than the time required for the formation of crystal-like clusters in the melt and reconstruction of the solid-phase structure in the adsorbed layer on the inner surface of the ampoule. By the time that the melt structure relaxes and the supercooled melt can already form a solid-phase nucleus with a composition corresponding to the equilibrium at the temperature in the conical part of the ampoule, a large volume of the melt turns out to be supercooled, and a few nuclei form in it simultaneously. In this case, the composition of nuclei differs from the solid phase composition for the liquidus temperature of the initial blend [18].

CONCLUSIONS

On the basis of statistical analysis of the Bridgman growth of crystals of binary IV–VI compounds and alloys based on them, the optimal conditions (ampoule construction, axial temperature gradient in a furnace, allowable superheating of a melt, and pulling rate of a ampoule) for forming a single-crystal seed and preventing formation of other crystallization centers in the ampoule are determined.

REFERENCES

1. V. M. Glazov and L. M. Pavlova, Zh. Fiz. Khim. **58** (2), 333 (1984).
2. V. M. Glazov and A. V. Shishkin, Neorg. Mater. **27**, 2274 (1991).
3. V. M. Glazov, L. M. Pavlova, and D. S. Gaev, Neorg. Mater. **20** (9), 1476 (1984).
4. V. M. Glazov, L. M. Pavlova, and A. V. Shishkin, Zh. Fiz. Khim. **65** (1), 42 (1991).
5. A. R. Regel' and V. M. Glazov, *Physical Properties of Electronic Melts* (Nauka, Moscow, 1980), p. 296.
6. Yu. A. Kanter and Yu. G. Sidorov, Izv. Akad. Nauk SSSR, Neorg. Mater. **16** (10), 1874 (1980).
7. Yu. O. Kanter, Cryst. Res. Technol. **16** (12), 1333 (1981).
8. B. I. Kidyarov, *Kinetics of Crystal Formation from Liquid Phase* (Nauka, Novosibirsk, 1979).
9. E. D. Andryushenko, T. N. Danil'chuk, V. P. Zlomanov, *et al.*, Izv. Akad. Nauk SSSR, Neorg. Mater. **15** (9), 1573 (1979).
10. M. A. Potapov, V. I. Shtanov, M. S. Chupakhin, and V. P. Zlomanov, Zh. Anal. Khim. **33** (6), 1062 (1978).
11. V. I. Shtanov, V. P. Zlomanov, A. A. Komov, *et al.*, Vysokochist. Veshchestva, No. 1, 5 (1989).
12. V. I. Shtanov, A. G. Usanov, V. P. Zlomanov, and A. A. Komov, Izv. Akad. Nauk SSSR, Neorg. Mater. **24** (11), 1796 (1988).
13. A. Polity, R. Krause-Rehberg, V. Zlomanov, *et al.*, J. Cryst. Growth **131**, 271 (1993).
14. N. B. Brant, Ya. G. Ponamarev, E. P. Skipetrov, *et al.*, Fiz. Tekh. Poluprovodn. (Leningrad) **17** (4), 645 (1983) [Sov. Phys. Semicond. **17**, 403 (1983)].
15. Yu. A. Mityagin, I. V. Kucherenko, L. K. Vodop'yanov, and V. I. Shtanov, Fiz. Tverd. Tela (Leningrad) **20** (10), 2974 (1978) [Sov. Phys. Solid State **20**, 1717 (1978)].
16. L. V. Yashina, S. P. Kobeleva, V. S. Neudachina, *et al.*, Surf. Interface Anal. **34**, 498 (2002).
17. R. Laudise and R. Parker, *The Growth of Single Crystals; Crystal Growth Mechanisms: Energetics, Kinematics, and Transport* (Prentice Hall, New York, 1970; Mir, Moscow, 1974).
18. A. L. Fripp, R. K. Crouch, W. J. Debnam, *et al.*, J. Cryst. Growth **73**, 3 (1985).
19. S. Takeda, Y. Tsuchiya, and S. Tamaki, J. Phys. Soc. Jpn. **45** (2), 479 (1978).
20. Yu. G. Poltavtsev, Ukr. Fiz. Zh. **20**, 2009 (1975).
21. Ya. I. Dutchak, N. M. Klym, and S. I. Mudryĭ, Neorg. Mater. **21** (6), 1049 (1985).
22. Yu. A. Kanter and Yu. G. Sidorov, Izv. Akad. Nauk SSSR, Neorg. Mater. **17** (8), 1373 (1981).

Translated by Yu. Sin'kov

Crystallography Reports, Vol. 49, No. 2, 2004, pp. 294–298. Translated from Kristallografiya, Vol. 49, No. 2, 2004, pp. 350–355.

CRYSTAL GROWTH

Influence of Various Conditions of Convective Mixing of Melt on the Structure and Magnetoresistance of Eutectic InSb–NiSb Alloys Obtained by Directional Crystallization[1]

D. V. Bryukvin, M. R. Raukhman, V. P. Shalimov, and V. S. Zemskov

Baĭkov Institute of Metallurgy and Materials Science, Leninskiĭ pr. 49, Russian Academy of Sciences, Moscow, 119334 Russia

e-mail: zemskov@ultra.imet.ac.ru

Received February 26, 2003

Abstract—The microstructures are analyzed of the eutectic alloys solidified in the quasi-binary InSb–NiSb system under different conditions of convective mixing of melts grown in an ampoule by the Czochralski and directional crystallization methods under earth and microgravity conditions. It is established that growth of the phases in directional solidification of the InSb–NiSb eutectics is determined not only by the diffusion mechanism of the component redistribution at the crystallization front but also by the diffusion–convection mechanism. The comparative analysis of the influence of the crystal microstructure on the value of the magnetoresistance, R_M, is performed for the first time. It is shown that the R_M value of directionally crystallized InSb–NiSb eutectics depends on the density of the NiSb needles, disorder of the eutectic structure, and electrophysical parameters of the matrix. © *2004 MAIK "Nauka/Interperiodica".*

INTRODUCTION

Below, we describe the experimental investigation of an insufficiently studied aspect of solidification of eutectic alloys—the influence of convective mixing on the formation of the structure in directionally crystallized eutectic alloys, and provide analysis of their properties depending on the structure parameters.

We studied the needle-like type eutectics of the semiconductor–metal class in the quasi-binary InSb–NiSb system (1.8 wt % NiSb) [1]. This eutectics is convenient for studying the general rules of eutectic system crystallization, because its structure is rather sensitive to variations in the intensity of convective mixing of melts [2]. Directionally crystallized eutectics in this system are widely used in practice, mainly because of their pronounced magnetoresistance [2, 3].

Various conditions of convective mixing of the melt were attained in a special series of growth experiments on eutectic InSb–NiSb crystals grown by the Czochralski technique and the method of directional crystallization in ampules at the horizontal and vertical (Bridgman method, heating from above) location of an ampoule on earth and by the method of directional crystallization in an ampoule onboard of the *Photon-11* satellite (Table 1) [4]. The methods of experiment preparation and conduction were described in detail elsewhere [4, 5].

[1] This work was presented at the National Conference on Crystal Growth (NCCG-2002, Moscow).

STUDY OF MICROSTRUCTURE OF DIRECTIONALLY CRYSTALLIZED InSb–NiSb EUTECTIC ALLOYS

The structure was studied by the metallographic methods on sections of longitudinal plates and transverse disks (Fig. 1). Using plates, we determined the length and configuration of needles, and, using disks, the specific needle density (the method is considered in detail elsewhere [4, 5]). As a result, we established (Table 2) that, during crystallization, the density and length of NiSb needles increase, whereas the spacing between the decreases.

Different microstructures of the directionally solidified eutectic alloys can be explained by different flow velocities in the melts, depending on the experimental conditions and method, and different character of heat and mass transfer in the melts. The intensity of convective flow in the melt was evaluated based on the hydrodynamic similarity criteria. The estimates showed that, under all the conditions of our experiments, the main contribution to the melt flow comes from a natural thermogravitational convection whose intensity is characterized by a Rayleigh number. The characteristic dimension in the expression for a Rayleigh number is the diameter of a growing crystal. During the crystallization process, the ratio of the length of the melt region to its diameter decreases, and the convection becomes less intense (Fig. 2). Under microgravity conditions, the convection is considerably less intense than on earth, and, therefore, the factors responsible for needle entanglement and breaks become less intense. Thus, needles can grow without distortions. On earth, where

1063-7745/04/4902-0294$26.00 © 2004 MAIK "Nauka/Interperiodica"

Table 1. Technological parameters of crystallization processes

Growth method	Crystal diameter, mm	Crystal length, mm	Growth direction	Velocity of crystal rotation, rev/min	Crystallization rate, mm/min
Czochralski technique	22	130	InSb $B\langle 111\rangle$	15	0.6
Method of directional crystallization in ampoule on earth and in space	16	110		No rotation	0.25

convective mixing is more pronounced, the flows in the melt negatively influence the needle length and shape and play the main role in the deterioration of the microstructure of directionally crystallized InSb–NiSb eutectics (Fig. 3).

The needle density, *N*, in the Czochralski-grown crystals is almost twice as high as in the Bridgman-grown ones (Table 2). According to the diffusion theory of growth of eutectics [6], the crystallization rate, *V*, and the interneedle distance, λ, should be related by the dependence $\lambda^2 V = \text{const}$. Therefore, one can assume that the different values of these parameters are associated with the higher crystallization rate in the Czochralski method than in the directional crystallization in ampoules (Table 1).

The λ and *N* values in crystals grown by the directional crystallization in ampoules under earth conditions at the same growth rates also differ. Therefore, the convective flows also influence the morphology of directionally crystallized InSb–NiSb eutectics. In this case, if the eutectic and melt compositions are different, the microstructure can change. One of the most probable explanations here is the fact that the homogeneity region of the NiSb phase is of about 10 at. %, and, therefore, in the directional crystallization at low rates, the growing needles may have a nonstoichiometric composition. The deviation of the melt composition from the eutectic composition during crystallization should result in the enrichment of the melt with Ni and Sn and the formation at the crystallization front of a diffusion layer that is rather sensitive to convective mixing. Thus, the growth of phases in eutectic crystallization of the system is determined not only by the diffusion mechanism of the component redistribution at the crystallization front but also by the diffusion–convective mechanism.

STUDY OF MAGNETORESISTANCE IN DIRECTIONALLY SOLIDIFIED EUTECTICS

The magnetoresistance of samples, R_M, is described by the expression $R_M = (\rho_M - \rho_0)/\rho_0$ [2, 3], where ρ_M is the resistivity of the sample in a magnetic field and ρ_0 is its resistivity without the field. Resistivity was measured on samples cut out from different regions of directionally solidified eutectics (Fig. 1) [4, 5]. The magnetic-field induction was 1 T. The R_M values measured are listed in Table 3.

The measurements performed at 300 K showed (Fig. 4) that R_M increases along the crystal from its origin to the end, with the maximum R_M values being consistent with the known experimental data [7, 8]. The maximum R_M value, R_M = 18.3, was measured in the end part of Czochralski-grown crystal *1*. The maximum R_M values of Czochralski-grown crystals *2* and *3* lie at the same level as the R_M values of crystals *4* and *6* obtained by directional crystallization in an ampoule under earth conditions. It is also established that the Czochralski-grown directionally crystallized eutectics are characterized by a more homogeneous R_M distribution.

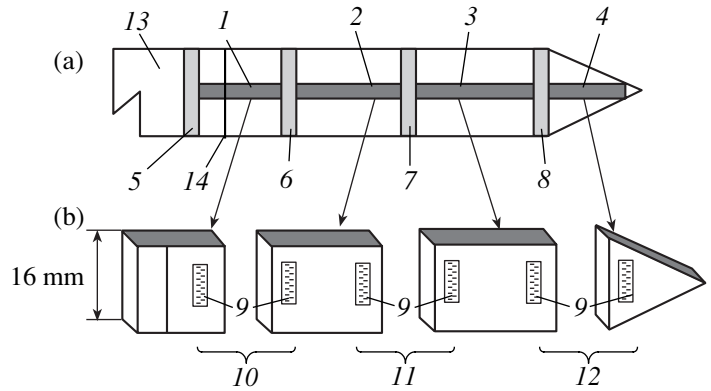

Fig. 1. Schematic of preparation of directionally crystallized InSb–NiSb eutectics in ampoules: (a) (*1–4*) plates and (*5–8*) disks for metallographic studies; (b) (*9*) samples for measuring magnetoresistance R_M. Crystal regions: (*10*) initial, (*11*) middle, (*12*) end, (*13*) seed, (*14*) initial crystallization front.

Table 2. Basic characteristics of the microstructure of directionally solidified InSb–NiSb eutectics under different conditions

Growth method			Region of crystal studied	Structure characteristic				
				needle diameter, μm	maximum needle length, l, μm	interneedle distance, λ, μm	density of needle distribution, $N \times 10^{-4}$, mm^{-2}	needle rectilinearity
Czochralski technique			beginning	~0.8	123	5.2	4.7	Rectilinear needles and entanglements
			middle		130	5.0	5.1	
			end		200	4.5	6.2	Rectilinear needles
Directional crystallization in ampoule	on earth	horizontally	beginning	~1.0	122	7.4	2.4	Entanglements and other defects
			middle		153	6.8	2.7	
			end		300	7.1	2.5	
		vertically	beginning	~1.0	197	6.8	2.7	Rectilinear needles slightly misoriented from the growth direction
			middle		257	7.1	2.5	
			end		333	5.8	3.8	
	under microgravity conditions		beginning	~1.0	160	7.9	2.0	Rectilinear needles and entanglements
			middle		518	6.3	3.2	
			end		392	6.2	3.3	Rectilinear needles

A higher R_M value in crystal *1* is explained mainly by a higher needle density, which provides a more efficient short circuiting of the Hall emf. The structure of space-grown crystal *7* is characterized by more homogeneous eutectic regions with longer rectilinear parallel needles. Short circuiting of the Hall emf in this crystal is more efficient and gives rise to a more pronounced increase in R_M in comparison with crystals *4–6* obtained by directional crystallization in an ampoule on earth.

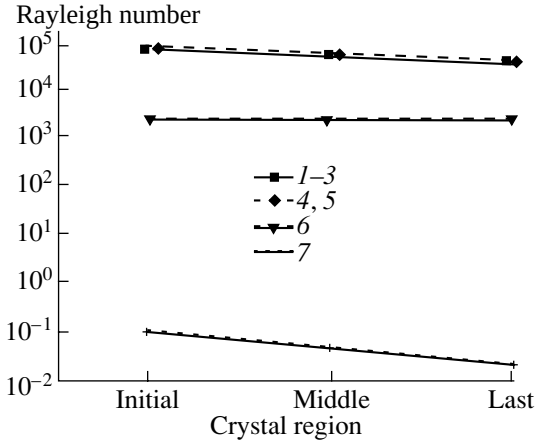

Fig. 2. Schematic illustrating the change in the intensity of the thermogravitational convection (Rayleigh number) in the melt in (*1–3*) Czochralski growth, growth by the method of directional crystallization in ampoule on earth at the (*4*, *5*) horizontal and (*6*) vertical position of the ampoule, and (*7*) by the method of directional crystallization under the microgravity conditions.

In eutectics directionally crystallized on earth by the same method, the R_M values varied from sample to sample. This is especially clearly seen in measurements made at 77 K. At this temperature, the tendency of R_M to increase in the direction toward the peripheral regions is preserved along, moreover, an increase in magnetoresistance is observed (Fig. 5). At the same time, the crystals grown obtained by directional crystallization in ampoules on earth manifest a considerable scatter in R_M values (crystals *4* and *5*).

The behavior of R_M at 77 K can be explained by the changes in electrophysical parameters of the eutectic matrix (InSb) such as the conductivity type and the concentration and mobility of charge carriers. To evaluate these parameters, we measured the Hall effect and resistivity on specially cut samples [4, 5]. These measurements showed that all the samples, except of the samples cut out from crystals *4* and *5*, were of the *n*-type both at 300 and 77 K. At 300 K, the electron concentration in all the samples was $n \sim 2 \times 10^{16}$ cm^{-3}, which corresponded to the intrinsic conductivity of InSb at 300 K. At 77 K, the measured carrier concentrations were about $n \sim (1–10) \times 10^{15}$ cm^{-3}, which indicated the impurity conductivity of the matrix [9]. Mobility of electrons in these samples were $\mu \sim (3–30) \times 10^4$ cm^2/(V s). On the other hand, it is well known that at 77 K, the electron mobility in doped uncompensated InSb at $n \sim 5 \times 10^{15}$ cm^{-3} is equal to about $\mu \sim 1 \times$

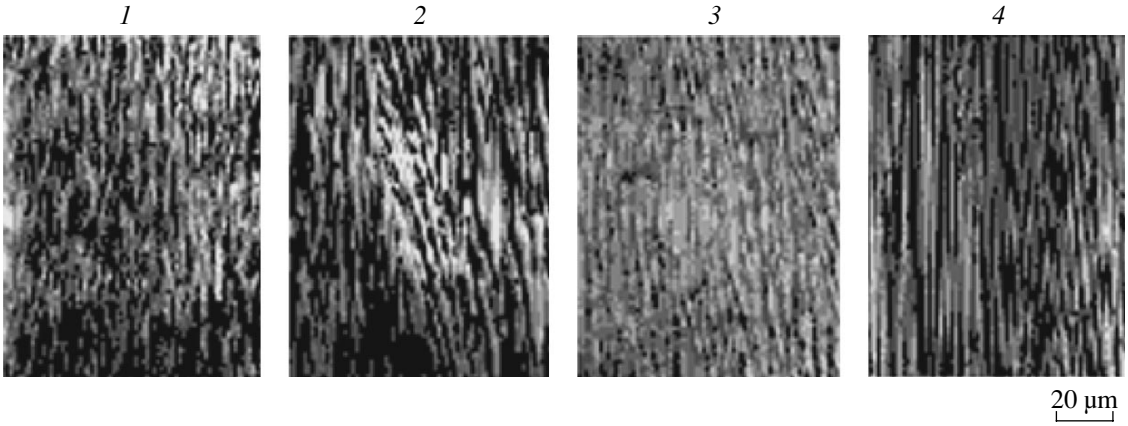

Fig. 3. Microstructures from the end portions of directionally crystallized InSb–NiSb eutectics under various conditions of convective melt mixing in (*1*) Czochralski growth, (*2*) growth by directional crystallization in an ampoule on earth at the (*2*) vertical and (*3*) horizontal position of the ampoule, and (*4*) by the method of directional crystallization in an ampoule under conditions of space flight.

10^5 $cm^2/(V\ s)$ [9]. This points out the fact that the matrix in the directionally crystallized eutectic samples can be partly compensated for, and that a decrease in mobility observed is explained by scattering from uncontrollable impurities and the structural defects of the samples.

It is possible to assume that the poor reproducibility of the R_M values is explained by the fact that the degree of compensation caused by uncontrollable impurities varied from crystal to crystal during growth. In high-purity InSb, the uncontrollable impurities can also be the accompanying impurities contained in other starting materials—Ni and Sb. Possibly, nickel (whose solubility in InSb equals $\sim 10^{18}$ at/cm^3) can also play the role of an acceptor impurity, although the behavior of the Ni impurity in InSb has not been studied in detail as

Table 3. Magnetoresistance effect in eutectic InSb–NiSb crystals grown under various conditions

Growth method		Experiment	Temperature, K	Magnetoresistance R_M in different regions of the crystal at the magnetic induction 1 T		
				at the beginning of the crystal	in the middle of the crystal	at the end of the crystal
Czochralski technique		1	300	16.2	17.1	18.3
			77	34.3	44.1	54.6
		2	300	13.6	13.9	13.5
			77	21.2	21.8	24.1
		3	300	14.4		14.9
			77	10.7		17.4
Method directional crystallization in ampoule	horizontal on earth	4	300	11.4	8.7	14.7
			77	23.1	0.3	30.1
		5	300	3.3	6.4	12.7
			77	0.02	0.03	6.6
	vertical on earth	6	300	14.7	15.6	15.9
			77	19.4	16.6	35.0
	in space	7	300	8.7	14.6	16.2
			77	13.3	29.6	36.0

Note: In experiment 3, no value for the crystal middle is indicated, because there was no sample appropriate for measurements and the middle part of the crystal was used as a preparation for recrystallization by the method of directional crystallization in ampoule.

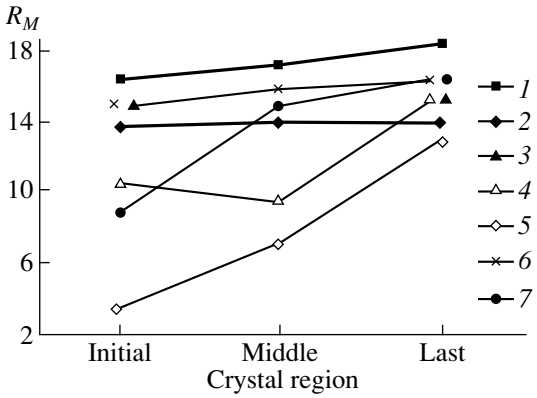

Fig. 4. Schematic illustrating the change in magnetoresistance R_M along the length of the directionally crystallized InSb–NiSb eutectics crystals at 300 K and the magnetic induction 1 T in (*1–3*) Czochralski growth, growth by directional crystallization in an ampoule on earth at the (*4*, *5*) horizontal and (*6*) vertical position of the ampoule, and (*7*) growth by the method of directional crystallization in ampoule under the microgravity conditions.

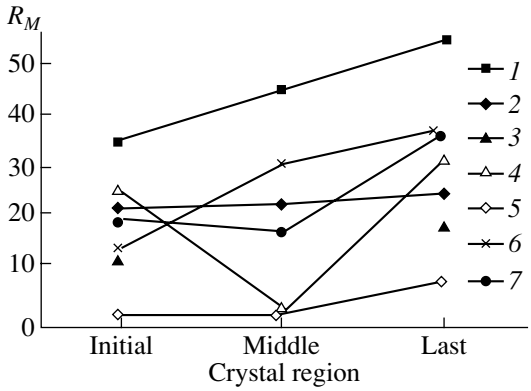

Fig. 5. Schematic illustrating the change in magnetoresistance R_M along the length of directionally crystallized InSb–NiSb eutectics crystals at 77 K and magnetic induction 1T (*1–3*) in Czochralski-grown crystals; crystals grown by the method of directional crystallization method at the (*4*, *5*) horizontal and (*6*) vertical position of the ampoule, and (*7*) crystals grown by the method of directional crystallization in ampoule under the conditions of space flight.

yet [10]. The compensation effect is also seen from the change of the conductivity type at 77 K (samples 4 and 5). Magnetoresistance in these samples is rather low, because the mobility of the current carriers (holes) is rather low. In the *n*-type samples with high mobilities, as follows from the theory of magnetoresistance effect, R_M can also have higher values [11].

CONCLUSIONS

Growth of phases by the method of directional crystallization of the InSb–NiSb eutectics is determined not only by the diffusion mechanism of component redistribution at the crystallization front but also by the diffusion–convective mechanism. It is shown that growth of the eutectics of the quasi-binary InSb–NiSb system differs from crystallization of the eutectics of other binary systems and can be determined by the extended homogeneity region of the NiSb phase. It is established that the microstructure considerably influences the magnetoresistance effect—its intensity increases with an increase in the needle density and length and a higher degree of needle parallelism. It is shown that the most efficient, both practically and economically, method for growth directionally solidified InSb–NiSb eutectics is the Czochralski technique, which allows one to obtain directionally solidified InSb–NiSb eutectics with a higher R_M value than in the directionally crystallized InSb–NiSb eutectics obtained by the method of directional crystallization in ampoules under microgravity conditions onboard space vehicles. The main tasks of the further studies of the synthesis of directionally crystallized InSb–NiSb eutectics of quasi-binary semiconductor–metal systems under microgravity conditions are formulated—the study of the influence of the crystallization rate on the structure and properties of directionally crystallized InSb–NiSb eutectic; and the study of the dependence of the structure and properties of directionally crystallized eutectics on the dimensions of the homogeneity region of the components in the quasi-binary system.

REFERENCES

1. F. S. Galasso, J. Met. **19** (6), 17 (1967).
2. G. Muller, *Crystal Growth from Melts* (Springer, Berlin, 1988; Mir, Moscow, 1991).
3. R. P. Elliot, *Eutectic Solidification Processing. Crystalline and Glassy Alloys* (Butterworths, London, 1983; Metallurgiya, Moscow, 1987).
4. D. V. Bryukvin, V. S. Zemskov, M. R. Raukhman, and V. P. Shalimov, Fiz. Khim. Obrab. Mater., No. 5, 79 (2001).
5. D. V. Bryukvin, V. S. Zemskov, and M. R. Raukhman, Fiz. Khim. Obrab. Mater., No. 1, 81 (2002).
6. K. A. Jackson and J. D. Hunt, Trans. Metall. Soc. AIME **236** (6), 843 (1966).
7. C. Uher and H. J. Goldsmid, J. Phys. D: Appl. Phys. **5**, 1478 (1972).
8. V. S. Vekshina, L. G. Elanskaya, L. Ya. Krol', *et al.*, Nauchn. Tr. Gos. Inst. Redkikh Met., No. 65, 150 (1975).
9. O. Madelung, *Physics of III, V Compounds* (Wiley, New York, 1964; Metallurgiya, Moscow, 1983).
10. P. I. Fedorov and R. Kh. Akchurin, *Indium* (Nauka, Moscow, 2000).
11. P. S. Kireev, *Physics of Semiconductors* (Vysshaya Shkola, Moscow, 1975).

Translated by L. Man

Crystallography Reports, Vol. 49, No. 2, 2004, pp. 299–306. Translated from Kristallografiya, Vol. 49, No. 2, 2004, pp. 356–363.

CRYSTAL GROWTH

Gold Distribution in Pyrrhotite Crystals Grown under Hydrothermal Conditions[1]

N. V. Smagunov, V. L. Tauson, and O. V. Ovchinnikova

Institute of Geochemistry, Siberian Branch of the Russian Academy of Sciences, ul. Favorskogo 1a, Irkutsk, 664033 Russia

e-mail: nicksm@igc.irk.ru

Received March 3, 2003

Abstract—The distribution of gold between pyrrhotite and greenockite was studied by the method of hydrothermal thermal-gradient cocrystallization of the components at a temperature of 450°C, a pressure of 1 kbar, and different activities of sulfur in the presence of As and Se impurities. The structural component of Au impurity in these minerals was selected by studying statistical samplings of the analytical data for single crystals. Ferrous greenockite incorporates a maximum of 10 ± 2 ppm Au in solid solution. The incorporation limit of Au in stoichiometric pyrrhotite was estimated to be 25 ± 9 ppm; for nonstoichiometric pyrrhotites, it is lower. The As and Se impurities barely affect the concentration of structural gold in the minerals. It was shown that constitutional vacancies in pyrrhotite do not capture Au impurity. The observed phenomenon may be the growth effect related to the surface properties of nonstoichiometric pyrrhotite crystals grown under hydrothermal conditions. Differences in the surface structure of pyrrhotites of different composition and the products of their sorption of gold were revealed by X-ray photoelectron spectroscopy. © *2004 MAIK "Nauka/Interperiodica"*.

INTRODUCTION

Pyrrhotite has a wide homogeneity range and, therefore, is a convenient model for studying the incorporation of impurities into crystals containing stoichiometric (constitutional) vacancies [1]. However, the nature of Au impurity in pyrrhotite, the isomorphic capacity of pyrrhotite with respect to Au, and the incorporation limit of Au have barely been investigated to date. In addition, despite well-known data on the sorption properties of pyrrhotite with respect to Au [2], the features of the surfaces of pyrrhotites of different composition and the interaction of pyrrhotite with absorbed gold have not been adequately investigated.

It should be noted that the principle of phase composition correlation used in petrology and geochemistry, which justifies the appropriate matched variation in the compositions of coexisting minerals under the action of pressure, temperature, and other equilibrium factors, is also applied to the interphase distribution of microelements [3] and, thus, can be used to study the mechanisms of incorporation and incorporation limits of microelements in minerals [4]. However, the principle of phase composition correlation applied to systems with real crystals, as well as in the case of wide variation in the parameters of a growth medium, has a number of specific features that, in particular, suggest the apparent phase composition correlation [5]. The purpose of this study was to gain an insight into gold distribution in pyrrhotite crystals during their growth and the features of the interaction of synthesized pyrrhotite crystals with solutions of gold. This purpose implied a check of the validity of the principle of phase composition correlation for the distribution of structural Au impurity between pyrrhotite Fe_xS and greenockite α-CdS during joint growth under hydrothermal conditions (greenockite is considered to be a reference mineral, which may contain a relatively large amount of Au structural impurity [6]) and the study of the surface of hydrothermally synthesized pyrrhotite samples of different composition and the products of sorption of Au from chloride solutions by these samples.

EXPERIMENTAL AND ANALYTICAL METHODS

Cocrystallization of pyrrhotite and greenockite was performed using the conventional method of hydrothermal thermal-gradient synthesis in stainless-steel autoclaves of about 200 cm^3 in volume that were equipped with titanium (VT-6) inserts of about 50 cm^3 in volume with passivated surface. The growth medium in the experiments was a 10% aqueous solution of NH_4Cl, the temperature in the growth zone was 450°C, and the pressure was 1 kbar (100 MPa). The experiments lasted 12 days. During the first three days, isothermal mode was supported to homogenize the blend and provide close-to-equilibrium conditions during subsequent thermal-gradient recrystallization, which was performed with a 15 K temperature drop over the outer

[1] This work was presented at the National Conference on Crystal Growth (NCCG-2002, Moscow).

1063-7745/04/4902-0299$26.00 © 2004 MAIK "Nauka/Interperiodica"

wall of the autoclave. The final stage was the quenching of autoclaves in cold running water. The blend consisted of finely grinded carbonyl iron, elemental sulfur, and cadmium sulfide. Gold was introduced into the blend in the form of a thin foil. High-purity and reagant-grade arsenic and selen were used as components facilitating saturation of the fluid (i.e., a supercritical aqueous salt (hydrothermal) solution with gold [4]). Arsenic and selen facilitate the incorporation of gold into the liquid phase. Thus, they make it possible to increase the Au content in the fluid and, accordingly, in the minerals coexisting with it. As a result, a phase-correspondence diagram can be plotted.

The composition of experimental pyrrhotite crystals was determined by the technique described in [7], from the diffraction reflection 102 using a NaCl internal standard. Measurements were performed on a DRON-3M diffractometer (FeK_α radiation) with a Mn filter. The accuracy of determination of the Fe content in pyrrhotite amounted to ±0.1 at %. The X-ray diffraction method was also used to find the greenockite composition (the content of FeS) from the unit cell parameter *a* [8] when the chemical analysis was not performed or was hindered by many pyrrhotite inclusions.

The content of Au in pyrrhotite and greenockite crystals was determined by graphite-furnace atomic absorption analysis on a Perkin–Elmer M503 spectrometer equipped with a deuterium background-absorption corrector and an HGA-74 graphite atomizer. The same analytical technique was used to determine the content of Se and As in the grown crystals. The details of the technique used to determine the Au content in extremely small amounts of substances have been reported in [9, 10]. The detection limit of Au was 0.2 mg/t, and the reproducibility of determination was ±10%. Several control determinations were performed using extraction of Au by organic sulfides. The structural component of Au impurity was selected by statistical sampling of analytical data for single crystals [9–11]. The physical basis of this method is the assumption that any sufficiently representative set of unit crystals will always contain several crystals that are free of active centers or defects responsible for the presence of nonstructural forms of an element. Nonstructural forms can only increase the total content of this element. The problem is to obtain a sampling over single crystals with very small, but significant, element contents. This was solved by using crystals of optimal size and of a quality that was sufficiently high for analysis [12]. The statistical sampling of analytical data, being a statistical method of selection of the structural form of the microelement impurity, is indirect and only indicates that a certain fraction of the element is distributed in the same way as the structural form is usually distributed. In the studies cited above, this fraction of Au ($\bar{x}_2$) was determined as the average over the second sampling of the analytical data for individual crystals, with the effect of nonstructural forms being eliminated. This quantity is considered to be the actual content of structural Au with the standard deviation ±σ. The structural character of a certain fraction of impurity can be justified more strictly with the use of special experiments. For this purpose, the impurity distribution in a system including the mineral being studied and a reference mineral should be analyzed. After filtration of the noise signal (introduced by other forms) in the first (statistical) stage, one can check if the impurity component of interest (the sought-after signal) obeys the general physico–chemical regularities of the distribution of isomorphous impurities, i.e., the principle of phase composition correlation and Henry's law. This problem is solved here for the pyrrhotite–greenockite system.

In order to obtain more detailed information on the composition of the pyrrhotite surface and the features of its interaction with Au solutions, the surfaces of stoichiometric and nonstoichiometric pyrrhotite samples, in which the Fe content was varied from 46.5 to 50.0 at %, were investigated by X-ray photoelectron spectroscopy (XPS). The surfaces of the same samples were studied after the sorption of gold in the trivalent form (Au III) from chloride solutions. The pyrrhotite samples were obtained with the same method and under the same conditions as in the case of the joint synthesis of pyrrhotite and greenockite. Sorption of Au III by pyrrhotite from chloride solutions was performed under static conditions with constant stirring by automatic shaking of test tubes for 15 h at a temperature of 20 ± 2°C. The ratio of the solution volume to the mineral weight amounted to 400 ml/g. The gold-containing solution was prepared by dissolving metallic gold (99.999%) in aqua regia. Then, HNO_3 was removed by multiple distillation in a water bath, with the addition of concentrated HCl, after which twice-distilled water was added to obtain an Au solution of the required concentration. A solution with a Au content of 173 mg/l (pH = 2.18) was used in experiments. The amount of gold absorbed by pyrrhotite was determined from the difference in the concentrations of the metal in the solutions before and after the sorption. The solutions were studied by the atomic-absorption method. The surfaces of the samples were analyzed by XPS on an LAS-3000 (Riber) instrument equipped with a hemispherical retarding-potential photoelectron analyzer. The photoelectron spectra were recorded using excitation of surface atoms by X-ray radiation from an aluminum anode (AlK_α = 1486.6 eV) at an emission current of 20 mA and a voltage across the tube of 10 kV. The spectra were calibrated using the carbon line C 1*s* with a binding energy of 285 eV. The pressure of the residual gases in the analytical chamber was 5×10^{-10} Torr.

EXPERIMENTAL RESULTS

We obtained crystals of hexagonal pyrrhotite and greenockite, the composition and properties of which depended significantly on the activity (fugacity) of sul-

fur in the system (f_{S_2}). The fugacity of sulfur characterizes its partial pressure in a nonideal gaseous medium. Under hydrothermal conditions, this quantity is relatively formal since, in this case, sulfur exists in different forms (including complex ions). Therefore, it is generally accepted that sulfur with some effective fugacity f_{S_2} affects the pyrrhotite composition in the same way as if sulfur was in the gas phase in the molecular form (S_2).

In the case of stoichiometric pyrrhotite ($\log f_{S_2}$ = –16.2 bar [7]), according to the XPS data, the blend retained α-Fe after the experiment, and magnetite in the form of octahedra up to 2 mm in size was observed in the final products. The grown pyrrhotite crystals had the form of flattened hexagonal prisms with the effective diameter of a circumscribed sphere of up to 1.5–2.0 mm; i.e., close to the limiting dimensional characteristic optimum for the sampling of crystals with minimum amounts of adsorbed Au [12]. Greenockite formed short prisms in combination with hexagonal pyramids with different face indices, nearly the same in size. Greenockite crystals were black or red-brown (in thin layers). With an increase in sulfur fugacity, the size of the crystals increased and attained the maximum value of 2–3 mm in the other experiments ($Fe_{0.98}S$, $\log f_{S_2}$ = –13.4 bar, $Fe_{0.87}S$, $\log f_{S_2}$ = –5.3 bar), i.e., was optimal for analysis of the Au content. In this case, the crystals became more isometric, especially with an increase in the content of arsenic and selen in the system, which, as noted above, facilitated gold incorporation. After all the experiments, gold foil was retained to one extent or another in the blend.

A series of special preliminary experiments was performed with the CdS–Fe–S–As(Se)–Au–NH_4Cl–H_2O system to find the incorporation limit for Au in ferric greenockite crystals at 450°C and 1 kbar. For this purpose, greenockite was synthesized in the presence of Fe with the addition of a maximum amount of As or Se: 2 wt % [6]. It was found that, despite the high total Au contents, which confirm the action of As and Se as guide elements for Au (facilitating Au incorporation), the concentration of uniformly distributed (in our understanding) form of Au remains approximately constant, being equal to $\bar{x}_2$ = 10 ± 2 ppm (10^{-3} wt %), and independent of the greenockite ferruginocity. Data on the incorporation limit of Au in the reference mineral are of fundamental importance for investigation of the phase composition correlation and determination of the corresponding value for the mineral under study [13]. The incorporation limit of Au in greenockite was first estimated to be 50 ± 10 ppm at 500°C and 1 kbar [6]. This value was confirmed by the data for individual crystals obtained by autoradiography in combination with atomic-absorption analysis [13]. If we use a regular one-parameter model for the (Cd,Au)S solid solution, the interaction parameter is Q = 65.6 kJ/mol and

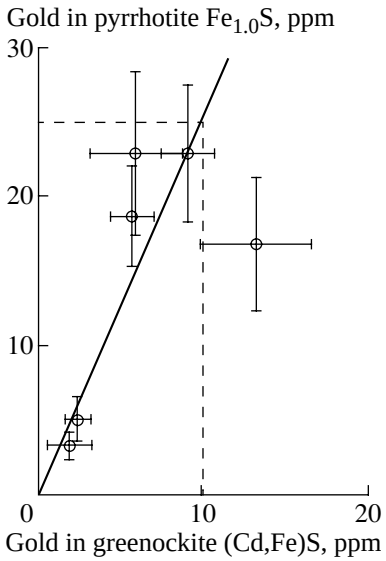

Diagram of phase composition correlation for the $Fe_{1.0}S$–(Cd,Fe)S–Au system at 450°C and 1 kbar.

the incorporation limit is equal to 25 ppm at t = 450°C. The experimental value we obtained is somewhat lower (even with regard to the total margin of error of ±7 ppm), but what is more important is that the (Cd,Au)S mixture behaves like an ordinary solid solution with respect to the temperature dependence of miscibility. This fact proves the structural character of Au impurity in greenockite. One might think that the composition of the solid solution deviates slightly from that of the regular mixture, but it should be taken into account that different methods were used for determining the incorporation limit in [6, 13] and in this study.

The data for the stoichiometric-pyrrhotite–greenockite system are listed in Table 1 and shown in the figure. Despite some spread of the data (which is within the margin of error in determining the coefficient of Au distribution between pyrrhotite and greenockite ($K_{Au}^{Po/Gr}$), it can be seen that the principle of phase composition correlation holds true in this case: the content of Au in greenockite and pyrrhotite increases with an increase in the amount of both As and Se. This circumstance makes it possible to plot a phase-correspondence diagram of this system (see figure) and, from the incorporation limit of Au in greenockite (Cd,Fe)S, estimate the corresponding value for pyrrhotite (dotted lines in the figure). These estimations show that the average value of the distribution coefficient is 2.5 and that the incorporation limit of Au in stoichiometric pyrrhotite is 25 ± 9 ppm. According to the ideas laid out in [4], the isomorphic capacity of FeS with respect to gold should have the same value. However, one should bear in mind that, at such low concentrations, the incorporation of Au in pyrrhotite can also be related to generally neglected defects in stoichiometric iron sulfide: Fe interstitials, S vacancies, and Fe atoms occupying sites

Table 1. Experimental data on the distribution of the structural component of Au impurity between greenockite and pyrrhotite of different composition at 450°C and 1 kbar in a 10% solution of NH_4Cl

Composition on the initial blend, wt %						Obtained phase	Au, ppm ($x_2 \pm \sigma$)		FeS in Gr, mol %	$K_{Au}^{Po/Gr}$	$\bar{K}_{Au}^{Po/Gr}$
Fe	S	CdS	As	Se	Au		Gr	Po			
$Fe_{1.0}S$ (log f_{S_2} = –16.2 bar)											
75.7	13.3	10			1	Po, Gr, Mt	1.8 ± 1.4	3.4 ± 0.9	26.6	1.9	2.5 ± 0.9
70.8	7.9	20	0.3		1	Gr, Po	6.0 ± 2.8	22.9 ± 5.5	27.4	3.8	
70.6	7.9	20	0.5		1	Po, Gr, Mt	9.1 ± 1.6	22.8 ± 4.6	26.8	2.5	
70.1	7.9	20	1.0		1	Po, Gr, Mt	13.3 ± 3.4	16.8 ± 4.4	27.0	1.3	
70.8	7.9	20		0.3	1	Po, Gr, Mt	2.3 ± 0.8	5.1 ± 1.5	26.5	2.2	
70.1	7.9	20		1.0	1	Po, Gr, Mt	5.8 ± 1.3	18.7 ± 3.4	25.2	3.2	
$Fe_{0.98}S$ (log f_{S_2} = –13.4 bar)											
55.3	23.7	20			1	Gr, Po	3.0 ± 1.1	2.9 ± 0.7	27.4	1.0	1.1 ± 0.6
55.1	23.6	20	0.3		1	Gr, Po	1.2 ± 0.3	2.8 ± 0.6	27.0	2.3	
55.0	23.5	20	0.5		1	Gr, Po	1.9 ± 0.2	3.3 ± 2.8	26.2	1.7	
54.6	23.4	20	1.0		1	Gr, Po	3.9 ± 1.0	2.5 ± 0.6	26.6	0.6	
55.1	23.6	20		0.3	1	Gr, Po	0.8 ± 0.2	0.7 ± 0.2	25.7	0.9	
55.0	23.5	20		0.5	1	Gr, Po	2.5 ± 0.8	2.3 ± 0.7	24.3	0.9	
54.6	23.4	20		1.0	1	Gr, Po	3.8 ± 2.4	1.7 ± 0.6	23.2	0.4	
$Fe_{0.87}S$ (log f_{S_2} = –5.3 bar)											
47.4	31.6	20			1	Gr, Po	6.2 ± 2.6	2.2 ± 0.6	13.4	0.3	0.2 ± 0.1
47.2	31.5	20	0.3		1	Gr, Po	5.9 ± 1.8	1.2 ± 0.6	12.6	0.2	
47.1	31.4	20	0.5		1	Gr, Po	6.3 ± 4.2	1.1 ± 0.5	13.0	0.2	
46.8	31.2	20	1.0		1	Gr, Po	5.4 ± 0.7	0.6 ± 0.1	12.6	0.1	
47.2	31.5	20		0.3	1	Gr, Po, Py*	5.8 ± 0.8	1.2 ± 0.4	12.8	0.2	
46.8	31.2	20		1.0	1	Gr, Po, Py*	7.6 ± 2.0	0.8 ± 0.3	11.9	0.1	

Note: Pyrrhotite, greenockite, magnetite, and pyrite phases are denoted as Po, Gr, Mt, and Py, respectively.
* Several crystals.

in the S sublattice. It can also be seen that the addition of As and Se impurities has no reproducible effect on the coefficient of Au distribution between pyrrhotite and greenockite within its reproducibility range.

The results obtained for the system consisting of pyrrhotite $Fe_{0.98}S$ and greenockite are also listed in Table 1. With an increase in the sulfur fugacity of the system and, therefore, an increase in the concentration of Fe vacancies in pyrrhotite, we expected the distribution coefficient to increase significantly in favor of pyrrhotite. These expectations were based on previous data on the incorporation of Cd in pyrrhotite [1], according to which the incorporation limit increases by almost two orders of magnitude due to the formation of elastic vacancy–impurity dipoles. However, in the case of Au, the situation turned out to be diametrically opposite: the average value of the coefficient of the distribution of Au between pyrrhotite and greenockite $\bar{K}_{Au}^{Po/Gr}$ decreased to 1.1 ± 0.6 for pyrrhotite $Fe_{0.98}S$ (Table 1). Hence, the incorporation limit of Au in pyrrhotite of this composition $IL_{Au}^{Fe_{0.98}S}$ is 11 ± 6 ppm. The value of the distribution coefficient shows no clear correspondence with the content of the guide elements As and Se, although a trend towards a decrease in the distribution coefficient was observed for the largest amounts of As and Se in the blend (1%). With an increase in sulfur fugacity, the distribution coefficient continues to decrease (Table 1); for the system composed of pyrrhotite $Fe_{0.87}S$ and greenockite, its value is only 0.2 ± 0.1, and the incorpo-

Table 2. Values of the binding energy of photoelectrons E_b and the atomic ratios of elements in pyrrhotite samples and products of gold sorption

Sample no.	Content of Fe, at %	Sample history	Binding energy of photoelectrons E_b, eV				Atomic ratios of elements		
			O1*s*	Fe $2p_{3/2}$	S 2*p*	Au $4f_{7/2}$	Fe/S	Au/Fe	Au/S
1	46.5	initial	530.8	711.3 713.1	164.4		0.98		
		after sorption of Au	530.2	709.0	162.4	84.0	0.10	2.73	0.46
2	49.6	initial	530.4	711.0	162.2 165.0 169.0		3.00		
		after sorption of Au	530.0	710.5	163.0	84.7	1.89	0.18	0.34
3	50.0	initial	530.9	712.3	162.4		2.50		
		after sorption of Au	530.8	711.3 712.8	161.3	83.3	2.00	0.02	0.03

ration limit is $IL_{Au}^{Fe_{0.87}S} = 2 \pm 1$ ppm. Notably, the lowest values again correspond to the largest amounts of As or Se (1%). Since the decrease in the distribution coefficient was also observed in the absence of guide elements (Table 1), it should be admitted that they do not play a key role, although the trend is fairly clear. The reason for this is yet to be understood. Obviously, the nature of this effect is not crystallochemical, as Se, for example, definitely replaces S in FeS and should not compete with Au upon incorporation in pyrrhotite (unless Au is incorporated into the anion sublattice, which is extremely unlikely). The substitution of sulfur with selen does not affect the positions of atomic layers containing Fe atoms, although the short-range order around Fe atoms somewhat changes due to the difference in the atomic radii of S and Se atoms [14].

In the case of nonstoichiometric pyrrhotite, in fact, arsenic and selen do not serve as guide elements for gold in the FeS structure: the concentration of structural gold obtained in both the absence and presence of these elements is approximately the same. In this case, the average total concentrations of Au in greenockite and pyrrhotite crystals are, respectively, higher and lower as compared to the case of absence of As and Se admixtures. Since total concentrations are characterized by a very large spread, they cannot be used to ascertain a relationship with Au. Thus, from the formal point of view, we can conclude that the incorporation limit of Au in pyrrhotite decreases with increasing the concentration of Fe vacancies by more than an order of magnitude. This result is relatively unexpected and deserves careful consideration.

As was noted above, the sample surfaces were studied by XPS in order to obtain additional data on the composition of pyrrhotite surfaces and the products of sorption of Au by this mineral. It has been ascertained previously that the pyrrhotite samples under study adsorb Au from chloride solutions. In this case, the capacity of pyrrhotite with respect to gold under the experimental conditions is as high as 74.7 mg/g.

The results of studying the surfaces of three pyrrhotite samples of differing composition before and after sorption are listed in Table 2. The analysis of the data obtained indicates significant differences in the composition of the surfaces of stoichiometric and nonstoichiometric pyrrhotite samples. For example, in the region S 2*p* of the X-ray photoelectron spectrum of the initial pyrrhotite sample with a deficit of iron and excess of sulfur (sample 1), a wide peak with a small maximum is observed at the energy corresponding to the binding energy E_b = 164.4 eV, which is due to the presence of free sulfur on the sample surface [15]. In other cases, peaks of S^{2-} dominate in the S 2*p* spectra. In the S 2*p* spectra of sample 2, maxima are observed at energies corresponding to the values of the binding energy of photoelectrons E_b = 165.0 and 169.0 eV, which can be attributed to the SO_3^{2-} and SO_4^{2-} groups [15].

Iron is present on the surfaces of the initial samples mainly in the oxide or oxide–hydroxide state. The values of E_b = 709.0–710.5 eV in the Fe $2p_{3/2}$ spectra are due to the presence of the FeS phase [15].

After the absorption of Au, the surface of pyrrhotite changes significantly, especially for sample 1: the maximum due to the presence of free sulfur vanishes in the S 2*p* spectrum, and the Fe/S ratio decreases by a factor of ten. A large amount of Au is present on the surface of sample 1, but, in determining the binding energy corresponding to the peak Au $4f_{7/2}$, difficulties arose from the low reproducibility of the spectrum, which shifted in the energy scale with time; therefore, the average value E_b = 84.0 eV is given for the peak Au $4f_{7/2}$. For samples 2 and, especially, 3, which contain adsorbed gold, the changes on the surface are less pronounced in compar-

ison with sample 1: the Fe/S ratio decreases to a lesser extent and the maxima at 165.0 and 169.0 eV vanish in the spectrum S 2*p* of sample 2. The binding energy corresponding to the peak Au $4f_{7/2}$ was determined quite reliably for sample 2, and the value found indicates that Au is in the chemically bound state. Gold in low concentrations was detected on the surface of stoichiometric pyrrhotite (sample 3), and the values of E_b for the peak Au $4f_{7/2}$, according to [2], suggest the presence of clusters composed of several Au atoms.

DISCUSSION

Thus, the phase composition correlation under the distribution of gold between pyrrhotite and greenockite cocrystallizing under hydrothermal conditions has features that do not follow from the analysis of interactions between an impurity and defects (Fe vacancies) in pyrrhotite. Only the data on the stoichiometric pyrrhotite under conditions of very low sulfur fugacity seem to correspond to a certain crystallochemical mechanism of Au incorporation in iron sulfide (see figure). This suggestion is confirmed by the appropriate matched variation in the content of Au in coexisting phases with increasing the concentrations of guide elements (As and Se) in the system. In other words, within the accuracy of determining the distribution coefficient, the system obeys the principle of phase composition correlation and Henry's law, which distinguishes the structural form from other impurity forms and makes it possible to determine the incorporation limit of Au in $Fe_{1.0}S$: 25 ± 9 ppm (2.5×10^{-3} wt %) at 450°C and 1 kbar. In a simple one-parameter model of a regular (Fe,Au)S solution, the interaction parameter can be estimated from the equation $Q \simeq -RT\ln IL$, taking into account that the molar fraction of AuS is much smaller than unity. The obtained value of $Q = 68.5$ kJ/mol is close to that for the (Cd,Au)S mixture (65.6 kJ/mol). Comparing the FeS–Au and FeS–Cd systems, one should bear in mind that the atomic volume of Au exceeds that of Cd. According to calculations in terms of the model of concentration expansion of an elastic medium [1], Fe vacancies should lead to a larger increase in the solubility of Au rather than Cd in pyrrhotite. The solubility of Cd in nonstoichiometric pyrrhotite increases by almost two orders of magnitude [1]. A significant increase in solubility with increasing the vacancy concentration in pyrrhotite was also observed for Pt [16, 17]. In contrast, in our experiments, we observed a decrease in the incorporation limit of Au with increasing vacancy concentration. We cannot yet explain the observed phenomenon unambiguously. It is quite likely that it has a pure growth nature.

It has been shown recently [18] that, during the growth of stoichiometric pyrrhotite under hydrothermal conditions in the presence of Cd impurity, a film of island CdS precipitates arises that is similar to that observed on the surface of pyrite [19]. We defined these precipitates as surface nonautonomous phases, using, as in [20, 21], the terminology introduced by Defay and Prigogine [22]. The role of defects in the formation of such phases should be noted. It would be quite reasonable to suggest a general mechanism for interaction of the crystal surface with an adsorbate that requires a certain surface configuration of defects and adatoms bound with them. As a result, a nonautonomous phase is formed that cannot be isolated beyond the given defect complex. This is a possible reason for existence of amorphized layers or layers with another structure on the surface of grown crystals [23]. It appears that a crystal growing from a hydrothermal solution bears a film of metastable surface phase depleted with metal. Such a nonequilibrium surface layer is formed upon the interaction of pyrrhotite with acids [24, 25]. The method we used for selecting structurally bound Au should, in principle, eliminate similar cases in the stage of statistical processing of analytical data on individual crystals. Nevertheless, if the appearance of a nonequilibrium layer on a pyrrhotite surface is indeed related to surface defects, it may be not always be formed on all the crystals grown in a single experiment. Crystals that contain none of the defect complexes necessary for the formation of a nonequilibrium layer cannot compete with neighboring crystals coated with such a layer in capturing impurities. Due to the high coefficient of distribution of Au between the nonequilibrium layer and a normal crystal, this layer continually extracts complex Au compounds from the growth front of the normal crystal, and the latter becomes pure with respect to the Au impurity. It appears that the higher the sulfur fugacity during the growth, the smaller the amount of Fe the forming layer contains, the larger the fraction of S–S bonds in the layer, and the larger the total coefficient of distribution of gold in favor of such crystals. Adsorbed gold-containing complex ions oxidize sulfur, forming metal precipitates or surface microphases containing sulfur and guide elements (As and Se). For this reason, a negative correlation between the content of structural Au (and its distribution coefficient) and the content of guide elements is observed for nonstoichiometric pyrrhotite. This is especially pronounced for As. The effect of S activity on Au distribution is enhanced, because pyrrhotite predominantly absorbs As (in comparison with greenockite). The properties of the nonequilibrium layer that chemically bounds Au in the form of surface complexes (like Au on the surface of As_2S_3 [26]) may also manifest themselves in this case. Gold is distributed extremely nonuniformly over the grown crystals, because it does not penetrate the growth zone of crystals containing no adsorption layer enriched with sulfur, arsenic, and selen and depleted with iron. As a whole, in the presence of such an absorbing layer, these elements cease to facilitate the Au-impurity saturation of both minerals (pyrrhotite and greenockite) coexisting with this layer. The surface layer enriched with sulfur can absorb almost all the gold penetrating the growth zone of pyrrhotite crystals, as when 100% of the gold is

absorbed by pyrrhotite from a hydrosulphide solution with low pH under normal conditions [2].

The investigation of pyrrhotite and the products of gold sorption by XPS confirmed our suggestions to some extent and expanded the knowledge of the state of the pyrrhotite surface and the features of the interaction between pyrrhotite and gold-containing solutions. Significant differences in the surface compositions of stoichiometric and nonstoichiometric pyrrhotite samples and a substantial reduction in the Fe/S ratio upon absorption of gold, which is characteristic of pyrrhotite with an iron deficit, suggest that a phase composed of not only sulphide and sulfur-containing compounds, but also including oxides and hydrated oxides of iron, is formed on the pyrrhotite surface. The high sorption properties of such compounds, in particular with respect to gold, are well known [27], and the significant contribution of the so-called secondary processes of absorption of gold to its accumulation in nature and technological extraction has been noted repeatedly [27].

CONCLUSIONS

The results of this study demonstrate an important feature of the phase composition correlation under hydrothermal conditions. The principle of phase composition correlation may be violated due to the specific features of the crystallization process occurring when an impurity cannot penetrate the structure of one of the coexisting minerals for some reason. When deviation from stoichiometry occurs and the sulfur fugacity in the system increases by several orders of magnitude, we have uncertain component ratios instead of a fairly distinct phase-correspondence diagram for stoichiometric pyrrhotite, which allows one to estimate the incorporation limit of gold in this mineral. The situation is aggravated by the fact that the guide elements (As and Se) stop performing their function, i.e., facilitating the incorporation of gold. Even when they saturate the fluid phase with gold, the redistribution of the forms of gold does not make it possible to saturate the structure of target phase with gold. One should bear in mind that the growth processes and defects of the real structure of minerals always affect to some extent the distribution of impurity elements, especially microelements [28]. In our case, we can ascertain only that Au impurity is not captured by structural vacancies of pyrrhotite under hydrothermal conditions. We attribute this fact to the anomalous adsorption properties of a nonequilibrium layer depleted with metal (the metastable nonautonomous phase) on the surfaces of most pyrrhotite crystals grown under hydrothermal conditions. This layer exists because of surface defects. Our experimental conditions are rather close to those typical of the formation of pyrrhotite in nature, where there is no doubt that the discovered factors also act. In our opinion, the available data [29–32] confirm that, in both nature and hydrothermal experiments, constitutional vacancies in pyrrhotite do not capture structural Au impurity. In this study, one of the possible reasons for the observed phenomenon is analyzed, namely, the anomalous sorption properties of the surfaces of grown nonstoichiometric pyrrhotite crystals. This cause is confirmed experimentally but requires more detailed investigation.

ACKNOWLEDGMENTS

We are grateful to A.N. Sapozhnikov, L.A. Bogdanova, L.P. Feoktistova, O.I. Bessarabova, V.I. Men'shikov, T.M. Pastushkova, K.V. Nepomnyashchikh, Yu.V. Shchegol'kov, and E.V. Savenkova for their help in the analytical part of the study.

This study was supported by the Russian Foundation for Basic Research, project no. 00-05-64577.

REFERENCES

1. V. V. Akimov, V. L. Tauson, I. Yu. Parkhomenko, *et al.*, Poverkhnost, No. 6, 31 (2002).
2. A. M. Wilder and T. M. Seward, Geochim. Cosmochim. Acta **66** (3), 383 (2002).
3. L. L. Perchuk and I. D. Ryabchikov, *Phase Correspondence in Mineral Systems* (Nauka, Moscow, 1976).
4. V. L. Tauson, Geol. Geofiz. **40** (10), 1488 (1999).
5. V. L. Tauson, in *Mineralogy: Papers of Soviet Geologists on 27th Session of MGK* (Nauka, Moscow, 1989), p. 77.
6. V. L. Tauson, A. G. Mironov, N. G. Bugaeva, and T. M. Pastushkova, Geol. Geofiz. **39** (5), 621 (1998).
7. P. Toulmin III and P. B. Barton, Jr., Geochim. Cosmochim. Acta **28** (5), 641 (1964).
8. B. J. Skinner and P. M. Bethke, Am. Mineral. **46** (11–12), 1382 (1961).
9. V. L. Tauson, A. Salikhov, I. Matshullat, *et al.*, Geokhimiya, No. 9, 951 (2001).
10. V. L. Tauson, O. I. Bessarabova, R. G. Kravtsova, *et al.*, Geol. Geofiz. **43** (1), 57 (2002).
11. V. L. Tauson and R. G. Kravtsova, Zap. Vseross. Mineral. O–va, No. 4, 1 (2002).
12. V. L. Tauson, O. V. Ovchinnikova, O. I. Bessarabova, *et al.*, Geol. Geofiz. **41** (10), 1480 (2000).
13. V. L. Tauson, Eur. J. Mineral. **11** (6), 937 (1999).
14. J. W. A. Kondoro, J. Alloys Compd. **289**, 36 (1999).
15. J. F. Moulder, W. F. Stickle, P. E. Sobol, and K. D. Bomben, *Handbook of X-Ray Photoelectron Spectroscopy* (Perkin-Elmer Co., Norwalk, CT, 1990).
16. M. Makovicky, E. Makovicky, and J. Rose-Hansen, *Metallogeny of Basic and Ultrabasic Rocks* (Inst. Mining Metal., London, 1986), p. 415.
17. Ch. Ballhaus and P. Ulmer, Geochim. Cosmochim. Acta **59** (23), 4881 (1995).
18. V. L. Tauson, I. Yu. Parkhomenko, V. I. Men'shikov, and K. V. Nepomnyashchikh, Geol. Geofiz. **43** (2), 182 (2002).
19. B. C. Bostick, S. Fendorf, and M. Fendorf, Geochim. Cosmochim. Acta **64** (2), 247 (2000).
20. V. V. Gusarov and S. A. Suvorov, Zh. Prikl. Khim. (Leningrad), No. 8, 1689 (1990).

21. V. V. Gusarov, A. A. Malkov, A. A. Malygin, and S. A. Suvorov, Neorg. Mater. **31** (3), 346 (1995).
22. R. Defay and I. Prigogine, *Tension Superficielle et Adsorption* (Desoer, Liege, 1951).
23. A. A. Shternberg, *Crystal Growth* (Erev. Gos. Univ., Erevan, 1977), Vol. 12, p. 115.
24. Yu. L. Mikhlin, Ye. V. Tomashevich, G. L. Pashkov, *et al.*, Appl. Surf. Sci. **125**, 73 (1998).
25. A. V. Kuklinskiĭ, Yu. L. Mikhlin, G. L. Pashkov, *et al.*, Élektrokhimiya **37** (12), 1458 (2001).
26. C. M. Cardile, J. D. Cashion, A. C. McGrath, *et al.*, Geochim. Cosmochim. Acta **57** (11), 2481 (1993).
27. O. V. Ovchinnikova and A. S. Chernyak, *Ion Exchange and Ionometry* (Leningr. Gos. Univ., Leningrad, 1988), p. 61.
28. V. S. Urusov, V. L. Tauson, and V. V. Akimov, *Geochemistry of Solids* (GEOS, Moscow, 1997).
29. A. C. L. Larocque, C. J. Hodgson, L. J. Cabri, and J. A. Jackman, Can. Mineral. **33**, 373 (1995).
30. N. J. Cook and S. L. Chryssoulis, Can. Mineral. **28**, 1 (1990).
31. G. C. Wilson, J. C. Rucklidge, and L. R. Kilius, Econ. Geol. **85**, 1252 (1990).
32. G. Chai, A. J. Naldrett, J. C. Rucklidge, and L. R. Kilius, Can. Mineral. **31**, 19 (1993).

Translated by Yu. Sin'kov

Crystallography Reports, Vol. 49, No. 2, 2004, pp. 307–311. Translated from Kristallografiya, Vol. 49, No. 2, 2004, pp. 364–368.

CRYSTAL GROWTH

The Growth of Single Crystals of Ni–W Alloy under Conditions of High Temperature Gradient[1]

V. M. Azhazha*, Yu. V. Gorbenko*, G. P. Kovtun*, A. N. Ladygin*, D. G. Malykhin*, T. Yu. Rudycheva*, V. Ya. Sverdlov*, A. P. Shcherban'*, P. D. Zhemanyuk, and V. V. Klochikhin*****

** Kharkov Institute of Physics and Technology, National Scientific Center, ul. Akademicheskaya 1, Kharkov, 61108 Ukraine*

e-mail: sverdlov@kipt.kharkov.ua

*** PJSC Motor-Sich, ul. Vos'mogo Marta 15, Zaporozhye, 69068 Ukraine*

**** Zaporozhye State University of Technology, ul. Zhukovskogo 66, Zaporozhye, 69600 Ukraine*

Received February 26, 2003

Abstract—The structure of single crystals of the NV-4 nickel alloy containing 32–36 wt % W is investigated. The temperature gradient at the crystallization front and the velocity of the crystallization front are the variable parameters of directional crystallization. The degrees of structural perfection of the single crystals grown under different conditions are compared. The crystallization parameters providing growth of single crystals that have high structural perfection and can be successfully used as seeds for the growth of single-crystal blades are determined. Typical defects formed upon directional crystallization of single crystals of the Ni–W (35 wt %) alloy are examined. The studied defects are classified, and the factors responsible for the disturbance of the single-crystal structure are analyzed. © *2004 MAIK "Nauka/Interperiodica".*

INTRODUCTION

Directional crystallization of alloys is an efficient method for improving the operational characteristics of articles manufactured from refractory materials [1–4]. This method is widely used in fabricating blades of gas-turbine engines [3]. When single-crystal blades are grown from seeds, the quality of the blades substantially depends on the structural perfection of the seeds.

In the technology of producing doped nickel alloys by the Bridgman method through directional crystallization, single crystals of the NV-4 alloy with nominal contents of 35 wt % W and 65 wt % Ni have been used as seeds [5]. In domestic practice, single-crystal blades are manufactured by the seeded growth method in a UVNK-8P apparatus in which an aluminum melt heated to $T = 750$°C serves as a liquid-metal coolant. Unfortunately, the production of seeds in these apparatuses does not meet the above requirements for high structural perfection of seeds, because the good-to-bad yield of seeds is small, whereas the power consumption is rather high. Moreover, the structure of the seeds thus produced is far from optimum.

A new efficient technology of producing seeds through directional crystallization at a high temperature gradient has been developed at the Kharkov Institute of Physics and Technology (National Scientific Center) in cooperation with PJSC Motor-Sich (Zaporozhye).

[1] This work was presented at the National Conference on Crystal Growth (NCCG-2002, Moscow).

The purpose of this work was to investigate the influence of crystallization conditions (temperature gradient, pulling speed) on the structure of single crystals of the NV-4 alloy and to perform a comparative analysis of the structure and properties of the single crystals grown under different conditions.

SAMPLE PREPARATION AND EXPERIMENTAL TECHNIQUE

The NV-4 alloy (TU 1-92-112-87) served as the initial material for preparing single-crystal seeds. The composition of this alloy is given in Table 1. The NV-4 alloy was industrially crystallized in a UVNK-8P apparatus under dynamic vacuum with a residual pressure of ~10^{-1} Pa. The alloy was transformed into a single-crystal state in a molding box fabricated from synthetic corundum. The molding box was preliminarily filled with a liquid melt and was then moved in a temperature field of the heater from the hot zone to a bath with liquid aluminum. The temperature gradient G at the crystallization front was equal to 8–10 K/mm, and the velocity R of the crystallization front was 10 mm/min.

Table 1. Composition of the NV-4 initial alloy

Ni	W, wt %	Impurities, wt % (no more)			
		Fe	Si	S	P
Basis metal	32–36	1.0	0.4	0.015	0.015

Table 2. Structural parameters and mechanical properties of the NV-4 alloy single crystals grown at different velocities of the front of directional crystallization

Velocity of the front of directional crystallization *R*, mm/min	0.4	1.2	2.6	4.0	10	20
Cell parameter λ, μm	253	294	266	223	186	
Depth of intercellular hollows *H*, mm	0.3	1.1	2.0	2.8		
Height of cellular asperities *H*/λ	1.2	3.8	7.7	12.4		
Crystal lattice parameter *a*, Å	3.5815	3.5809	3.5806	3.5804	3.5842	3.5841
Calculated W content in alloy, wt % (according to the data taken from [11])	31.65	31.80	31.30	31.25	32.65	32.65
Microhardness H_μ, kg/mm^2	265	255	245	237	255	255
Brinell hardness, kg/mm^2	160.8	148	137	137	142	160.8

Under laboratory conditions, the velocity of the crystallization front was changed stepwise from 0.4 to 20 mm/min, and the temperature gradient *G* was approximately equal to 20 K/mm. The high temperature gradients were achieved with the use of a specially designed crystallizer in which a Ga–In (25 wt %) alloy with a melting temperature of ~16°C was used as a liquid-metal heat-transfer material.

With the aim of investigating the location and shape of the crystallization front, the samples were quenched by rapidly dipping the molding box into the crystallizer. The quenching was performed in the central region of the crystallizing samples. After the directional crystallization, the ceramic box was broken and the NV-4 alloy samples were withdrawn for further investigations. The single-crystal samples were prepared in the form of cylindrical rods 9 mm in diameter and ~150 mm long.

The microstructure of the samples was examined with the use of a Neophot-32 optical microscope. The lattice constants, the crystallographic orientation, and the degree of perfection of the single crystals were determined by the X-ray diffraction analysis on HZG-4A12 and DRON-4 diffractometers (CuK_α radiation). The microhardness of the samples was measured on transverse metallographic sections with a PMT-3 instrument at a load of 50 g. The hardness of the samples was measured on metallographic cross sections by a Brinell durometer.

RESULTS AND DISCUSSION

The evolution in the microstructural morphology of the NV-4 alloy single crystals with an increase in the velocity of the front of directional crystallization is illustrated in Fig. 1. This figure displays the micrographs of the transverse metallographic sections of the single crystals with the [001] orientation. It should be noted that the critical velocity, i.e., the velocity at which the crystallization front loses stability, is less than the minimum velocity of crystallization front *R* (0.4 mm/min) used in our work. This result disagrees with the data obtained by Barabash and Voĭnash [6, 7], who found that the planar front during crystallization of the Ni–W (35 wt %) congruent alloy is retained up to a maximum velocity of 7.5 mm/min (*G* = 15 K/mm). At first glance, this discrepancy can be explained by the fact that the W content in the NV-4 alloy differs from that of the congruent alloy (~35 wt % W). Table 2 presents the experimental data on the parameters of the microstructure, crystal lattice parameters, microhardness, and hardness of the NV-4 alloy single crystals as a function of the velocity of the front of directional crystallization. Our measurements of the lattice parameters and the results of calculations of the alloy composition demonstrated that the W content in the alloy is close to the lower limit given by the State Standard (TU 1-92-112-87); i.e., it is close to 32 wt %. This deviation of the alloy composition from the congruent composition can lead to loss of stability of the planar crystallization front due to the existence of the crystallization range Δ*T*, which is one of the main criteria for stability of the planar front during crystallization of alloys.

According to the model of concentration supercooling, the planar front during crystallization of binary alloys is stable under the following condition [8]:

$$\frac{G}{R} \geq -\frac{m_L C_0 (1-k)}{kD}, \quad (1)$$

where *G* is the temperature gradient in a melt at the crystallization front, *R* is the velocity of the crystallization front, m_L is the slope of the liquidus curve, C_0 is the concentration of a dissolved element in the melt, *k* is the equilibrium distribution coefficient, and *D* is the diffusion coefficient of the dissolved element in the melt. This criterion can be approximately represented in the following form (which is especially convenient for analyzing the crystallization of multicomponent alloys [3]):

$$G/R \geq \frac{\Delta T}{D}. \quad (2)$$

Here, Δ*T* is the crystallization range, which is equal to the difference between the liquidus and solidus temper-

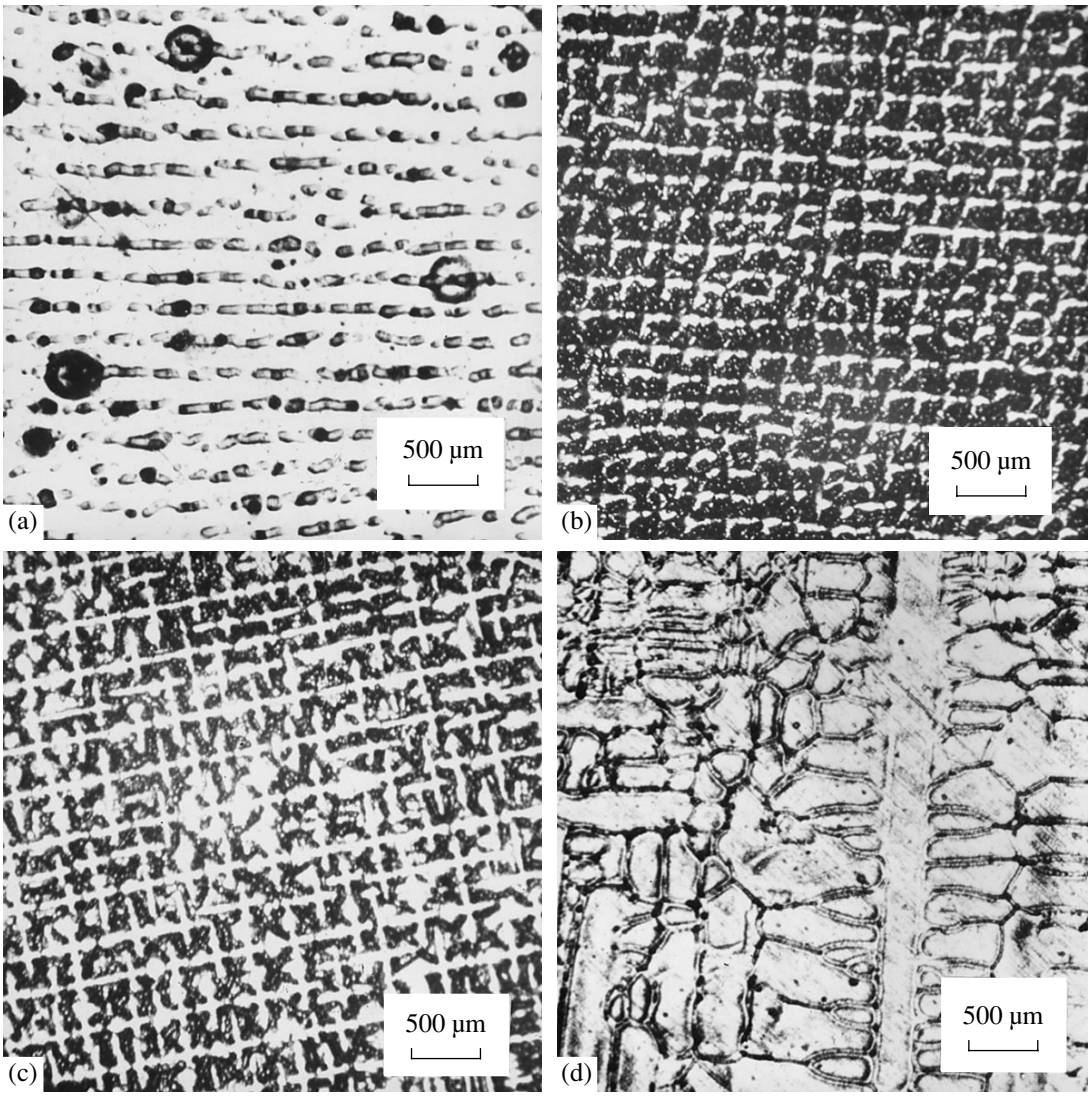

Fig. 1. Transverse metallographic sections of the NV-4 alloy single crystals grown at different velocities of the crystallization front R = (a) 0.4, (b) 2.6, and (c, d) 10 mm/min.

atures. Barabash and Voĭnash [6, 7] precisely measured the crystallization ranges ΔT for Ni–W alloys of different compositions and determined the values of R_{cr} above which the crystallization front loses stability [the critical velocity R_{cr} corresponds to the sign "equality" in relationships (1) and (2)]. For the Ni–32 wt % W alloy, the crystallization range ΔT is equal to 4 K and R_{cr} = 3.3 mm/min. This value of R_{cr} is one order of magnitude greater than that observed in our case.

In order to elucidate the origin of the aforementioned contradiction, we consider the effect of majority impurities in the NV-4 alloy (Table 1) on the possible increase in the crystallization range. According to the known phase diagrams of the Ni–Fe and Ni–Si systems [9, 10], the Fe and Si impurities (in amounts given in Table 1) each can increase the crystallization range by no more than 4–6 K. The total contribution of the Fe and Si impurities to the crystallization range ΔT of our alloy does not exceed 8–10 K. Therefore, the allowance made for the Fe and Si impurities cannot change the situation radically. At the same time, owing to the small equilibrium distribution coefficients of sulfur ($k \le 0.01$) and phosphorus ($k < 0.02$) impurities, their concentrations in the melt ahead of the crystallization front increase by approximately two orders of magnitude, which can result in the loss of stability of the planar front. Actually, the values of m for sulfur and phosphorus are approximately equal to 20 and 30 K/%, respectively [9]. Hence, it follows that, according to criterion (1), the crystallization ranges ΔT increase by ~20 and 15 K, respectively. Therefore, the presence of even small amounts of sulfur and phosphorus in the congruently melting binary alloy (Ni–35 wt % W) can lead to an appreciable decrease in the critical velocity. In this case, the critical velocity can be substantially less than

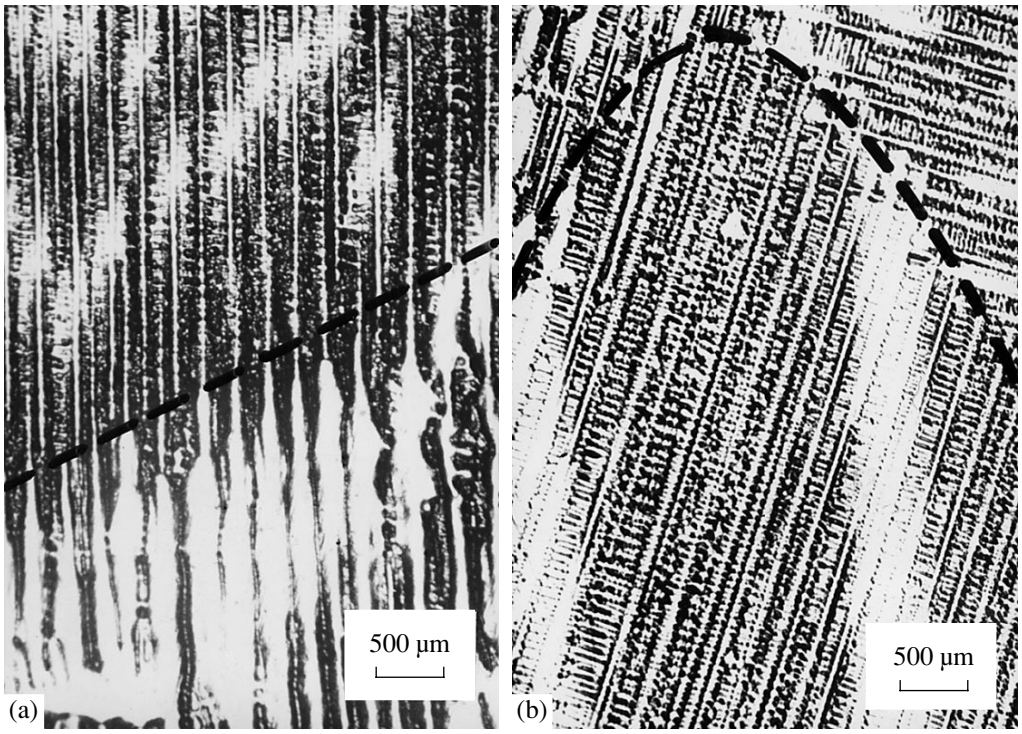

Fig. 2. Longitudinal metallographic sections of the quenched regions of the NV-4 alloy single crystals. R = (a) 1.2 and (b) 4 mm/min. The dashed line represents the envelope of the crystallization front.

0.4 mm/min. The exact value of the critical velocity is determined by three factors: (i) the actual content of these (rather volatile) impurities in the melt, (ii) the Fe and Si contents, and (iii) the deviation of the W content from 35 wt %.

The disagreement between our data and the results obtained in [6, 7] can be associated, to some extent, with the difference in the techniques used for directional crystallization. In particular, Barabash and Voĭnash [6, 7] used crucibleless electron-beam recrystallization, whereas, in our case, the crystals were grown by the Bridgman method in crucibles. In order to verify this assumption, we performed experiments on directional electron-beam recrystallization of the NV-4 alloy at front velocities of 9 and 15 mm/min. Note that, in our experiments, the use of the special narrow-slit electron-beam gun made it possible to obtain the narrower melted zone (5 mm instead of 10 mm in [6, 7]) and, hence, the higher temperature gradient. Microstructural investigations of the samples confirmed the existence of the planar front at high velocities of the crystallization front. The crystallization fronts fixed by quenching were examined on the longitudinal metallographic sections. The microstructures of these single-crystal regions are shown in Fig. 2. In the micrographs of the longitudinal metallographic sections, it is possible to measure the depth H of intercellular hollows as a function of the velocity of the front of directional crystallization (Table 2). As the velocity of the crystallization front increases from 0.4 to 4 mm/min, the value of H increases from 0.3 to 2.8 mm. In this case, the amplitude of cellular asperities H/λ also monotonically increases from 1.2 to 12.4.

When analyzing the structural perfection of the single crystals industrially grown in a UVNK-8P apparatus at PJSC Motor-Sich and the single crystals grown in the apparatus at a high temperature gradient at the Kharkov Institute of Physics and Technology (National Scientific Center), it should be remembered that, in these cases, the crystallization conditions (G, R) differed significantly. As can be seen from the micrographs given in the figures, this difference leads to the formation of different microstructures: a dendritic structure in the UVNK-8P apparatus (Fig. 1d) and a more perfect cellular structure in the apparatus at a high temperature gradient at the Kharkov Institute of Physics and Technology (Figs. 1b, 1c).

The macroscopic shape of the crystallization front depends on the ratio G_Z/G_R between the axial and radial components of the temperature gradient. The longitudinal metallographic sections of the quenched regions of the single crystals clearly illustrate the variations in the shape of the envelope of the crystallization front with an increase in R. The envelope is nearly planar at low velocities R = 0.4 and 1.2 mm/min, convex at moderate velocities R = 2.6 and 4.0 mm/min, and planar and concave at high velocities R = 10 and 20 mm/min, respectively. The convexity of the crystallization front eliminates the formation of opposing fronts and decreases the probability of generating structural defects. This

shape of the crystallization front at moderate velocities R = 2.6 and 4.0 mm/min corresponds to the most perfect structure of the single crystals. This is confirmed by the results of the metallographic (Figs. 1, 2) and X-ray diffraction investigations. Moreover, it was revealed that the velocity of the crystallization front has an insignificant effect on the hardness characteristics (Table 2).

During the growth of NV-4 alloy single-crystal rods, we observed several types of defects of the single-crystal structure.

The first-order subboundaries in nickel alloys are intergrowth boundaries [2] formed in the case of a concave crystallization front. The misorientation angles between subgrains can be as large as ~10° [2]. A similar situation is observed when the crystallization front bends around solid obstacles in the melt, such as oxide films, small-sized ceramic inclusions, etc. According to our data, these inclusions can change the crystallographic orientation of crystals by an angle of the order of 5°.

The mosaic structure of the single crystals grown is one of the most widespread defects. The mosaicity in the single crystals studied manifests itself in the formation of one or, rarely, two block boundaries. In our opinion, this defect is formed when the crystallization front is concave or even broken in shape, which, in particular, is observed in the form of opposing crystallization directions in the metallographic sections. The formation of the block boundary due to the effect of opposing directions is observed even more frequently than the formation of subgrain boundaries. The block boundary is identified by the X-ray diffraction analysis. The presence of the block boundary results in the splitting (or other distortions) of the rocking curve in the angle range up to 2°.

The misorientation of structural cells, as a rule, arises when the crystallographic orientation of single crystals varies through small angles. In the cross section of the single crystals, the structural inhomogeneity manifests itself as rotations of cells in arbitrary directions and a change in the size of cells and their shape. The origin of the observed imperfections can be associated with an irregular shape of the crystallization front. These irregularities can be caused by convective flows and mechanical vibrations of the apparatus during growth of single crystals. The resultant disturbances do not necessarily lead to distortions of the single-crystal structure.

In conclusion, it should be noted that more than 10 000 seeds were produced from the NV-4 alloy according to the developed technology of directional crystallization at a high temperature gradient. Examinations revealed that seeds satisfy the aforementioned requirements to their structure. The use of these seeds under industrial conditions demonstrated that the yield of good blades with respect to the crystallographic orientation increases by a factor of 1.7–2.

REFERENCES

1. A. I. Somov and M. A. Tikhonovskiĭ, *Eutectic Compositions* (Metallurgiya, Moscow, 1975).
2. A. A. Chernov, E. I. Givargizov, Kh. S. Bagdasarov, *et al.*, in *Modern Crystallography*, Vol. 3: *Crystal Growth*, Ed. by B. K. Vaĭnshtein, A. A. Chernov, and L. A. Shuvalov (Nauka, Moscow, 1980; Springer, Berlin, 1984).
3. R. E. Shalin, I. L. Svetlov, E. B. Kachanov, *et al.*, *Single Crystals of Nickel-Based High-Temperature Alloys* (Mashinostroenie, Moscow, 1997).
4. V. E. Semenenko and G. P. Kovtun, Funct. Mater. **5** (2), 226 (1998).
5. B. E. Paton, G. B. Stroganov, S. T. Kishkin, *et al.*, in *High-Temperature Strength of Casting Nickel Alloys and Their Protection from Oxidation*, Ed. by B. E. Paton (Naukova Dumka, Kiev, 1987).
6. O. M. Barabash and V. Z. Voĭnash, Metallofiz. Noveĭshie Tekhnol. **22** (2), 94 (2000).
7. O. M. Barabash and V. Z. Voĭnash, Metallofiz. Noveĭshie Tekhnol. **22** (3), 100 (2000).
8. M. Flemings, *Solidification Processing* (McGraw-Hill, New York, 1974; Mir, Moscow, 1977).
9. M. Hansen and K. Anderko, *Constitution of Binary Alloys*, 2nd ed. (McGraw-Hill, New York, 1958; Metallurgizdat, Moscow, 1962), Vol. 2.
10. O. M. Barabash and Yu. N. Koval', in *A Handbook on the Structure and Properties of Metals and Alloys* (Naukova Dumka, Kiev, 1986).

Translated by O. Borovik-Romanova

Crystallography Reports, Vol. 49, No. 2, 2004, pp. 312–317. Translated from Kristallografiya, Vol. 49, No. 2, 2004, pp. 369–375.

CRYSTAL GROWTH

Investigation of the Possibility of Obtaining Homogeneous $Ga_{1-x}In_xSb$ Crystals under Weak Flow Conditions[1]

S. V. Bykova*, V. D. Golyshev*, M. A. Gonik*, V. B. Tsvetovsky*, T. Duffar, M. P. Marchenko***, and I. V. Frjazinov*****

** Center for Thermophysical Researches Thermo, Institutskaya ul. 1, Aleksandrov, 601650 Russia*
e-mail: thermo.ltd@relcom.ru
*** EPM-MADYLAM, ENSHMG, BP-95, 38402 St. Martin d'Héres, Grenoble, France*
**** Institute of Mathematical Modeling, Russian Academy of Sciences, Miusskaya pl. 4, Moscow, 125047 Russia*
Received February 26, 2003

Abstract—The possibility of growing macrohomogeneous $Ga_{1-x}In_xSb$ crystals with $x = 0.2$ was studied using the axial heating process close to the melt/crystal interface. The grown ingots were analyzed by a JSM-5300 scanning electron microscope and the experimental results were compared with the results of numerical simulation. It was shown that, as a whole, the mathematical model adequately describes the processes of the steady-state heat and mass transfer. It was found that, at the crystallization of $Ga_{1-x}In_xSb$ by the axial heating process under conditions of weak laminar flows, longitudinal homogeneity is observed when a dead zone is formed in the melt and that the crystallization regime is similar to diffusion. It was shown that the composition of the grown crystals strongly depends on the structure of a melt flow and its dynamics. © *2004 MAIK "Nauka/Interperiodica".*

INTRODUCTION

The concentrated $Ga_{1-x}In_xSb$ mixture is an ideal solution in both the solid and liquid states. Changing the ratio of the components in the pseudobinary GaSb/InSb compound, one can obtain materials with specified properties, in particular required band gap width and lattice parameters, for optoelectronic devices. Since stringent requirements are imposed on the macro- and microhomogeneity of optoelectronic materials, this problem has been widely studied.

In solving the problem of obtaining macrohomogeneous $Ga_{1-x}In_xSb$ single crystals, main efforts of researchers were aimed at enhancing the flow in the liquid phase in order to stir the melt near the crystallization front and supply the material during growth. In particular, interesting data on the growth of homogeneous ternary single crystals were obtained for $Ga_{1-x}In_xSb$ with $x \le 0.05$ grown by the Czochralski method, applying strong mixing to the liquid by counter rotation of the melt and seed [1, 2]. The Czochralski method, with a floating crucible, was used to obtain $Ga_{0.98}In_{0.02}Sb$ crystals with a constant concentration of In along the crystal axis due to the supply through a floating crucible [3]. Homogeneous $Ga_{1-x}In_xSb$ with $0 < x < 0.1$ crystals were grown in [4] using a rotating heater submerged in the melt. Due to the melt stirring, the composition gradient in the grown ingot was smoothed and, thus, no cracks appeared during the growth. It was shown in [5] that intensifying the melt stirring (using matched vibrational stirring) improves the chemical homogeneity of crystals grown by the Bridgman method. At the same time, enhancing the flow creates convective nonstationarity and the appearance of turbulent pulsations, which, in turn, leads to the formation of macro- and microinhomogeneities in a material. The growth at weak laminar flows has no such drawbacks; however, the effect of the parameters of a laminar flow on the macro- and microhomogeneity of the composition of grown ingots has not been adequately studied. In particular, $Ga_{1-x}In_xSb$ crystals with highly homogeneous radial composition were grown using the method of freezing in a vertical gradient for $x = 0.05$ [6] and by the Bridgman method for $x = 0.01$ and 0.04 [7]. In these studies, a weak flow was obtained by using a crucible with a small diameter (10 mm). Along with the investigation of the effect of thermal regimes on the character of radial and longitudinal inhomogeneities, a numerical analysis of the processes of heat and mass transfer was performed in [7]. It was shown in [7] that, in a weakly convective crystallization regime (velocity of the melt flow $v = 10^{-4}$ m/s), the composition of $Ga_{1-x}In_xSb$ crystals is more homogeneous than in the case of flows close to diffusion ($v = 10^{-5}$ m/s). However, it was found in [8] on the basis of numerical simulation that the growth of $Ga_{0.8}In_{0.2}Sb$ single crystals under conditions of axial heating process (AHP) close to the solid-liquid interface leads to a homogeneous composition of ingots in the range of flow velocities $v = 10^{-6}$–10^{-4} m/s. This contradiction between the data of [7, 8] indicates that the interference of different processes at crystallization of

[1] This work was presented at the National Conference on Crystal Growth (NCCG-2002, Moscow).

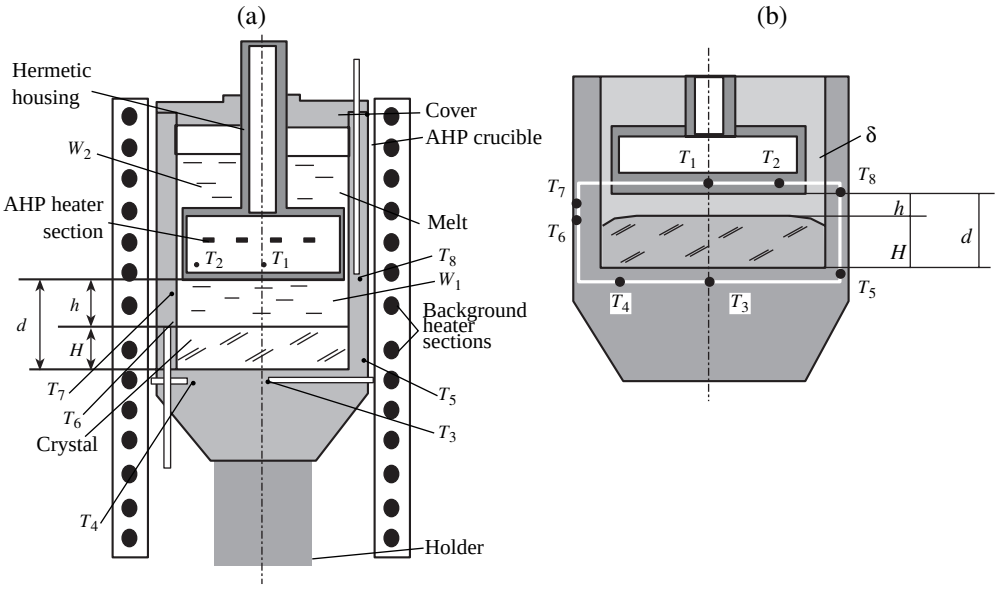

Fig. 1. (a) Schematic diagram of the AHP crystallizer and (b) simulated region of the crystal–melt system.

$Ga_{1-x}In_xSb$ should be analyzed more carefully. The quality of $Ga_{1-x}In_xSb$ crystals is determined by the complex interaction of many physical processes: segregation, interphase kinetics, heat and mass transfer, concentration supercooling, and others. Since this analysis is extremely complex, it has not been performed in full measure until now. One of the reasons for this is that conventional growth methods do not provide the necessary accuracy of setting boundary conditions.

In contrast to conventional methods, the AHP method [9] makes it possible to set exactly the boundary conditions with respect to temperature and composition during the growth. Since an submerged heater is used, the natural convection near the crystallization front in the AHP method is suppressed to 10^{-5} of its value for the Bridgman growth, with the crucible diameter being the same. The melt flow is laminar, and its velocity does not exceed a few tenths of a millimeter per second [10]. This circumstance, in turn, makes it possible to use the AHP method to study the interaction between the processes of segregation and heat and mass transfer at weak flows.

In this paper, we report the results of numerical simulation and experimental study of the regularities of mass transfer and interface formation, depending on the thermal conditions of the crystallization of $Ga_{1-x}In_xSb$, as well as the determination of conditions allow obtaining uniform ingots with the AHP method.

EXPERIMENTAL TECHNIQUE AND THE FEATURES OF THE NUMERICAL MODEL

The schematic diagram of the AHP method is shown in Fig. 1a. An AHP heater is submerged into a melt and installed at a small distance h from the interface, which provides a controlled axial thermal flux near the crystallization front, the shape of which can now be controlled. The AHP heater divides the melt into two zones (W_1 and W_2) connected via a narrow gap δ. When a crucible moves with respect to the AHP heater, the melt flows from zone W_2 above the heater to zone W_1 under the heater. In order to obtain a homogeneous over height crystallized ingot, $Ga_{0.3}In_{0.7}Sb$ and $Ga_{0.8}In_{0.2}Sb$ melts were placed in zones W_1 and W_2, respectively. According to the phase diagram [11], crystallization of a $Ga_{0.3}In_{0.7}Sb$ melt gives rise to the solid phase $Ga_{0.8}In_{0.2}Sb$. In order to fill the shortage of Ga, the composition $Ga_{0.8}In_{0.2}Sb$ is fed from zone W_2 to zone W_1. Thus, zone W_2 plays the role of a feeder.

Two experiments were carried out. $Ga_{1-x}In_xSb$ was crystallized in a graphite crucible with an inner diameter of 46 mm in Ar atmosphere. Thermocouples tungsten/rhenium (VR5/20) were installed in the walls of the graphite crucible and in the housing of the AHP heater at the points $T_1 - T_8$ (Fig. 1). Crystallization was performed so as the temperature drop ΔT at the melt layer h in zone W_1 was equal to the temperature drop between the solidus and liquidus lines for the target composition $Ga_{0.8}In_{0.2}Sb$ (ΔT = 70 K). In this case, the temperature at the point T_1 was maintained constant and equal to the liquidus temperature of T = 685°C during crystallization. The temperature in zone W_2 was somewhat higher than the liquidus temperature for the $Ga_{0.8}In_{0.2}Sb$ composition (T > 685°C).

Crystallization was performed without a seed and began with a spontaneous nucleation at the crucible bottom as a result of lowering a crucible into the cold zone of the furnace at a specified rate. During the

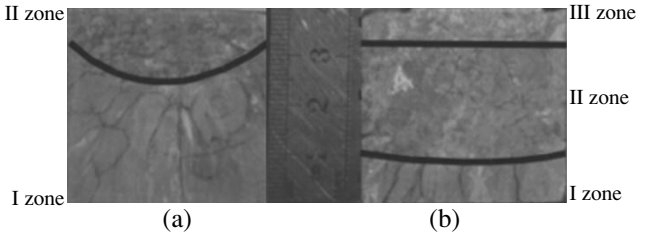

Fig. 2. Longitudinal cut of $Ga_{1-x}In_xSb$ ingots after etching: experiments (a) I and (b) II.

growth, the temperature of the crucible bottom was decreased so as to maintain the thickness of the molten layer h = const using a computer control system [12].

In order to check the effect of thermal conditions on the crystallization of $Ga_{1-x}In_xSb$ under weak-flow conditions, growth regimes were different in the experiments. In the first experiment, a positive radial temperature gradient was formed at the AHP heater ($T_1 < T_2$). The pulling rate and the radial temperature gradient were not changed during the crystallization. At the end of the experiment, in order to reveal the shape of the crystallization front, the pulling of the crucible was stopped and the melt was cooled rapidly. Then, after heating and melting of the ingot part that had been rapidly crystallized, the pulling of the crucible continued at the same rate. In the second experiment, a negative radial temperature gradient was formed at the AHP heater ($T_1 > T_2$), which was increased during the growth. The pulling rate was varied during the crystallization.

The crystallized ingots were cut in the longitudinal direction. In order to reveal the crystallization front and the crystal structure, samples were treated in a solvent of the following composition: CrO_3 (34.2 g) : 40% HF (5 ml) : H_2O (250 ml). The grown ingots were analyzed using a JSM-5300 scanning electron microscope equipped with a Link ISIS analytical unit.

The interference of complex processes occurring during the crystallization of $Ga_{1-x}In_xSb$ was analyzed by mathematical simulation of the processes of heat and mass transfer and formation of the composition of a grown crystal. The simulation assumed that the upper zone W_2 does not affect the heat and mass transfer in zone W_1 under the AHP heater and serves only as a container. The processes of heat and mass transfer were simulated using a Karma software package modified for the processes occurring during the AHP crystallization [13]. The axisymmetric problem was solved with regard to the moving interface. The model takes into account the concentration convection, interdiffusion, and a change in the melting temperature with changing the composition. Taking into account the geometric dimensions of the calculated region; the properties of the grown crystal, melt, and crucible material; and the boundary conditions of the first kind, the model used makes it possible to calculate the temperature fields in the growth volume, the position and shape of the crystallization front, the melt flows, and the composition distributions in the melt and crystal. The temperature values recorded in the experiment by the computer control system were used as the boundary conditions. The simulated region is shown in Fig. 1b. For more details, see [8].

RESULTS AND DISCUSSION

Figure 2 shows the longitudinal cuts of $Ga_{1-x}In_xSb$ ingots. In the first experiment (Fig. 2a), one mark is observed in the cut, which divides a crystal into two zones (the thick concave line). This mark corresponds to the point at which the pulling was stopped and the melt was rapidly crystallized with further melting and pulling. In the region preceding the mark (zone I), visible single-crystal grains oriented perpendicular to the crystallization front can be distinctly seen. Zone II contains small, differently oriented grains.

In the second experiment (Fig. 2b), two marks are observed in the cut. The first mark is at the height H_1 = 8 mm, and the second is at H_2 = 32 mm. The first mark corresponds to the passage from the value of the pulling rate V = 0.5 to 1 mm/h, and the second mark corresponds to the emergence of the AHP heater from the melt. These marks divide the ingot into three zones. Zone I contains single-crystal grains oriented along the vertical axis. Then, the structure of the ingot changes. In zone II, grains decrease in size and become randomly oriented, and, in zone III, the ingot structure is even more fine-grained.

Figures 3 and 4 show the experimental data on the longitudinal and transverse distribution of indium that were obtained using the techniques mentioned in the previous section. It can be seen that, in both cases, from the very start of the crystallization process, the composition of the grown crystals somewhat differs from the target composition $Ga_{0.8}In_{0.2}Sb$. The reasons for this are the specific features of the crystallization of $Ga_{1-x}In_xSb$ and the conditions of the aforementioned experiments. We intended to carry out an experiment for a melt layer with h = 15 mm and the temperature drop at the layer ΔT = 70 K (the difference between the liquidus and solidus temperatures for the composition $Ga_{0.8}In_{0.2}Sb$). The volume of the initial load in zone W_1 with the composition $Ga_{0.3}In_{0.7}Sb$ was calculated for the initial distance d_0 = 15 mm between the bottom of the AHP heater and the crucible bottom. However, we failed to obtain the value of ΔT = 70 K at a distance of 15 mm due to the insufficient temperature gradient in the furnace. To obtain this drop, we had to increase the initial values of d_0 to 16.2 and 18.3 mm in the first and second experiments, respectively. As a result, the $Ga_{0.8}In_{0.2}Sb$ melt moved from zone W_2 to zone W_1 and the composition of the melt in zone W_1 became enriched with Ga. The initial compositions of the melt in zone W_1 became $Ga_{0.37}In_{0.63}Sb$ and $Ga_{0.39}In_{0.61}Sb$ in

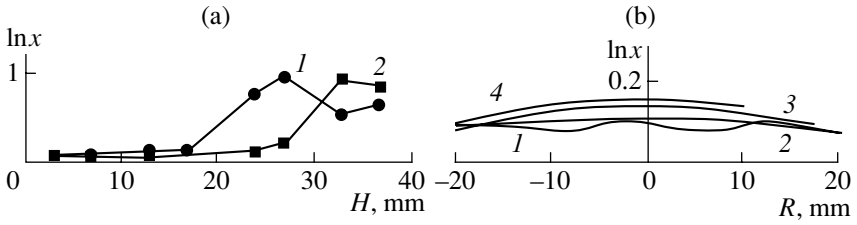

Fig. 3. Experimental distributions of In in $Ga_{1-x}In_xSb$ in experiment I: (a) longitudinal (R = (*1*) 0 and (*2*) 20 mm) and (b) transverse (H = (*1*) 3, (*2*) 7, (*3*) 13, and (*4*) 17 mm).

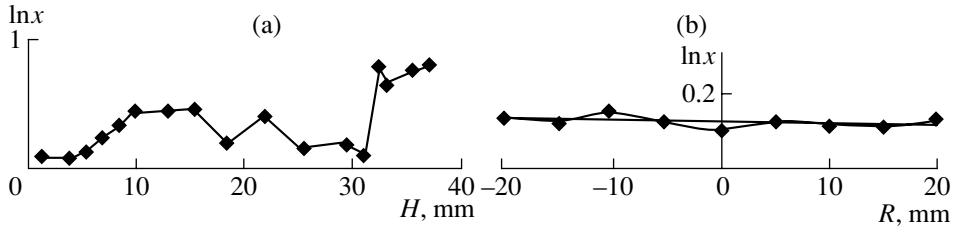

Fig. 4. Experimental distributions of In in $Ga_{1-x}In_xSb$ in experiment II: (a) longitudinal (R = 0 mm) and (b) transverse (H = 3 mm from the crucible bottom).

the first and second experiments, respectively. At the same time, the blend composition in zone W_2 remained the same: $Ga_{0.8}In_{0.2}Sb$. Investigation of the composition of crystallized ingots revealed the following: In the first experiment, the In concentration along the axis and lateral surface weakly increased within 4–6% up to the moment when the temperature conditions changed (H = 25 and 30 mm at the axis and lateral surface, respectively) (Fig. 3a). This increase in the In concentration in the longitudinal direction meets theoretical expectations and is explained below. At the initial moment of crystallization, due to the increase in the height of the melt layer, the composition in zone W_1 became enriched with Ga, while the composition in zone W_2 remained the same. When the crystallization front is concave, the composition at the lateral surface remains constant for a longer time (Fig. 3a). In the longitudinal distribution at the axis, a step increase in the In concentration is observed after 20 mm, which is caused by the change in the crystallization conditions and the introduction of a mark. It can be seen from Fig. 3b that the radial inhomogeneity in the region preceding the mark is small in the first experiment.

The second experiment was performed under nonstationary conditions. It can be seen from Figs. 4a and 4b that, in the initial region, in the range of ingot heights of H = 0–5.5 mm, where the crystallization conditions changed only insignificantly, the ingot was fairly homogeneous both in the axial and transverse directions. A change in the growth rate leads to a strong increase in the In concentration in the range H = 5.5–10.5 mm. Then, the concentration remains constant at H = 10.5–15.5 mm up to the point where the pulling was stopped. Furthermore, in crystallization by the gradient-freezing method, the concentration changes significantly.

Figure 5a shows the results of numerical simulation of the longitudinal distribution of Ga in comparison with the experimental data (experiment I). It can be seen that, while the crystallization conditions are constant, the results of the numerical simulation of the longitudinal distribution of Ga are agree closely with the experimental data. Then, the numerical simulation also indicates a decrease in Ga concentration after rapid crystallization and melting. However, this decrease is significantly smaller than in the experiment, and, in addition, there is no irregularity in the impurity distribution. We attribute these differences to an error in set-

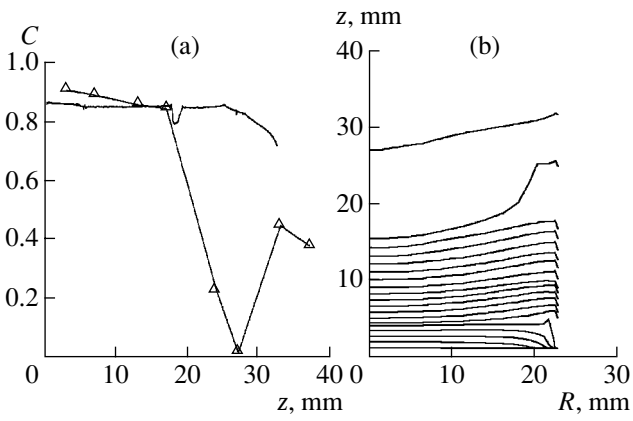

Fig. 5. (a) Calculated (solid line) and experimental (triangles) distributions of Ga in a crystal grown in experiment I (z and R are the height and radius of the crystal, respectively; R = 0). (b) Calculated position and shape of the crystallization front in experiment II.

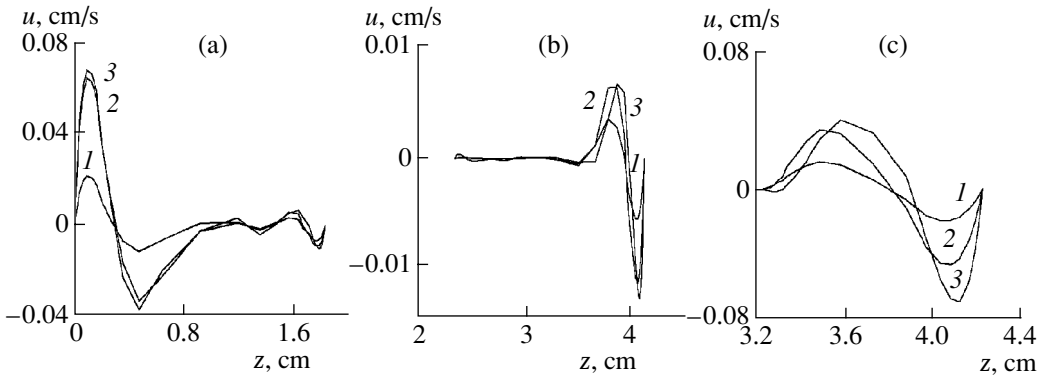

Fig. 6. The change in the flow structure in experiment I (r = (*1*) 0, (*2*) $R/2$, and (*3*) R mm; u is the longitudinal component of the flow velocity; z is the current coordinate in the axial direction): (a) before crystallization; (b) after the pulling was switched on; and (c) after rapid cooling with subsequent melting and pulling.

ting the initial conditions with respect to concentration after rapid crystallization.

The numerical simulation for nonstationary crystallization conditions (experiment II) describes the heat transfer fairly well. According to the numerical calculations, the position and shape of the crystallization front during the growth are, as a whole, in agreement with the data obtained by etching of the longitudinal cut of a $Ga_{1-x}In_xSb$ ingot (Fig. 5b). The results of numerical calculations of the composition distribution agree with the experimental data only up to the point at which the pulling was stopped for a short time and then changed.

The calculations (experiment I) showed that, before the onset of crystallization, the structure of the flow is characterized by the presence of two vortices with a maximum velocity of 10^{-4} m/s (Fig. 6). When the crystallization begins, the vortex near the crystallization front vanishes and a wide (10–15 mm) dead zone arises. The velocities of the flow in this zone are about 10^{-6} m/s. The vortex near the AHP heater does not vanish, and the maximum velocity of the flow in this region is about 7×10^{-5} m/s. This flow structure remains until rapid cooling begins.

In zone II of the ingot grown in the first experiment (Fig. 2a), the In concentration abruptly increases (Fig. 3a) and then changes irregularly. This zone is characterized by a large microinhomogeneity. The calculations show that the flow structure in this region differs from that in others. One well-developed vortex with a maximum flow velocity of about 4×10^{-4} m/s is present.

In experiment II, the flow structure also changes during the growth (Fig. 7). Before the crystallization, the flow is characterized by the presence of two vortices with a maximum velocity of 4×10^{-4} m/s. By the time crystallization begins, the vortex near the crystallization front disappears and a small dead zone (2.5 mm) with a flow velocity of about 10^{-5} m/s and a well-developed vortex with a flow velocity of 4×10^{-4} m/s arise. The presence of a dead zone, as in the first experiment, leads to longitudinal homogeneity (with concentration changes within 2%).

Furthermore, with a simultaneous increase in the growth rate and the value of negative radial temperature gradient, the flow structure changes. One well-developed vortex with a flow velocity of 5×10^{-4} m/s appears. As a result, the composition along the axis changes: the In concentration increases significantly. The front shape becomes concave. Then, after some time, the flow structure changes again: a wide (15 mm) dead zone arises and a weak vortex with a maximum flow velocity of 4×10^{-5} m/s is observed near the AHP heater. Once again, due to the presence of a dead zone in the melt, the composition is constant in the longitudinal direction (Fig. 4a, the interval from 10.5 to 15.5 mm).

A further increase in the radial gradient to −3 deg/cm and the cessation of pulling lead to a strongly concave crystallization front and a strong change in the flow structure, which is now characterized by the presence of one vortex with a flow velocity of 10^{-3} m/s. This flow structure is retained up to the end of crystallization and the flow velocity doubles. This zone is characterized by strong macro- and microinhomogeneities.

Thus, we can conclude the following: The proposed model, as a whole, adequately describes the formation of the composition of a growing ingot, and, therefore, the flows in a melt under stationary conditions. In the case of nonstationary conditions, the accuracy of the mass-transfer description drastically decreases, and the results of simulation of the mass transfer in terms of this model contradict the experiment. However, the accuracy of the model remains sufficiently high with respect to heat-transfer processes. The appearance of a dead zone in a melt near the crystallization front, in which the concentration changes linearly due to the diffusion transfer, leads to uniform longitudinal distribution of concentration and a fairly high grown-ingot

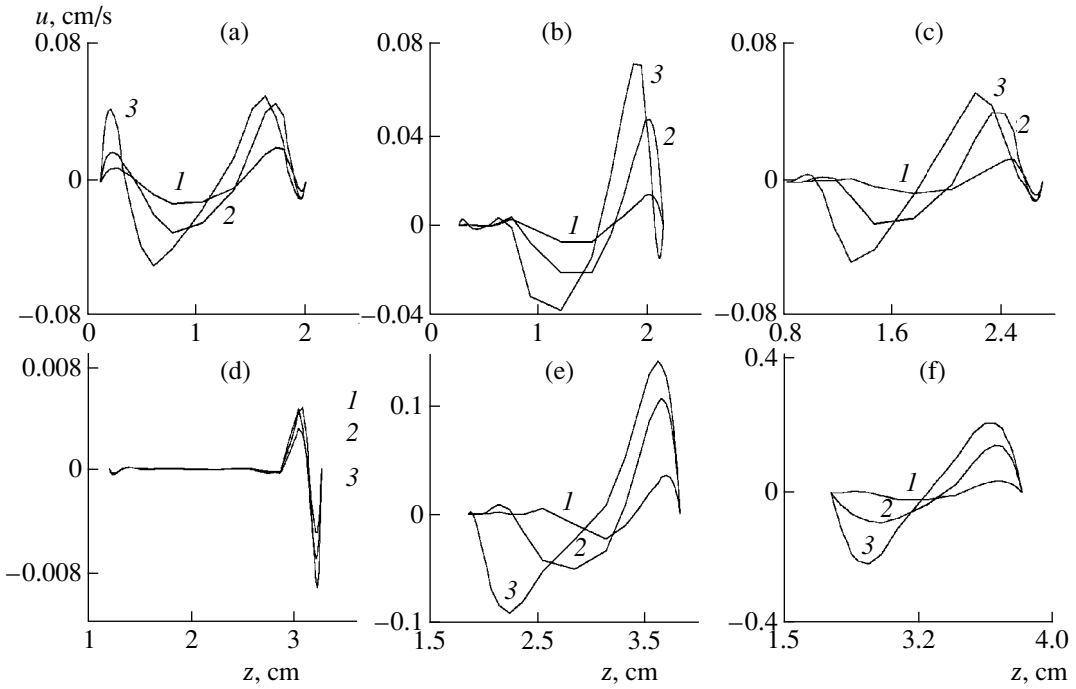

Fig. 7. The change in the flow structure in experiment II (r = (*1*) 0, (*2*) $R/2$, and (*3*) R mm; u is the longitudinal component of the flow velocity; z is the current coordinate in the axial direction): (a) before the crystallization; (b) after the pulling was switched on; (c) after changing the pulling rate; (d) in the interval z = 10–15 mm with constant concentration; (e) in the interval z = 15–20 mm with changing concentration; and (f) in the final stage of crystallization.

radial homogeneity. This conclusion differs from the findings of [7], where it was noted that composition homogeneity increases in going from the diffusion to the convective mode. We attribute this difference to the fact that, in contrast to [7], the crystallization in this study was performed at much lower rates: 0.5–1 mm/h.

CONCLUSIONS

Our investigations confirmed a previous theoretical suggestion [8] that the AHP method makes it possible to obtain macrohomogeneous single crystals of concentrated mixtures. In the crystallization of $Ga_{1-x}In_xSb$ under conditions of weak laminar flows by the AHP method, longitudinal homogeneity is observed when a dead zone is formed in the melt and the crystallization regime is similar to diffusion. It is found that the composition of the crystals obtained strongly depends on the flow structure, a change in which leads to significant crystal-composition inhomogeneity.

ACKNOWLEDGMENTS

This study was supported by the International Association for the Promotion of Cooperation with Scientists from the Newly Independent States of the Former Soviet Union, grant no. 99-01814.

REFERENCES

1. W. A. Bonner, B. J. Skromme, E. Berry, *et al.*, Inst. Phys. Conf. Ser., No. 96, 337 (1989).
2. W. A. Bonner, R. E. Nahory, H. I. Gilchrist, and E. Berry, in *Semi-Insulating III–V Materials* (Shiva, Orpington, UK, 1990), p. 199.
3. G. N. Kozhemyakin, J. Cryst. Growth **220**, 39 (2000).
4. P. S. Dutta and A. G. Ostrogorsky, J. Cryst. Growth **194**, 1 (1998).
5. Y. C. Lu, J. J. Shran, R. S. Feigelson, and R. K. Route, J. Cryst. Growth **102**, 807 (1990).
6. P. Garandet, T. Duffar, and J. J. Favier, J. Cryst. Growth **106**, 426 (1990).
7. C. Stelian, T. Duffar, J. L. Santailler, and I. Nicoara, J. Cryst. Growth (in press).
8. M. Marchenko, J. Frjazinov, S. Bykova, *et al.*, in *Proceedings of 4th International Conference on Single Crystal Growth and Heat and Mass Transfer* (Obninsk, 2001), Vol. 3, p. 706.
9. V. D. Golyshev and M. A. Gonik, RF Patent No. 1800854 (1990).
10. M. P. Marchenko, I. V. Fryazinov, V. D. Golyshev, *et al.*, J. Cryst. Growth **237–239**, 1886 (2002).
11. I. Anzara, M. Gambino, and J. P. Bros, J. Cryst. Growth **32**, 101 (1976).
12. V. D. Golyshev, M. A. Gonik, and V. B. Tsvetovskiĭ, Poverkhnost, No. 5, 49 (2002).
13. M. P. Marchenko and I. V. Fryazinov, Zh. Vychisl. Mat. Mat. Fiz. **37** (8), 988 (1997).

Translated by Yu. Sin'kov

Crystallography Reports, Vol. 49, No. 2, 2004, pp. 318–323. Translated from Kristallografiya, Vol. 49, No. 2, 2004, pp. 376–381.

CRYSTAL GROWTH

Effect of Ultrasound on the Growth of Semiconductor Single Crystals[1]

G. N. Kozhemyakin

East Ukrainian National University, Molodezhnyĭ bul'v. 20a, Lugansk, 91034 Ukraine

e-mail: gkozh@snu.edu.ua

Received February 26, 2003

Abstract—The influence of ultrasound on striations in InSb, GaAs, and Bi–Sb single crystals grown by the modified Czochralski method was studied. Ultrasonic waves with a frequency ranging from 0.15 to 10 MHz were introduced into a melt parallel to the pulling direction. It was found that striations in single crystals pulled in the ultrasonic field are significantly reduced. GaAs layers were grown by modified liquid-phase epitaxy under the action of 3-MHz ultrasound. The effect of ultrasound on morphological changes during epitaxial growth was studied by *in situ* observation technique based on near-infrared microscopy. It was found that ultrasonic waves affect the growth of macroscopic steps. The effect of 1-MHz ultrasound on the convective flow and formation of standing waves in distilled water under different conditions (with the temperature gradient, disc-rotation speed, and fluid depth being varied) was studied using the light-cut technique. © *2004 MAIK "Nauka/Interperiodica".*

INTRODUCTION

It is well known that external fields strongly affect the mass transfer occurring in melts during the growth of semiconductor single crystals and help to make the distribution of components in such melts more uniform. A promising method allowing reduction of lamination is the use of magnetic or electromagnetic fields [1–3]. Studies of crystallization processes in water and some insulators show that crystallization is accompanied by a simultaneous generation of broadband (from 10 Hz to several MHz) electromagnetic and acoustic radiation [4]. This clearly demonstrates that electromagnetic and acoustic processes are intimately correlated in a crystallizing medium; thus, the use of ultrasound looks rather promising for growing semiconductor single crystals.

Hayakawa *et al.* studied the effect of 10-kHz ultrasound on the uniformity of component distribution in the growth of InSb and $In_xGa_{1-x}Sb$ single crystals by the Czochralski method in detail [5–7]. It was found that ultrasonic waves with a power up to 30 W eliminate the "face effect" in InSb crystals pulled along the ⟨111⟩ direction. However, striations do not disappear completely in these crystals even under the action of ultrasound with a power up to 120 W.

Experimental studies on the effect of ultrasound with a frequency up to 10 MHz on growth-induced striations in semiconductor single crystals have been performed in our laboratory over the last 20 years [8–11]. However, the mechanism of the effect of ultrasound on striations was not identified in these experiments.

In this paper, we report the results of studying the growth of semiconductor single crystals by the Czochralski method and semiconductor layers by liquid-phase epitaxy, as well as modeling the effect of ultrasound on convection in liquids.

EXPERIMENTAL

To introduce ultrasonic waves into a melt, we developed a modified Czochralski method allowing transmission of ultrasonic waves within the melt parallel to the pulling direction from the crucible bottom towards the crystal–melt interface [12]. InSb single crystals doped with tellurium up to 10^{-3} at % were pulled in the ⟨111⟩ direction. Single crystals of bismuth–antimony (5 at %) alloy were grown using a single-crystal seed with the (111) plane inclined at an angle of 10° to the pulling direction. Single crystals of these materials up to 10 mm in diameter were grown from melt with a mass of up to 150 g in a high-purity argon atmosphere with an excess pressure of 0.4 atm. The crystal-pulling rate was 0.05 mm/min at a rotation speed up to 10 rpm. The crucible with melt was not rotated. As starting materials, we used In, Bi, Sb, Ga, and As of special purity (99.9999 wt %). Ultrasonic waves with frequencies of 0.15, 0.25, 0.6, 1.2, 2.5, 5, and 10 MHz were introduced into the melt from a piezoelectric transducer via a 300-mm-long quartz waveguide 10 mm in diameter welded to the bottom of the quartz crucible (with a diameter and height of 40 and 30 mm, respectively). GaAs single crystals 50 mm in diameter doped with chromium up to 10^{16} cm^{-3} were grown in the All-Russia

[1] This work was presented at the National Conference on Crystal Growth (NCCG-2002, Moscow).

1063-7745/04/4902-0318$26.00 © 2004 MAIK "Nauka/Interperiodica"

Research Institute of Material for Electronics (Kaluga) by V.G. Kosushkin and S.Yu. Kurochkin. The crystals were pulled from melt (with a mass of 1.5 kg) using B_2O_3 as the flux. The single crystals were pulled at a rate of 0.17 mm/min by means of rotating the crystal and quartz crucible in opposite directions at rates of 5 and 18 rpm, respectively. Ultrasonic waves with a frequency of 150 kHz were introduced through the bottom of the quartz crucible 90 mm in diameter via an adjoined graphite waveguide 30 mm in diameter. The lower part of the waveguide was connected to a piezoelectric transducer. The graphite waveguide was installed in a special system allowing transmission of signals from the ultrasonic generator to the piezoelectric transducer during the waveguide rotation.

The grown crystals were cut parallel to the growth direction. The cut surfaces were ground, polished, and etched in selective etchants to reveal the growth bands, which were observed in an optical microscope and a Nanolab 2100 electron microscope. Each single crystal under study contained regions pulled with and without ultrasound.

The effect of 3-MHz ultrasound on the growth of GaAs layers from Ga melt by modified liquid-phase epitaxy was studied in collaboration with Yu. Inatomi in Japan's Institute of Space and Astronautical Science. The experimental setup included an evacuated quartz ampoule with an inner diameter of 8 mm. A graphite crucible with an inner diameter of 4 mm was placed in the ampoule. The GaAs substrate was attached to the crucible bottom (Fig. 1). One gram of Ga was put into the graphite crucible. A quartz waveguide 3 mm in diameter with a piezoelectric transducer attached to one end had its other end immersed in gallium. The lower part of the ampoule was heated by a ring lamp with a power of up to 1 kW. Epitaxial growth was observed at the interface through the ampoule bottom using an infrared digital camcorder. The characteristic growth images were obtained by computer processing of the video recordings.

Convection in distilled water containing Al and Al_2O_3 particles was studied by the light-cut technique under conditions similar to those of the crystal growth by the Czochralski method. The dimensions of a stainless-steel crucible and the diameter of an aluminum disc imitating the pulled single crystals exceeded the dimensions of the crucible and crystals in the case of the growth of InSb single crystals and Bi–Sb alloys by a factor of five. The images of the convective flows under the effect of ultrasound were recorded with a digital camcorder, with subsequent computer processing of the video recordings.

RESULTS AND DISCUSSION

In InSb single crystals, we observed Te layers parallel to the crystallization front. The interlayer distance was up to 250 μm. The layer width in the vicinity of the

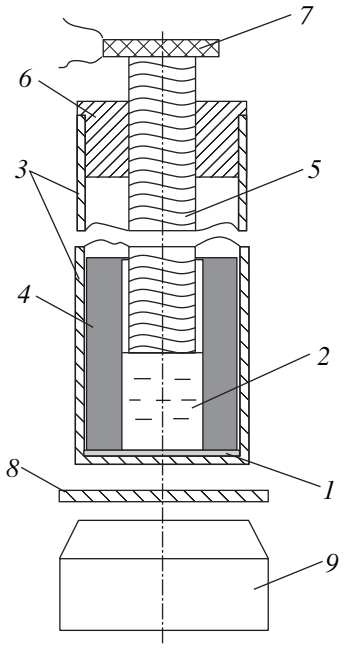

Fig. 1. Schematic of the setup for epitaxial growth: (*1*) GaAs substrate; (*2*) Ga solution; (*3*) quartz ampoule; (*4*) graphite crucible; (*5*) quartz waveguide; (*6*) BN ring; (*7*) piezoelectric transducer; (*8*) quartz glass; and (*9*) infrared digital-camcorder lens.

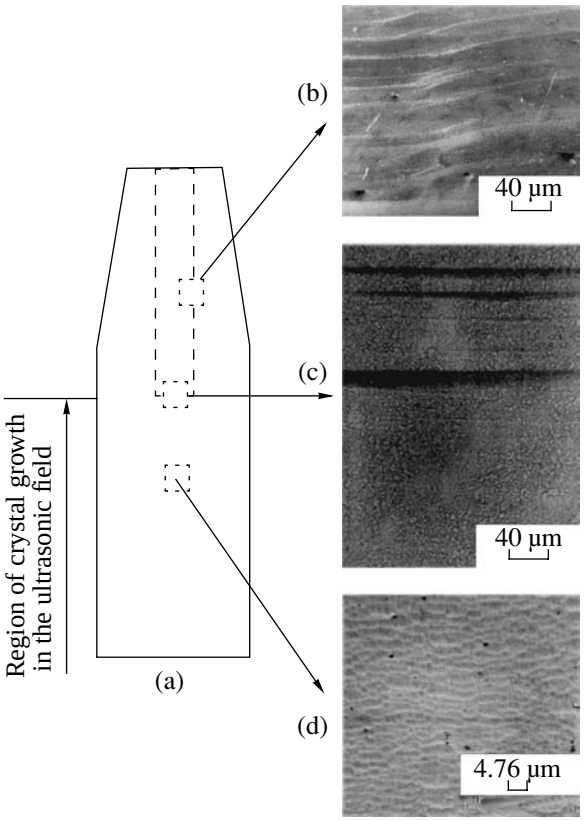

Fig. 2. Growth regions in an InSb single crystal grown with 0.6 MHz ultrasound: (a) pulled single crystal; (b) periphery region of the crystal "face"; (c) region corresponding to the beginning of the ultrasound action; and (d) region of crystal growth with ultrasound.

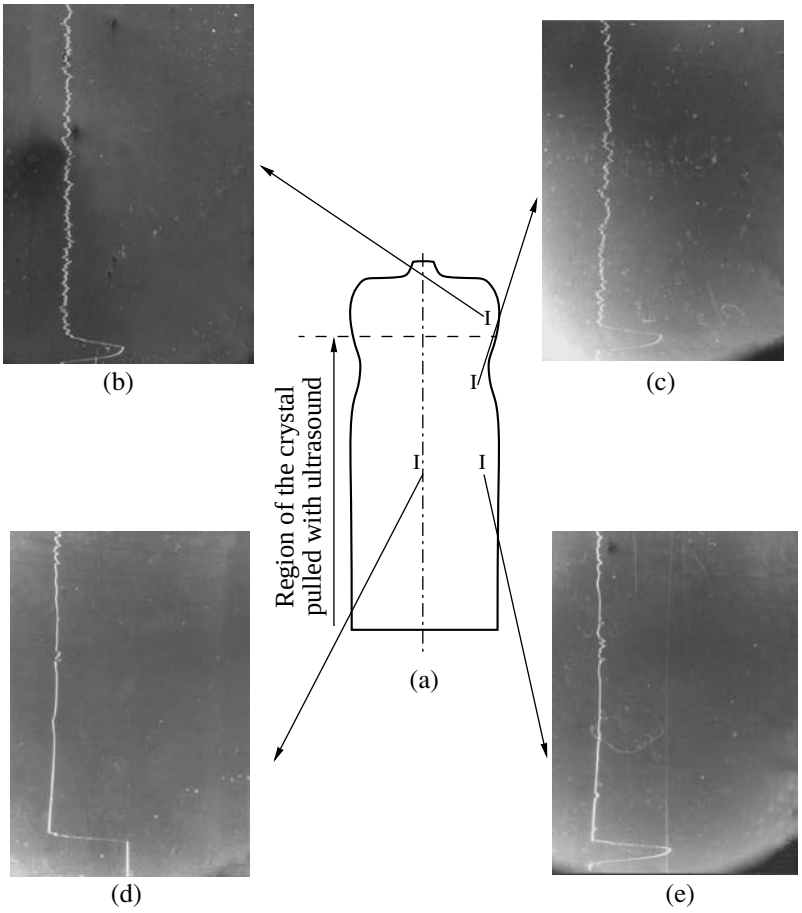

Fig. 3. Distribution of As in a GaAs single crystal grown with 0.15 MHz ultrasound: (a) pulled single crystal; (b) region of crystal growth without ultrasound; (c, d, e) regions of crystal growth with ultrasound in different parts of the single crystal.

crystal face was as large as 15 μm. After introducing ultrasonic waves into the melt, we did not observe any layers near the "face" (Fig. 2). However, it was impossible to eliminate thinner layers using ultrasound. Similar results were obtained for InSb single crystals grown using ultrasound with frequencies ranging from 0.25 to 10 MHz.

In contrast to most semiconductors, the Sb-enriched layers revealed in Bi–Sb single crystals were distributed nonuniformly in the crystal bulk and concentrated in limited regions, being oriented parallel or at an angle of 60° to the crystallization front. The interlayer distance ranged from 7 to 400 μm. The exposure to ultrasound completely eliminated the Sb layers in alloy single crystals of constant diameter. In Bi–Sb single crystals the initial parts of which were pulled with ultrasound we observed an aftereffect phenomenon: even after switching the ultrasound off, single crystals with constant diameters containing no layers grew over 2–2.5 h. Variations in the diameter of alloy single crystals were accompanied by the formation of Sb layers. It seems that this phenomenon is due to changes in the thermal conditions that affect convective flows in the melt.

We studied the distribution of As in the GaAs single crystals pulled with 0.15 MHz ultrasound. In the single crystals under study, the As-enriched layers were parallel to the crystallization front, and the interlayer distance was up to 140 μm. Figure 3 shows the distribution of As in the bulk of a GaAs single crystal. In the ultrasonic field, the distribution of As became more uniform only in the growth zone with a constant crystal diameter (Figs. 3d, 3e). Periodic switch-offs of the ultrasonic transducer facilitated the formation of inhomogeneity in the As distribution. The positive effect of ultrasound was observed only for single crystals grown from the melt 30 mm deep. When the melt depth was doubled, it was impossible to reduce the inhomogeneity of the As distribution under the influence of ultrasound, which may be caused by the enhanced convective mixing in the melt. The increase in the Rayleigh number by a factor of eight under these growth conditions lends additional support to this conjecture.

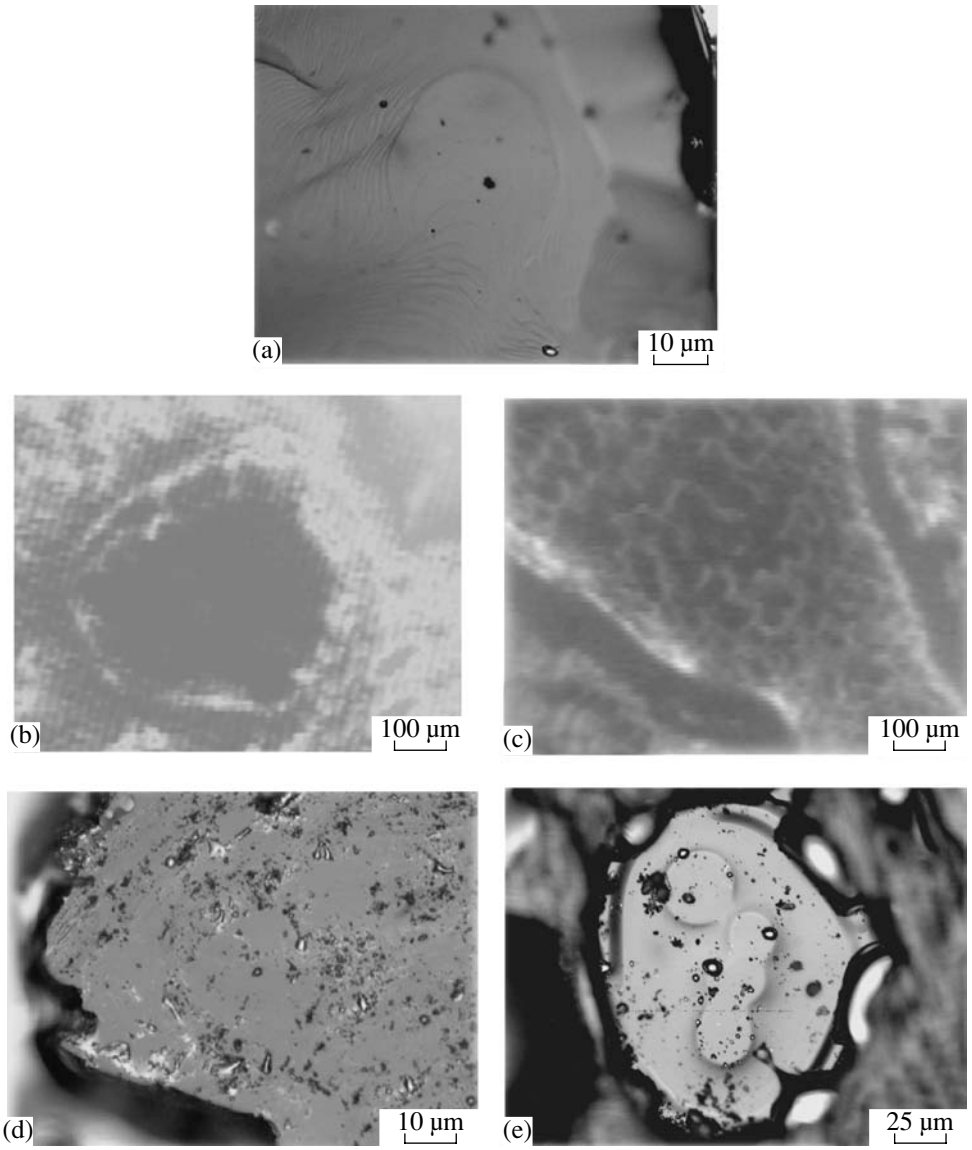

Fig. 4. Photographs of GaAs layers grown with 3 MHz ultrasound: (a) layers grown without ultrasound; (b) growth of a layer with a planar interface in the ultrasonic field; (c) growth with the concave interface using ultrasound; (d) layer with a planar interface grown in the ultrasonic field; (e) layers with a planar interface grown with periodical switching of the ultrasound on and off.

Figure 4a shows a typical photograph of epitaxial GaAs layers grown without ultrasound. As a rule, these layers had several macroscopic steps. The effect of ultrasound on the epitaxial growth was observed only for layers having a planar phase interface in the initial growth stage. In this case, the layers were piled up by atomically smooth surfaces without kinks and steps. (Figs. 4b, 4d). Superheating of the Ga solution by 3–5 K favored the concentration supercooling near the interface and the growth of layers in which several steps were observed even under the influence of ultrasound. The situation was similar to the growth from a nonplanar interface (Fig. 4c). Periodic switch-offs of ultrasound also caused the growth of several steps (Fig. 4e).

The use of the light-cut technique for modeling the effect of ultrasound on crystal growth by the Czochralski method (Fig. 5a) allowed us to observe the formation of standing waves in the volume of liquid between the end of the waveguide and the interface. We did not observe convective flows in this volume: Al_2O_3 particles did not move in the liquid but concentrated at antinodes of standing waves (Fig. 5b). Standing waves arose for 6–7 s after switching the ultrasound on. Disc rotation at a speed of up to 20 rpm (imitating the crystal growth), as well as the convex or concave interface shape, did not appreciably affect the dimensions of the cylindrical channel with standing waves. However, a significant increase in the vertical temperature gradient,

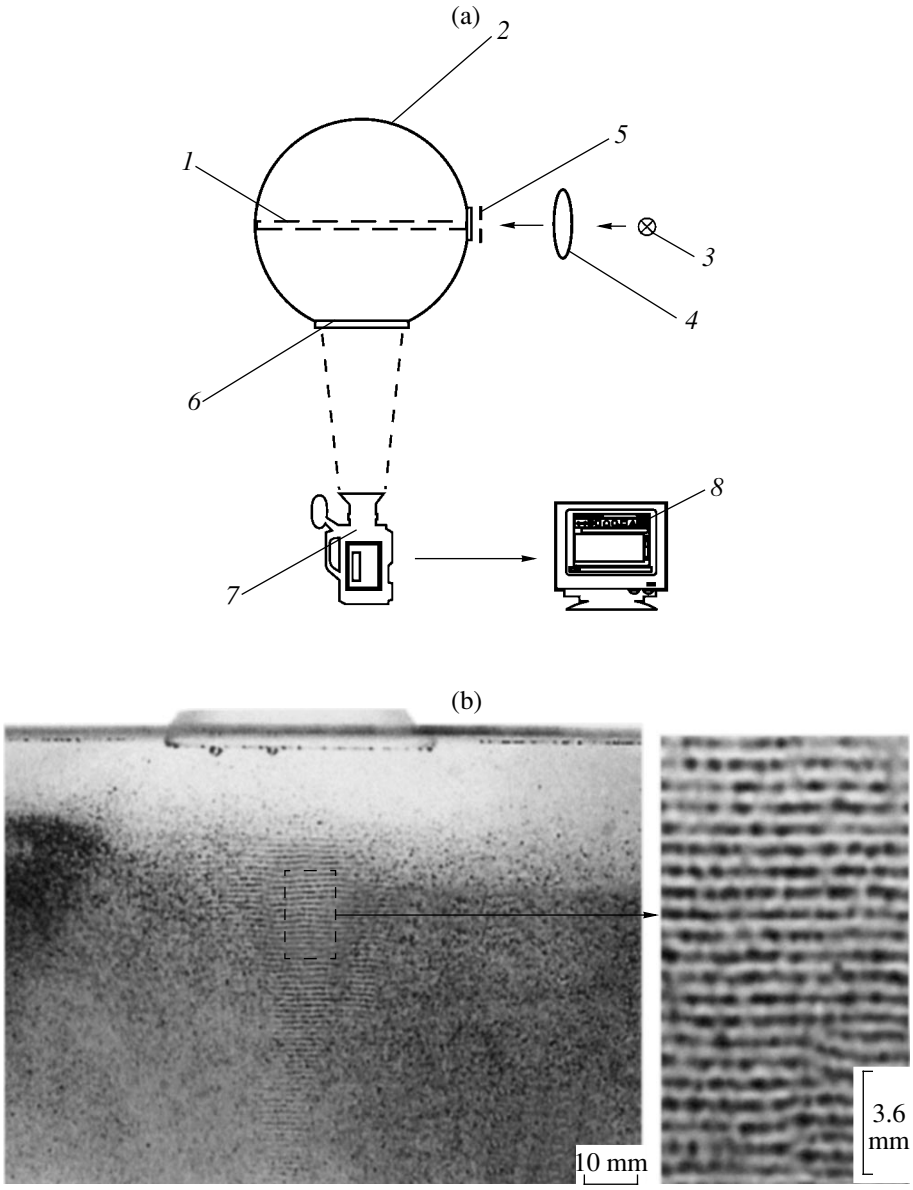

Fig. 5. (a) Schematic of the setup: (*1*) narrow light beam in water; (*2*) stainless-steel chamber; (*3*) light source; (*4*) focusing lens; (*5*) collimator; (*6*) inspection window; (*7*) digital camcorder; and (*8*) computer. (b) Photographs obtained using the light-cut technique and showing the convection in distilled water containing Al_2O_3 particles: standing waves in the ultrasonic field with a frequency of 1 MHz below the interface.

leading to the increase in the Rayleigh number in water (more than 10^5), destroyed the standing waves.

CONCLUSIONS

Similar behavior of the effect of ultrasound on the growth of single crystals from melt and epitaxial layers from a solution was observed only for growth from the planar phase interface towards which ultrasonic waves were directed. This may indicate the formation of standing ultrasonic waves in the liquid phase. Standing ultrasonic waves in melts can stabilize convective flows under the interface because the force F_{st} acting in these flows on a particle of radius R obeys the law $F_{st} \sim R$, whereas, for a traveling wave, we have $F_{tr} \sim R^4$ at very small R. The observation of the Czochralski growth modeled by the light-cut technique in distilled water containing Al_2O_3 particles by digital video recording gave clear experimental evidence of the formation of standing waves in the volume of liquid between the interface and waveguide.

REFERENCES

1. H. A. Chedzey and D. T. J. Hurle, Nature **210**, 933 (1966).

2. K. Hoshikawa, Jpn. J. Appl. Phys. **21**, L545 (1982).
3. V. S. Zemskov, M. R. Raukhman, D. Sh. Mgaloblishvili, *et al.*, Fiz. Khim. Obrab. Mater., No. 2, 64 (1986).
4. L. G. Kachurin, S. Kolev, and V. F. Psalomshchikov, in *Proceedings of All-Union Scientific Meeting on Electropulse Technology and Electromagnetic Processes in Loaded Solids* (Tomsk, 1982).
5. Y. Hayakawa, Y. Sone, K. Tatsumi, and M. Kumagawa, Jpn. J. Appl. Phys. **21**, 1273 (1982).
6. Y. Hayakawa and M. Kumagawa, Cryst. Res. Technol. **20**, 3 (1983).
7. T. Tsuruta, Y. Hayakawa, and M. Kumagawa, Jpn. J. Appl. Phys. **27**, 47 (1988).
8. G. N. Kozhemyakin, V. G. Kosushkin, and S. U. Kurochkin, J. Cryst. Growth **121**, 240 (1992).
9. G. N. Kozhemyakin and L. G. Kolodyazhnaya, J. Cryst. Growth **147**, 200 (1995).
10. G. N. Kozhemyakin, J. Cryst. Growth **149**, 266 (1995).
11. G. N. Kozhemyakin, Ultrasonics **35**, 599 (1998).
12. G. N. Kozhemyakin, RF Patent No. 2,035,530, Byull. Izobret., No. 14 (1995).

Translated by K. Kugel

Crystallography Reports, Vol. 49, No. 2, 2004, pp. 324–326. Translated from Kristallografiya, Vol. 49, No. 2, 2004, pp. 382–384.

CRYSTAL GROWTH

Behavior of the Resistivity of Metal Alloys during Collective Recrystallization[1]

Kh. P. Zhilokov, T. A. Orkvasov, and V. A. Sozaev

Kabardino-Balkarian State University, ul. Chernyshevskogo 173, Nal'chik, 360004 Russia

e-mail: sozaevv@kbsu.ru

Received March 3, 2003

Abstract—The kinetics of collective recrystallization in Sn–Pb, Sn–In, Sn–Zn, Pb–Sn, Pb–Bi, and Pb–In alloys have been studied using the conductivity method at $T = 180$°C. © *2004 MAIK "Nauka/Interperiodica".*

INTRODUCTION

The regularities of the grain growth in polycrystalline alloys have been intensively studied in view of the development of new nanocrystalline materials [1–4]. This problem is of interest because the grain size determines mechanical, electric, magnetic, and other properties of polycrystals.

Impurity atoms adsorbed on grain boundaries penetrate the grain bulk during collective recrystallization. The decrease in the grain-boundary area also contributes to this process. As a result, the degree of lattice distortion increases. In addition, the screened radius of impurity atoms in the grain bulk is larger than at the boundaries [5]. Due to these phenomena, the impurity contribution to the resistivity, $\Delta\rho = \rho - \rho_0$ (where ρ and ρ_0 are the resistivities of an alloy and a pure metal of the matrix, respectively), increases. Assuming that the increase in $\Delta\rho$ during the collective recrystallization is mainly due to the increase in the grain size D and that the recrystallization kinetics obeys the Beck relation [6], we obtain

$$\Delta\rho \sim D \sim t^n \quad (1)$$

or

$$\Delta\rho = k(t/t_0)^n, \quad (2)$$

where t is the annealing time, t_0 is the maximum duration of isochronous annealing (we used $t_0 = 3$ h in our experiments), and k and n are constants at a specified temperature.

For most pure metals, at $D \gg D_0$ (where D_0 is the initial grain size), $D \sim t^{1/2}$. The reason is that the proportionality factor has the meaning of the product of the boundary surface tension on the boundary mobility. Therefore, the proportionality factor has the dimension of the ratio of the squared length to time. Various factors may affect the value of the exponent n: composition, annealing temperature, preliminary treatment, alloy decomposition, effects of detachment of grain boundaries from an impurity cloud, and so on [7]. The aim of this study is to estimate the kinetics of collective recrystallization in alloys on the basis of tin and lead by a change in the resistivity during isochronous annealing.

Values of the parameters k and n in equation (2) for $T = 180$°C

Alloy composition	k	n	
		this study	data of [6]
Sn-0.4 at % Zn	0.059	0.12	0.15 (at 175°C)
Sn-0.5 at % Zn	0.046	0.14	
Sn-0.3 at % Pb	0.003	0.25	
Sn-0.5 at % Pb	0.003	0.29	
Sn-0.5 at % In	0.080	0.15	0.31 (at 180°C)
Sn-1.0 at % In	0.006	0.22	
Pb-0.1 at % Sn	0.005	0.17	
Pb-0.3 at % Sn	0.005	0.21	
Pb-0.5 at % Sn	0.005	0.24	
Pb-1.0 at % Sn	0.004	0.26	
Pb-0.1 at % In	0.003	0.14	
Pb-0.5 at % In	0.003	0.18	
Pb-1.0 at % In	0.002	0.27	
Pb-0.1 at % Bi	0.093	0.07	
Pb-0.3 at % Bi	0.072	0.12	
Pb-0.5 at % Bi	0.050	0.18	
Pb-1.0 at % Bi	0.041	0.29	

[1] This work was presented at the National Conference on Crystal Growth (NCCG-2002, Moscow).

1063-7745/04/4902-0324$26.00 © 2004 MAIK "Nauka/Interperiodica"

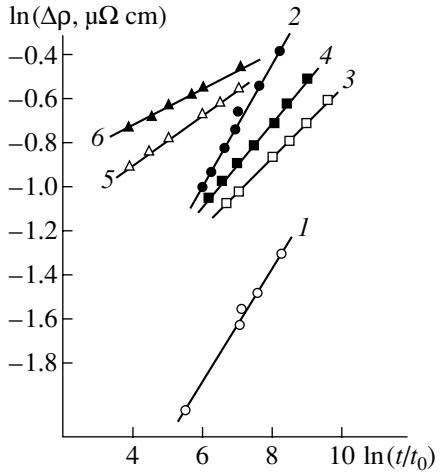

Fig. 1. Dependences of the impurity contribution to the resistivity, Δρ, on annealing time for the alloys Sn–Pb with (*1*) 0.3 and (*2*) 0.5 at % of Pb; Sn–Zn with (*3*) 0.4 and (*4*) 0.5 at % of Zn (4); and Sn–In with (*5*) 0.5 and (*6*) 1.0 at % of In.

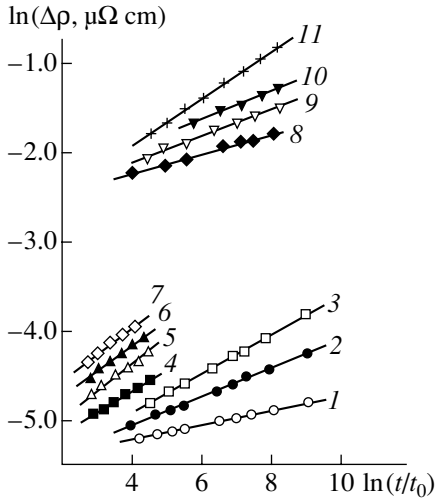

Fig. 2. Dependences of the impurity contribution to the resistivity, Δρ, on the annealing time for the alloys Pb–In with (*1*) 0.1, (*2*) 0.5, and (*3*) 1.0 at % of In; Pb–Sn with (*4*) 0.1, (*5*) 0.3, (*6*) 0.5, and (*7*) 1.0 at % of Sn; and Pb–Bi with (*8*) 0.1, (*9*) 0.3, (*10*) 0.5, and (*11*) 1.0 at % of Bi.

METHOD AND EXPERIMENTAL RESULTS

An extrusion technique for preparation of alloys based on Sn and Pb and experimental samples was described in [8]. The concentrations of the alloy components were chosen to be below the solubility limit for each system. Samples $120 \times 1.28 \times 0.88$ mm^3 in size were prepared by extruding alloy ingots through a spinneret with a rectangular aperture. Before the extrusion, the ingots were heated in a pressform to 150–160°C. Then, a wire was extracted, from which samples were cut. The samples were annealed in a thermostat filled with silicon oil for $t_0 = 3$ h at 180°C. During the annealing, the resistivity of the samples was measured by the four-probe compensation method using a P363-2 dc potentiometer.

It was found that the resistivity ρ of alloys increases nonlinearly during annealing at 180°C for 30 min and does not change within experimental error with a further increase in annealing time (more than 1 h).

The measurement results are shown in Figs. 1 and 2. The dependences of the impurity contribution to the resistivity, Δρ, on the annealing time in logarithmic coordinates for Sn- and Pb-based alloys are shown in Figs. 1 and 2, respectively. As can be seen from Figs. 1 and 2, the dependences lnΔρ on the annealing time are close to linear.

The equations of the straight lines $\ln\Delta\rho = f(\ln t/t_0)$ were found by the least-squares method and, then, the constant n was estimated. The values of n are listed in the table. It can be seen from the table that, for all the alloys under investigation, $n < 0.5$. With an increase in the concentration of impurity atoms, the values of n increase but do not exceed 0.3, which is characteristic of many Sn- and Pb-based alloys [6]. Apparently, the differences in the dependences of n on alloy composition are due to the different characters of the interrelations between the moving force for the grain migration and the energy of interaction of impurity atoms with grain boundaries [9].

In alloys of other metals, the behavior of n may be different. For example, it was found in [10] that the size of grains in nanocrystalline Ni_3P at 710 K is proportional to $\sim t^{1/2}$; i.e., $n = 0.5$ as in pure metals.

Thus, we studied the kinetics of the increase in the impurity contribution to the resistivity of Sn–Zn, Sn–In, Sn–Pb, Pb–Sn, Pb–Bi, and Pb–In alloys upon annealing at 180°C for 3 h. It was shown that, for all the alloys under study, the observed increase in the impurity contribution to the resistivity upon annealing (which is absent in pure Sn or Pb) can be described by the dependence $\Delta\rho = k(t/t_0)^n$. It has been ascertained that the values of the exponent n increase with an increase in the impurity concentration; however, $n < 0.3$, which is in agreement with the data in the literature on the kinetics of the grain growth in Sn- and Pb-based alloys.

ACKNOWLEDGMENTS

This study was supported by the Russian Foundation for Basic Research, project no. 02-02-1688.

REFERENCES

1. A. I. Gusev, Usp. Fiz. Nauk **168** (1), 55 (1998) [Phys. Usp. **45**, 49 (1998)].

2. R. A. Andrievskiĭ and A. M. Glezer, Fiz. Met. Metalloved. **88** (1), 50 (1999).
3. R. A. Andrievskiĭ and A. M. Glezer, Fiz. Met. Metalloved. **89** (1), 91 (2000).
4. N. P. Lyakishev, M. I. Alymov, and S. V. Dobatkin, Metally, No. 3, 3 (2003).
5. V. I. Arkharov, S. D. Vangengeĭm, I. B. Klyueva, and V. P. Serikova, Fiz. Met. Metalloved. **26** (2), 289 (1967).
6. N. L. Pokrovskiĭ and T. G. Smirnova, *Surface Phenomena in Melts and Solid Phases Formed* (Kab.-Balk. Kn., Nalchik, 1965).
7. V. E. Fradkov and L. S. Shvindlerman, *Structure and Properties of Internal Boundary Surfaces in Metals* (Nauka, Moscow, 1988), p. 213.
8. T. A. Orkvasov, P. A. Savintsev, V. A. Sozaev, and Kh. T. Shidov, Metally, No. 1, 98 (1995).
9. E. L. Maksimova, B. B. Straumal, and L. S. Shvindlerman, Fiz. Met. Metalloved. **63** (5), 885 (1987).
10. K. Lu, Scr. Metall. Mater. **25** (9), 2047 (1991).

Translated by Yu. Sin'kov